universität wien

DISSERTATION / DOCTORAL THESIS

Titel der Dissertation / Title of the Doctoral Thesis

„Of barriers and pathways: Understanding rare event mechanisms and their connection to system dynamics“

verfasst von / submitted by

Clemens Moritz Bsc Msc

angestrebter akademischer Grad / in partial fulfilment of the requirements for the degree of

Doktor der Naturwissenschaften (Dr.rer.nat.)

Wien, 2024 / Vienna, 2024

Studienkennzahl lt. Studienblatt / degree programme code as it appears on the student record sheet:	UA 796 605 411
Dissertationsgebiet lt. Studienblatt / field of study as it appears on the student record sheet:	Physik
Betreut von / Supervisor:	Univ.-Prof. Mag. Dr. Christoph Dellago

Für meine Eltern, Maria und Erwin.

Danksagung

Die Zeit, in der diese Dissertation entstanden ist, wie auch die Arbeit an ihr hat mich beruflich als auch privat in vielerlei Hinsicht geprägt. Im Folgenden möchte ich einigen Personen danken, die ein Teil der Entstehungsgeschichte dieser Arbeit waren.

Zutiefst dankbar bin ich meinen Eltern, Maria und Erwin. Das Vertrauen und die unbedingte Unterstützung, die ihr mir immer entgegengebracht habt, sind die Grundlage, die alles andere möglich gemacht hat. Bei jenen, die meinen Vater und mich kennen, besteht sicherlich auch kein Zweifel daran, dass seine Begeisterung für Physik und Wissenschaft auf mich abgefärbt hat und damit ihren Teil zu meinem Werdegang beigetragen hat. Vielen Dank euch beiden!

Herzlich bedanken möchte ich mich auch bei meinem Betreuer, Prof. Christoph Dellago, der mir die Arbeit in seiner Gruppe ermöglicht hat, mich organisatorisch und inhaltlich unterstützt hat, und dessen umfassendes Wissen und seine Fähigkeit physikalische Zusammenhänge zu erfassen, mir immer ein Vorbild sein wird. Weiters sei meinen Koautoren für ihre Beiträge zu dieser Arbeit gedankt: Andreas Tröster der mich bereits bei meiner Masterarbeit begleitet hat, Max Innerbichler, Marcello Sega und Phillip L. Geissler. Prof. Geisslers brillante physikalische Einsichten und prägnante Art, diese darzustellen, hatten einen entscheidenden Einfluss auf diese Arbeit.

Eine herausragende Eigenschaft der Dellago Gruppe ist die Hilfsbereitschaft, Offenheit und Diskussionsfreudigkeit, die ihre Mitglieder an den Tag legen. So habe ich viel Handwerkliches und viel Physik von meinen Kolleginnen und Kollegen gelernt, aber auch Freunde gefunden, bei denen ich mich für ihre Unterstützung bedanken möchte. Besonders richte ich mich hier an Andreas, Christian, Claudia, Georg, Jaffar, Martin, Philipp und Salvatore: danke für eure Hilfe, eure Freundschaft und euer offenes Ohr!

Und zu guter Letzt, Barbara: wenn ich zweifle, gibst du Vertrauen, wenn ich keinen Plan habe, denkst du zu Ende und wenn das alles nicht hilft, gehst du mit mir ein Schnitzi essen. Für all diese Unterstützung, vielen lieben Dank!

Contents

Part I.

Introduction

1. A short introduction to metastability and rare events

1.1. Metastability

In 1724 Daniel Gabriel Fahrenheit published his notes on *Experiments and Observations on freezing of water in vacuum* [1–4][1] that describe a surprising phenomenon he observed while experimenting with water. Fahrenheit prepared little glass spheres filled with water from which as much air as possible had been evacuated and then left the spheres out in the winter cold to freeze. Despite freezing overnight temperatures—a thermometer showed a temperature of roughly -9 °C in the morning—the water in some spheres was still liquid after they were left outside overnight. The water, however, could be coaxed into freezing (at least partially) by disturbing it, for example by letting air back into the spheres or by shaking them.

This is an example of *metastability*: when a system remains in a state for a considerable amount of time even though an energetically or otherwise more favorable state is available under the given conditions.

Metastability is ubiquitous in nature: ranging from short-lived phenomena like the nuclei of radioactive isotopes that may only exist for femtoseconds at a time to diamond that is a metastable form of carbon[2]—yet, the time it would take a spherical diamond with a diameter of 1 mm to transform into graphite can roughly be estimated to be 10^{20} times the age of the universe[3]. Or put differently: at ambient conditions diamond is for all intents and purposes *kinetically* stable. At the same time a more

[1] Original title: Experimenta & observationes de Congelatione aquae in vacuo factae

[2] Graphite is the stable phase of carbon under ambient conditions.

[3] This is a crude estimate arrived at by extrapolating the Arrhenius dependence observed by Butenko *et al.* [5] to a temperature of 293 K. This is an extrapolation of the data presented there into a range where such a transformation can not possibly ever be observed in experiment. The numbers should therefore be taken with a grain of salt.

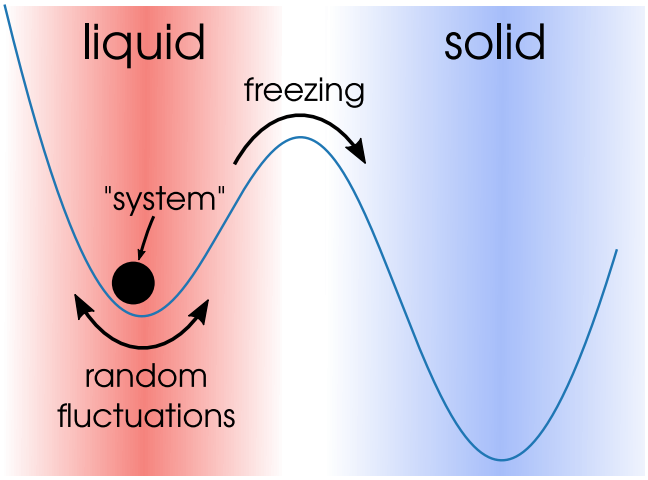

Figure 1.1.: Metastability is often visualized as the state of the system evolving in a landscape such as the one shown here. In order for freezing to occur a barrier has to be overcome first. Hence, even though the solid state is the thermodynamically preferred state for supercooled water (below 0 °C) the transition may not occur for some time.

favorable state does exist and it is therefore *thermodynamically* metastable. In between these two extremes many scientifically and technologically interesting systems can be found that also involve metastability of one kind or another. The transfer of electrons from one molecule to another [6], the folding of proteins [7, 8], or the formation and dissolution of traffic jams [9, 10] are just a few examples.

In physics and chemistry metastable systems are often illustrated using diagrams such as the one shown in Fig. 1.1. It pictures the state of a system of interest as a point that is located in one well (that represents the liquid state in the example of metastable water) and in order to transition to the lower and therefore more stable well, some sort of barrier has to be overcome first.

As a simple example, consider the escape of an α-particle from the nucleus of a radioactive atom. Two forces acting on the α-particle are relevant here [11, 12]: the strong force that is very short-ranged and that binds the α-particle to the nucleus and the electrostatic force that pushes the like-charges of the α-particle and the nucleus apart. The latter is long-ranged and therefore becomes the dominant force far from the nucleus. A sketch of the resulting potential energy landscape is shown on the left

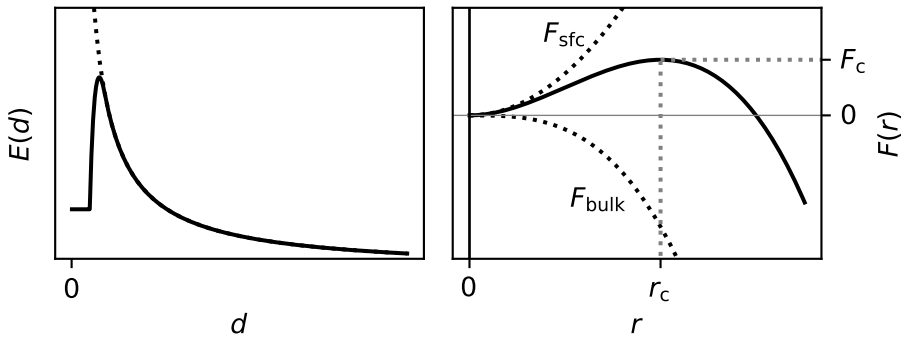

Figure 1.2.: Sketches of energy landscapes of systems that exhibit metastability. Left: Sketch of the potential energy of an α-particle bound to the nucleus of an atom as a function of the distance from the center, d [11, 12]. The dotted line is the contribution due to the Coulomb force. Right: Work required to form a small nucleus of a thermodynamically favorable phase inside another phase according to classic nucleation theory [13–15]. Here, r is the radius of the nucleus, F_{sfc} is the free energy contribution due to the surface of the nucleus (proportional to r^2), and F_{bulk} is the contribution from the internal parts of the nucleus, away from the surfaces (proportional to r^3). F_{c} is the maximum in free energy that has to be overcome.

in Fig. 1.2. In order to escape from the nucleus the α-particle has to get to the other side of the potential energy barrier and, hence, is initially stuck close to the nucleus even though separating from the nucleus and escaping is energetically favorable [4].

In the case of freezing water, the barrier that causes the metastability comes about because small ice crystals that form in the water (or on impurities or the container walls) have to grow against the surface tension that acts between ice and water [13–15] (see Fig. 1.2). This causes small crystals to melt away most of the time. However, at a critical nucleus size marked by r_{c} in Fig. 1.2, the work that can be extracted from ordering the molecules becomes larger than the work required to expand the interface by the corresponding amount. This causes the nuclei to grow spontaneously. The result is a (Gibbs- or Helmholtz) *free energy* barrier that has to be overcome by a

[4] This is indicated by the fact that the energy is lower at large d than close to the nucleus around $d = 0$.

small nucleus in order to grow (see Fig. 1.2). But when a nucleus has become larger than r_c it is likely to grow to macroscopic sizes because the total free energy can be lowered by growing the new, frozen phase.

So we know why some systems remain in a state that is not the global minimum. However, unstable atoms eventually decay and water does eventually freeze when it is put into freezing conditions. So how are these barriers overcome? The answer to this question depends on the system under scrutiny: in the case of α-decay the rules of quantum mechanics make it possible to cross the barrier without obtaining the required energy first[5].

In this thesis, however, I focus on systems that are treated classically. In this case barriers can be crossed with the help of the spontaneous rearrangement of molecules in the system [16] that occurs at finite temperature [6]. In super-cooled water these fluctuations sometimes, by chance, result in an ice nucleus that is larger than the critical radius r_c and so it is likely to continue to grow and eventually consume the liquid water that is available and turn it into ice. This process is known as *nucleation*. Hence, the question of how long it takes for water inside a container to freeze can be answered by determining how long it takes on average for nucleation to occur.

In addition to the time it takes for such an event to occur, we also want to understand how the event unfolds, i.e. what is the mechanism of the barrier crossing? For example, does the ice phase grow via the formation of a single cluster or via multiple clusters that coalesce at some point? Are the little ice-clusters that form spherical in shape, or do they form little needles? What is the crystal structure of these clusters?

Answers to the above questions are hard to come by using experiments alone because the time and length scales on which a barrier crossing happens are so small that measuring how individual atoms move at the precise instance a barrier crossing occurs is often not possible with presently available experimental techniques [4, 16]. Nevertheless, barrier crossings have been directly observed in experiments with select systems. For example, direct observations of protein folding using either force microscopy [17–22] or spectroscopic methods [23, 24] have been reported. Nucleation has been directly observed in protein clusters [25, 26] and using electron microscopy in systems of large molecules [27], as well as in constrained volumes such as inside carbon nanotubes [28] and in droplets [29].

[5] This is known as quantum mechanical tunneling
[6] This is the molecular motion that also causes *Brownian motion*.

In the case of freezing water the size of the critical structures is on the order of nanometers [30, 31] and the crossing of the nucleation barrier happens within 100s of picoseconds up to a couple of nanoseconds, depending on temperature [30]. Experimental methods that pick out structures this small in a bulk volume of water with the required time resolution to witness the mechanism of nucleus formation are not presently available.

Here, computer simulations become an important tool because we can build models where we have full knowledge about all degrees-of-freedom of the system, where we can control parameters we might not be able to control in an experiment, and where we can capture the complex interplay of the possibly many constituent parts of a system that can not be described using pen and paper alone. This allows us to form and test hypotheses regarding the mechanism of a given process, and to experiment with the model and its parameters in order to understand the key components of a system. However, these freedoms to tinker with a system come at a price: in the end we are only simulating a simplified model of the system of interest built inside our computers and, hence, conclusions about real physical processes based on results from computer simulations have to be drawn carefully and can sometimes only be made indirectly.

In this thesis I use computer simulations to investigate the mechanisms of barrier crossings in a number of different systems. These crossings share a common feature: they are so-called *rare events*.

1.2. Rare events and computer simulations

To explain what a rare event is, consider the example shown in figure Fig. 1.3. This is the result of a simple simulation of a particle that moves in a 1-dimensional potential energy landscape, $V(x)$, with two wells (denoted by A and B in Fig. 1.3). The particle is periodically pushed to the left or to the right by a random force, but the force that results from the potential energy pulls the particle toward the centers of the wells. In addition, a friction force acts on the particle that removes the energy added into the system by the random force so that the particle has a finite temperature [7]. The result is a trajectory where the particle stays close to the two minima in potential energy for

[7] Details on the simulation can be found in App. A.

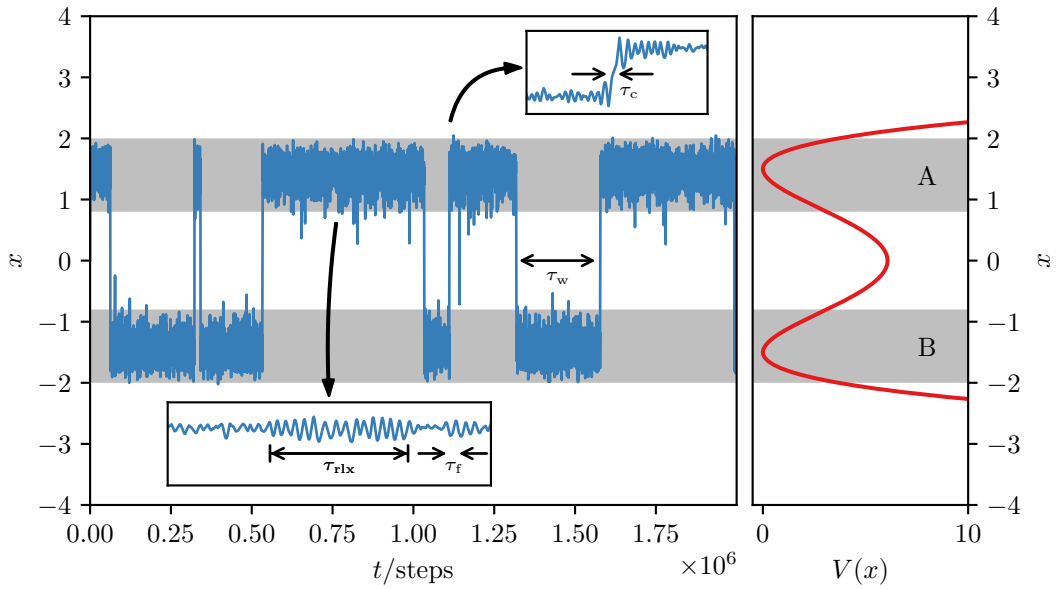

Figure 1.3.: Example trajectory of a particle in a double well potential that is subject to a random force and to friction. Insets show magnifications of the trajectory. Marked are examples of the basic oscillation period of the particle's movement close to the potential minima (τ_f), of the time it takes for an excitation of the particle's energy to form and decay again (τ_{rlx}), of the time it takes a particle to cross from one potential energy well to the other (τ_c), and of the waiting time until a crossing occurs (τ_w).

most of the time. However, sometimes, when the movement of the particle and the pushes by the random force combine in the right way, the particle switches from one basin to the other in a fast transition.

This behavior of long quiescent periods where the system stays within a basin that are interrupted by fast switching events between the basins, is prototypical for rare events. To put this behavior into more technical terms, we observe that there are four different *timescales* that can be identified from the graph:

1. the period of the oscillations in particle position close to the bottoms of the potential energy wells, τ_f,

2. the characteristic time it takes for a fluctuation of the particle's energy to form and relax again, τ_{rlx},

3. the average waiting time between two successive barrier crossings, τ_{w}, and

4. the average time the barrier crossing itself takes, τ_{c}, measured from leaving one basin to arriving at the other basin.

The fact that τ_{rlx} is much smaller than τ_{w}—i.e., we expect many fluctuations in the particles energy to appear and decay before a crossing occurs—is an example of a *separation of timescales* and the crossing event is a rare event [16, 32, 33]. This property,

$$\tau_{\mathrm{rlx}} \ll \tau_{\mathrm{w}}, \tag{1.1}$$

implies that the way the barrier crossing occurs does not depend on the details of how the system was prepared initially. This is because the system "forgets" the initial condition it was prepared in during the many fluctuations that occur between preparing the system and the eventual crossing. This makes it possible to think of a rare event as connecting two sets of states $\mathcal{A}$ and $\mathcal{B}$ that is characterized by a single reaction rate $r \sim \tau_{\mathrm{w}}^{-1}$, rather than considering different ensembles of crossings for each initial condition, each associated with their own average waiting time [16] [8].

From the point-of-view of computer simulations, another important timescale is τ_{f} because it determines the timespans we are able to simulate. In order for our simulation to resolve the vibrations of the particle, we have to use a timestep that is smaller than τ_{f} by about an order of magnitude, or more generally, the timespan we can cover using a simulation is determined by the timescale of the fastest process we want to include in our simulations [37] together with the computational demands of our simulation and the computing power available to us. Hence, the number of simulation steps required to simulate a rare event is approximated by the ratio $\tau_{\mathrm{w}}/\tau_{\mathrm{f}}$ as this is the approximate number of simulation steps that need to be done in order to see a single event. If we want to gather a sufficient number of these events to be able to do statistics, the number of simulation steps required grows even further.

For many barrier crossings $\tau_{\mathrm{w}}/\tau_{\mathrm{f}}$ is exceedingly large. Take the example of freezing

[8] Two notes are in order here: first, the separation $\tau_{\mathrm{rlx}} \ll \tau_{\mathrm{w}}$ is only one possibility. In what is known as the *energy-diffusion limit*, the timescale of energy dissipation τ_{rlx} itself is the limiting factor for the rate of a reaction, i.e. $\tau_{\mathrm{rlx}} \approx \tau_{\mathrm{w}}$ [34–36]. In this case, the separation of timescales can be found between the bath coupling timescale γ^{-1} and τ_{w}. Second, in more complex systems we are usually presented with multiple processes associated with different timescales occuring at the same time resulting in a spectrum of timescales. In this case, rare events are characterized by gaps in this spectrum.

water: freezing did not occur for hours during a freezing night in Fahrenheit's experiments, so the barrier crossing timescale is at least on the timescale of hours or roughly 10^3 seconds. On the other hand bond-stretching vibrations in water molecules occur on the order of femtoseconds, or 10^{-15} s resulting in a ratio between the two of 18 orders of magnitude.

At first glance such a separation of timescales in a rare event is devastating for our chances to use computer simulations to investigate it. Anton 3, the fastest supercomputer for performing molecular dynamics simulations in operation at the time of writing, reports impressive simulation rates of 121.1 µs per day simulating a satellite tobacco mosaic virus (STMV) system comprised of roughly one million atoms [38]. Nevertheless, performing a simulation that covers the timespan of one hour still requires a wallclock time of roughly 80000 years.

Fortunately, many rare events can be approached in a different manner due to the fact that the crossing timescale τ_c itself is accessible to computer simulations. By focussing our simulation time on the parts of trajectories where a barrier crossing happens and reducing the simulation time that is spent on the system being close to the stable basins of the system we can investigate the barrier crossings even though a full continuous trajectory that contains a barrier crossing is out of reach for our simulations [16].

These circumstances have led to the development of a large and ever-increasing number of simulation methods that try to do exactly that: gain an accurate understanding of the rates of rare events and their mechanism while reducing the computational effort required to do so. Comprehensive reviews about these methods can be found e.g. in Refs. [16, 39]. Here, however, I want to introduce two key concepts that are used in many of these methods: collective variables and free energy landscapes.

2. Exploring rare events

2.1. Collective variables and free energy landscapes

Many systems that feature rare events have many more degrees of freedom than the one-dimensional system presented in the previous section. Consider the example of n-butane: a simple organic molecule that consists of four carbon atoms and ten hydrogen atoms (see Fig. 2.1). The backbone of this molecule takes on different conformations that are usually described in terms of the relative position of the two methyl (CH_3) groups at either end of the molecule. The C-C bonds that attach these groups to the central pair of C atoms (bonds 1-2 and 3-4 in Fig. 2.1) form a dihedral angle about the central C-C bond (2-3) that is denoted by ϕ.

Figure 2.2 shows an example of the time evolution of ϕ obtained from an equilibrium classical MD trajectory and the distribution of ϕ observed during the trajectory. Three conformational states can be identified: the trans- or anti conformation where the methyl groups point in opposite directions ($\phi \approx \pi$), and two gauche conformations where $\phi \approx \frac{\pi}{3}$ and $\phi \approx \frac{5\pi}{3}$. Also here we find that the transitions between these states happen much faster than the waiting times between them, making them rare events.

The classical MD simulation that was used to generate this trajectory is based on integrating the classical equations of motion starting from an initial state $\{\mathbf{x}_0^N, \mathbf{p}_0^N\}$ where $\mathbf{x}_0^N$ and $\mathbf{p}_0^N$ are the positions and momenta of the molecule's 14 particles[1] at time $t = 0$. The result is a trajectory in the (6×14)-dimensional phase space spanned by the positions and momenta of the particles. Working directly with this high-dimensional description—i.e., by inspecting it using a visualization package to inspect the positions and movement of the particles in 3-dimensional space over time—is often the first step in analyzing simulation results.

However, to do quantitative analysis such as counting the number of transitions

[1] We do not simulate solvent particles here. Instead the molecule is coupled to a bath by a stochastic equation of motion.

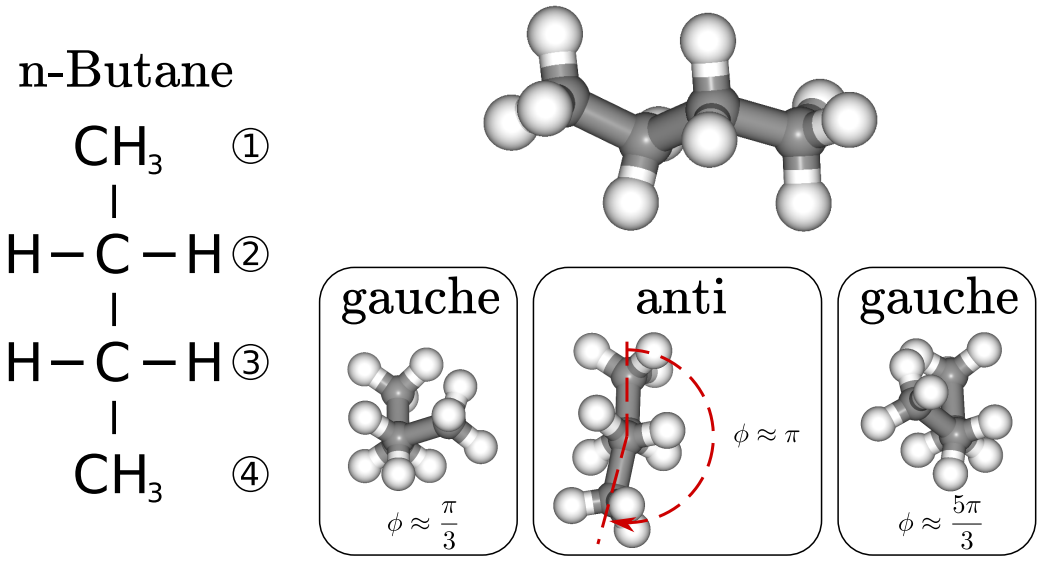

Figure 2.1.: Structural formula (left) and sketch of an n-butane molecule (top right) and its conformational states (bottom right).

between states and calculating rates usually requires a lower dimensional representation of the systems state. In this thesis I will refer to quantities that are functions of the positions and momenta of the constituent particles of a system as *collective variables*. A collective variable that indicates whether a system is in a certain state will be referred to as an *order parameter* for the transitions between states it can identify [16, 49]. The dihedral angle ϕ is an order parameter for the anti-gauche transition in n-butane.

Given a collective variable we can now introduce one of the basic concepts used to analyze systems with rare events: *free energy landscapes*[2].

Consider a system of N particles governed by the Hamiltonian

$$\mathcal{H}(\mathbf{x}^N, \mathbf{p}^N) = \sum_{i=1}^{N} \frac{\mathbf{p}_i^2}{2m_i} + U(\mathbf{x}_1, \ldots, \mathbf{x}_N), \tag{2.1}$$

where $\mathbf{x}_i$ and $\mathbf{p}_i$ are 3-dimensional vectors that represent the position and momentum of

[2] I use the term landscape here to differentiate from the free energy $F = -k_B T \log Z$ where Z is the partition function. Such landscapes are often referred to as Landau free energies [16].

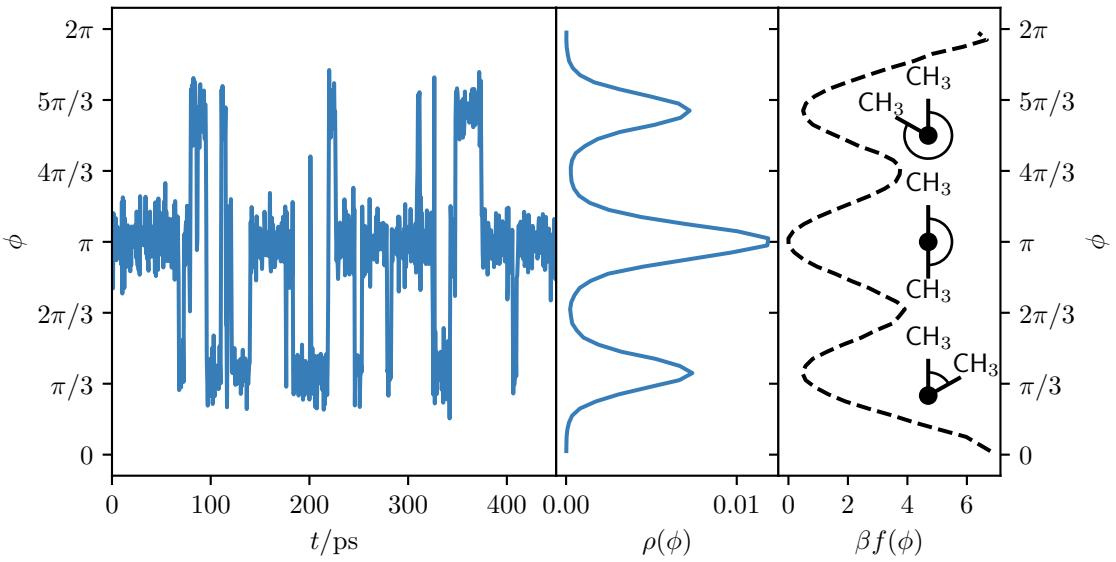

Figure 2.2.: Left: time evolution of the dihedral angle $\phi(t)$ of an n-butane molecule as obtained from a molecular dynamics simulation using the OpenMM simulation package [40–45] with the OPLS-AA model [46–48]. A Langevin-type integrator was used. Right: distribution of dihedral angles (blue bars), $\rho(\phi)$, and the associated reduced free energy $\beta f(\phi) = -\log \rho(\phi) + c$. The shift c has been chosen so that the minimum value of βf is zero. The total length of the simulation used to calculate ρ and f is 50 ns.

particle i, m_i is the mass of particle i, and $U(\mathbf{x}_1, \ldots, \mathbf{x}_N)$ is a potential energy that only depends on the collection of particle positions $\mathbf{x}^N$. The state of the system is determined by the positions and momenta of all particles and is denoted by $\{\mathbf{x}^N, \mathbf{p}^N\}$. In the classical limit ($\hbar \to 0$) of the canonical (or NVT-) ensemble, the probability of finding a system in the phase space volume enclosed by $\{\mathbf{x}^N, \mathbf{p}^N\}$ and $\{\mathbf{x}^N + \mathrm{d}\mathbf{x}^N, \mathbf{p}^N + \mathrm{d}\mathbf{p}^N\}$, where $\mathrm{d}\mathbf{x}^N$ and $\mathrm{d}\mathbf{p}^N$ are infinitesmal displacements, is given by [50]

$$P(\mathbf{x}^N, \mathbf{p}^N)\,\mathrm{d}x^{3N}\mathrm{d}p^{3N} = \frac{1}{Q_{NVT}} \frac{e^{-\beta\mathcal{H}(\mathbf{x}^N, \mathbf{p}^N)}}{(2\pi\hbar)^{3N} N!}\,\mathrm{d}x^{3N}\mathrm{d}p^{3N}, \tag{2.2}$$

where Q_{NVT} is the canonical partition function

$$Q_{NVT} = \frac{1}{(2\pi\hbar)^{3N}\, N!} \int \mathrm{d}x^{3N}\mathrm{d}p^{3N} e^{-\beta\mathcal{H}(\mathbf{x}^N, \mathbf{p}^N)} \tag{2.3}$$

that normalizes the distribution and $P(\mathbf{x}^N, \mathbf{p}^N)$ is the canonical probability density. The integration $\int \mathrm{d}x^{3N}\mathrm{d}p^{3N}$ runs over the $6N$ position and momentum components. The canonical expectation value of an observable $\mathcal{O} = \mathcal{O}(\mathbf{x}^N, \mathbf{p}^N)$ is therefore given by

$$\langle \mathcal{O} \rangle = \frac{\int \mathrm{d}x^{3N}\mathrm{d}p^{3N} e^{-\beta \mathcal{H}(\mathbf{x}^N, \mathbf{p}^N)}\, \mathcal{O}(\mathbf{x}^N, \mathbf{p}^N)}{\int \mathrm{d}x^{3N}\mathrm{d}p^{3N} e^{-\beta \mathcal{H}(\mathbf{x}^N, \mathbf{p}^N)}}. \tag{2.4}$$

For our purposes we will focus on observables that only depend on the positions of particles $A = A(\mathbf{x}^N)$, which allows us to simplify this expression by integrating over the momenta. This calculation yields

$$\langle A \rangle = \frac{1}{Z} \int \mathrm{d}x^{3N} e^{-\beta U(\mathbf{x}^N)}\, A(\mathbf{x}^N), \tag{2.5}$$

where Z is the so-called configuration integral $Z = \int \mathrm{d}x^{3N} e^{-\beta U(\mathbf{x})}$. By integrating over the momenta in Eq. (2.2) we arrive at the probability density in configuration space

$$P_{\mathrm{c}}(\mathbf{x}^N) = \frac{1}{Z} e^{-\beta U(\mathbf{x}^N)}. \tag{2.6}$$

Suppose now that we have set of n collective variables $\{\psi_1, \ldots, \psi_n\}$, where each of the variables is a function of the positions of particles in the system: $\psi_i = \psi_i(\mathbf{x}^N)$. The probability density projected into the space spanned by the ψ_i can be written as [4, 50, 51]

$$\begin{aligned} \rho(\tilde{\psi}_1, \ldots, \tilde{\psi}_n) &= \frac{1}{Z} \int \mathrm{d}x^{3N} e^{-\beta U(\mathbf{x}^N)} \prod_{i=1}^{n} \delta(\tilde{\psi}_i - \psi_i(\mathbf{x}^N)) \\ &= \left\langle \prod_{i=1}^{n} \delta(\tilde{\psi}_i - \psi_i(\mathbf{x}^N)) \right\rangle. \end{aligned} \tag{2.7}$$

The free energy landscape in the space spanned by the ψ_i is then defined as:

$$f(\tilde{\psi}_1, \ldots, \tilde{\psi}_n) = -k_{\mathrm{B}} T \log \left(\frac{\rho(\tilde{\psi}_1, \ldots, \tilde{\psi}_n)}{\rho_0} \right), \tag{2.8}$$

where ρ_0 is a constant that represents a global shift of the values of f but has otherwise no physical consequence. Examples of these concepts are shown in Fig. 2.2 where the probability density ρ and the dimensionless free energy βf are plotted as a function of

the dihedral angle ϕ. The preferred conformations of the molecule can be mapped to the minima in the free energy landscape and these states are separated by free energy barriers of differing height.

Free energy landscapes and the associated probability densities are an important tool in the analysis of rare event systems. They provide a quantitative representation of the likely states a system can be in, are an important ingredient to many rate calculation methods, and can be calculated efficiently as long as the number of collective variables is kept low.

However, they also have their limitations. In interpreting free energy landscapes we have to be aware that they are always tied to the collective variables used to construct them [4, 52]. A particular variable may not be able to distinguish some important states, keeping them hidden from our analysis and the shape of a free energy landscape can be changed by applying any non-linear coordinate transformation to the collective variables it spans [52] [3]. Furthermore, while the relationship between ρ and the free energy f that follows from (2.8),

$$\rho(\tilde{\psi}_0, \ldots, \tilde{\psi}_n) = \rho_0 \, e^{-\beta f(\tilde{\psi}_0, \ldots, \tilde{\psi}_n)}, \tag{2.9}$$

is reminiscent of the relationship between the configurational density Eq. (2.6) and the potential energy U, the derivative of f with respect to the ψ_i should not be taken as an indication of the direction a system evolves in next—not even on average. In general the projection $\mathbf{x}^N \to \{\psi_i\}$ does not retain the full state information about the system, meaning that in principle very different states may be mapped to the same values of ψ_i. Depending on which of these states the system is actually in when we see a certain set of values ψ_i, the prediction of the states the system evolves next to may be different.

But even if only roughly similar states are mapped to the same collective variable values, the dynamics that result from the projection of the full dynamics to the space spanned by the ψ_i is likely to be different along different directions. This is because the ψ_i are usually designed to capture different physical processes within the system that themselves proceed on different timescales and, hence, the ψ_i also proceed on different timescales. In the following section I will demonstrate the effect such a difference in

[3] For example, the nucleation free energy landscape associated with an ice nucleus that forms during freezing depends on whether we choose the radius or its volume to describe its size.

dynamics can have on the likely pathways within a system using a simple diffusive toy model.

2.2. Static vs. dynamic quantities and the transition path ensemble

To facilitate the following discussion note that for an equilibrium system the quantities ρ and f presented in the previous section only depend on the potential energy of the system and on temperature. In this thesis I refer to such observables as *static observables*. However, in order to perform a computer simulation we need to also specify the time evolution rules the system will follow. This may be a deterministic scheme such as molecular dynamics with a deterministic thermostat, a stochastic integration scheme such as a Monte Carlo simulation, or any other method that yields an equilibrium distribution in the limit of long simulation runs. The particular choice of simulation method depends on the system and on the goals of our simulation. However, while the equilibrium distributions that these methods produce are the same, the details of the trajectories themselves differ and, hence, we can find observables that will be different depending on the choice of integration scheme. I will refer to quantities that depend on the choice of dynamics as *dynamic observables* [4].

Both the reaction rate of a rare event as well as the pathway that is taken during a rare event are dynamic observables. To demonstrate that this is the case [5], consider the following 2-dimensional system of overdamped Langevin equations:

$$\begin{aligned} \mathrm{d}x_1(t) &= -\beta D_1 \frac{\partial u(\mathbf{x}(t))}{\partial x_1}\mathrm{d}t + \sqrt{2D_1}\,\mathrm{d}W_1(t) \\ \mathrm{d}x_2(t) &= -\beta D_2 \frac{\partial u(\mathbf{x}(t))}{\partial x_2}\mathrm{d}t + \sqrt{2D_2}\,\mathrm{d}W_2(t) \end{aligned} \tag{2.10}$$

Here $\mathbf{x}$ is the two dimensional vector made up of components x_1 and x_2, $u = u(\mathbf{x})$ is the potential energy and the $W_i(t)$ are Wiener processes with variance $\mathrm{Var}\,[W(t)] = t$. The parameters D_i are diffusion coefficients along the two coordinates. These equations

[4] This nomenclature aims to avoid the association of dynamic observables with the term non-equilibrium. Dynamic observables can be found both in equilibrium and in non-equilibrium systems and simulations.

[5] This demonstration is inspired by the work of Metzner *et al.* [53].

can also be written in the form

$$\mathrm{d}x_i(t) = -\beta \sum_{j=1}^{2} D_{ij} \frac{\partial u(\mathbf{x})}{\partial x_j} \mathrm{d}t + \sum_{j=1}^{2} g_{ij} W_j(t) \tag{2.11}$$

where $D_{ij} = D_i \delta_{ij}$ (without summation convention) and $g_{ij} = \sqrt{2D_i}\delta_{ij}$ are both diagonal matrices and δ_{ij} is Kronecker's delta. For long trajectories the position distributions of the solutions of these stochastic differential equations approach the equilibrium distribution [54]

$$\rho_{\mathrm{equ}}(\mathbf{x}) = \frac{1}{Z} e^{-\beta u(\mathbf{x})}, \tag{2.12}$$

where $Z = \int \mathrm{d}x_1 \, \mathrm{d}x_2 e^{-\beta u(\mathbf{x})}$. Notice, that the equilibrium distribution is independent of the diffusion coefficient.

To convince ourselves of this fact, consider the potential energy landscape $u(\mathbf{x})$ shown in the background of Fig. 2.3. This potential is the sum of four hard walls that form a square shaped well and four Gaussians, two with a negative prefactor that form minima in the energy landscape on the bottom-left and the top-right and two with a positive prefactor centered on the top-left and the bottom-right [6].

To perform simulations I use a simple Euler integration scheme [54], namely (with $x_i^j = x_i(j\Delta t)$)

$$\mathbf{x}^{j+1} = \mathbf{x}^j - \beta \Delta t D \cdot \nabla u(\mathbf{x})|_{\mathbf{x}=\mathbf{x}^j} + \sqrt{2\Delta t D} \cdot \zeta^j, \tag{2.15}$$

where the ζ^j are a sequence of two-dimensional vectors where each component is drawn from a Gaussian probability distribution with zero mean and unit variance. Figure 2.3 shows two trajectories obtained from simulations with different ratios of diffusion coefficients D_1/D_2: one where $D_1 = D_2$ and one where $D_1 = 10\, D_2$, resulting in markedly different trajectories.

Nevertheless, for long trajectories the distributions of the positions observed in the

[6] The potential is given by the function (in dimensionless units)

$$u(\mathbf{x}) = -G(\mathbf{x}; -0.5, -0.5) - G(\mathbf{x}; 0.5, 0.5) + G(\mathbf{x}; -0.5, 0.5) + G(\mathbf{x}; 0.5, -0.5) + \sum_i x_i^6, \tag{2.13}$$

where

$$G(\mathbf{x}; c_1, c_2) = \exp\left[-12\,(x_1 - c_1)^2 - 12\,(x_2 - c_2)^2\right]. \tag{2.14}$$

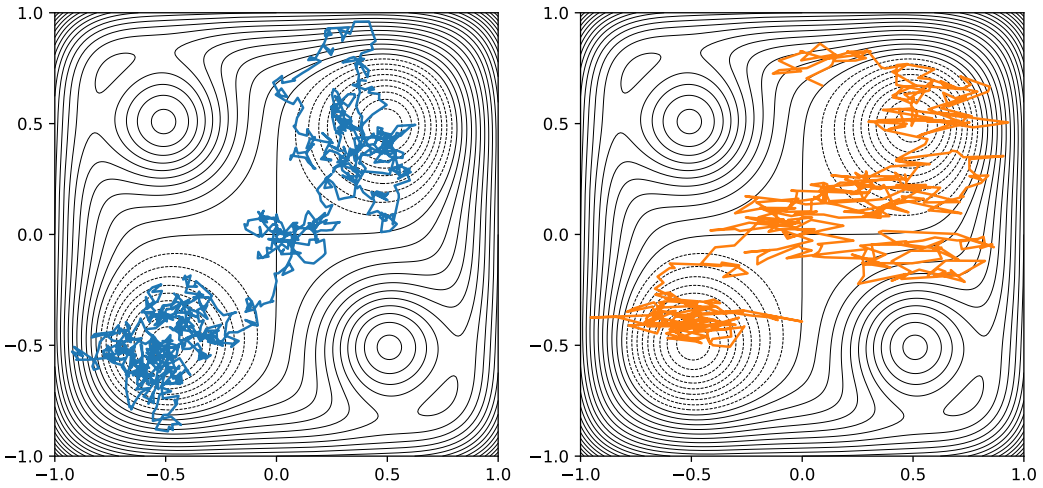

Figure 2.3.: Example trajectories governed by Eq. 2.11 with $D_1 = 1, D_2 = 1$ (left) and $D_1 = 10, D_2 = 1$ (right). Solid isolines indicate positive values of the potential $f(\mathbf{x})$ and dashed lines indicate negative values. Isolines are drawn in increments of 0.1 energy units and the temperature is set to $0.5/k_\mathrm{B}$.

simulations approach each other, as can be seen in Fig. 2.4, where empirical estimates of the free energy landscapes are shown. Note, that the landscapes have been shifted so that their value at $x_1 = 0, x_2 = 0$ is zero. The resulting estimated free energy landscapes are shown in Fig. 2.4. Except for some deviations in areas of low population (or high energy) that are due to the finite length trajectories used to calculate the estimate, the two landscapes are very close to each other despite the differences in the dynamics of the system.

Even though the equilibrium distributions in the two systems are the same, the pathways along which the system evolves are not—including the transition pathways between the two potential energy minima. To demonstrate the effect of the different dynamics on the transition pathways I first define two regions in configuration space

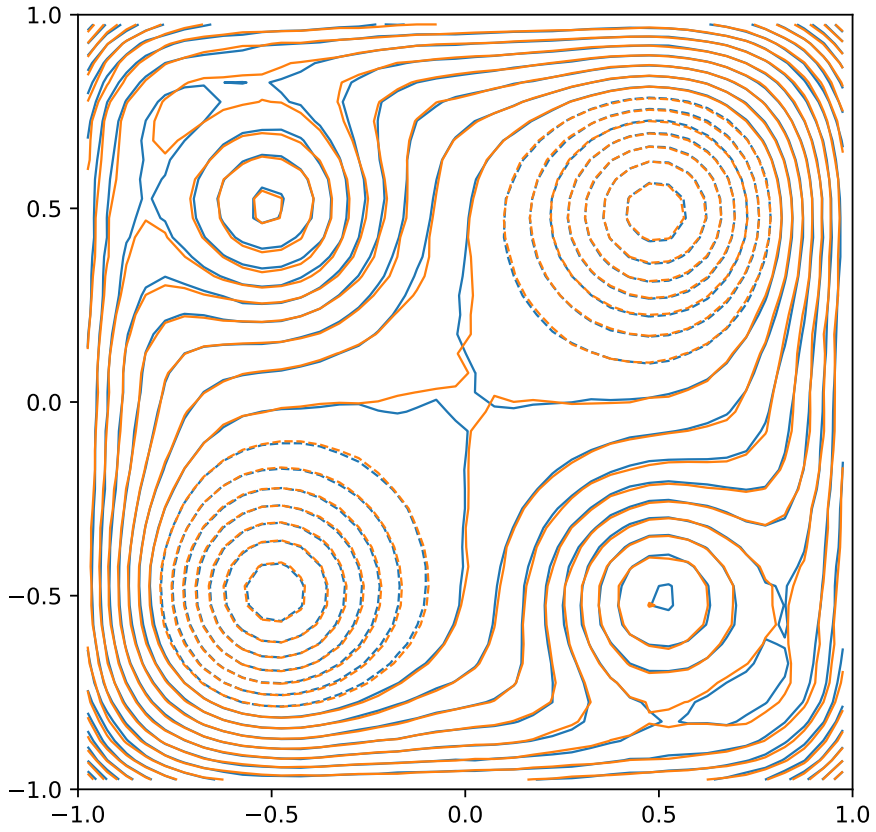

Figure 2.4.: (Free) energy landscapes estimated by histogramming the locations visited by long simulation runs where $D_1 = D_2$ (blue isolines) and where $D_1 = 10\,D_2$ (orange isolines). Isolines are spaced in increments of $k_\mathrm{B}T/2$. The energy values have been shifted so that the value at location $(0, 0)$ is 0. Dashed isolines represent negative values and solid lines positive values.

(see Fig. 2.5). Region $\mathcal{A}$ encompasses the lower left minimum of $u(\mathbf{x})$ and region $\mathcal{B}$ contains the minimum in the upper right corner of Fig. 2.4:

$$\begin{aligned} \mathcal{A} &= \{\mathbf{x} | x_1 < -0.25 \wedge x_2 < -0.25\} \\ \mathcal{B} &= \{\mathbf{x} | x_1 > 0.25 \wedge x_2 > 0.25\} \end{aligned} \tag{2.16}$$

The *transition path ensemble* (TPE) between states $\mathcal{A}$ and $\mathcal{B}$ is the collection of

trajectories that have a starting point in $\mathcal{A}$, an endpoint in $\mathcal{B}$ and all other points that are part of the trajectory are outside both regions[7]. The top part of Fig. 2.5 shows example trajectories from the $\mathcal{A} \to \mathcal{B}$ TPE. These were obtained by performing TPS simulations [56–58] with flexible path length [59] using the OpenPathSampling simulation package [60, 61] and a custom implementation of the integrator (2.15). As you can already see in this figure, the transition pathways differ quite significantly from each other. This becomes even more apparent in the the lower part of Fig. 2.5 that shows the related *transition path density*, $\rho(\mathbf{x}|\mathrm{TP})$, which is the conditional probability density of points in configuration space given that they are part of a transition path [62, 63]. As you can see, this distribution strongly depends on the ratio of the diffusion coefficients even though the equilibrium distribution is unaffected. Hence, the same free energy landscape is compatible with different transition path ensembles that arise from different time-propagation rules in the system.

2.3. Reaction coordinates and the committor

Another important concept used in rare event analysis is the *committor probability* [65–68] (or the *committor*). Given two regions in configuration space $\mathcal{A}$ and $\mathcal{B}$, and a configuration $\mathbf{x}$, the committor $p_{\mathcal{B}}(\mathbf{x})$ for the transition from $\mathcal{A}$ to $\mathcal{B}$ is the probability that trajectories started from $\mathbf{x}$ with randomly chosen momenta reach state $\mathcal{B}$ before they reach state $\mathcal{A}$. If the studied system has a stochastic component, one usually also samples over different noise histories.

For equilibrium systems that are complex and/or stochastic in nature, the committor associated with a configuration is in many ways an ideal *reaction coordinate* as it is a well defined measure for how far a configuration has progressed along a transition pathway [63, 69]. Furthermore it can be used to define the *transition state ensemble* (TSE) by identifying the states where $p_{\mathcal{B}} = \frac{1}{2}$[8]. The TSE in turn delineates the basins of attraction of the state $\mathcal{A}$ and $\mathcal{B}$. For diffusive barrier crossings the committor has been shown to be closely connected to the rate of a diffusive barrier crossing and to the associated optimal one-dimensional reaction coordinate [62, 70].

[7] I use here the definition by E & Vanden-Eijnden [55] that does not include a length constraint on the trajectories that are part of the TPE.
[8] This is often also referred to as the *stochastic separatrix*.

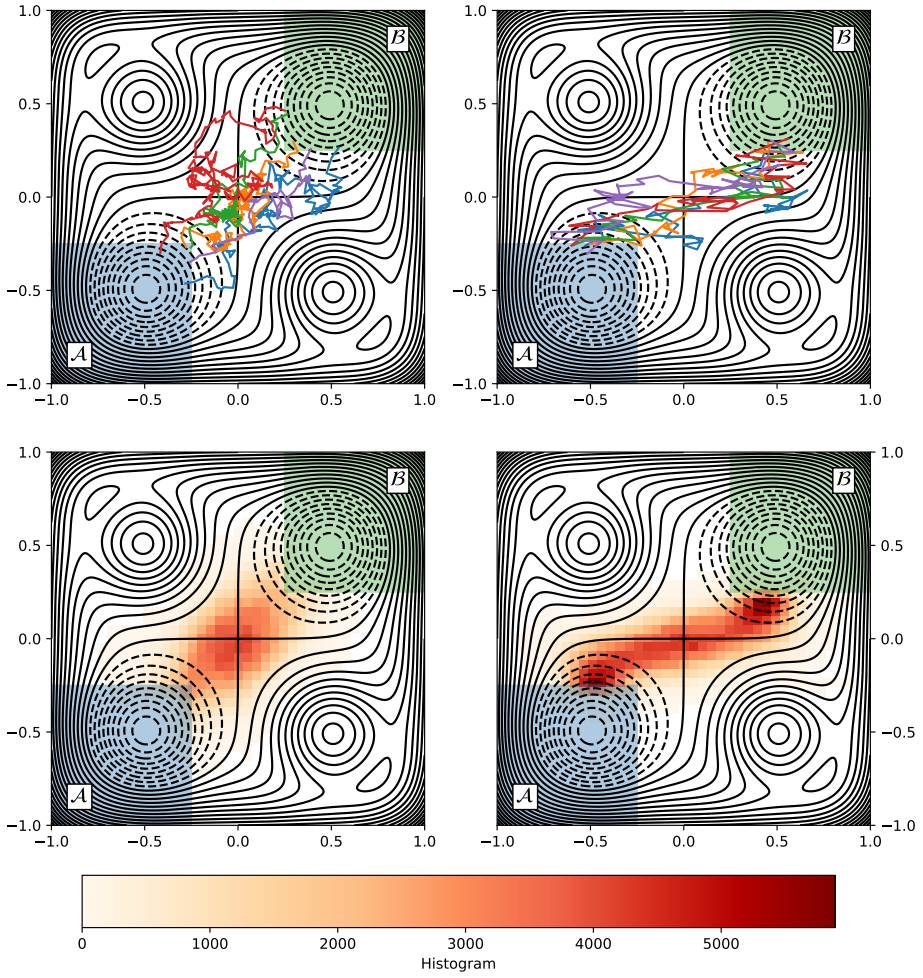

Figure 2.5.: Results from transition path sampling (TPS) simulations for the system of Langevin equations Eq. 2.11 and the potential energy $u(\mathbf{x})$ described in Sec. 2.2. Simulations were performed using the OpenPathSampling simulation framework [60, 61] and a one-way shooting scheme [64]. In the left column the diffusion components were chosen such that $D_1 = D_2$, while in the right column $D_1 = 10\,D_2$. The top row shows a small sample of example trajectories while the bottom row shows the transition path density $\rho(\mathbf{x}|\mathrm{TP})$. The isolines represent the potential energy landscape with dashed isolines indicating negative potential energies while solid lines indicate positive values. The areas shaded in blue and green represent the configurational states $\mathcal{A}$ and $\mathcal{B}$ used in the TPS simulations.

However, calculating the committor is computationally expensive [9] and the committor on its own provides no physical insight into the reaction mechanism [63, 69] since it is only a probability associated with a configuration [16, 71]. To derive physical insights from the committor we try to find one or more collective variables $\psi_i(\mathbf{x})$ that can be combined to construct a reaction coordinate $q(\{\psi_i\})$ that, in turn, has a one-to-one relationship to the committor [63, 69, 71, 72] so that

$$q(\psi_1(\mathbf{x}), \ldots, \psi_n(\mathbf{x})) \approx p_{\mathcal{B}}(\mathbf{x}). \tag{2.17}$$

Ideally, these ψ_i carry some physical meaning that helps us better understand the process at hand.

We can also calculate the committor for our 2-dimensional toy model by starting simulation runs from points on a grid and following them until they reach either $\mathcal{A}$ or $\mathcal{B}$. The different outcomes starting from the same initial state are then due to the different random numbers that are chosen as part of the simulation algorithm.

Figure 2.6 shows the results of this calculation. Since the symmetry between the x- and y-coordinate is broken by the difference in diffusion coefficient, also the committor is not symmetric with respect to exchanging the x- adnd y coordinates anymore. In particular, the regions behind the "hills" in the energy landscape (the top-left and bottom-right corners of the landscape) are now committed to the state located to the right and to the left, respectively. This is due to the faster evolution along the x-axis that makes it highly likely that our random walker reaches the slopes of the basin that is located at the same y-values before it has a chance to diffuse in the y-direction and reach to the slopes of the basin located above or below. Hence, just like the transition path density $\rho(\mathbf{x}|\mathrm{TP})$, also the committor $p_{\mathcal{B}}(\mathbf{x})$ depends on the dynamics of the system.

2.4. Implications for complex systems

So far in this section we have used a simple 2-dimensional toy model to demonstrate that we need to consider the dynamical rules a system follows on top of the (free) energy landscape in order to calculate quantities related to the transition path ensemble. In a more realistic system the aim is, of course, not to arbitrarily change the dynamics of

[9] Calculating the committor involves the calculation of many, sometimes long, simulation trajectories.

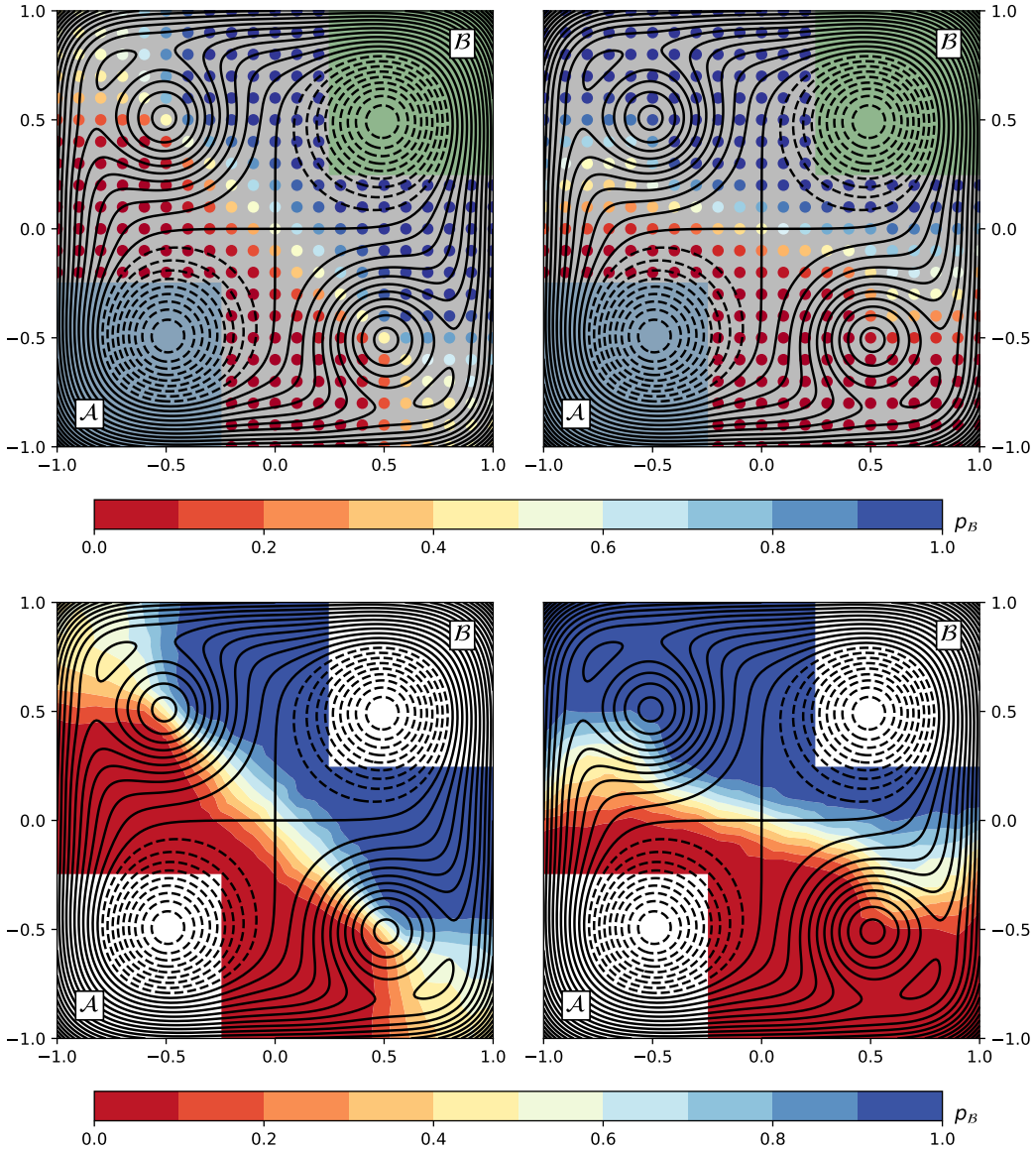

Figure 2.6.: Committor probability $p_{\mathcal{B}}$ estimated by starting trajectories from a grid of initial starting points. The diffusion components are chosen such that $D_1 = D_2$ (left) and $D_1 = 10\,D_2$ (right). Shown are the committor estimates for different positions (top) and the overall commitor function estimated from these individual calculations (bottom) using a linear interpolation. See Fig. 2.5 for system details.

the system—after all we want to accurately reflect the actual dynamics encountered in an experiment.

Nevertheless, dynamics play an important role in rare event investigations. To understand this, consider that in a more complex system we use collective variables ψ_i instead of the x and y coordinate to describe a given rare event and the dynamics along the ψ_i are likely different from each other. At the same time the potential energy landscape is replaced by a free energy landscape, βf. Since we have seen here, that the same energy landscape is compatible with different transition path ensembles we can note a key takeaway: *in order to accurately characterize the transition path ensemble we need to take the dynamics of the system into account.* The free energy landscape alone will not suffice.

This result is also reflected in rate theories [16], such as Berezhkovskii-Szabo (BK) theory [70] and harmonic transition state theory [73] where the calculation of rates and the optimal reaction coordinate involves an analysis of the systems dynamics at the critical $p_{\mathcal{B}} = \frac{1}{2}$ isosurface. In particular, BK theory shows that the direction of flow of critical trajectories is determined by the dynamics along the different CVs at the critical surface.

In the following investigations of rare events this is a recurring theme: in order to understand the details of a rare event's mechanism, the dynamics of a system have to be investigaed thoroughly and, hence, large parts of the the three papers contained in this thesis are concerned with characterizing system dynamics.

3. Paper summaries and background

What follows in part II of this thesis are three papers that examine different rare events: two of them take place in the 2-dimensional Ising model and one in ice. While all of them involve a barrier crossing of one kind or another, the methods used to investigate them are different owing to differences in the specifics of the systems, computational demands, as well as differences in the question we are trying to answer.

The remainder of this section provides short summaries as well as some additional background for the papers that form part II of this thesis. It is my hope that this collection of studies provides the reader with a repository of ideas and methods that can be employed to understand other systems, as well as interesting and useful insights about the investigated systems themselves.

Paper 1: Interplay of fast and slow dynamics in rare transition pathways: The disk-to-slab transition in the 2d Ising model

In addition to the short accessible timescales, molecular simulations also suffer from only being able to cover miniscule volumes compared to the macroscopic systems they often aim to represent. The effects that small simulation volumes have on systems are referred to as *finite-size effects*. One such finite-size effect is the consequence of a simple fact of geometry: if we decrease the volume of a body while keeping the same shape, the surface of that body scales as $(\text{volume})^{\frac{2}{3}}$. This means that as we reduce the volume of a physical system down to a size we can simulate, we increase the surface to volume ratio of that system [1]. For the system sizes that are accessible to molecular dynamics simulations this would mean that—if no precautions are taken—a large number of atoms would be at the surface of our simulation box which is an environment that is untypical for an atom in a macroscopic scale system [50].

[1] Consider atoms arranged on $10 \times 10 \times 10$ cubic grid. Out of 1000 atoms, 488 will be on the surface; a ratio of 0.488 [50]. In a cube of $10^8 \times 10^8 \times 10^8$ (corresponding roughly to a sodium-chloride crystal with edges 2.8 cm in length counting both sodium and chloride atoms) the ratio is approximately 6×10^{-8}.

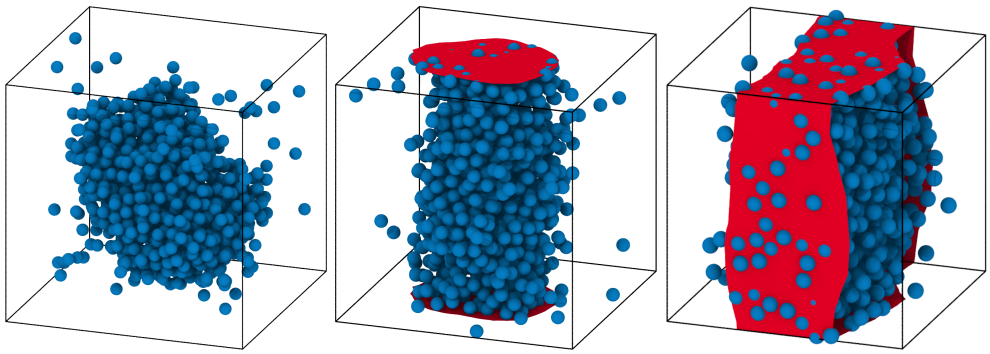

Figure 3.1.: Snapshots taken from simulations of a Lennard-Jones system in the liquid-vapor coexistence region at reduced densities of $\hat{\rho} = 0.15$ (left), $\hat{\rho} = 0.2$ (center), and $\hat{\rho} = 0.35$ (right) where geometric phases form. Simulations were performed using the OpenMM simulation package [40–45]. The red shaded area indicates where the liquid drop is connected to itself through periodic boundary conditions. The visualization was rendered using OVITO [74].

To mitigate this problem, molecular simulations of bulk materials usually use *periodic boundary conditions* [50, 75] (PBCs). In their simplest form, PBCs can be thought of as copying the simulation box and shifting it along the x-, y- z-direction infinitely many times until 3-dimensional space is filled. When a given particle moves, all of its copies move in the same direction and by the same distance. Practically this means that we only simulate the original box of particles and when a particle leaves through one side of the simulation box it enters again through the opposite side. To calculate short-ranged interactions between particles [2] only the closest copy of each particle is used (this is known as the *minimum image convention*)—thereby keeping the number of pair interactions limited and the simulation tractable. In simulations of bulk materials, this procedure removes the interfaces in the simulation and has proven to be an indispensable approximation for computer simulations of bulk systems as it eliminates one of the largest finite-size effects [3].

A side-effect of periodic boundary conditions is the introduction of *geometric phases* [80, 81] in systems with phase separation—i.e., systems where different thermodynamic phases are present at the same time (e.g., gas and liquid). The interfaces

[2] Handling long-ranged interactions is more involved [50, 76].
[3] However, other finite size effects remain [50, 52, 75, 77–79].

between these phases give rise to an energetic cost that is (in first approximation [82]) proportional to the area of the interfaces in the system [4]. Hence, such a system is driven towards minimizing the area of the interfaces between the different phases.

Take as an example a system that is simulated at constant density in its liquid-vapor coexistence region and has separated into a liquid drop and a surrounding gas like the one shown in the left panel of Fig. 3.1. The ellipsoidal shape that can be seen in this figure is the result of the liquid-gas surface tension that acts in such a way that the interface area between the two phases is driven towards its minimum while thermal fluctuations introduce deviations from the ideal spherical shape.

In a simulation with periodic boundary conditions additional drop shapes become optimal for certain drop sizes because for a drop that *spans* the simulation box—i.e. a drop that is connected to itself through a periodic boundary—the PBCs eliminate the interfaces where the drop is connected to itself over the walls of the simulation box. In a 3-dimensional simulation three shapes are stable: the sphere, the cylinder and the slab (see Fig. 3.1) while in two dimensions disks and slabs can be observed (see Fig. 3.2). The volume fractions or area fractions of the drop where each of the different shapes is the lowest energy configuration can be estimated by calculating the respective surface area and picking the shape that results in the smallest overall surface [83].

The emergence of geometric phases also changes the overall free energy landscape of the system, as can be seen in Fig. 3.3 for the example of the 2-dimensional Ising model. The presence of the slab-shaped clusters leads to a flat free energy landscape in the magnetization range where slabs are stable. This is because adding an additional spin pointing upward to a layer in a slab does not change the overall length of the contact line between the up- and down phases and, hence, is not associated with an increase in interfacial free energy [83, 84].

While in the range of $-0.30 \lesssim m \lesssim 0.30$ the slab shape is the most likely shape, the disk-shaped states still form a metastable basin in the free energy landscape of the system and the same is true for slab shaped clusters in the range of m where disks are the stable configuration. This is because in order for the shape of a drop to transition from disk-like to slab-like the drop has to elongate until it comes into contact with itself, momentarily increasing the overall surface area of the drop [80, 81, 85]. This

[4] This is the same effect that we experience as surface tension in the macroscopic world.

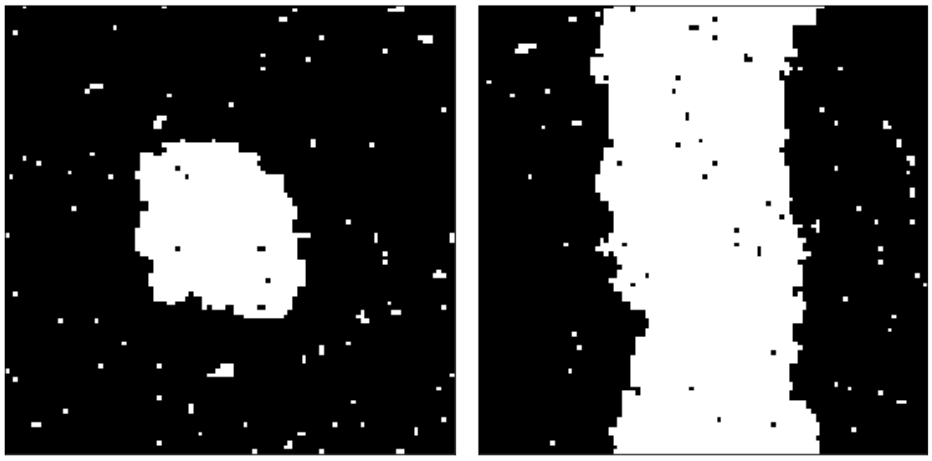

Figure 3.2.: Example configurations in the disk- (left) and slab state (right) taken from umbrella sampling simulations of the 2-dimensional Ising model at temperature $T = 0.7\,T_\mathrm{c}$, where T_c is the critical temperature.

results in a free energy barrier between the different cluster geometries. The same is true in 3-d systems and the cluster geometries that appear there.

In the first paper contained in this thesis titled *Interplay of fast and slow dynamics in rare transition pathways: The disk-to-slab transition in the 2d Ising model*, we investigate the disk-to-slab transition in the 2-dimensional Ising model under the constraint that the overall magnetization of the system stays fixed.

To describe the transitions between disks and slabs we introduce two collective variables, d and s, that capture different aspects of the transition[5]. During the transition d acts as an order parameter with $d < 0$ indicating that the largest cluster in the simulation box is spanning and $d > 0$ indicating that it is not. In addition, the value of d acts as a local descriptor of the configuration of the cluster close to where the bridge to the neighboring periodic image will form or rip. This coordinate changes rapidly during the transition because the movements of single spins can have a significant impact on d when the interfaces of the cluster approach each other. The

[5]See Sec. 4.2 for details on these collective variables.

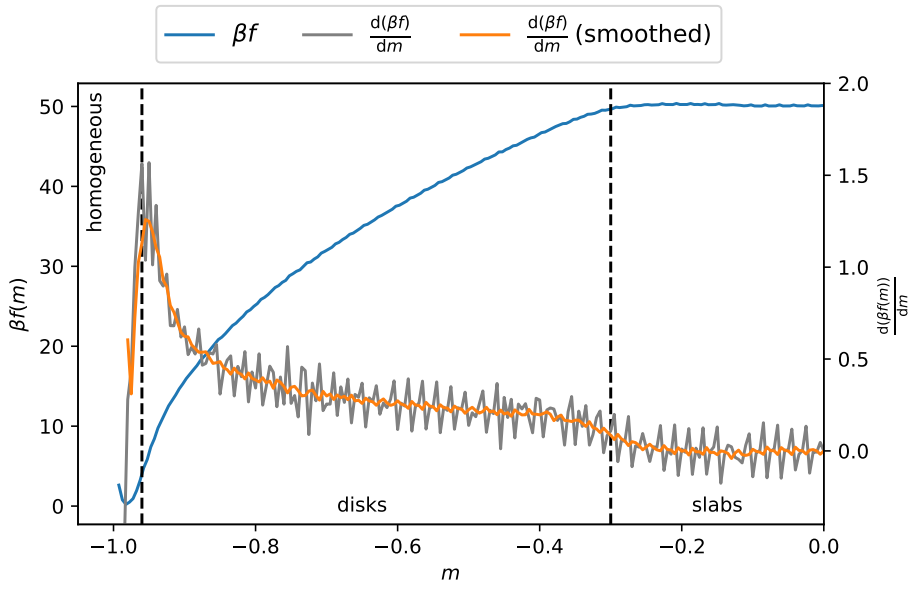

Figure 3.3.: Reduced free energy $\beta f(m)$ (blue line) as a function of magnetization m for a 48×48 Ising model at a temperature of 0.7 times the critical temperature. The dashed lines delimit the magnetizations where different geometric shapes of the largest cluster of spins pointing up in the system are the lowest free energy states. The evaporation-condensation transition takes place at $m \approx -0.92$. Below this magnetization the spins pointing upwards are homogeneously distributed throughout the system. The boundaries of the different phases are best determined by locating changes in the behavior of the slope $(\mathrm{d}(\beta f)/\mathrm{d}m)$ (grey line) which has been smoothed by averaging over neighboring bins (orange line).

variable s on the other hand measures the global shape of the cluster: is it overall more disk-like or more slab-like? Changing the overall shape of a cluster involves moving many spins around, making the dynamics along the s coordinate slow compared to the d direction.

A calculation of the free energy landscape $f(d, s)$ (see Fig. 3.4) yields the intuitively expected result where the $d = 0$ plane—i.e. the states where the cluster just comes into contact with itself—form a ridge in the landscape. This seems to suggest that in order to predict whether a cluster will proceed to the slab- or to the disk state we only have to look at whether the cluster has connected to itself. If so, it is likely to become a slab rather than a disk. Surprisingly, a calculation of the commitor shows

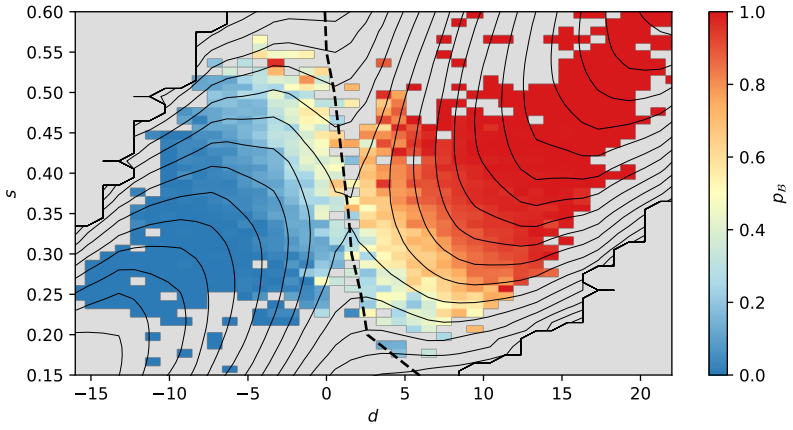

Figure 3.4.: The free energy landscape of the disk-to-slab transition in the 2-d Ising model as a function of the collective variables d and s (black isolines) and the averaged committor probabilities towards the disk state, $p_{\mathcal{B}}$ (colored tiles). The disk state is located in the top right corner and the slab state in the bottom left corner. The dashed black line indicates the ridge that separates the disk- and the slab state that was determined using the free energy landscape alone.

a more complex relationship where the value of s has significant influence on the commitor probabilities. Configurations where a cluster has not yet formed a bridge to its periodic images are sometimes more likely to end up as a slab than returning to the disk state and vice-versa (see Fig. 3.5 for example configurations).

At first, we suspected that the committor could be reconciled with the free energy landscape by introducing a third, yet unknown collective variable. However, a search for this third collective variable that involved testing a number of different candidate variables[6] using techniques described by Peters & Trout [63] proved ultimately unsuccessful. Instead, the seeming discrepancy between the free energy landscape and the committor has to be explained by taking the dynamics along the d and s coordinates into account.

In this paper we do so by modelling the dynamics of the system as a diffusive process in the measured free energy landscape using diffusion coefficients that were measured from simulations. The resulting model correctly predicts the shape of the committor

[6]The additional variables considered were mostly additional shape descriptors.

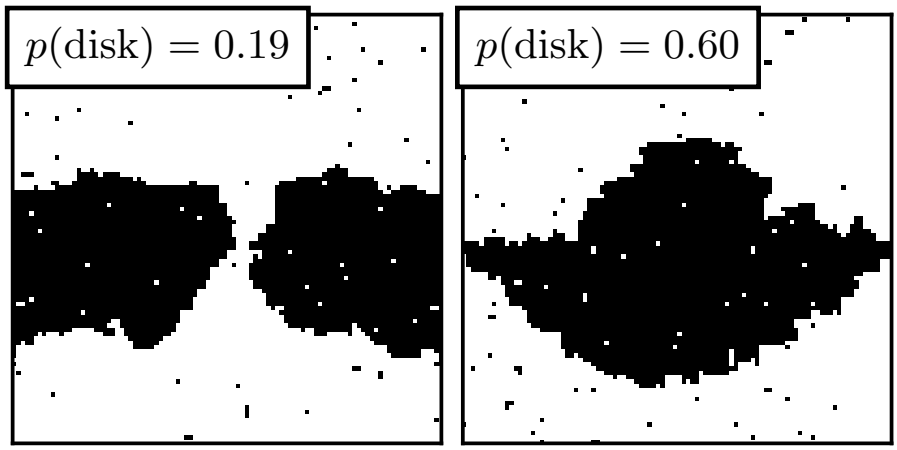

Figure 3.5.: Snapshots taken from simulations of the 2-dimensional Ising model. Shown is a non-spanning cluster (left) and a spanning cluster (right) together with the probability that a trajectory started from the respective configuration ends up in the disk state.

probability.

Paper 2: Weak scaling of the contact distance between two fluctuating interfaces with system size

A starting point for the second paper of this thesis is this question: at which magnetization m does the disk-to-slab transition occur if m is allowed to vary?

The equilibrium analysis presented in Fig. 3.3 suggests that the transition between slabs and disks should occur at a fixed magnetization of roughly $m = -0.30$ or, expressed as a fraction of the total area of the system, the spins pointing up should take up approximately 35% of the system, irrespective of system size. However, we have already learned that the geometric phases are separated from each other by free energy barriers that might hinder this transition and it has previously been predicted by Venturoli *et al.* [85] that the nucleation of a cluster in the Ising model at vanishing external field proceeds via the rapid expansion of the cluster in one direction until it spans the cluster followed by growth in the orthogonal direction.

Indeed, when we prepare systems with a slab that fills half the simulation and let them run we find that as the systems become larger the volume fraction at which a

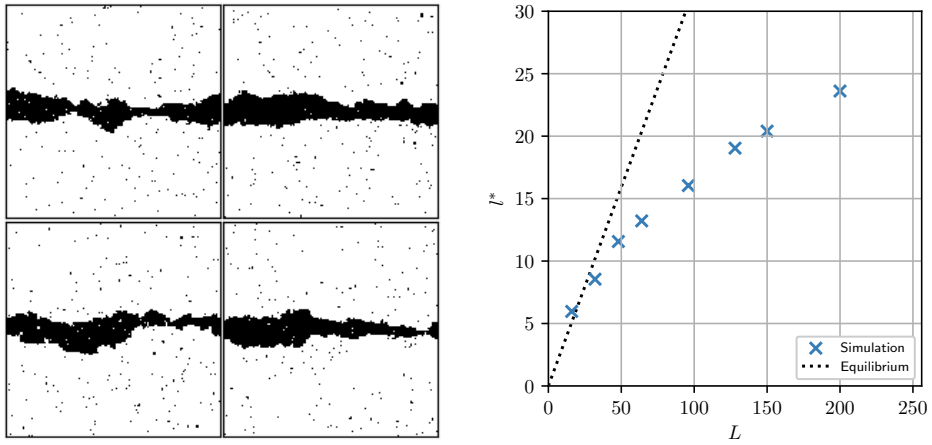

Figure 3.6.: (Left) Last configurations observed before slabs ruptured and turned into disks in trajectories that were set up with a perfect slab at magnetization $m = 0.0$. The system is a 200×200 Ising model with vanishing external field. (Right) average width of the last slabs observed, ℓ^*, in 2-dimensional Ising model simulations of varying linear system size L set up in the same way. The expected slab width at the coexistence magnetization $m = -0.36$ is shown as a dashed black line.

slab breaks down and turns into a disk becomes progressively smaller. The left panel of Fig. 3.6 shows a number of example configurations taken from simulations that were started from a slab configuration and that show the last slab configuration observed before a rupture of the slab occurred and the largest cluster turned into a disk. The right panel presents the average widths of the last slabs observed [7], ℓ^*, as a function of system size which shows the discrepancy between the expected width of these clusters based on the free energy landscape alone and the actual width of the clusters when the slab-to-disk transition occurs in simulations.

Now that the magnetization m, varies we can draw a free energy landscape such as the one shown in Fig. 3.7. Again we are using the d order parameter to distinguish between slab- and disk states that are represented by $d < 0$ and $d > 0$, respectively, but now we are using m as the x-axis in our analysis. From this picture the reason why the slabs tend to be smaller than expected can be seen: the free energy barrier between slab- and disk-shaped clusters becomes smaller as m decreases and the slab

[7] See Sec. 5.5 for details of this calculation.

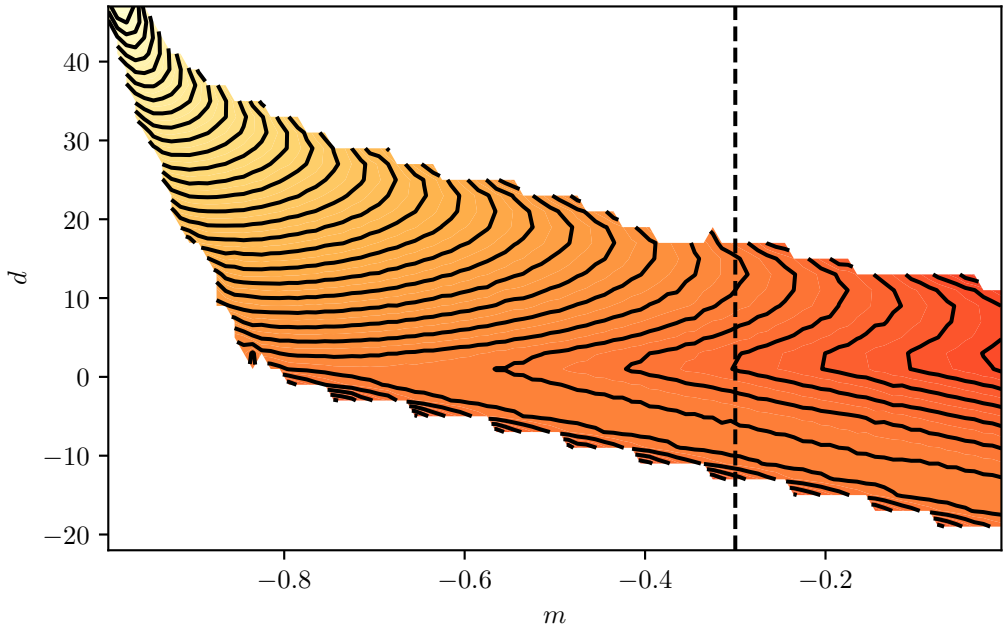

Figure 3.7.: Free energy landscape for a 48×48 2d-Ising model as a function of the magnetization m and order parameter d that characterizes the shape of the largest cluster in the system (see chapter 4 for details). Black isolines are spaced $2\,k_\mathrm{B}T$ apart. The landscape was calculated using a set of umbrella sampling simulations with harmonic biases and reweighted using WHAM [86–88]. The dashed line at $m = -0.30$ indicates the magnetization where disk- and slabs are equally likely.

becomes narrower. However, as we have seen in the introduction, the manner in which a free energy barrier is crossed depends on the dynamics along different collective variables and this is no different in this case. Two timescales are relevant here: how fast does the width of a slab change (resulting in changes in m) and what is the rate of fluctuations of a slabs interface that modulate the value of d.

In principle, determining the distribution of crossing points could be undertaken using the same methods that are used in the first paper: determine local diffusion coefficients and solve a diffusion model to determine the likely pathways the system will take. However, in the case of transitions from the slab- to the disk-shape we

can go a different route that allows us to derive an analytic expression for ℓ^*. To do so, we approximate a slab by two interfaces that are evolving independent of each other. The centers-of-mass of both interfaces independently diffuse along one axis of our simulation box making the slab smaller and larger, and both interfaces undergo thermal fluctuations that modulate their shape. In this model, in order for the slab to rupture and turn into a disk the two interfaces would have to deform so that they come into contact with each other and form a hole. Since there are always fluctuations happening in the shape of the interfaces, the distance of the centers-of-mass to each other—which is the width of the slab—will be non-zero when the first contact occurs. Hence, the question of which average width a slab has when it ruptures can be mapped onto another question: how close do the centers-of-mass of two interfaces approach each other before the interfaces come into contact due to the fluctuations of their shape? This is the subject of the second paper contained in this thesis titled *Weak scaling of the contact distance between two fluctuating interfaces with system size.*

In this paper we use a differential equation similar to a reaction-diffusion equation to derive an analytical expression for the distribution of contact distances between two interfaces based on two inputs: the diffusion constant associated with the center-of-mass motions of the two interfaces relative to each other, D_{int}, and the rate of formation for a fluctuation that covers a gap of width ℓ, $k(\ell)$. The result is a strikingly simple condition for the most likely contact distance, ℓ^*:

$$\sqrt{\frac{k(\ell^*)}{D_{\text{int}}}} = \frac{3}{4}\left|\frac{k'(\ell^*)}{k(\ell^*)}\right| \tag{3.1}$$

Determining the rate function $k(\ell)$ requires a model for the dynamics of the two interfaces and in our work we use the Edwards-Wilkinson (EW) model [89] for which a number of analytical and simulation results are available [89–93]. Of particular importance for our work are results regarding the *maximum relative height* (MRH) of interfaces [94–100]—i.e. the amplitudes of interface fluctuations—because the points with the maximum deviation in an interface are likely the ones that come into contact with another surface first. Hence, a large part of our paper is devoted to investigating the dynamics of the MRH in the EW model.

With knowledge of $k(\ell)$ we are then able to derive scaling laws for the most likely contact distance between two interfaces, ℓ^*, as a function of system size L in 2-

and 3-dimensional systems. These scalings fit excellently to the last slab widths we observe in 2- and 3-dimensional Ising model simulations as well as in a 3-dimensional Lennard-Jones simulation in the liquid-gas coexistence region.

Our theoretical description confirms what we can already see in the data presented in Fig. 3.6: as the system size becomes larger the volume fraction at which slabs break down due to their interface fluctuations increasingly diverges from the coexistence volume fraction between slabs and the next geometric shape. In particular, in the case of a 2-dimensional slab embedded in a 3-dimensional system, ℓ^* grows only logarithmically with system size. Hence, even for a macroscopically sized 2-dimensional slab, the breakdown width predicted based on our model of two non-interacting interfaces is still microscopic because the rate of forming a hole in the slab is exceedingly small for larger widths of the slab.

Paper 3: The microscopic mechanism of bulk melting of ice

Ice at close to ambient conditions (in a fridge for example) forms in a structure called hexagonal ice I (ice Ih). This structure is made up of water molecules arranged in hexagonal rings where each molecule is hydrogen bonded to its neighbors in a particular way that is governed by the so-called ice rules [101]. Various forms of defects can occur in this structure: classic defects that can be found in many solids such as ionic defects and interstitial-vacancy (I and V) pairs, and defects in the hydrogen bond network that are specific to ice, such as L-D (leer-doppel) defects [101, 102] and 5+7 defects [103, 104]. All of these defects are regularly formed and dissolved again in an ice crystal at ambient conditions.

How such an ice Ih crystal melts is the topic of the third paper contained in this thesis, titled *The microscopic mechanism of bulk melting in ice*. This study investigates the early stages of melting; from a crystal with a few defects up to the time when a sizable liquid nucleus has formed.

This process is in many ways more challenging than the rare events in the Ising model studied in the previous two papers. The existence of many different defect types in ice Ih leads to a complex web of states the ice Ih crystal can be in and a priori it is not clear which of these defects play a role in the melting mechanism. Some hints, however, are provided by previous studies of melting: Donadio *et al.* [105] investigated the free energy landscape of melting ice and found a pre-melt state that consists of defects that encompass around 50 molecules and that are aggregates of multiple 5+7

defects. Mochizuki *et al.* [106] investigated melting of ice under a higher degree of superheating where melting can be observed to occur spontaneously in molecular dynamics simulations, and found that the separation of pair defects such as I-V or L-D are the critical step in melting. Furthermore, they observed 5+7 defects prior to to the formation of separated defect pairs hinting at their importance in the melting mechanism.

Our study expands on these papers by investigating a large number of melting trajectories at moderate superheating, where the formation of a liquid nucleus is so rare that we can not expect melting events to occur spontaneously in our simulations. Instead, we take a different approach: we seed our simulations [30, 107–109] with pre-melted liquid nuclei embedded in an otherwise perfect ice lattice and run simulations until the liquid nucleus has frozen and only 5+7 defects are left in the system. Since the integration scheme used is time reversible, we can then invert these trajectories and interpret this set of trajectories as a sample of trajectories that lead from a crystal with 5+7 defects up to a liquid nucleus. These trajectories are then analyzed frame by frame in terms of the defects that are present, giving us a dynamical picture of which defects play a role in melting.

Choosing the shape of the final cluster to be perfectly spherical is of course an approximation: the shape of the critical liquid cluster is likely not perfectly spherical. To gain an understanding of the effects that the geometry of the final liquid domain has on the early stages of melting, we performed additional simulations with trajectories that end in a slab-shaped liquid cluster. A comparison of the results of these simulations gives us a good idea of which features are independent of the shape of these clusters.

In our simulations we find most of the features found in previous works on the same system: 5+7 defects play an important role in the melting mechanism, we find extended topological defects (E defects) that form inside the domain that later becomes liquid, and we find that the appearance of separated defects is an important step in this process. However, the availability of a large number of dynamic trajectories allows us to add significant detail to the role of all of these elements.

A detailed description of findings about these different defects can be found in the paper. However, the results can be summarized like this: (i) a liquid nucleus forms by the interaction of mobile defects (mostly I and V) that interact with pre-existing E or 5+7 defects; (ii) these mobile defects are often formed close to 5+7 defects themselves

and in many cases (36% of trajectories at 303 K) outside of the volume that later becomes the liquid nucleus; (iii) I-V defects diffuse quite freely once they are formed; (iv) the timespan between forming the first mobile defect pair and the appearance of a liquid nucleus depends strongly on the geometry of the simulation box; (v) L-D defects quickly (typically within 500 ps) spawn I-V defects. Together, results (ii) through (iv) suggest that, as the simulation box becomes larger, the mobile defects that trigger the formation of a liquid nucleus form further away from the nucleation site.

This analysis shows that the mechanism of homogeneous melting involves a number different types of defects at different stages of the mechanism and, ultimately, occurs via the accumulation of defects at the location where a liquid nucleus first forms.

List of papers and contributions by the author

Papers contained in this thesis:

- Moritz, C., Tröster, A. & Dellago, C. *Interplay of fast and slow dynamics in rare transition pathways: The disk-to-slab transition in the 2d Ising model.* J. Chem. Phys. **147**, 152714 (2017).

  The author performed all simulations and data analysis, and, with input from collaborators, designed the research, carried out mathematical analysis and wrote the paper.

- Moritz, C., Sega, M., Innerbichler, M., Geissler, P. L. & Dellago, C. *Weak scaling of the contact distance between two fluctuating interfaces with system size.* Phys. Rev. E **102**, 062801 (2020).

  The author performed all simulations except simulations of the Lennard-Jones system, carried out data analysis and, with input from collaborators, designed the research, carried out mathematical analysis and wrote the paper.

- Moritz, C., Geissler, P. L., Dellago, C. *The microscopic mechanism of bulk melting of ice.* J. Chem. Phys. **155**, 124501 (2021).

  The author performed all simulations and data analysis, and, with input from collaborators, designed the research, carried out mathematical analysis and wrote the paper.

Other published papers that are not part of this thesis:

- Gieseler, J., Novotny, L., Moritz, C., & Dellago, C. *Non-equilibrium steady state of a driven levitated particle with feedback cooling* New J. Phys. **17**, 045011(2015).

  The author contributed to simulation work and data analysis.

- Jain, V., Gieseler, J., Moritz, C., Dellago, C., Quidant, R., & Novotny, L. *Direct Measurement of Photon Recoil from a Levitated Nanoparticle* Phys. Rev. Lett. **116**, 243601 (2016).

  The author contributed to simulation work and data analysis, and proof-read the paper.

- Coluzza et al. *Perspectives on the Future of Ice Nucleation Research: Research Needs and Unanswered Questions Identified from Two International Workshops* Atmosphere 2017, **8**(8), 138 (2017).

  The author contributed to the writing of the paper.

Part II.

Papers

4. Interplay of fast and slow dynamics in rare transition pathways: The disk-to-slab transition in the 2d Ising model

The contents of this chapter have previously been published in *The Journal of Chemical Physics*. Reproduced from

> Moritz, C., Tröster, A. & Dellago, C. *Interplay of fast and slow dynamics in rare transition pathways: The disk-to-slab transition in the 2d Ising model.* J. Chem. Phys. **147**, 152714 (2017),

with the permission of AIP Publishing.

Abstract

Rare transitions between long-lived stable states are often analyzed in terms of free energy landscapes computed as functions of a few collective variables. Here, using transitions between geometric phases as example, we demonstrate that the effective dynamics of a system along these variables are an essential ingredient in the description of rare events and that the static perspective provided by the free energy alone may be misleading. In particular, we investigate the disk-to-slab transition in the two-dimensional Ising model starting with a calculation of a two-dimensional free energy landscape and the distribution of committor probabilities. While at first sight it appears that the committor is incompatible with the free energy, they can be reconciled with each other using a two-dimensional Smoluchowski equation that combines the free energy landscape with state dependent diffusion coefficients. These results illustrate that dynamical information is not only required to calculate rate constants but that neglecting dynamics may also lead to an inaccurate understanding of the mechanism of a given process.

4.1. Introduction

Free energy landscapes are a ubiquitous tool in the study of rare events—such as nucleation events in phase transitions or conformational changes in biomolecules—as they are often used to get a first sense of which regions in configuration space are relevant for a given process. Calculating such a landscape requires the choice of a small number of order parameters that are supposed to capture the important degrees of freedom of the process in question. Examples of such order parameters include the potential energy, the size of the largest cluster in the system (in the case of nucleation), or quantities like the number of native contacts, radii of gyration or root-mean-square deviations from the target structure (in biological systems).

However, care has to be taken in the interpretation of such free energy landscapes, since the choice of coordinates is not unique, even if the relevant degrees of freedom are captured. In particular, any non-linear transformation of the coordinates will change the free energy landscape, including features like the existence and height of free energy barriers [52]. Due to this arbitrariness, additional information on the dynamics along a chosen order parameter is required in order to reliably interpret a free energy landscape [110–114].

With higher-dimensional free energy landscapes additional complications arise, especially if there is no clear physical relationship between the different order parameters used, as is often the case. For instance, one may be tempted to associate the gradient in such a landscape with a probability flux. However, flow directions [70, 115, 116], the channels in which the transition proceeds [51, 117–119], and isocommittor lines [120, 121] are determined both, by the free energy landscape and the dynamics of the system along the different order parameters and may deviate significantly from naive expectations. In particular, the combination of a fast and a slow degree of freedom which we will encounter in this work, has been discussed using a toy model by Metzner *et al.* [53].

Often, especially in the context of rate calculations, one would like to project the system onto a single variable, called a reaction coordinate, that is not only capable of distinguishing between reactant and product state, but also describes the progress of the transformation in between. Due to the effects mentioned above, the free energy landscape may mislead us into a suboptimal choice for this reaction coordinate, which in turn negatively impacts the efficiency and accuracy of common rate calculation

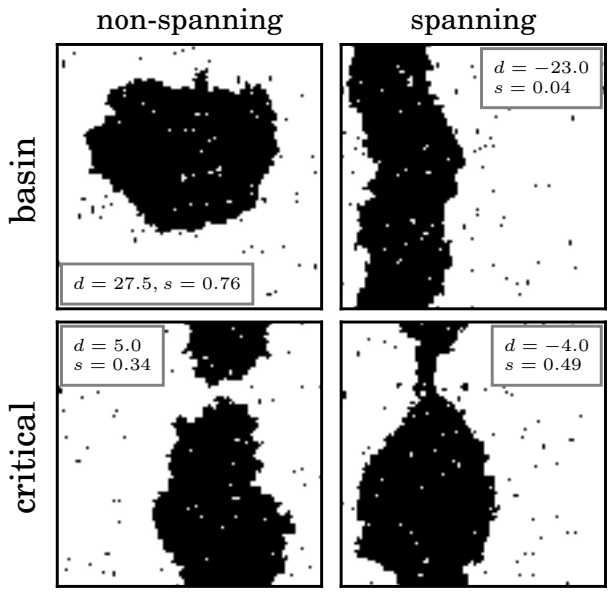

Figure 4.1.: Example configurations taken from simulations of the ferromagnetic Ising model at fixed magnetization of $m = 0.36$ and temperature $T = 0.7\ T_c$. The configurations in the top row are taken from the stable basin of the disk- and the slab state respectively. The ones in the bottom row are critical configurations in the sense that their committor probabilities are close to $1/2$. d and s are order parameters discussed in section 4.2.

methods.

In the following, we use a simple model process to demonstrate some of the issues mentioned above: the disk-to-slab phase transition in the two-dimensional Ising model. Disk and slab phase are so called geometric phases [80], which arise due to periodic boundary conditions used in simulations. They are characterized by different cluster shapes—spherical, cylindrical and slablike in three dimensions—where the stability of the non-spherical shapes is due to the reduction of surface free energy that can be achieved by connecting a cluster to its periodic images. In two dimensions the number of geometries reduces to two: a disk- and a slab phase.

The disk-to-slab transition is an example of a transition between different cluster (or bubble) geometries that play a role in different physical situations [83, 122–126], including the dewetting transition observed in volumes that are confined between

hydrophobic surfaces [127–133].

The mechanism of this dewetting has recently been discussed in detail by Remsing *et al.* [134], who showed that it may involve the formation of a vapor bubble on one of the surfaces which subsequently changes its shape to a vapor tube that connects the plates. Under some conditions, this mechanism reduces the free energy barrier that has to be overcome, by, in essence, circumventing the states that involve a vapor tube size that is close to critical. The disk-to-slab phase transition can be seen as a simplified version of this process.

Another interesting parallel can be drawn between the cylinder to sphere transition and the Rayleigh-Plateau instability [135–137]. As shown originally by Plateau [135], a cylinder stabilized by surface tension is unstable against axial surface deformations with a wavelength larger than its circumference. Given a fixed box size, this sets a minimum radius a cylinder must have to be stable. However, in two dimensions, this (purely geometric) effect does not exist since a deformation of a 2d slab always leads to a larger surface and hence, to a barrier opposing the decay of the slab.

In simulations of the Ising model, geometric phases have played a role in various cases. In particular, they can be used to calculate surface tensions [138, 139], and geometric phase transitions have been observed to hamper the sampling of free energy landscapes [81, 140]. Furthermore, in an application of the string method [51, 55], geometric phase transitions have been discussed [85] as being part of the transition from the spin-down to the spin-up phase. Depending on the value of the external field, two transition mechanisms are possible. For strong fields, the critical configurations contain a disk shaped cluster. For weak fields, however, the the disk-to-slab becomes the bottleneck transition. In this work we focus on the details of this disk-to-slab transition under conditions where the overall magnetization is fixed.

The remainder of this paper is structured as follows: section 4.2 specifies the model that is investigated and introduces two order parameters that are then used to investigate the transition. In section 4.3 we discuss the free energy landscape and the distribution of committor probabilities as well as the apparent disconnect between the two. Section 4.4 explains how diffusion coefficients can be calculated reliably in this system, which are then used, in section 4.5, to build a two-dimensional model of the system that predicts the distribution of committor probabilities. In section 4.6 we recapitulate our findings and discuss some of their implications.

4.2. Model and Order Parameters

We investigate the disk-to-slab phase transition in the two-dimensional Ising model with ferromagnetic nearest-neighbor interactions on a square lattice of size $N = 100 \times 100$ and a vanishing magnetic field. The Hamiltonian is given by

$$\mathcal{H} = \sum_{<ij,i'j'>} \sigma_{ij}\sigma_{i'j'}, \tag{4.1}$$

where the sum extends over all nearest-neighbor pairs and we have set the coupling constant to 1. The spins, denoted by σ_{ij} with i being the position in x-direction and j the position in y-direction, can take on values of $+1$ (up) and -1 (down) and the magnetization per spin of the system is given by $m = (\sum_{i,j} \sigma_{ij})/N$. Periodic boundary conditions apply in all directions. Since under these conditions the model is symmetric with respect to a flip of all spins, we restrict the discussion to positive m.

In this case, given a fixed temperature T below the critical temperature T_c, three distinct phases can be found in order of descending magnetization: a homogeneous phase without a single dominant cluster of down spins, a disk phase where the bulk of the spins pointing down are in a single disk-shaped (*non-spanning*) cluster and a slab phase where this cluster is in contact with its own periodic copies (*spanning*). See Fig. 4.1 for examples of disk- and slab-shaped clusters.

In this study, the dynamics of the system are given by a Metropolis Monte Carlo procedure with moves that keep the magnetization constant by only exchanging spin positions. We distinguish between local (Kawasaki [141]) dynamics where only exchanges of neighboring spins are allowed and non-local dynamics that allow arbitrary exchanges. Local dynamics, which mimic mass transport in a more realistic system, are used in all simulations where dynamic properties are probed, while non-local moves are used for free energy calculations to enhance sampling. The unit of time t is a Monte Carlo sweep, i.e., N attempted single spin-exchange moves.

In the following discussion the reduced temperature is set to $\theta = T/T_c = 0.7$ and the magnetization to $m = 0.36$, where the slab state is metastable with respect to the disk state.

We will now introduce the order parameters d and s, that we will use to describe transitions between the disk- and the slab state. For reference, Fig. 4.1 shows examples of configurations together with their respective d- and s-values.

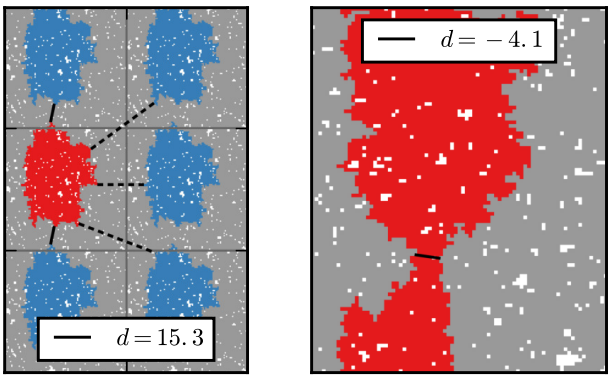

Figure 4.2.: Examples of the construction of the minimum distance/width order parameter d for non-spanning clusters (left) and spanning clusters (right). The cluster indicated in red is the largest cluster of spins pointing down and the one in gray is the largest cluster pointing in the up direction. White spins do not belong to either of these clusters and the blue clusters are periodic copies of the red cluster. On the left, the smallest distance between the largest cluster and its periodic images is used as an order parameter while on the right the smallest distance between the two surfaces of the oppositely oriented cluster is measured. The latter is a proxy for the smallest width found along the length of the red cluster.

4.2.1. The minimum distance/width order parameter d

We first introduce an order parameter that is capable of distinguishing between disk- and slab-shaped clusters as well as between intermediate shapes. To do so, we identify the largest (geometric [142, 143]) cluster of spins, i.e. the largest connected cluster of spins that are neighbors of each other and point down. If this cluster is a non-spanning cluster, we characterize its shape by finding the shortest distance, d_{image}, between the surface of the cluster and the surfaces of any of its periodic images (see Fig. 4.2). If the cluster is a spanning one, we instead characterize constrictions along its length by finding the smallest distance between the surfaces of the delimiting cluster of up spins, which is shown in gray on the right side of Fig 4.2. This quantity is denoted by d_{width}.

The combined minimum distance/width coordinate d is then given by

$$d = \begin{cases} d_{\text{image}} & \text{for non-spanning clusters} \\ -d_{\text{width}} + 3 & \text{for spanning clusters} \end{cases}, \tag{4.2}$$

where the number 3 is added to -d_{width} in order to close a gap in the possible values of d that is due to the lowest possible d_{image} and d_{width} being $\sqrt{2}$ (when the closest spins of the two clusters are offset by one diagonal step) and 2 (when there is a bridge of exactly one spin left), respectively. Consequently, for spanning clusters d is less than or equal to 1 and for non-spanning clusters d is larger than 1. Furthermore, the order parameter d differentiates between different cluster shapes both for spanning and non-spanning clusters and yields information on the local structure of the cluster around the connecting bridge to its periodic images.

The distance order parameter d has units of one lattice constant.

4.2.2. The shape order parameter s

As we will see later, in order to arrive at a complete picture of the dynamics of the transition a second order parameter that characterizes the overall shape of the cluster is required. A straightforward way to do that for non-spanning clusters would be to use the ratio of the main moments of inertia of the cluster. However, this method breaks down as soon as the cluster is a spanning cluster since the main moments of inertia are no longer well defined.

Instead, we will use a proxy in Fourier space, where, for a system with $n \times n$ spins, we first take a Fourier transform of the configuration yielding the components

$$\tilde{\sigma}_{jk} = \frac{1}{n^2} \sum_{l,m=1}^{n} \sigma_{lm} \exp\left[\frac{2\pi i}{n} (jl + km)\right] \tag{4.3}$$

and then take the (dimensionless) ratio

$$s = \min\left(\frac{|\tilde{\sigma}_{01}|}{|\tilde{\sigma}_{10}|}, \frac{|\tilde{\sigma}_{10}|}{|\tilde{\sigma}_{01}|}\right). \tag{4.4}$$

Here, $\tilde{\sigma}_{10}$ and $\tilde{\sigma}_{01}$ are the longest wavelength components in x and y direction, respectively.

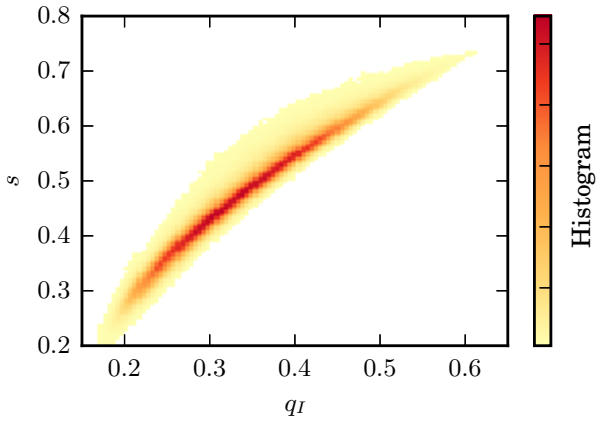

Figure 4.3.: Histogram of q_I-s value pairs calculated from configurations that contain non-spanning clusters found in trajectories obtained from transition path sampling simulations [144] of the disk-to-slab transition. q_I is defined as the ratio of the smaller main moment of inertia of the cluster to the larger one. The s values are highly correlated to the q_I values indicating that they are an equally good measure for how disk-like a cluster's shape is.

The order parameter s takes on values from close to 0—indicating configurations that are asymmetric with respect to an exchange of the x and y directions—to 1 indicating that the largest cluster in the system is close to being symmetric. Its values are highly correlated to the ratio of the main moments of inertia for non-spanning clusters (see Fig. 4.3), but it is also well defined for spanning clusters.

4.3. Free energies and the committor

We start our investigation of the mechanism of the disk-to-slab phase transition by computing the free energy landscape $\beta F(d, s) = -\log[P(d, s)]$, where $P(d, s)$ is the equilibrium probability density as a function of d and s, $\beta = 1/k_\mathrm{B}T$, and k_B is Boltzmann's constant. We do so by performing umbrella sampling simulations in the plane spanned by the d and s coordinates. Configurations are biased using a series of harmonic bias potentials that are centered at different points in the d-s plane. The resulting probability distributions are then reweighted using the weighted histogram analysis method (WHAM) [86, 87]. Figure 4.4 shows the result of these calculations.

The slab state, $\mathcal{A}$, is metastable with respect to the disk state, $\mathcal{B}$, by 6.4 $k_\mathrm{B}T$ and the two states are separated by a barrier with a height of roughly 8 $k_\mathrm{B}T$ measured from the minimum within state $\mathcal{A}$.

In order to assess the quality of the two chosen order parameters d and s, transition path sampling [144] (TPS) simulations using aimless shooting [63] and variable trajectory lengths have been used to obtain trajectories transitioning from state $\mathcal{A}$ to state $\mathcal{B}$. Configurations are assumed to have reached the basins if the value of d is smaller than -15 or greater than 26, respectively. The trajectories consist of segments with a length of 2000 MC sweeps each and the shooting point is randomly shifted forward or backward in time by 20 segments or the same shooting point as in the previous trajectory is chosen. Figure 4.6 shows example trajectories obtained from these simulations.

As was mentioned in the introduction, a good reaction coordinate is able to characterize the progress of the transition. This means, that solely based on this coordinate one is able to predict the so called committor probability. The committor probability, $p_\mathcal{B}$, of a configuration is the probability of reaching state $\mathcal{B}$ before reaching state $\mathcal{A}$

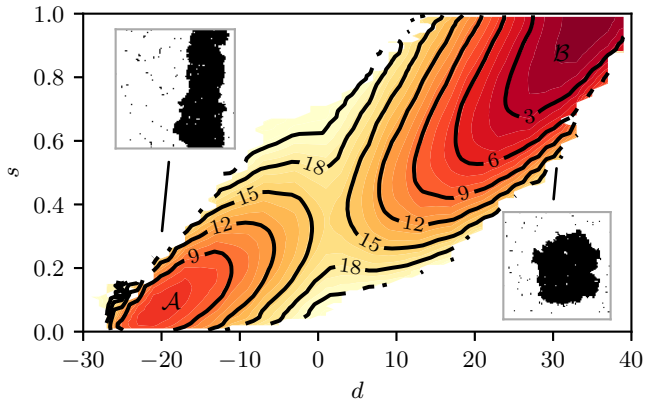

Figure 4.4.: Free energy $F/k_\mathrm{B}T$ (black isolines) of the 2D Ising model at magnetization per spin $m = 0.36$ and reduced temperature $\theta = 0.7$ as a function of the minimum distance/width order parameter d and the shape order parameter s. The insets show examples of a slab-shaped (top left, basin $\mathcal{A}$) and a disk-shaped cluster (bottom right, basin $\mathcal{B}$). The zero-point of the free energy is chosen to coincide with the free energy minimum found in state $\mathcal{B}$. The data were obtained by a series of umbrella sampling simulations with harmonic biases and subsequent reweighting using WHAM [86–88].

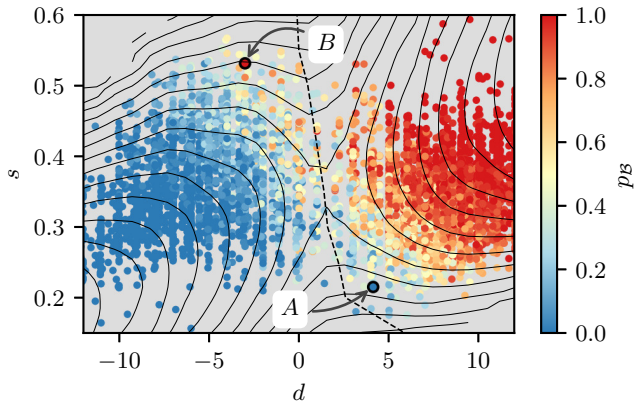

Figure 4.5.: Committor probabilities $p_{\mathcal{B}}$ calculated for a section of the free energy landscape in the d-s plane shown in Fig. 4.4. The black lines are isolines of the free energy drawn in intervals of $k_{\mathrm{B}}T$. The colored dots indicate the committor probabilities towards the disk state and the dashed black line represents the ridge of the free energy landscape that separates the basins of attraction of the disk and the slab state. The configurations marked with A and B are shown in Fig. 4.8.

averaged over trajectories started from the configuration. In our case, the averaging is done over trajectories computed with different random number generator seeds.

We computed committor values for configurations from pathways harvested in TPS runs. We estimated $p_{\mathcal{B}}$ by shooting trajectories from a given configuration and counting the number of times these trajectories reach state $\mathcal{B}$ first. The number of shots was chosen such that the statistical uncertainty of the estimated probability is smaller than 10% [145].

Figure 4.5 shows the resulting committor probabilities together with the free energy $\beta F(d, s)$. The shape of the free energy barrier suggests that the committor probability is determined by the value of the d-coordinate only. However, an examination of the committor probabilities calculated from simulation paints a different picture, in which there is a significant dependence of the committor on the value of the s-coordinate. In particular, some configurations that, based on the free energy landscape, seem to be in the basin of attraction of state $\mathcal{A}$ ($\mathcal{B}$) have a greater (smaller) than 1/2 chance to evolve into the disk state $\mathcal{B}$. Such configurations, marked with A and B, are shown in Fig. 4.8.

At this point one may suspect that we have not yet captured all the relevant degrees

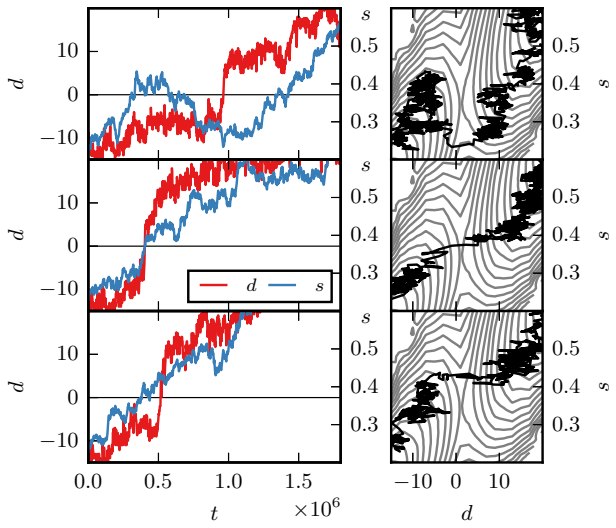

Figure 4.6.: Example trajectories of the disk-to-slab transition obtained from transition path sampling. The order parameters d and s are shown as a function of time (left) and as they appear projected onto the free energy landscape (right, isolines are placed 1 $k_\mathrm{B}T$ apart). Time is given in units of Monte Carlo sweeps. Note that the transition over the ridge of the free energy landscape at $d = 0$ progresses at a timescale that is much faster than the evolution of the s coordinate.

of freedom that determine the progress of the transition. However, Fig. 4.7—which shows an optimized coordinate obtained using a likelihood maximization method due to Peters & Trout [63]—suggests that the committor can be fairly accurately described using only d and s. In the following we will reconcile this apparent disconnect by including the dynamics along d and s into our considerations.

We start by noting that in the trajectories shown in Fig. 4.6, the system spends a much larger amount of time close to the free energy barrier than it takes to cross the barrier to the other side. The s-coordinate evolves slowly because a large number of spins need to change collectively in order to change the shape parameter s appreciably. Hence, for the dynamics chosen for the system, changing s corresponds to the diffusive rearrangement of spins over long distances. In contrast, close to the barrier region, a change in the d-coordinate only requires the movement of relatively few spins and hence

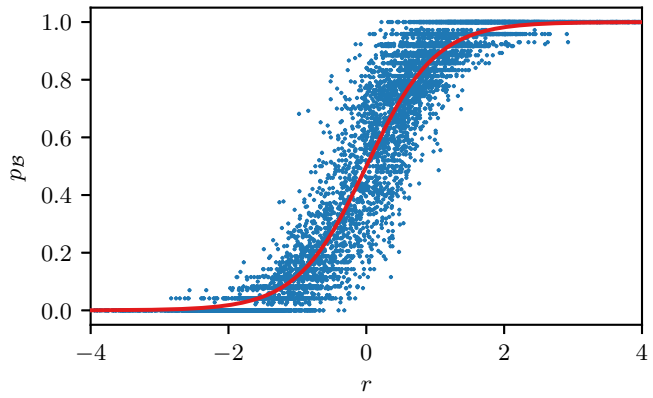

Figure 4.7.: Committor probabilities towards the disk state as a function of a combined reaction coordinate $r = 0.18\ d + 6.4\ s - 2.6$. The parameters have been determined using a likelihood maximization procedure [63]. The red line represents the committor model function used for the optimization.

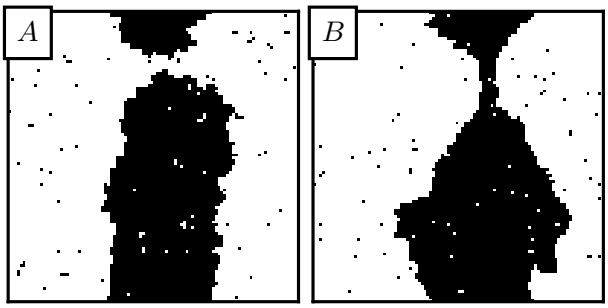

Figure 4.8.: Example configurations A and B marked in Fig. 4.5. These configurations are located at $(d = 4.1, s = 0.216)$ and $(d = -3.0, s = 0.532)$ and have committor probabilities towards the disk state of 0.362 and 0.958 respectively.

changes along the d-direction proceed much faster. As we will see later, this difference in relaxation times along the d- and s-direction strongly influence the distribution of committor probabilities. This dynamical behavior can be characterized using a coordinate dependent diffusion coefficient tensor [51, 53, 54, 146] $D_{ij}(d, s)$, which we will calculate in the following section.

4.4. Characterizing System Dynamics

In order to determine D_{ij}, we first employ the method of Im and Roux [147, 148] to calculate mean square displacements (MSDs) along the two coordinate directions that are corrected (up to first order) for the drift of the order parameters that is due to the underlying free energy landscape. Starting from equilibrium configurations within narrow ranges of d- and s-values, we generate short, unbiased trajectories. Using the coordinate d as an example, the MSD is then estimated by

$$\left\langle \delta\tilde{d}^2 \right\rangle_t = \left\langle \left(\tilde{d}(t) - \left\langle \tilde{d} \right\rangle_t \right)^2 \right\rangle_t . \tag{4.5}$$

Here $\tilde{d}(t) = d(t) - d(0)$ and the averages $\langle \ldots \rangle_t$ are taken over the trajectories at time t from their start. This procedure takes the mean drift (given by $\left\langle \tilde{d} \right\rangle_t$) , as well as the slightly different starting points of the trajectories into account.

Figure 4.9 shows the results of this calculation. In principle, linear fits to the data shown then yield the diffusion coefficients D_{XX}. While this is certainly true for the D_{ss} component, the MSDs along the d-direction are highly non-linear even for long times, making it impossible to reliably determine the value for D_{dd} this way.

Before we address this problem, note that Fig. 4.10 shows the correlations

$$C_{ds}(t) = \frac{\left\langle (\delta\tilde{d})(\delta\tilde{s}) \right\rangle_t}{\sqrt{\left\langle (\delta\tilde{d})^2 \right\rangle_t} \sqrt{\left\langle (\delta\tilde{s})^2 \right\rangle_t}}, \tag{4.6}$$

which are small and, hence, in the following we will treat the fluctuations in d- and s-direction to be independent of each other by assuming D_{ij} to have the diagonal form

$$\left(D_{ij}\right)(\mathbf{x}) = \begin{pmatrix} D_d(\mathbf{x}) & 0 \\ 0 & D_s(\mathbf{x}) \end{pmatrix}. \tag{4.7}$$

The values for D_s obtained by fitting to the MSDs are shown in the lower panel of Fig. 4.12.

In order to obtain reliable results for $D_d(\mathbf{x})$, we use a Bayesian method introduced by Best and Hummer [113, 149], which is based on discretizing order parameter axes

into bins followed by the maximization of the likelihood

$$L = \prod_{\alpha} \left(e^{t_\alpha R}\right)_{i_\alpha, j_\alpha} . \tag{4.8}$$

Here, R is the matrix of transition rate constants between the bins, t_α is the lag time between two measurements of the order parameter and the product runs over all transitions of the system observed in a set of trajectories. The components of R obey

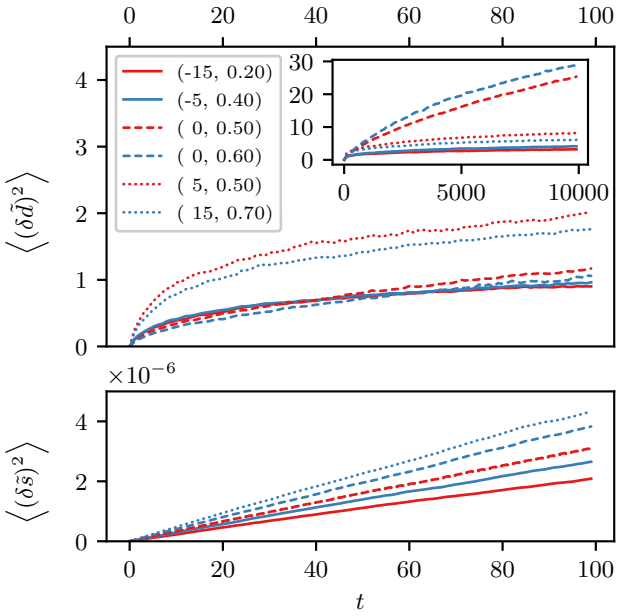

Figure 4.9.: Estimates for local mean square displacements measured using the method of Im and Roux [116, 147, 148]. Different lines correspond to different starting points of the trajectories, which are given in the legend as d-s pairs. Notice the distinct non-linear behavior along the d direction (top), indicating the presence of strong memory effects at short timescales. The starting points at the top of the free energy barrier (dashed lines) show a markedly different behavior for long times (inset) due to the fact that two groups of trajectories separate—those developing towards the slab basin and those headed towards the disk basin.

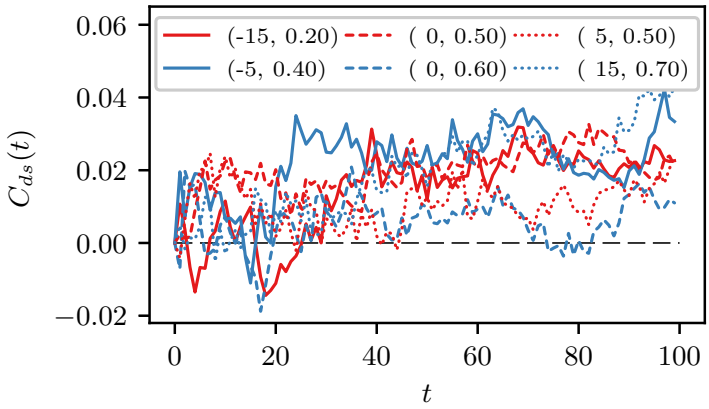

Figure 4.10.: Correlation C_{ds} of mean displacements given by equation (4.6). The displacements in d- and s- direction are largely uncorrelated from each other.

the conditions

$$R_{ij} = \begin{cases} -\sum_{l \neq i} R_{il} & \text{if } i = j, \\ R_{ji} P_i / P_j & \text{if } i < j, \end{cases} \tag{4.9}$$

where P_i is the equilibrium probability of finding the system in bin i. Assuming that only the transition rates between neighboring bins are non-zero (i.e., we assume that the system transitioning from bin i to j has to pass through all bins in between), leaves us with $\mathcal{N} - 1$ independent components, where $\mathcal{N}$ is the number of bins used. The diffusion coefficient between bin i and $i + 1$ along a coordinate X with a bin width of ΔX, is then given by [149, 150]

$$D_{i,i+1} = \Delta X^2 R_{i+1,i} \left(\frac{P_i}{P_{i+1}} \right)^{1/2}. \tag{4.10}$$

The advantage of this method is that we can choose a lag time $\tau = t_\alpha$ that is long enough, such that the memory effects seen in the mean square displacements subside while we can still deal with the considerable drift that occurs within this lag time.

Since D_d is considered to be independent of the s-direction and the evolution along

the s-direction is slow, we can perform this calculation independently in parallel slices along lines of constant s. These slices have a width of $\Delta s = 0.025$ and each of these slices is split into bins of size $\Delta d = 2$. As suggested in Refs. 149 and 113, we count the number of transitions between these bins, N_{ij}, for a set of trajectories and subsequently vary the rate parameters R_{ij} in order to maximize the log-likelihood

$$\begin{aligned} \log \tilde{L} = \sum_{i,j} N_{ij} \log \left[\exp\left(\tau R\right)_{ij} \right] \\ + \sum_{i} \frac{\left(D_{i+1,i} - D_{i,i-1}\right)^2}{2\varepsilon^2}, \end{aligned} \tag{4.11}$$

where the second sum is a smoothing prior. We take the P_i from previous free energy calculations. The matrix exponential $\exp\left(\tau R\right)$ is evaluated using a scaling-and-squaring method [151] as implemented in the python package scipy [152]. The value of ε was chosen to be $3 \cdot 10^{-4}$, which is on the order of the eventual values obtained for D_d, in order to smooth large statistical fluctuations.

The lag time is chosen by varying the lag time until one observes a plateau in the resulting diffusion coefficients. Figure 4.11 shows the results of such a calculation as a function of lag time for a single slice. At $\tau = 30\,000$ the values of the diffusion coefficients seem to have reached a plateau while statistics are still reasonably good. This lag time is used to calculate the values of D_d shown in the upper panel of Fig. 4.12.

4.5. Understanding the Committor

In this section we will demonstrate that the shape of the committor distribution can be largely explained on the basis of the order parameters we have already introduced, d and s, if one includes the dynamics of the system. Based on the free energy landscape and the diffusion coefficients we have obtained, we will first identify and estimate the timescales involved in the transition in order to gain an intuitive understanding, followed by an approach that uses a Smoluchowski equation to model the process.

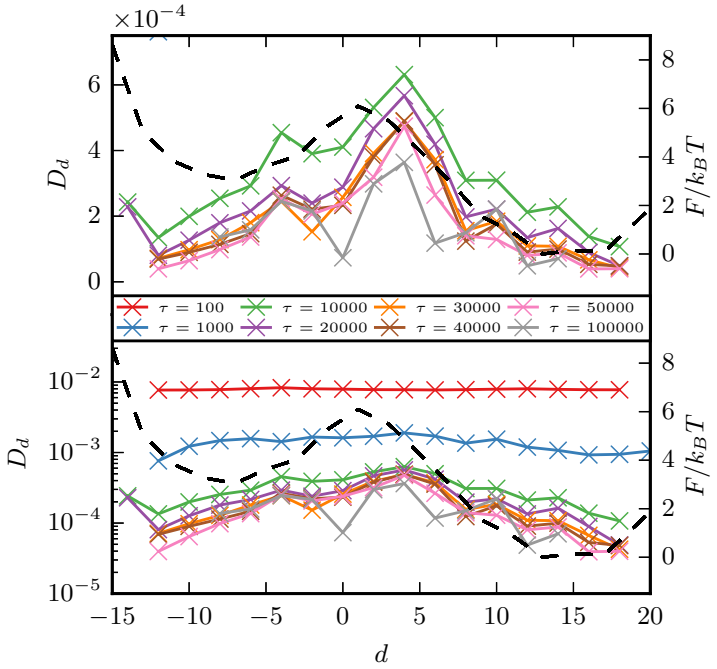

Figure 4.11.: Diffusion coefficient D_d measured using the likelihood maximization method as a function of the chosen lag time τ for the $s = 0.375$-0.400 slice, chosen here as an example. Both panels show the same data but the lower one uses a logarithmic y-axis. The dashed, black line indicates the free energy profile along the slice. Time is measured in units of Monte Carlo sweeps.

4.5.1. A qualitative explanation

We start by noting that the drift towards the stable basins along the s-direction is slow compared to the relaxation time along the d-direction. Hence, in the following calculation we assume that a local equilibrium along slices of constant s develops and consequently crossing the barrier becomes a one-dimensional problem associated with a timescale $\tau_{\text{cross}}(s)$, similar to a previous discussion of multicomponent nucleation by Trinkaus [115].

We then compare τ_{cross} to the timescale τ_{drift} that is associated with the diffusion along the s-direction; if $\tau_{\text{cross}} \gg \tau_{\text{drift}}$, the system is likely to stay on the same side of the barrier, whereas if they are comparable, one expects to see a finite probability of

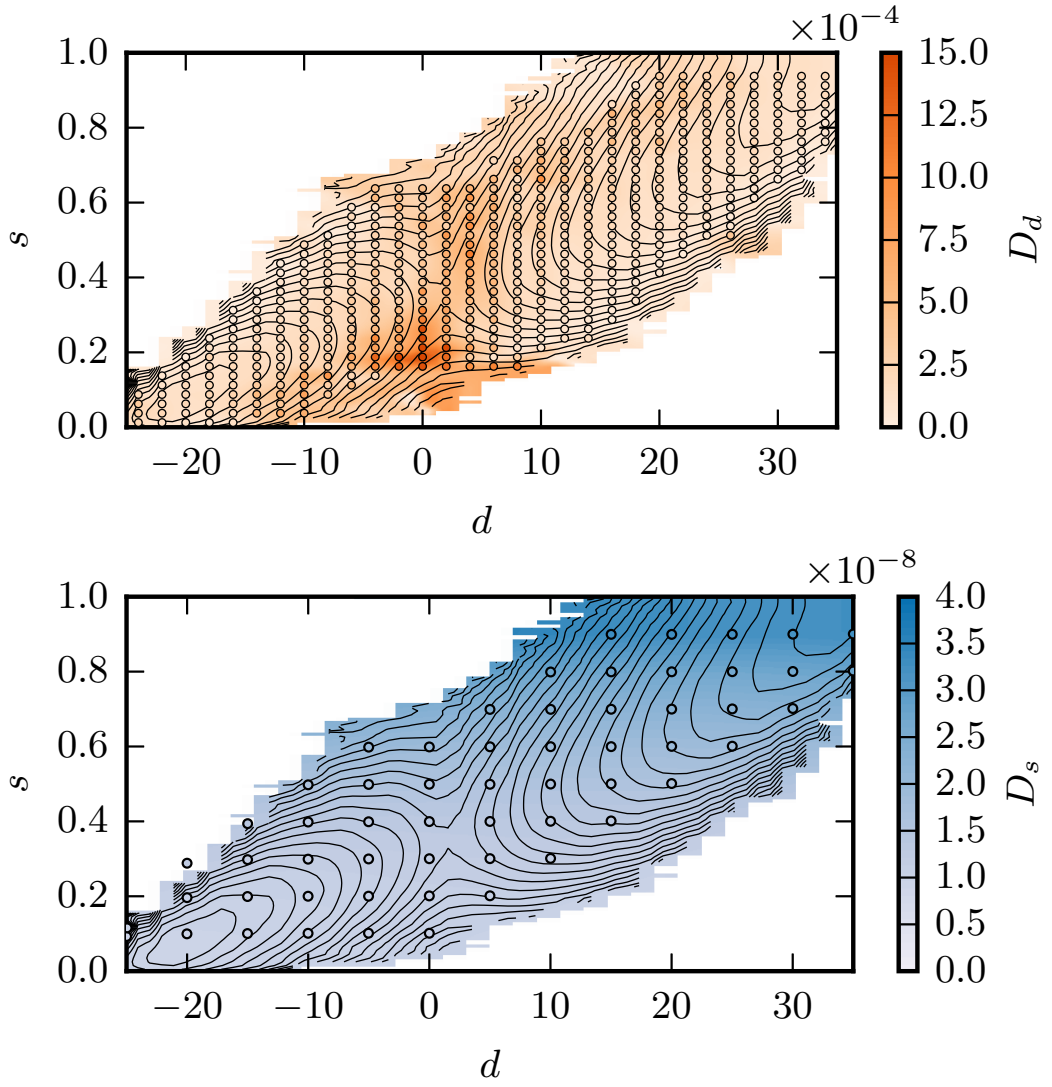

Figure 4.12.: Measured diffusion coefficients (circles) and cubic spline interpolation of these values (background) for the D_d component (top) and the D_s component (bottom). The diffusion coefficients are measured using a likelihood maximization method due to Hummer and coworkers [113, 149] in the d-direction and the mean-square displacement based ansatz by Im and Roux [116, 147, 148] in the s-direction. The unit of time t is 1 Monte Carlo sweep and the black lines indicate the free energy landscape where the lines are separated by 1 $k_\mathrm{B}T$.

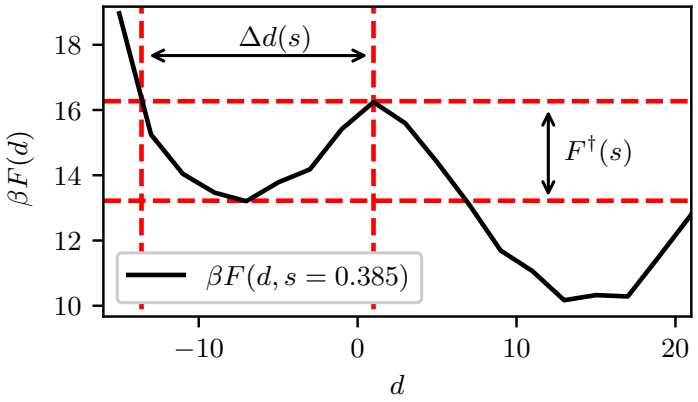

Figure 4.13.: Illustration of the quantities used to estimate the timescale of barrier crossing given by equation (4.12). The black line indicates the free energy $\beta F(d)$ along a slice of constant s. The quantities shown are used to estimate the crossing time from the basin of attraction of slab states towards the disk states. The calculation for crossing from disk to slab proceeds analogously using the width and depth of the disk basin (located at $d \approx 15$) instead.

crossing to the other side of the barrier.

Given the free energy landscape and the diffusion coefficient $D_d(s)$, we can estimate τ_{cross} by the expression

$$\tau_{\text{cross}} \sim \frac{[\Delta d(s)]^2}{D_d(s)} e^{\beta F^\dagger(s)} \tag{4.12}$$

where $F^\dagger(s)$ is the height of the free energy barrier found when one looks only at a slice of the free energy landscape along a line of constant s and Δd is a length scale given by the width of the basin as seen along the slice (see Fig. 4.13). Note the similarity of expression (4.12) to the Kramers [34, 153] rate expression, where, in contrast, the length scales are provided by the curvatures of the free energy profile.[1]

τ_{drift} is related to the drift of the system along the s-axis. As the system moves towards the stable basin and the barrier height $F^\dagger$ becomes larger, τ_{cross} grows exponentially as a function of $F^\dagger$. This change in barrier height can be used to

[1] Note that in slices with higher free energy barriers, we are likely to underestimate τ_{cross} since $1/[\Delta d]^2$ will be smaller than the product of curvatures used in Kramers' theory.

estimate the time it takes until the system has moved to an area within the free energy landscape, where the rate of transitions has considerably changed relative to where the system has started from. We define a characteristic length Δs as the distance at which the barrier height has increased by $\Delta F^\dagger = 1\ k_\mathrm{B}T$:

$$1 = \beta \Delta F^\dagger(s) \approx \beta \frac{\partial F^\dagger(s)}{\partial s} \Delta s. \tag{4.13}$$

In order to estimate τ_drift, we look at the mean first passage time of trajectories started at $s = s_0$ at a point $s_0 - \Delta s$, assuming that the free energy landscape has a constant slope. This time is given by (see App. B and Ref. 54)

$$\begin{aligned} \tau_\mathrm{drift} &\sim \frac{\Delta s}{D_s \beta \left(\frac{\partial F(s)}{\partial s}\right)_{s=s_0}} \\ &= \frac{1}{D_s \beta^2 \left(\frac{\partial F(s)}{\partial s}\right)\left(\frac{\partial F^\dagger(s)}{\partial s}\right)}, \end{aligned} \tag{4.14}$$

where $\beta F(s) = -\log\left[\int \mathrm{d}d' \exp\left(-\beta F(d', s)\right)\right]$ and the integration extends over the appropriate free energy basin.

The ratio of the two timescales, given by

$$\frac{\tau_\mathrm{cross}}{\tau_\mathrm{drift}} = \frac{D_s}{D_d} \beta^2 (\Delta d(s))^2 \left| \frac{\partial F(s)}{\partial s} \frac{\partial F^\dagger(s)}{\partial s} \right| e^{\beta F^\dagger(s)}, \tag{4.15}$$

is shown in Fig. 4.14.

One can see that in the outer regions with $s \lesssim 0.25$ and $s \gtrsim 0.45$ the crossing time becomes comparable to the drift time. Furthermore, if $\tau_\mathrm{cross}/\tau_\mathrm{drift}$ is close to 1 in one direction of the transition, it is orders of magnitude larger in the reverse direction. This suggests that in these regions the probability of crossing from one side of the barrier to the other is non-zero and, on the other hand, after the barrier has been crossed, the probability of going back is small. Hence, we arrive at the explanation of why the committor probabilities in these regions take on the values shown in Fig. 4.5. It takes a long time to change the overall shape of the cluster and in this time fluctuations can occur that make the system cross the barrier. However, once the barrier has been crossed, the probability of going back the other way is small because the global shape of the cluster disfavors such fluctuations. In other words, there is a

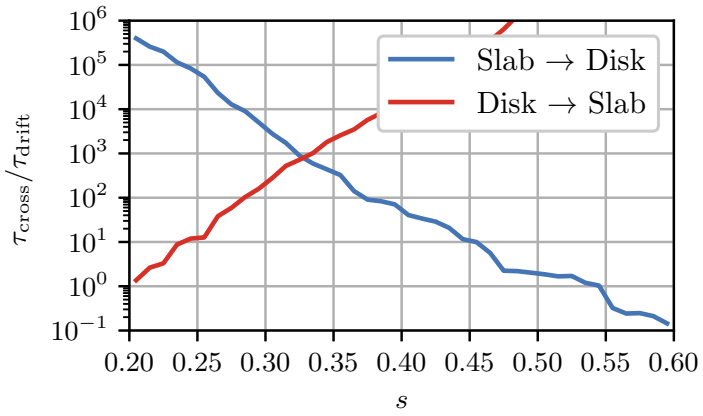

Figure 4.14.: Comparison of the timescales that are required to drift towards the stable basin, τ_{drift}, and to cross the barrier to the other side of the transition, τ_{cross}, if one assumes equilibrium along a slice of constant s. The results have been obtained by numerical evaluation of Equ. (4.15) using the free energy data shown in figure 4.4 and assuming $D_s/D_d = 3.2 \cdot 10^{-5}$, which is the value at the saddle point.

high probability that the bridge of spins that can be seen in the right panel of Fig. 4.8 is severed before the cluster has changed its shape into a slab and, conversely, the likelihood of a bridge forming in the left panel before the cluster becomes disk-shaped is high.

4.5.2. Smoluchowski analysis

A more accurate analysis of the system's behavior given the free energy landscape and the diffusion coefficients can be achieved by modeling the dynamics of the system using a two-dimensional Smoluchowski equation. A similar approach has previously been employed by Metzner *et al.* [53] in order to predict the behavior of a two-dimensional toy model. We use a generalized ansatz that takes into account state dependent diffusion coefficients [54, 146]. In this case, the probability density $\rho(\mathbf{x}, t)$ satisfies the

equation

$$\frac{\partial \rho}{\partial t} = -\sum_{i,j} \frac{\partial}{\partial x_i} \left[\left(\frac{\partial D_{ij}}{\partial x_j} - \beta D_{ij} \frac{\partial F}{\partial x_j} \right) \rho \right] + \sum_{i,j} \frac{\partial^2}{\partial x_i \partial x_j} \left[D_{ij} \rho \right], \tag{4.16}$$

where $\mathbf{x} = (d, s)$, $F = F(\mathbf{x})$ is the free energy shown before, and $D_{ij}(\mathbf{x})$ are position dependent diffusion coefficients. This form of the Fokker-Planck equation[2] mimics a random walk on a potential of mean force given by the free energy F and, at the same time, guarantees that the steady state solution is given by the equilibrium distribution $e^{-\beta F}$.

In this model the committor $p_{\mathcal{B}}(\mathbf{x})$ is then determined by the corresponding backward (or adjoint) equation [53, 54]

$$\sum_{i,j} \left(\frac{\partial D_{ij}}{\partial x_j} - \beta D_{ij} \frac{\partial F}{\partial x_j} \right) \frac{\partial p_{\mathcal{B}}(\mathbf{x})}{\partial x_i} + \sum_{i,j} D_{ij} \frac{\partial^2 p_{\mathcal{B}}(\mathbf{x})}{\partial x_i \partial x_j} = 0. \tag{4.17}$$

The reflecting boundary condition

$$\sum_i n_i D_{ij} \frac{\partial p_{\mathcal{B}}(\mathbf{x})}{\partial x_j} = 0, \tag{4.18}$$

where $\mathbf{n}$ is a normal vector on the domain, and the boundary conditions that surround regions $\mathcal{A}$ and $\mathcal{B}$

$$p_{\mathcal{B}}(\mathbf{x})|_{\partial \mathcal{A}} = 0, \, p_{\mathcal{B}}(\mathbf{x})|_{\partial \mathcal{B}} = 1 \tag{4.19}$$

close the set of equations.

This system of equations can be solved using a finite difference scheme similar to the one employed in Ref. 53 using the free energy and diffusion coefficients measured from simulation as input. The result of such a calculation is shown in Fig. 4.15. It recovers the basic features of the committor observed in the brute force simulations.

[2] The Smoluchowski equation (4.16) is often rewritten in the form $\frac{\partial \rho}{\partial t} = \sum_i \frac{\partial}{\partial x_i} \left[\sum_j D_{ij} e^{-\beta F} \frac{\partial}{\partial x_j} \left(e^{\beta F} \rho \right) \right]$, that makes it immediately obvious that the equilibrium distribution is the stationary solution.

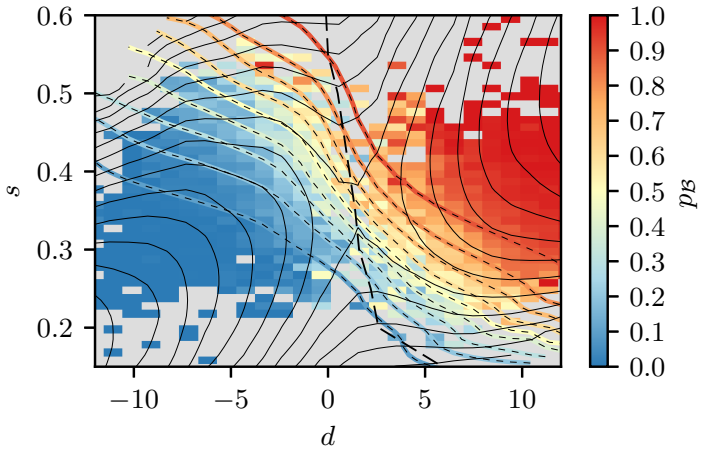

Figure 4.15.: Solution $q(d, s)$ of the adjoint Smoluchowski equation (4.17) (isolines with black dashes) using the free energy data obtained from simulation of the disk-slab transition and the diffusion coefficients shown in figure 4.12. The background color shows committor values shown in Fig. 4.5 averaged over squares of size $1.0[d] \times 0.01[s]$ and the dashed black line represents the ridge of the free energy landscape that separates the basins of attraction of the disk and the slab state.

In particular, the $p_{\mathcal{B}} = 1/2$ committor line significantly deviates from the ridge of the free energy landscape and the regions close to the barrier that have large or small values of s have a significant probability of evolving to the other side of the free energy barrier.

We can also write down a corresponding Langevin-equation, whose realizations will—if evaluated using Ito's interpretation (i.e. by evaluating the drift and diffusion terms at the beginning of each step)—evolve according to Equ. (4.16) [154]. It is given by

$$\frac{\mathrm{d}x_i(t)}{\mathrm{d}t} = \sum_j \left[\frac{\partial D_{ij}}{\partial x_j} - \beta D_{ij} \frac{\partial F}{\partial x_j} \right] + \sum_j g_{ij} \eta_j(t), \tag{4.20}$$

where $\mathbf{x}(t)$ is the position of a random walker, D_{ij}, F and their derivatives are evaluated at $\mathbf{x}(t)$, η is delta-correlated white noise with zero mean and unity variance (i.e. $\langle \eta_i \rangle = 0$, $\langle \eta_i(t) \eta_j(t') \rangle = \delta(t - t') \delta_{ij}$), and $\sum_k g_{ik} g_{kj} = 2D_{ij}$ [146]. The latter condition simplifies to $g_{ij} = \sqrt{2D_i} \delta_{ij}$ if we assume the diffusion coefficient is diagonal

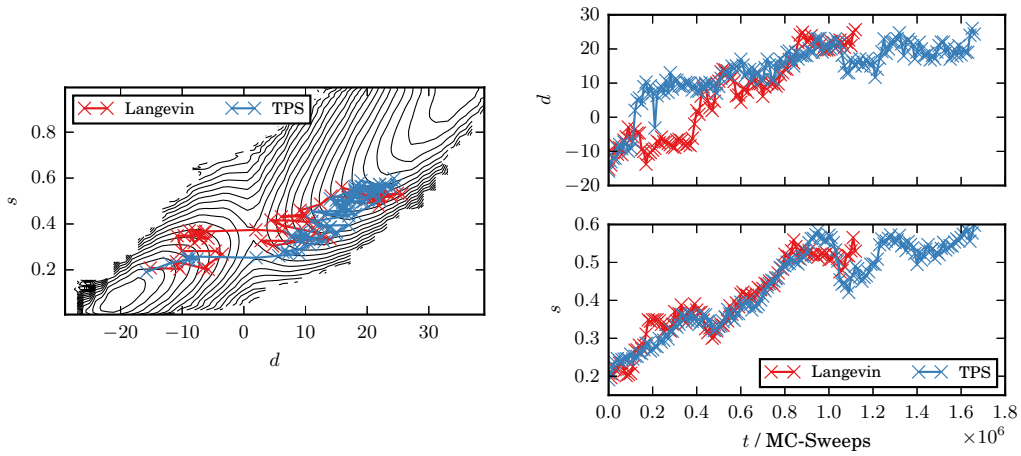

Figure 4.16.: Example trajectories obtained from TPS simulations (blue) and by integrating the Langevin equation (4.20) (red) from a state at the saddle point as they appear projected onto the d-s-plane (top) and as a function of time (bottom).

and given by Equ. (4.7). Figure 4.16 shows an example Langevin trajectory compared to a trajectory obtained by TPS and Fig. 4.17 shows the probability distribution of finding a random walker as a function of time.

These two diagrams demonstrate two things: the trajectories generated using a full simulation and the ones generated from the Langevin equation very much look alike and, secondly, that indeed a relaxation towards equilibrium along the d coordinate occurs before the system has time to evolve to the stable basins.

4.6. Discussion

We have investigated the disk-to-slab transition in the 2d-Ising model using a variety of methods, including a model based on a two-dimensional Smoluchowski equation. This model allows us to take the different timescales involved in this process into account: the fluctuations of the narrow bridge between the clusters (characterized by the d-coordinate) and the change of the overall shape of the cluster (captured by the s-coordinate). By comparing committor distributions obtained by brute-force using the full dynamics of the system, to the committor distribution obtained by solving

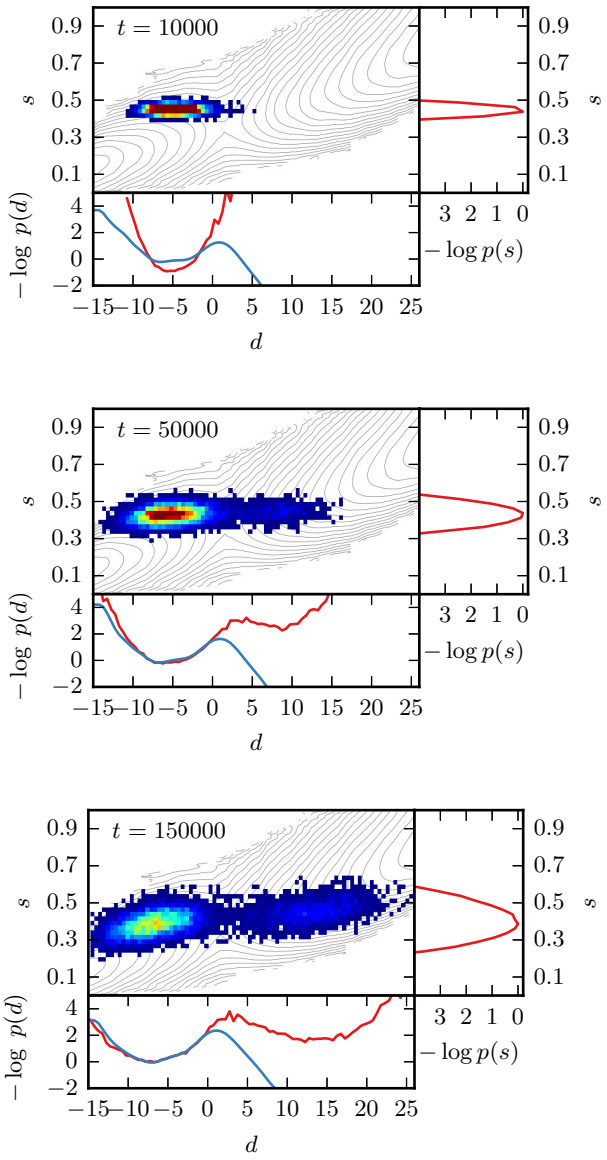

Figure 4.17.: Time evolution of the probability density function $\rho(\mathbf{x}, t)$ as obtained by integrating trajectories using equation (4.20) and subsequently averaging over the positions $x(t)$. The random walkers are started at position $d = -5$ and $s = 0.45$. Red indicates high densities and blue low densities. In each of the plots, the bottom and the right plot show the negative logarithm of the probability density projected on each axis (red). In the bottom plot, the equilibrium free energy $\beta F(d, s = \langle s \rangle_t)$ is shown (blue), where $\langle s \rangle_t = \int \mathrm{d}d \int \mathrm{d}s \; s\rho(d, s; t)$ is the mean value of s at the given time.

the adjoint equation (4.17) (Fig. 4.15) we find that the dynamics of the transition are well described by the Smoluchowski equation (4.16).

This suggests that, with the coordinates d and s, we have indeed captured the degrees of freedom that are most relevant for the disk-to-slab transition. Increased values of s, corresponding to disk-like clusters, enhance the likelihood of a trajectory started from a configuration to develop towards the disk state. While stated in this way, this result does not seem surprising, it is nonetheless interesting to note, that this effect only becomes apparent when one includes the dynamics of the system into consideration, while the free energy landscape alone does not capture this feature.

In the disk-to-slab transition considered here, this behavior is caused by the large difference in timescales associated with the crossing of the free energy barrier and the relaxation towards the stable basins. As a consequence, a local quasi-equilibrium forms where the global shape of the cluster is fairly stable, while its surface fluctuates.

It is worth pointing out that this difference in timescales is due to the choice of dynamics that mimic local mass transport. A different choice of dynamics, for example allowing the exchange of arbitrary spins or allowing the magnetization of the system to fluctuate [85], will result in different behavior.

Our analysis highlights the fact that, even in the context of a fairly simple model system, the dynamics of a system are crucial to identifying transition mechanisms, especially when one needs to use a combination of multiple order parameters to obtain a good reaction coordinate. In particular, including dynamics may help to reconcile free energy landscapes and committor probabilities, or their combination may point to the existence of other important degrees of freedom.

4.7. Acknowledgments

The authors thank Georg Menzl and Phillip L. Geissler for many enlightening discussions. C.M. is supported by an uni:docs fellowship of the University of Vienna. A.T. acknowledges support from the Austrian Science Fund (FWF) Project Nr. P27738-N28. The computational results presented have been achieved in part using the Vienna Scientific Cluster (VSC).

5. Weak scaling of the contact distance between two fluctuating interfaces with system size

The contents of this chapter have previously been published in *Physical Review E* and can be found under the following citation:

> Moritz, C., Sega, M., Innerbichler, M., Geissler, P. L. & Dellago, C. *Weak scaling of the contact distance between two fluctuating interfaces with system size.* Phys. Rev. E **102**, 062801 (2020).

Abstract

A pair of flat parallel surfaces, each freely diffusing along the direction of their separation, will eventually come into contact. If the shapes of these surfaces also fluctuate, then contact will occur when their centers of mass remain separated by a nonzero distance ℓ. An example of such a situation is the motion of interfaces between two phases at conditions of thermodynamic coexistence, and in particular the annihilation of domain wall pairs under periodic boundary conditions. Here we present a general approach to calculate the probability distribution of the contact distance ℓ and determine how its most likely value, ℓ^*, depends on the surfaces' lateral size L. Using the Edward-Wilkinson equation as a model for interfaces, we demonstrate that ℓ^* scales weakly with system size, i.e. the dependence of ℓ^* on L for both (1+1)- and (2+1)-dimensional interfaces is such that $\lim_{L\to\infty}(\ell^*/L) = 0$. In particular, for (2+1)-dimensional interfaces ℓ^* is an algebraic function of $\log L$, a result that is confirmed by computer simulations of slab-shaped domains formed under periodic boundary conditions. This weak scaling implies that such domains remain topologically intact

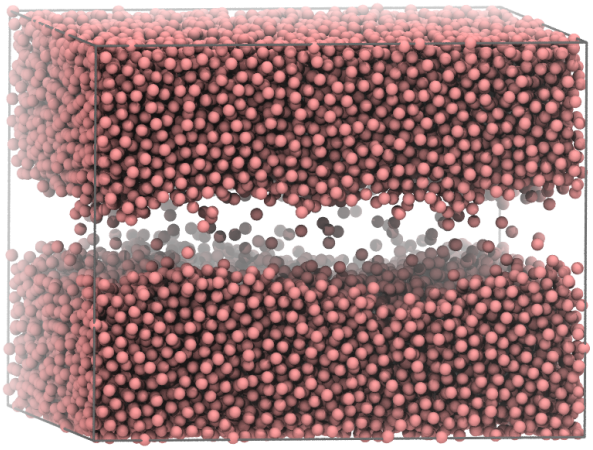

Figure 5.1.: Example configuration of a Lennard-Jones gas slab enclosed by liquid. The configuration has been obtained from a molecular dynamics simulation at liquid-gas coexistence using periodic boundary conditions. This snapshot has been rendered using VMD [168, 169].

until ℓ becomes very small compared to the lateral size of the interface, contradicting expectations from equilibrium thermodynamics.

5.1. Introduction

In the initial stages of many large-scale changes in the shape of interfaces, microscopic thermal fluctuations play a crucial role. The rupture of a thin liquid film [155–157], the breakup of a liquid jet [158–162], and the fusion of two liquid droplets [163–167] are examples of processes that on the meso- and macroscopic scale are governed by surface tension and hydrodynamics, while at their earliest stages they are controlled by thermal undulations.

Thermal fluctuations also govern the distance up to which two planar interfaces will approach before they come into contact for the first time; a situation which can be viewed as an approximation to the droplet fusion problem for large radii. Figure 5.1 shows a snapshot taken from a computer simulation of a Lennard-Jones fluid that is

an example of this kind of interfacial system. The two interfaces are formed by a single slab of atoms in the liquid phase that is connected through the periodic boundaries of the simulation box. Figure 5.2 shows a similar scenario for a two-dimensional Ising model at coexistence. The aim of this paper is to determine how close the centers-of-mass of two such interfaces approach before they come into contact for the first time.

Larger surfaces, whose topographical fluctuations are generally more extreme, should contact each other at larger average separation. At the same time, interfaces that diffuse more slowly relative to each other are expected to come into contact at a larger distance, since more configurations can be explored by the system while the center-of-mass moves over a certain length. We find both of these trends reflected in our analysis. However, the dependence of the most likely distance of the centers-of-mass at the time of first contact, ℓ^*, on both the linear system size L and on the diffusion coefficient of the centers of mass of the interfaces, D_{int}, turns out to be weak. In particular, in the case of a two-dimensional interface that is embedded in three-dimensional space (a (2+1)-dimensional interface), L and D_{int} enter the result for ℓ^* as an algebraic function of $\log L$ and $\log D_{\mathrm{int}}$ only. This dependence of ℓ^* on $\log L$ resembles previous results obtained by Ponthus *et al.* [170] for static (2+1)-dimensional interfaces, where it has been observed that the average distance between two such interfaces when they are in single point contact grows with system size in a similar manner.

Our results not only imply that the distance at which two freely diffusing, macroscopic interfaces come into contact for the first time is still likely microscopic, but also has interesting consequences for the situations shown in Figs. 5.1 and 5.2. In both cases, the slab is thermodynamically metastable at conditions that fix the relative proportions of coexisting phases. Alternate geometries—a spherical gas bubble and a disk formed by spins pointing in the same direction—would have a considerably smaller surface and, therefore, also a lower free energy [77, 80, 83, 84, 171]. Nevertheless, these slab geometries are remarkably long-lived. In fact, we will show that the critical widths of these slabs, at which they transition into the thermodynamically preferred shape, grow with L much more slowly than the scaling $\ell^* \sim L$ expected from equilibrium considerations (see Sec. 5.5 for details on how this scaling comes about). Hence, this two-interface system has the interesting property that with increasing system size the behavior of the system increasingly diverges from the behavior expected based on

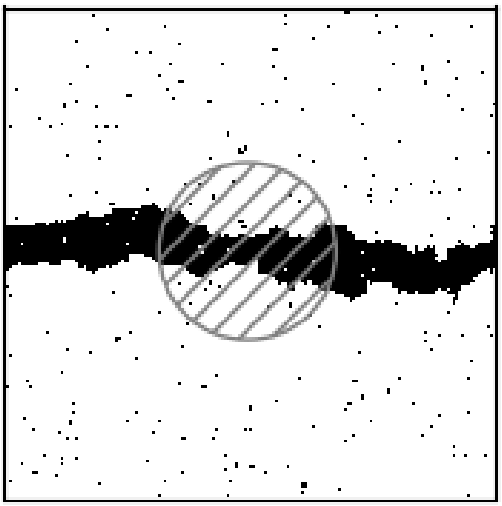

Figure 5.2.: Example configuration obtained from a simulation of the 200×200 Ising model with vanishing external field. The gray circle indicates a disk with the same area as the slab composed of black spins. This circle has a circumference that is roughly 45% smaller than the surface of the slab. Matplotlib [173] has been used to generate graphs and Ising model simulation snapshots throughout this work.

equilibrium principles, eventually leading to a complete suppression of the transition to the stable state altogether [172].

The remainder of the article is structured as follows: in Sec. 5.2 we present a rough estimate of the expected scaling of the most likely contact distance, ℓ^*, with system size L. In Sec. 5.3 we explain our approach to calculating the distribution of contact distances $u(\ell)$. Section 5.4 introduces the Edward-Wilkinson (EW) equation as a model for surface dynamics and goes through all the steps necessary to predict the scaling of the contact distance between two EW interfaces with system size. In Sec. 5.5 we report on simulations of slabs in the Ising model and in a Lennard-Jones system at liquid-gas coexistence. The predicted scaling behavior of the EW model is then compared with the critical width of slabs observed in simulation. Section 5.6 provides a summary and a discussion of the results.

5.2. A simple scaling argument

One expects the meeting of initially distant interfaces to occur through a combination of two basic processes. First, the interfaces' mean positions (averaged over directions perpendicular to their separation) each execute a random walk with diffusion coefficient $D_{\text{int}} \sim 1/L^d$, where L is the surfaces' linear size and d is their dimensionality. Second, as their shapes change in the course of natural fluctuations, a point on one interface can draw transiently nearer to a point on the other interface, even if the mean separation ℓ is fixed. An extreme fluctuation in interfacial shapes can thus achieve contact while the mean positions remain separated by a considerable distance. Contact occurs when the rate $k(\ell)$ of contact-forming shape fluctuations is roughly comparable to a rate k_D of further diffusion

$$k(\ell) \sim k_D(\ell). \tag{5.1}$$

This diffusion rate, $k_D \sim D/\lambda^2$, is determined by the diffusion constant $D = \sqrt{2}D_{\text{int}}$, that is associated with the time evolution of the mean distance between the two interfaces, together with a length scale λ whose magnitude is not straightforward to anticipate. For the purpose of roughly calculating ℓ^*, we assume simply that λ is independent of L.

According to notions of transition state theory, the rate of an extreme shape fluctuation that establishes contact at fixed ℓ should be proportional to its equilibrium probability, i.e. the probability of an undulation that closes the mean gap. The distribution $P(x)$ of the fluctuating height x at a single point on an interface is simply estimated from Gaussian field theories as [174]

$$P(x) \sim \exp[-x^2/(2w^2)], \tag{5.2}$$

where w is the *roughness* of the interface and $w^2 \sim L$ for $d = 1$ and $w^2 \sim \log L$ for $d = 2$. Assuming the gap-closing probability to follow these simple statistics, we estimate $k(\ell) \sim \exp[-\ell^2/(2w^2)]$.

Assembling these arguments, we expect the typical separation ℓ^* at contact to scale with L as

$$\ell^*_{1d} \sim \sqrt{L \log L} \qquad \text{and} \qquad \ell^*_{2d} \sim \log L \tag{5.3}$$

for one- and two-dimensional interfaces, respectively. According to this rough predic-

tion, growth of ℓ^* with system size is so gradual that ℓ^* can remain microscopic even for macroscopic systems.

This line of reasoning is loose, imprecise, and incomplete. First, as mentioned, the balance between $k(\ell)$ and k_D involves a length scale λ, which is not specified here. Secondly, the gap-closing probability should reflect extreme value statistics of the *closest* points on the two interfaces, not that of arbitrarily chosen points [170]. Finally, since long-wavelength undulations of an interface evolve very slowly in time, the assumptions of transition state theory are difficult to justify in this context.

Sections 5.3 and 5.4 present a much more careful treatment of the dynamics that lead to interfacial contact. By making controlled approximations for well-defined models, they reveal and clarify subtleties associated with all of the issues listed above. The theory developed yields improved scaling predictions for ℓ^* that confirm an extremely slow divergence of ℓ^* with system size.

5.3. A framework for calculating contact distance distributions

5.3.1. Reaction-diffusion equation for the contact distance distribution

As a first step towards the estimation of the typical contact distance ℓ^*, we devise a simple reaction-diffusion equation that governs the time evolution of the distribution of distances between fluctuating interfaces. Consider two planar interfaces, in a 2- or 3-dimensional simulation box with periodic boundary conditions, that do not interact with each other until they are brought in contact by thermal fluctuations. These interfaces are released at an initial distance ℓ_0 that is much larger than the typical size of interface fluctuations. As shown in Fig. 5.3 we describe the geometry of the surfaces by two continuous functions $h_1(\mathbf{x})$ and $h_2(\mathbf{x})$, where the vector $\mathbf{x}$ collects the lateral coordinates (i.e., those orthogonal to the h-direction). The distance between the two interfaces at a given position $\mathbf{x}$ is denoted by $\Delta h(\mathbf{x}) = h_2(\mathbf{x}) - h_1(\mathbf{x})$ and the mean distance of the two interfaces is given by $\ell = \bar{h}_2 - \bar{h}_1$, where $\bar{h}_1$ and $\bar{h}_2$ are the spatially averaged means of h_1 and h_2, respectively. The distance between the two interfaces at the point where they are closest is denoted by

$$s = \min_{\mathbf{x}} \left[\Delta h(\mathbf{x})\right]. \tag{5.4}$$

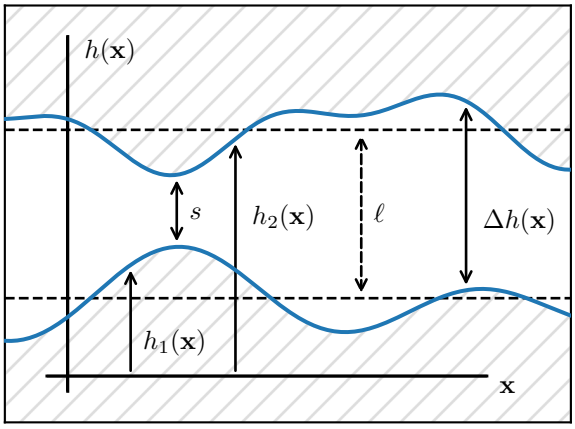

Figure 5.3.: Two surfaces are described by functions $h_1(\mathbf{x})$ and $h_2(\mathbf{x})$ where $\mathbf{x}$ is a vector that collects the lateral coordinates (those orthogonal to the surface normal). The dashed lines indicate the average positions $\bar{h}_1$ and $\bar{h}_2$ of the interfaces, ℓ is the average distance between the interfaces, and s is the minimum distance between the two interfaces, i.e. $s = \min_{\mathbf{x}} [\Delta h(\mathbf{x})] = \min_{\mathbf{x}} [h_2(\mathbf{x}) - h_1(\mathbf{x})]$.

As long as the two interfaces are not in contact with each other, $\bar{h}_1$ and $\bar{h}_2$ freely diffuse relative to each other along the h-direction governed by the diffusion coefficient D_{int}. In the case of a liquid slab, the interfaces diffuse due to mass transport in the slab, due to evaporation and condensation on the surface, and, in the case of simulations at constant pressure, due to fluctuations of the box size.

The rate $k(\ell)$ with which fluctuations of the interfaces are formed that are large enough to bridge the gap between the two interfaces depends on ℓ, i.e. $k = k(\ell)$. This situation is formally equivalent to a particle that diffuses along a single direction ℓ and undergoes a reaction with a position dependent reaction rate $k(\ell)$. Using this analogy we write down the following partial differential equation that governs the evolution of the probability density, $\rho(\ell, t)$, that two interfaces have not yet touched, and have mean distance ℓ at time t:

$$\frac{\partial \rho(\ell,t)}{\partial t} = D_{\text{int}} \frac{\partial^2 \rho(\ell,t)}{\partial \ell^2} - k(\ell)\rho(\ell,t) \tag{5.5}$$

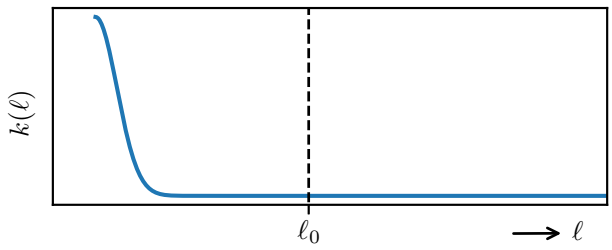

Figure 5.4.: Sketch of an example rate function $k(\ell)$: the Gaussian rate function suggested by Eq. (5.2). The initial position is marked by ℓ_0.

The initial condition is given by

$$\rho(\ell, 0) = \delta(\ell - \ell_0), \tag{5.6}$$

where $\delta(x)$ is the Dirac δ-function and ℓ_0 is the initial separation of the interfaces.

This equation is reminiscent of the theory of diffusion-controlled reactions [175–177], however, instead of reactions that occur at a boundary, the reaction in our model is controlled by a position- and concentration dependent loss-term $k(\ell)\rho(\ell, t)$. The time integral over the loss term yields the distribution of distances at which the reaction occurs,

$$u(\ell) = \int_0^\infty \mathrm{d}t \; k(\ell)\rho(\ell, t). \tag{5.7}$$

In the next section we introduce a path-integral formalism that allows us to calculate $u(\ell)$.

5.3.2. A path-integral formulation of $u(\ell)$

In order to derive an expression for the probability distribution $u(\ell)$, we use a well-known correspondence between reaction-diffusion equations and the Schrödinger equation that has been pointed out by various authors before; see Refs. 178, 146, 179, and 180 for comprehensive treatments. Furthermore, our derivation is closely related to the Feynman-Kac path integral formula [181].

We start by considering a discrete diffusive trajectory Λ that consists of N steps and that has been obtained by sampling a continuous trajectory $\ell(t)$ at times $i\Delta t$. We

write

$$\Lambda = \{\ell_0, \ell_1, \ldots, \ell_n, \ell_{n+1}, \ldots \ell_N\}, \tag{5.8}$$

where $\ell_i = \ell(i\Delta t)$. The probability of observing Λ for given initial position ℓ_0 is given by

$$P_{\text{diff}}[\Lambda] = \prod_{i=0}^{N-1} p(\ell_i \to \ell_{i+1}), \tag{5.9}$$

where $p(\ell_i \to \ell_{i+1})$ is the transition probability of a freely diffusing random walker:

$$p(\ell_i \to \ell_{i+1}) = \frac{1}{\sqrt{4\pi D_{\text{int}} \Delta t}} \exp\left[-\frac{(\ell_{i+1} - \ell_i)^2}{4D\Delta t}\right] \tag{5.10}$$

Now let us assume that the first contact between the interfaces occurs in the time interval between steps n and $n+1$. The probability of observing such a trajectory is then given by the product of P_{diff} with the conditional probability $P_{\text{nr}}[n|\Lambda]$ that no reaction occurs until time step n given that we are following trajectory Λ, and the probability $P_{\text{r}}[n|\Lambda]$ that the reaction occurs between $n\Delta t$ and $(n+1)\Delta t$,

$$P[\Lambda] = P_{\text{diff}}[\Lambda] P_{\text{nr}}[n|\Lambda] P_{\text{r}}[n|\Lambda] \tag{5.11}$$

We approximate $P_{\text{r}}[n|\Lambda]$ by

$$P_{\text{r}}[\ell_n, \ell_{n+1}] \approx 1 - e^{-k(\ell_n)\Delta t} \approx k(\ell_n)\Delta t, \tag{5.12}$$

i.e. we assume that $k(\ell)$ is approximately constant in the region the particle visits between ℓ_n and ℓ_{n+1}. In the same manner we also approximate $P_{\text{nr}}[n|\Lambda]$ by

$$P_{\text{nr}}[n|\Lambda] \approx \prod_{i=0}^{n-1} e^{-k(\ell_i)\Delta t} = \exp\left[-\Delta t \sum_{i=0}^{n-1} k(\ell_i)\right]. \tag{5.13}$$

Note that for ease of notation we define here that the product in this equation is equal to one if its end index is smaller than its starting index and, by extension, that the sum on the right hand side is 0 in the same situation. Substituting these expressions into (5.11) and expanding P_r for small Δt yields the probability of a specific trajectory

Λ that reacts at time $n\Delta t$,

$$P\left[\Lambda\right] = \frac{k(\ell_n)\Delta t}{\left(4\pi D_{\mathrm{int}}\Delta t\right)^{N/2}} \exp\left[-\Delta t \sum_{i=0}^{n-1} k(\ell_i) - \right. \\ \left. - \sum_{i=0}^{N-1} \frac{\left(\ell_{i+1}-\ell_i\right)^2}{4D_{\mathrm{int}}\Delta t}\right]. \tag{5.14}$$

The probability $u(\ell)$ of observing a reaction at a specific position ℓ is now the sum of $P[\Lambda]$ over all possible paths Λ and path lengths n where the initial point ℓ_0 and the final point $\ell_n = \ell$ are kept fixed:

$$\begin{aligned} u\left(\ell\right) &= \lim_{N\to\infty} \sum_{n=0}^{N-1} \int \frac{\mathrm{d}\ell'_1 \ldots \mathrm{d}\ell'_{N-1}}{\left(4\pi D_{\mathrm{int}}\Delta t\right)^{N/2}} \delta(\ell'_n - \ell) \exp\left[-\sum_{i=0}^{N-1} \frac{\left(\ell'_{i+1}-\ell'_i\right)^2}{4D_{\mathrm{int}}\Delta t} - \Delta t \sum_{i=0}^{n-1} k(\ell'_i)\right] k(\ell'_n)\Delta t \\ &= k(\ell) \sum_{n=0}^{\infty} \Delta t \int \frac{\mathrm{d}\ell'_1 \ldots \mathrm{d}\ell'_{n-1}}{\left(4\pi D_{\mathrm{int}}\Delta t\right)^{n/2}} \exp\left[-\sum_{i=0}^{n-1} \Delta t \left(\frac{\left(\ell'_{i+1}-\ell'_i\right)^2}{4D_{\mathrm{int}}(\Delta t)^2} + k(\ell'_i)\right)\right] \end{aligned} \tag{5.15}$$

In the second line we have carried out the integrations over all ℓ'_i with $i \geq n$ and have taken the limit $N \to \infty$. We now take the limit $\Delta t \to 0$ while keeping the trajectory lengths $T = n\Delta t$ fixed. With the abbreviations

$$\int_0^\infty \mathrm{d}T \int \mathcal{D}[\ell_T] \equiv \lim_{\Delta t\to 0} \sum_{n=0}^{\infty} \Delta t \int \frac{\mathrm{d}\ell_1 \ldots \mathrm{d}\ell_{n-1}}{\left(4\pi D_{\mathrm{int}}\Delta t\right)^{n/2}}, \tag{5.16}$$

and

$$\begin{aligned} S[\ell_T(t)] &= \int_0^T \mathrm{d}t' \left\{\frac{v_T(t')^2}{4D_{\mathrm{int}}} + k\left[\ell_T(t')\right]\right\} \\ &\equiv \lim_{\Delta t\to 0} \sum_{i=0}^{n-1} \Delta t \left\{\frac{\left(\ell_{i+1}-\ell_i\right)^2}{4D_{\mathrm{int}}(\Delta t)^2} + k(\ell_i)\right\}, \end{aligned} \tag{5.17}$$

this yields

$$u(\ell) = k(\ell) \int_0^\infty \mathrm{d}T \int \mathcal{D}[\ell_T(t)] e^{-S[\ell_T(t)]}. \tag{5.18}$$

Here $\ell_T(t)$ is a trajectory of length T and $v_T(t) = \dot{\ell}_T(t)$. As suggested by a comparison to Eq. (5.7), the probability density $\rho(\ell, t)$ is given by

$$\rho(\ell, t) = \int \mathcal{D}[\ell_T(t)] e^{-S[\ell_T(t)]}. \tag{5.19}$$

Equation (5.19) is known as a path-integral in quantum mechanics (QM) and in the following we will use results obtained there to calculate an approximation for $u(\ell)$. In particular, in analogy to the semi-classical approximation in QM, we can calculate an expression for the probability of the most likely path between two points ℓ_0 and ℓ. This can be done most easily by comparing Eq. (5.17) to the classical action of a particle in a potential that follows a trajectory $x(t)$,

$$S\left[x(t)\right] = \int_0^T \mathrm{d}t \left[\frac{m\dot{x}(t)^2}{2} - V(x(t))\right], \tag{5.20}$$

with the kinetic energy $K = m\dot{x}^2/2$ and the potential energy V. The paths with extremal action are the paths that are solutions of the classical equations of motion. Hence, the path $\tilde{\ell}(t)$ that minimizes the action (5.17) is the Newtonian trajectory taken by a classical particle with mass $1/2D_{\mathrm{int}}$ in a potential $V(\ell) = -k(\ell)$ [178], i.e. the inverted reaction rate function. Hence, the trajectories with maximum probability (or the *classical paths*), $\tilde{\ell}_T(t)$, are solutions of the equation

$$\dot{\tilde{\ell}}_T(t) = \pm\sqrt{4D_{\mathrm{int}}\left(E + k(\tilde{\ell}_T(t))\right)} \tag{5.21}$$

that fulfill the boundary conditions $\tilde{\ell}_T(0) = \ell_0$ and $\tilde{\ell}_T(T) = \ell$. The constant E that is determined by these boundary conditions together with T (i.e. $E = E(\ell, \ell_0, T)$), resembles the total energy of the classical particle $E = K + V$. Alternatively, Eq. (5.21) can be derived by optimizing the ℓ_i in Eq. (5.14) for maximum $P[\Lambda]$ and subsequently taking the limit $\Delta t \to 0$.

It is reasonable to assume that the rate of gap-closing fluctuations shrinks with increasing mean distance ℓ, so in the following we assume that the derivative of the rate function fulfills $k'(\ell) < 0$. This situation is sketched in Fig. 5.4. In addition, we place a reflecting boundary at the initial position ℓ_0. This has two effects: first, the average length of trajectories is finite in this case (which is not necessarily the case if the rate function $k(\ell)$ goes to zero fast enough as $\ell \to \infty$); secondly, the solution to Eq. (5.21) is unique for any given set of boundary conditions (ℓ_0, ℓ, and T), i.e. there is only a single classical path that leads from ℓ_0 to ℓ in time T. Note, that we have chosen $\ell_0 > \ell$ and will keep this convention through the rest of the derivation.

Dynamics with such a reflecting boundary can be mapped onto an unbounded system

with a symmetrized rate function $k_{\mathrm{sym}}(x)$ such that $k_{\mathrm{sym}}(\ell) = k_{\mathrm{sym}}(2\ell_0 - \ell)$[180, 182], i.e.

$$k_{\mathrm{sym}}(\ell) = \Theta\left(\ell - \ell_0\right) k(\ell) + \Theta\left(-\ell + \ell_0\right) k(2\ell_0 - \ell), \tag{5.22}$$

where $\Theta(x)$ is the Heaviside step function. The transition probability from ℓ_0 to ℓ in time T, $p(\ell_0, \ell, T)$, is then given by

$$\begin{aligned} p(\ell_0, \ell, T) &= p_{\mathrm{sym}}(\ell_0, \ell, T) + p_{\mathrm{sym}}(\ell_0, 2\ell_0 - \ell, T) \\ &= 2p_{\mathrm{sym}}(\ell_0, \ell, T) \end{aligned} \tag{5.23}$$

where $p_{\mathrm{sym}}(\ell_0, \ell, T)$ is the transition probability calculated using the extended rate function k_{sym} without boundaries and in the second line we have used the symmetry of k_{sym} and the fact that $\ell = \ell_0$ at $t = 0$. In other words, one has to sum the path probabilities that move from ℓ_0 to ℓ and another set of paths that move from ℓ_0 to the symmetrically equivalent $2\ell_0 - \ell$. We calculate the probabilities of these paths using a semiclassical approximation. The principal difficulty in this calculation lies in the fact that the extended rate function $k_{\mathrm{sym}}(\ell)$ is not analytic at ℓ_0 and, hence, can only be treated perturbatively [182]. In the following calculation, we assume that, due to the shape of the rate function $k(\ell)$, the corrections to our semiclassical calculations are small. In App. C.2 we then numerically check our results for exponential and Gaussian rate functions and find that our calculations are in excellent agreement for small but finite D_{int}.

We approximate the path integral in Eq. (5.18) by expanding the action S up to leading order around the likeliest paths [178, 180, 183]. This approximation yields

$$u\left(\ell\right) = \frac{k(\ell)}{Z} \int_0^{T_0} \mathrm{d}T \; e^{-\tilde{S}_T(\ell, \ell_0, T)} \tilde{F}_T(\ell, \ell_0, T), \tag{5.24}$$

where T_0 is the length of the longest possible path which has the minimum "energy" $E_0 = -k(\ell_0)$, $\tilde{S}_T(\ell, \ell_0, T) = S[\tilde{\ell}_T(t)]$ is the action of the likeliest path and the factor $\tilde{F}_T(\ell, \ell_0, T)$ arises from the expansion around the likeliest path. It is given by [180]

$$\begin{aligned} \tilde{F}_T(\ell, \ell_0, T) = \Bigg\{ & 2\pi \sqrt{D_{\mathrm{int}}} \kappa(\ell, \ell_0, E(T)) \\ & \times \int_\ell^{\ell_0} \mathrm{d}\ell' \; \left[E(T) + k(\ell')\right]^{-3/2} \Bigg\}^{-1/2} \end{aligned} \tag{5.25}$$

with

$$\kappa(\ell, \ell_0, E) = \sqrt{(E + k(\ell_0))\,(E + k(\ell))}. \tag{5.26}$$

The normalization constant

$$Z = \int_{-\infty}^{\ell_0} \mathrm{d}\ell \left[k(\ell) \int_0^{T_0} \mathrm{d}T\; e^{-\tilde{S}_T(\ell,\ell_0,T)} \tilde{F}_T(\ell, \ell_0, T) \right] \tag{5.27}$$

is introduced in Eq. (5.24) to normalize the distribution $u(\ell)$ and includes contributions that are neglected due to the assumptions we made regarding the boundary condition at ℓ_0 and the multiplicity of the classical paths; because the initial position ℓ_0 is also the location of a reflecting boundary, there are two identical paths for each value of T with the same energy E.

The action of the likeliest path of length T can be expressed in terms of an integral over the velocity $\dot{\tilde{\ell}}(t)$,

$$\begin{aligned}
\tilde{S}_T(\ell, \ell_0, T) &= \int_0^T \mathrm{d}t\;\; [K - V] = \int_0^T \mathrm{d}t\;\; [-E + 2K] \\
&= -E(T)T + \int_0^T \mathrm{d}t\; \dot{\tilde{\ell}}_T \frac{\dot{\tilde{\ell}}_T}{2D_{\mathrm{int}}} \\
&= -E(T) \int_{\ell_0}^{\ell} \frac{\mathrm{d}\ell'}{\dot{\tilde{\ell}}_T(\ell')} + \int_{\ell_0}^{\ell} \mathrm{d}\ell'\; \frac{\dot{\tilde{\ell}}_T(\ell')}{2D_{\mathrm{int}}},
\end{aligned}$$

where we have used the fact that

$$T = \int_{\ell_0}^{\ell} \frac{\mathrm{d}\ell'}{\dot{\tilde{\ell}}_T(\ell')}. \tag{5.28}$$

By substituting Eq. (5.21) (using the minus sign because we consider the path from $\ell_0 > \ell$ to ℓ) we arrive at the expression

$$\tilde{S}_T(\ell, \ell_0, T) = \int_{\ell}^{\ell_0} \mathrm{d}\ell'\; \frac{E(T)/2 + k(\ell')}{\sqrt{D_{\mathrm{int}}(E(T) + k(\ell'))}}. \tag{5.29}$$

Due to the placement of the reflecting boundary at ℓ_0 and the assumption that $k' < 0$, $E(T)$ is a monotonic function of T so that we can rewrite the integral in

Eq. (5.24) as an integral over E by using the derivative

$$\frac{\mathrm{d}T}{\mathrm{d}E} = -\frac{1}{8\pi D\kappa(\ell,\ell_0,E)\tilde{F}_T(\ell,\ell_0,E)^2}, \tag{5.30}$$

leading us to the expression

$$u\left(\ell\right) = \frac{k(\ell)}{8\pi DZ}\int_{E_0}^{\infty}\mathrm{d}E\ \frac{e^{-\tilde{S}_E(\ell,\ell_0,E)}}{\kappa(\ell,\ell_0,E)\tilde{F}_E(\ell,\ell_0,E)}, \tag{5.31}$$

where the notation $\tilde{S}_E$ and $\tilde{F}_E$ indicates that these functions are now evaluated using E as the independent variable instead of T.

This integral can be evaluated using a saddle point approximation. A calculation of the derivatives

$$\frac{\partial\tilde{S}_E(\ell,\ell_0,E)}{\partial E} = \int_{\ell}^{\ell_0}\mathrm{d}\ell'\ \frac{E}{4\sqrt{D_{\mathrm{int}}(E+k(\ell))^3}}. \tag{5.32}$$

and

$$\frac{\partial^2\tilde{S}_E(\ell,\ell_0,E)}{\partial E^2} = \int_{\ell}^{\ell_0}\mathrm{d}\ell'\ \frac{2k(\ell)-E}{\sqrt{64D_{\mathrm{int}}(E+k(\ell))^5}}, \tag{5.33}$$

demonstrates that the minimum of $\tilde{S}_E$ can be found at $E=0$, as long as the rate function itself is larger than zero in the whole range between ℓ_0 and ℓ. $E=0$ corresponds to the paths where

$$\dot{\tilde{\ell}}(0) = -\sqrt{4D_{\mathrm{int}}k(\tilde{\ell}(0))} \tag{5.34}$$

and their action is given by

$$\tilde{S}_0(\ell,\ell_0) = \int_{\ell}^{\ell_0}\mathrm{d}\ell'\ \sqrt{k(\ell')/D_{\mathrm{int}}}. \tag{5.35}$$

Rewriting Eq. (5.31) by setting $\tilde{S}_E(\ell,\ell_0,E) = \tilde{s}_E(E)/\sqrt{D_{\mathrm{int}}}$ so that $\tilde{s}_E(E)$ is independent of D_{int}, yields

$$u\left(\ell\right) = \frac{k(\ell)}{8\pi DZ}\int_{E_0}^{\infty}\mathrm{d}E\ \frac{e^{-\tilde{s}_E(E)/\sqrt{D_{\mathrm{int}}}}}{\kappa(E,\ell)\tilde{F}_E(E)}. \tag{5.36}$$

In the limit of small but finite D_{int} we can now use Laplace's method [184] to approximate the integral using the minimum of $\tilde{S}_E$ at $E = 0$, resulting in

$$u(\ell) \approx \frac{e^{-\tilde{S}_0(\ell,\ell_0)} k(\ell)^{3/4}}{2{D_{\text{int}}}^{1/2} k(\ell_0)^{1/4} Z}. \tag{5.37}$$

It is instructive to calculate the location of maximum probability, ℓ^*, by setting

$$\left.\frac{\mathrm{d}\log u(\ell)}{\mathrm{d}\ell}\right|_{\ell=\ell^*} = 0. \tag{5.38}$$

Evaluating the derivative yields one of the main results of this paper: a simple condition that determines the likeliest reaction distance ℓ^* in terms of the rate function $k(\ell)$ and the diffusion coefficient D_{int}:

$$\sqrt{\frac{k(\ell^*)}{D_{\text{int}}}} = \frac{3}{4}\left|\frac{k'(\ell^*)}{k(\ell^*)}\right| \tag{5.39}$$

The prime indicates a derivative with respect to ℓ^*. Note, that this result hinges on the validity of the quadratic expansion (5.24) which depends on the details of $k(\ell)$ [1]. In App. C.2 we calculate the distributions $u(\ell)$ for the rate functions $k(\ell)$ that are of interest to us later on and compare them to numeric results in order to test the theory developed so far. This comparison shows excellent agreement as D becomes small which corresponds to the limit of inifinite system size when we consider the contact distance of two interfaces later on.

By squaring both sides and rearranging the factors we can rewrite Eq. (5.39) to read

$$k(\ell^*) = \frac{D_{\text{int}}}{[(4/3)(k(\ell^*)/k'(\ell^*))]^2} = \frac{D_{\text{int}}}{[\lambda(\ell^*)]^2}, \tag{5.40}$$

where $\lambda(\ell^*) = (4/3)(k(\ell^*)/k'(\ell^*))$. This expression recalls the reasoning of Sec. 5.2,

[1] The problem discussed in this paper is in structure very similar to the problem of diffusion in a potential as discussed e.g. in Refs. 185, 186, and 187. In this context it has been pointed out that the second order expansion of the path integral breaks down in the case of effective potentials V that feature degenerate, or quasi-degenerate minima. Similarly, for rate functions $k(\ell)$ that feature minima at either ℓ or ℓ_0 a treatment along the lines of Refs. 186 or 187 may be necessary. In the case of the Gaussian rate function, which is discussed in the following, ℓ_0 is never located at a minimum of the effective potential and, hence, the expansion becomes exact in the limit of small but finite D.

equating reaction and diffusion rates at the critical separation ℓ^*. The systematic approximation to the reaction-diffusion equation developed in this section allows us to identify the diffusive length scale (λ in Eq. (5.1)) that was previously left ambiguous. It is dictated by how quickly $\log[k(\ell)]$ changes with distance. Specifically, contact of the two interfaces occurs when the reaction time scale $1/k(\ell)$ becomes comparable to the time it takes to diffuse to a location where $k(\ell)$ has changed significantly.

By using a rate function $k(\ell)$, the ansatz (5.5) tacitly assumes that the equilibration of the shape of the interface happens faster than the center-of-mass diffusion. Based on Eq. (5.40) we can check the internal consistency of this assumption using the pertinent timescale of diffusion, $\tau_D(\ell) = \lambda(\ell)^2/D$. For the interfaces to be equilibrated up to the first contact between them, τ_D has to be larger than the timescale associated with the relaxation of the interface, τ_{rlx}, for all values of ℓ that the system visits before first contact. This yields the condition

$$1 \ll \left.\frac{\tau_D}{\tau_{\mathrm{rlx}}}\right|_{\ell>\ell^*} = \left.\frac{1}{\tau_{\mathrm{rlx}}}\frac{(k(\ell)/k'(\ell))^2}{D}\right|_{\ell>\ell^*}, \tag{5.41}$$

Coming back to our initial problem of determining the scaling of contact distance ℓ^* with system size, Eq. (5.39) demonstrates that this scaling is determined by the scaling of both $k(\ell)$ and D_{int}. In the following section we investigate these scaling behaviors for a simple interface model as an example: the Edward-Wilkinson model.

5.4. Application to the EW model

5.4.1. The EW-equation as a microscopic model for interfaces

The Edward-Wilkinson (EW) model [89] was first introduced to model the statistics of surfaces that are produced by depositing a granular material onto a surface. It is given by the stochastic differential equation

$$\frac{\partial h(\mathbf{x},t)}{\partial t} = \beta\gamma c_D \frac{\partial^2 h(\mathbf{x},t)}{\partial \mathbf{x}^2} + \tilde{\eta}(t), \tag{5.42}$$

where $h(\mathbf{x},t)$ is the height of the surface, as shown in Fig. 5.3, γ is the surface- or line tension, c_D is an effective diffusion constant, and $\tilde{\eta}(t)$ represents random noise that is specified separately. Together with the Kardar-Parisi-Zhang equation [188] it has

since become one of the basic equations used to model surface growth [91]. In order to perform simulations we discretize Eq. (5.42) in space resulting, in the case of the (1+1)-dimensional EW interface, in the set of $N = L/\Delta x$ equations of motion

$$\dot{h}_j = \beta\gamma D_{\text{int}0}\Delta x \left(\frac{h_{j+1} - 2h_j + h_{j-1}}{(\Delta x)^2}\right) + \sqrt{2D_{\text{int}0}}\eta_j(t), \tag{5.43}$$

where $D_{\text{int}0} = c_D/\Delta x$. We choose the $\eta_j(t)$ to be independent, delta-correlated noise processes with $\langle\eta_j\rangle = 0$ and $\langle\eta_i(t)\eta_j(t')\rangle = \delta_{ij}\delta(t-t')$. The equations (5.43) then become a set of N coupled overdamped Langevin equations where each random walker h_j diffuses with a diffusion coefficient $D_{\text{int}0}$ and is coupled to its immediate neighbors by harmonic springs. These equations can also be derived from a discretization of the Hamiltonian

$$\mathcal{H} = \frac{\gamma}{2}\int \mathrm{d}^{(d-1)}x\ (\nabla h(\mathbf{x}))^2\,, \tag{5.44}$$

where d is the dimensionality. This is the Hamiltonian of an interface with an energy that is proportional to its surface area provided that gradients $\nabla h(\mathbf{x})$ in the height function are small. The generalization of the above equations to d dimensions is given in App. C.1.

An expansion of $h(\mathbf{x}, t)$ into a Fourier series, substituted into the equations of motion (5.43), demonstrates that the relaxation timescale τ_{rlx} scales with system size like $\tau_{\text{rlx}} \sim L^2$ [99, 100, 174]. This result is independent of the dimensionality of the system.

Consider now a pair of identical EW interfaces which we assume to be non-interacting. We are ultimately interested in the rate $k(\ell)$ of interfacial fluctuations that result in the two interfaces coming into contact with each other. As before, $\ell = \bar{h}_2 - \bar{h}_1$ is the distance between the mean positions of the two interfaces. The position of the interface at each point $\mathbf{x}$ can be written as $h_i(\mathbf{x}) = \bar{h}_i + \delta h_i(\mathbf{x})$, where the δh_i are the *relative heights* of the two interfaces with respect to their mean position $\bar{h}_i$. We can then write the separation between the two interfaces as

$$\begin{aligned}\Delta h(\mathbf{x}) &= h_2(\mathbf{x}) - h_1(\mathbf{x}) \\ &= \ell - (\delta h_1(\mathbf{x}) - \delta h_2(\mathbf{x})) = \ell - \Delta(\mathbf{x}),\end{aligned} \tag{5.45}$$

where we have used the abbreviation $\Delta(\mathbf{x}) = \delta h_1(\mathbf{x}) - \delta h_2(\mathbf{x})$ in the last line. The

two interfaces touch if there is a point where the separation between them is less than or equal to zero, i.e. if

$$\min_{\mathbf{x}} \left[\Delta h(\mathbf{x})\right] = \ell - \max_{\mathbf{x}} \left[\Delta(\mathbf{x})\right] \leq 0. \tag{5.46}$$

Rearranging these terms results in the condition

$$\max_{\mathbf{x}} \left[\Delta(\mathbf{x})\right] \geq \ell \tag{5.47}$$

that all fluctuations that close the gap between the interfaces must fulfill. These are the events that contribute to the rate $k(\ell)$.

Note, that we can infer the equilibrium statistics of $\Delta(\mathbf{x})$ from the equilibrium statistics of a solitary interface $h(\mathbf{x})$ by using the fact that the equilibrium fluctuations of the EW interface are Gaussian [174]. Hence, also the $\Delta(\mathbf{x})$ are distributed according to a Gaussian distribution. In addition, the spatial correlations of $\Delta(\mathbf{x})$ are simply given by [189, 190]

$$\langle \Delta(0)\Delta(\mathbf{x})\rangle = 2\,\langle \delta h_i(0)\delta h_i(\mathbf{x})\rangle\,, \tag{5.48}$$

i.e. the correlations are the same, except their variance $\langle \Delta(0)\Delta(0)\rangle$ is doubled. This variance is also known as the square of the *roughness*, w, of the EW interface which is given by [189]

$$w^2 = \frac{L}{12\beta\gamma} \tag{5.49}$$

for the (1+1) dimensional EW interface and by [90]

$$w^2 = \frac{f(L)}{2\pi^2\beta\gamma} \tag{5.50}$$

for the (2+1)-dimensional EW interface. Here, $f(L)$ is a system size dependent, dimensionless factor that approaches $f(L) \sim \log(L)$ as $L \to \infty$ [90]. Hence, the correlations of $\Delta(\mathbf{x})$ are the same as the correlations of a solitary EW-interface where the surface tension γ has been halved [170]. In the following we use this property to make contact with results that are available in literature as well as to reduce the computational effort required to perform simulations. In particular, instead of calculating the rate of fluctuations of two interfaces that fulfill condition (5.47), we instead calculate the rate $K(\zeta)$ at which the *maximum relative height* (MRH) of a

single EW-interface, $\max_{\mathbf{x}}[\delta h(\mathbf{x})]$, reaches a threshold value ζ.

For $\gamma = \tilde{\gamma}/2$, where $\tilde{\gamma}$ is the surface tension of each of the two interfaces of interest, the rate $k(\ell)$ is then given by

$$k(\ell) = K(\ell). \tag{5.51}$$

5.4.2. Simulation details and rate calculation method

To calculate $K(\zeta)$ for the EW interface we numerically integrate the equations of motion (5.43) using the Euler forward-like scheme

$$h_i(t + \Delta t) = h_i(t) + \beta D_0 \Delta t F_i(t) + \sqrt{2D_0 \Delta t}\xi, \tag{5.52}$$

where ξ is a random number chosen from a Gaussian distribution with unit variance and $F_i(t)$ is the force on random walker i that is given by

$$F_i(t) = \gamma \left(\frac{h_{i+1}(t) - 2h_i(t) + h_{i-1}(t)}{\Delta x} \right) \tag{5.53}$$

in the case of a 1-dimensional interface. The straightforward generalization to higher dimensions is given in App. C.1. The timestep Δt is chosen such that $(\beta\gamma D_0/\Delta x)\Delta t = 0.005$ and $\beta\gamma D_0 \Delta t = 0.01$ for (1+1) and (2+1) dimensional simulations, respectively. A calculation of the MRH at each timestep then yields trajectories $\zeta(t)$ that we use in the following to calculate the rate $K(\zeta)$.

We define the rate $K(\zeta)$ via the so-called mean first-passage time (MFPT), $\tau(\zeta)$, which is the average time it takes for a configuration to occur with an MRH that is larger than ζ given that one starts from a configuration drawn from an initial ensemble $\mathcal{E}$ (see Fig. 5.5). If t_j are the times where configurations from the ensemble $\mathcal{E}$ are found, then this average is given by

$$\tau(\zeta_i) = \lim_{n\to\infty} \frac{1}{n} \sum_{j=1}^{n} \left(T_i(t_j) - t_j \right), \tag{5.54}$$

where n is the number of samples t_j and $T_i(t_j)$ is the next time checkpoint ζ_i is reached after time t_j. $K(\zeta_i)$ is then calculated via the relationship

$$K(\zeta_i) = \frac{1}{\tau(\zeta_i)}, \tag{5.55}$$

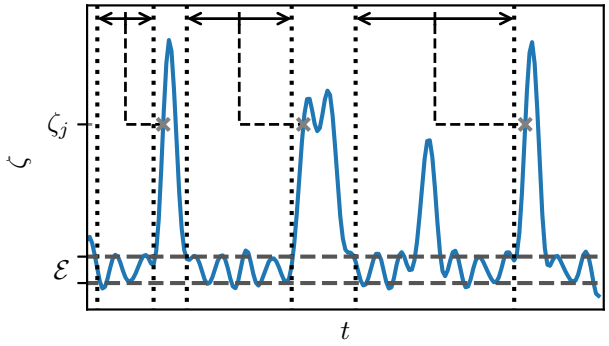

Figure 5.5.: Sketch of the direct method used to calculate the mean first passage time at a checkpoint ζ_i starting from a region $\mathcal{E}$ close to the minimum of the free energy landscape. Each time the checkpoint ζ_i is crossed, the time difference to all points within the equilibrium region $\mathcal{E}$ that have been visited since the last time ζ_i has been crossed, are added to a running average.

that holds for the so called flux-over-population rate [191]. In our case the ensemble $\mathcal{E}$ consists of configurations with an MRH close to the most likely MRH (see App. C.3 for details).

The definition (5.54) can be used to estimate the MFPT directly by evaluating it based on a finite set of samples, e.g. those generated by propagating a long unbiased trajectory. This has the advantage that no assumptions are made about the dynamics of $\zeta(t)$ and that, in principle, the method is exact in the limit $n \to \infty$. However, in practice this *direct method* is strongly limited by the length of trajectories available. If the MFPT that one wants to estimate is on the same order as or larger than the length of the trajectory used, $\mathcal{T}$, then the resulting estimates of $\tau(\zeta)$ are systematically smaller than the true MFPT because not all waiting times can be observed with an equal prior probability (consider, for example, waiting times longer than $\mathcal{T}$ which can not be observed at all). In App. C.4 it is shown that for a flat distribution of waiting times the expected observed waiting time is $\mathcal{T}/4$, which is where the MFPTs measured using the direct method level off in Figs. 5.6 and 5.8.

Despite this limitation, in the following we use a slight variation of this direct method (see App. C.3 for details) to estimate MFPTs without having to make prior assumptions about the statistics of crossing events. We then compare these results

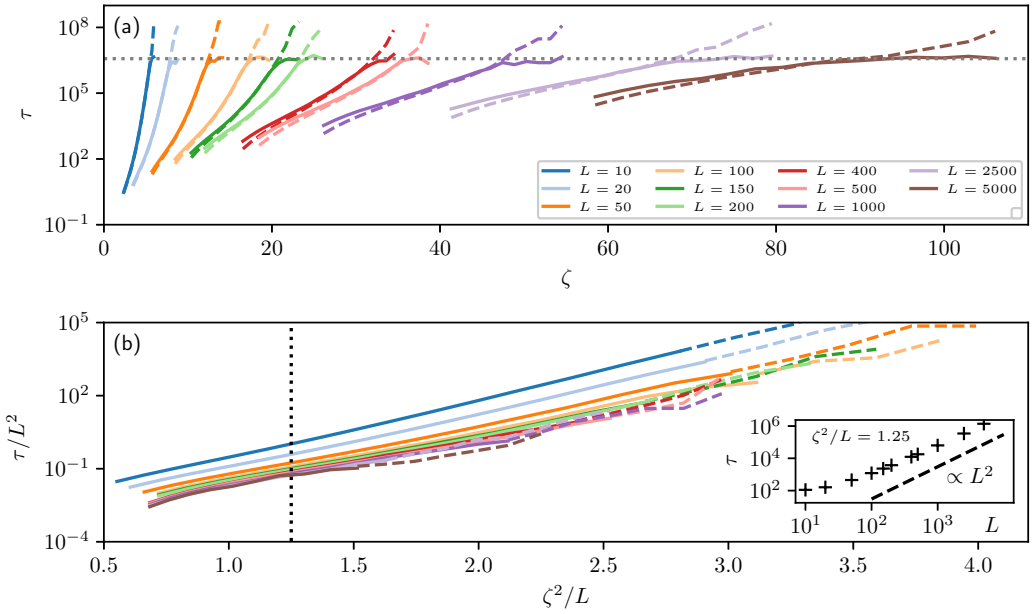

Figure 5.6.: (a) Mean first-passage times τ as functions of the MRH ζ calculated by integrating the Langevin equations of motion (5.43) for (1+1) dimensional interfaces for several system sizes L [L increases from left to right in (a) and from top to bottom in (b)]. The MFPTs are calculated from initial configurations where ζ is close to its average value (see App. C.3 for details of the calculation). Solid and dashed lines indicate results obtained using the direct and the Poisson method, respectively. The dotted gray line indicates the value of $\tau = \mathcal{T}/4 = 3.75 \times 10^6$ (in dimensionless units) that we expect to be the result of the direct method in the limit $\tau \to \infty$ (see App. C.4 for details). (b) Same data with scaled axes as suggested by Eq. (5.57). For clarity, the results of the direct and the Poisson method are stitched together so that the results of each method are shown where we expect them to be accurate. Inset: τ as a function of L at a fixed value of $\zeta^2/L = 1.25$. See App. C.5 for the same plot at other values of ζ^2/L.

to a second set of calculations, where we assume that the statistics of first crossing events—i.e. the crossings of a checkpoint for the first time after visiting $\mathcal{E}$—are those of a Poisson process. With this approximation the rate can simply be estimated by calculating

$$K(\zeta_i) = \frac{n_i}{\mathcal{T}}, \tag{5.56}$$

where n_i is the number of first-crossing events observed at checkpoint ζ_i over time $\mathcal{T}$. For this method (the *Poisson method*) the results from different simulations can be combined by simply summing over the respective n_is and the simulation lengths of the individual simulations. The Poisson method significantly extends the range of MFPTs that can be estimated and, additionally, allows us to gauge the influence of correlations between crossing events on their statistics.

5.4.3. The (1+1)-dimensional EW interface

For the (1+1)-dimensional EW interface a wide array of results is available. It has been shown that a tagged random walker within the interface behaves according to fractional Brownian motion [192, 193] with a Hurst exponent of $H = 1/4$ [100, 194] (for conventional diffusion $H = 1/2$). This suggests that also the MRH shows some non-Markovianity. Nevertheless, a calculation of first-passage times (FPTs) by Gross [100], from an initially flat interface to a given value of the MRH, found that they follow a Kramers-like form [34] of

$$\tau(\zeta) = \tau_0 \exp\left[\frac{\zeta^2}{2\sigma_{\mathrm{1d}}^2}\right] \tag{5.57}$$

where $\sigma_{\mathrm{1d}}^2 \sim L/(\beta\gamma)$ and $\zeta \gg w$. A dimensional analysis in Ref. 100 shows that $\tau_0 \sim L^\alpha$. No theoretical argument has yet predicted the value of the exponent α, but numerical results in Ref. 100 suggest that $\alpha = 2$.

Figure 5.6 presents a similar analysis, however, we calculate the MFPT not from an initially flat configuration but rather from configurations observed along long trajectories. For small τ the Poisson method underestimates the MFPTs, as judged by results from the direct method that should be accurate in this regime. In the intermediate range of τ-values we find excellent agreement between the two methods, indicating that different crossing events are indeed largely uncorrelated. For large values of τ we expect the MFPTs measured using the direct method to approach $\mathcal{T}/4$ (see App. C.4) and, indeed, this is the behavior we observe.

To estimate the scaling behavior of $\tau(\zeta)$, we show in the lower panel of Fig. 5.6 the MFPTs as a function of ζ^2/L as suggested by Eq. (5.57). We observe that for values ζ^2/L larger than 1, $\tau(\zeta)$ is approximately proportional to $e^{a\zeta^2/L}$, where a is a constant (as was previously observed for the FPTs). The scaling of the prefactor τ_0 approaches

a behavior proportional to L^2 in the limit $L \to \infty$.

In summary, we observe the MFPTs to approach the form of Eq. (5.57) as the system size and the value of ζ increase. Assuming, that Eq. (5.57) holds, we substitute $k(\ell) = K(\ell) = 1/\tau(\ell)$ into Eq. (5.40). Solving for ℓ^* then yields a prediction for the most likely contact distance between two interfaces,

$$(\ell^*)^2 = 2\sigma_{1\mathrm{d}}^2 W\left(\frac{8\sigma_{1\mathrm{d}}^2}{9D\tau_0}\right), \tag{5.58}$$

where $W(x)$ is the inverse of $f(x) = x\exp(x)$, otherwise known as the Lambert-W function. Substituting $\tau_0 \sim L^\alpha$, $\sigma_{1\mathrm{d}}^2 \sim L$, $D \sim L^{-1}$ and using the fact that for large arguments W becomes logarithmic [195] [2], we get

$$\ell^* \sim \sqrt{L\log(cL)}, \tag{5.59}$$

where c is an L-independent constant, just as anticipated from the simple reasoning of Sec. 5.2. The exponent α ultimately only appears as an argument to a logarithm and, hence, becomes a multiplicative factor in front of the scaling function. Notice the key result here, that the most likely contact distance between two EW interfaces scales sublinearly with the system size.

The equilibrium condition (5.41) can now be assessed by substituting the rate function (5.57). Since the diffusion timescale increases with increasing ℓ, it is sufficient to show that the equilibrium condition is fulfilled at $\ell = \ell^*$. Hence, we substitute the solution (5.58), approximate W by the logarithm and simplify the expression to

$$\left.\frac{\tau_D}{\tau_{\mathrm{rlx}}}\right|_{\ell=\ell^*} \approx \frac{1}{2}\frac{\sigma_{1\mathrm{d}}^2}{\tau_{\mathrm{rlx}}D} \sim \frac{L}{L^2(1/L)} \sim \text{const.} \tag{5.60}$$

This implies that, if the interfaces have time to relax at one system size around ℓ^*, the relaxation condition (5.41) is fulfilled for all system sizes, allowing us to extrapolate our results to large system sizes.

In Sec. 5.5 we test these results using simulations of the two-dimensional Ising model as an example. First, however, we present a similar analysis of the (2+1)-dimensional interface.

[2] In particular $\log x - \log\log x < W(x) < \log x$.

5.4.4. The (2+1)-dimensional EW interface

Less is known about the properties of the (2+1)-dimensional EW interface than the (1+1)-dimensional interface. The equilibrium probability distribution $P(\zeta)$ is expected to be Gaussian for large values of ζ [94, 96, 97] and in the limit $N = L/\Delta x \to \infty$ the distributions for different system sizes (but the same value of $\beta\gamma$) can be collapsed by applying the transformation [96]

$$\tilde{\zeta} = \zeta - \sqrt{\frac{2}{\pi\beta\gamma}} \log\left(\frac{L}{\Delta x}\right) = \zeta - S(L), \tag{5.61}$$

as shown in Fig. 5.7. Here, we have defined the shift $S(L) = \sqrt{2/(\pi\beta\gamma)}\log(L/\Delta x)$. Notice, that this expression explicitly references the discretization length Δx even in the continuous limit. This is a direct consequence of the fact that the width of the (2+1)-dimensional interface diverges in the same limit [89, 90] and, therefore, one has to choose a fixed discretization length in order to predict quantities related to the width of the interface. Figure 5.7 shows the free energies $\beta F(\tilde{\zeta}) = -\log P(\tilde{\zeta})$ for a number of system sizes together with a fit of

$$\beta F_{\text{gauss}}(\tilde{\zeta}) = \frac{\left(\tilde{\zeta} - \tilde{\zeta}_0\right)^2}{2\sigma_{\text{g}}^2} \tag{5.62}$$

to the large $\tilde{\zeta}$ tail of βF. While the fact that the tail of these distributions is Gaussian can be shown from first principles [96], no theoretical argument that determines the constant $\tilde{\zeta}_0$ exists so far. We determined σ_g and $\tilde{\zeta}_0$ from the fit shown in Fig. 5.7.

The functional form of $\tau(\zeta)$ is not known analytically. As was done in the (1+1) dimensional case, also here one can propose a Kramers-like form for the MFPT based on Eq. (5.62), given by

$$\tau(\tilde{\zeta}) = \tau_0 \exp\left[\frac{(\tilde{\zeta} - \tilde{\zeta}_0)^2}{2\sigma_{\text{g}}^2}\right]. \tag{5.63}$$

Figure 5.8 shows the MFPTs calculated from simulations. For the smallest system size of $L = 10$ excellent agreement with Eq. (5.63) is found by fitting τ_0 while using the parameters $\tilde{\zeta}_0$ and σ_{g} determined from the free energy landscape.

As L increases, however, two changes can be observed: first, the ζ-ranges where direct- and Poisson method yield different results become larger and, secondly, as

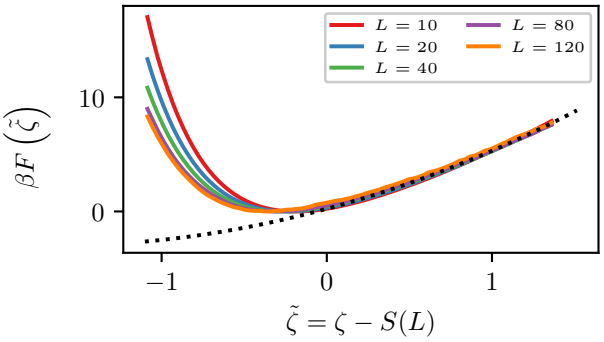

Figure 5.7.: Free energy $\beta F(\tilde{\zeta}) = -\log P(\tilde{\zeta})$ as a function of the shifted maximum relative height, $\tilde{\zeta}$, for the (2+1)-dimensional Edward-Wilkinson interface and several system sizes L. The dotted line is a fit of Eq. 5.62 with parameters $\tilde{\zeta}_0 = -1.66$ and width $\sigma_g = 0.65$. The data has been obtained using umbrella sampling simulations with harmonic biases that were subsequently matched using the WHAM method [86–88]. For details on these simulations see App. C.7.

L becomes larger the $\tau(\zeta)$ is not well described by Eq. (5.63). Rather, the MFPTs depend exponentially on ζ, like

$$\tau(\tilde{\zeta}) = \tau_0 \exp\left[\frac{\tilde{\zeta} - \tilde{\zeta}_0}{\sigma_e}\right], \tag{5.64}$$

where $\tau_0 \sim$ const. We are not aware of any theoretical prediction of this behavior, and in the following we will explore the consequences of both the behavior of Eq. (5.63) and the exponential behavior of Eq. (5.64) on the most likely contact distance, ℓ^*.

We start with the exponential rate function implied by Eq. (5.64), which appears to hold for large L in the EW model:

$$k(\ell) = \tau_0^{-1} \exp\left[-\frac{\tilde{\zeta} - \tilde{\zeta}_0}{\sigma_e}\right] \tag{5.65}$$

Substituting into Eq. (5.39) and solving for ℓ^* yields

$$\ell^* = \sigma_e \log\left(\frac{16\sigma_e^2}{9D\tau_0}\right) + S(L) + \tilde{\zeta}_0. \tag{5.66}$$

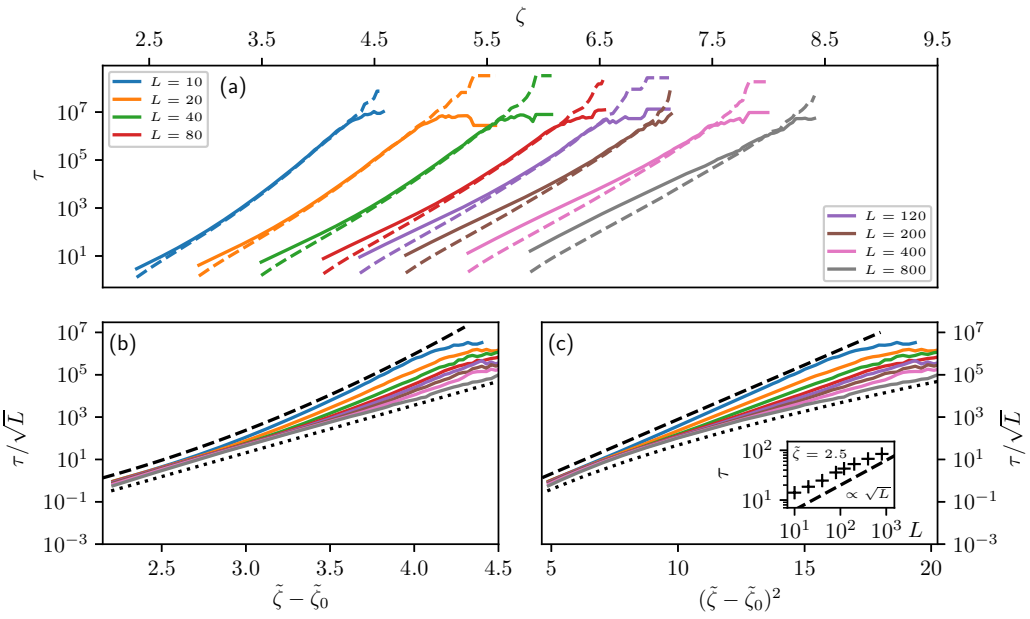

Figure 5.8.: Mean first-passage times of the maximum relative height at checkpoints ζ, $\tau(\zeta)$ calculated from long equilibrium simulations of (2+1)-dimensional EW interfaces of several sizes L [L increases from left to right in (a) and from top to bottom in (b) and (c)]. (a) shown are the results obtained using the direct method (solid lines), and using the Poisson method (dashed lines). (b) same data scaled by $\sqrt{L}$ and as a function of the shifted values $\tilde{\zeta} - \tilde{\zeta}_0$. (c) same data as a function of $(\tilde{\zeta} - \tilde{\zeta}_0)^2$. The dashed black lines represent Eq. (5.63) where τ_0 has been used to shift the curve. The values of σ_g and $\tilde{\zeta}_0$ were taken from the fit shown in Fig. 5.7. The dotted lines show the exponential behavior of Eq. (5.64) where the parameters τ_0 and σ_e were chosen by fitting to the data and the curve was subsequently shifted towards smaller τ for clarity. As in the (1+1)-dimensional case, τ_{direct} approaches $\mathcal{T}/4$ in the limit of large τ. Inset: τ as a function of L at a fixed value of $\tilde{\zeta} = \zeta - S(L) = 1.25$. See App. C.5 for the same plot at other values of $\tilde{\zeta}$.

With the scalings $\sigma_e \sim$ const., $D \sim L^{-2}$, and $\tau_0 \sim \sqrt{L}$ the scaling of ℓ^* with system size becomes

$$\ell^* \sim \log(cL), \tag{5.67}$$

where c gathers all L-independent factors. With the same scalings the equilibrium

condition (5.41) yields

$$\frac{\tau_D}{\tau_{\mathrm{rlx}}} = \frac{\sigma_{\mathrm{e}}^2}{\tau_{\mathrm{rlx}} D} \sim \frac{\text{const.}}{L^2 L^{-2}} \sim \text{const.}, \tag{5.68}$$

indicating that, if the system fulfills the equilibrium condition at one system size, it also fulfills it at larger system sizes and that we can extrapolate our results to large L.

The above scaling is exactly what was expected based on the simple derivation sketched in Sec. 5.2. However, the path that leads to this result is unexpected: it requires a careful treatment of the contact distance distribution and is based on the unexpected rate expression (5.64) that likely is the result of strong correlations in the dynamics of the interface.

The Kramers rate expression (5.63), that was the basis of the argument in Sec. 5.2, leads to the slightly different result

$$\left(\ell^* - S(L) - \tilde{\zeta}_0\right)^2 = 2\lambda^2 W\left(\frac{8\sigma_{\mathrm{g}}^2}{9D\tau_0}\right), \tag{5.69}$$

where, again, $W(x)$ is the Lambert W-function. Substituting the above scalings then leads to

$$\ell^* \sim \sqrt{\log(cL)} + \sqrt{\frac{2}{\pi\beta\gamma}} \log\left(\frac{L}{\Delta x}\right) + \tilde{\zeta}_0, \tag{5.70}$$

where c is a constant with regard to L and we have approximated $W(x)$ by $\log(x)$ [195] as before.

The equilibrium condition (5.41) reads as

$$\frac{\tau_D}{\tau_{\mathrm{rlx}}} = \frac{1}{2}\frac{\sigma_{\mathrm{g}}^2}{D\tau_{\mathrm{rlx}}} \sim \frac{\text{const.}}{L^2(1/L^2)} \sim \text{const.}, \tag{5.71}$$

once again indicating that, if the interface has time to equilibrate at a given system size, it also has sufficient time to do so at larger system sizes. The above result is somewhat more involved since it involves the discretization length Δx. But also here, the growth of ℓ^* with system size L is expected to be slow.

Note, that the first term of the result (5.70) resembles the first term of the semiempirical expression for the average distance between two static (2+1)-dimensional interfaces

that are in contact with each other at a single point,

$$\frac{\ell_{\mathrm{cont}}}{w_s} = \sqrt{4\log(\kappa_u L)} + \frac{0.5772}{\sqrt{4\log(\kappa_\alpha)}}, \tag{5.72}$$

proposed by Ponthus *et al.* [170] based on results from extreme value theory by Preumont [196]. Here, ℓ_{cont} is the average distance between two interfaces that are in contact in a single location, w_s is the root mean square width of the interfaces, and κ_u and κ_α are factors derived from moments of the power spectral density that describe the fluctuations of the interface at hand.

In the next section we compare these predictions derived using the EW model to simulations of more realistic systems: the Ising model and a system that contains Lennard-Jones liquid-vapor interfaces.

5.5. The stability of slabs in simulations

As an example for systems where the interactions of two interfaces play an important role, we examine the stability of slabs formed in molecular simulations of phase-separated systems where periodic boundary conditions are used (see Figs. 5.1 and 5.2 for examples). Here, the slab shape is the thermodynamically stable shape for clusters within a certain range of sizes, because the overall surface is smaller than the surface that would be formed by other geometries (spheres, cylinders, or disks). The sizes where the slab is thermodynamically stable can be determined by comparing the surface area of the slab to the competing geometries—a disk in (1+1) dimensions and a cylinder in (2+1) dimensions. Denoting with Ω the area or volume of the system simulated and with Ω_{c} the area or volume of the critical cluster where the slab geometry becomes stable with respect to the competing geometries, the result is $\Omega_{\mathrm{c}}/\Omega = 1/\pi$ in both (1+1)- and (2+1) dimensions. In other words: the slab geometry becomes thermodynamically stable when the cluster makes up more than a certain area/volume fraction of the system. As the cluster becomes larger than half the size of the system, the two phases switch their roles and the sequence of geometries inverts; the phase that previously formed the cluster now envelopes a cluster of the other phase that takes on the different geometries.

In order for a slab to change its shape to another geometry the two interfaces have to come into contact first. Assuming that this is the rate controlling step of the process,

the width of slabs that are observed immediately prior to their transition to a disk- or a spherical shape is therefore expected to scale according to Eq. (5.59) and Eq. (5.66), in (1+1) and (2+1) dimensions, respectively.

In the following we investigate these widths in simulations of the ferromagnetic Ising model for zero field in (1+1) and (2+1) dimensions as well as in simulations of a Lennard-Jones liquid at coexistence with the gas phase. All quantities are presented in terms of reduced units of the respective system.

5.5.1. Simulation details

Ising model simulations are performed on square and cubic lattices with ferromagnetic nearest-neighbor interactions, vanishing external field, and periodic boundary conditions in all directions. We set up a simulation box that contains a slab of spins pointing in the up direction, which includes 50% of the available spins. Trajectories are run until the first hole appears in the slab and the configuration observed just prior is analyzed. The detection of holes in the slabs is detailed in App. C.6. Roughly 500 trajectories have been generated for each system size.

In order to find the average width of the slabs in these configurations, the configurations are then aligned according to each slab's center-of-mass and the spin values are averaged over the in-plane directions of the slab. From the resulting distribution (see Fig. 5.9 for examples) we calculate the full-width-half-maximum distance (FWHM) which is plotted as l^* in Figs. 5.10 and 5.11. Alternatively, the width of the slab can be calculated from the magnetization of the configurations, taking into account the bulk magnetization of the all-up and the all-down phase at the given temperature (see App. C.8 for details). Both approaches yield similar results.

In the case of the 3-dimensional LJ system, we first calculate the vapor pressure of a system of 20133 atoms in a slab configuration (periodic boundary conditions applied in all directions), in the canonical ensemble at $T = 0.63$, using a simulation box of $35 \times 35 \times 35$. After averaging over 500 000 timesteps, sampling every 10 steps, we obtain a reduced pressure of $p = (5.9 \pm 0.5) \times 10^{-3}$, which we use as the reference pressure for the subsequent sets of NpT simulations. All molecular dynamics simulations were performed using the GROMACS simulation package [197] (version 5.1.2) with an interaction cut-off of 2.05. We integrated the equations of motion using the leap-frog integrator with a time step of 4.65×10^{-4} which is equivalent to 1 fs using parameters

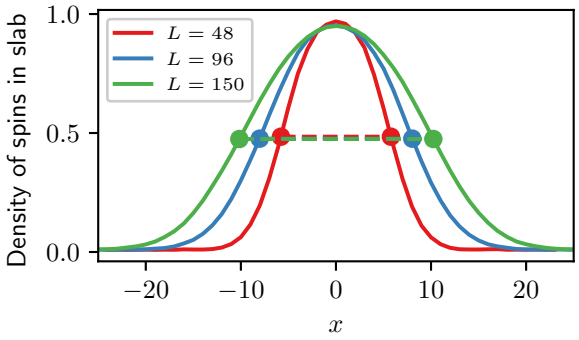

Figure 5.9.: Density of spins that belong to slabs that are observed just prior to a hole forming in trajectories of the 2d-Ising model. Prior to averaging, the slabs have been aligned with respect to their centers-of-mass at $x = 0$. The distance x is measured in units of the lattice spacing between spins. Different colors correspond to different linear system sizes L. The widths indicated are the full width at half maximum.

for argon. To simulate the NVT and NpT ensembles, we used the Nosè–Hoover [198, 199] thermostat and the Parrinello–Rahman barostat [200], respectively.

Next, we prepare the systems for the NpT simulations with different cross-sectional areas by cutting out boxes of 4.4×4.4, 8.8×8.8, 17×17, and 26×26 from the original one. For each size, we run a short NVT relaxation and generate 20 different initial states by choosing random initial velocities taken from a Maxwell distribution at $T = 0.63$. We integrate the equations of motion at constant temperature ($T = 0.63$) and normal pressure ($p = 5.9$) for 200 000 timesteps for each of the randomized starting configurations. For this particular setup that sets only the pressure normal to the interfaces, we use three uncoupled Parrinello-Rahman barostats, each in one of the three spatial directions, but we vary the box length only along the direction of the interface normal. In this way, we impose a constant length for the simulation box edges along the two directions perpendicular to the surface normal. Because the conditions chosen are close to coexistence, during these runs some of the simulation boxes increase their volume, while some others decrease it, bringing the two interfaces eventually in contact.

Unlike in the Ising model, in an off-lattice system like the Lennard-Jones fluid it is necessary to introduce an ad-hoc characteristic distance d_c to determine which

molecules belong to the vapor phase, and when two interfaces can be considered to be in contact. We have chosen the value $d_c = 1.32$, roughly corresponding to the distance at which the pair distribution function crosses 1.0 after the first maximum. We used the distance d_c to perform a cluster analysis of the frames, where we determined the liquid fraction of the system to be the largest connected cluster in the system. Next, we performed an analysis of the interfacial atoms using the ITIM algorithm [201] in the `pytim` analysis package [202][3] using a probe sphere radius of 0.5 [203]. In a last step, we use an additional clustering analysis with the same cutoff parameter d_c, this time performed only on the set of interfacial atoms, and consider the two interfaces to be in contact as soon as the two interfacial layers become a single cluster.

Since the interfacial analysis is computationally expensive, a bisection approach can be helpful in the analysis of trajectories, where one checks only the frame in the middle of the search interval, updating the search interval to the right half if no contact is found. This strategy reduces the number of frames to be analyzed from the order of the total number $\mathcal{O}(N_t)$ to $\mathcal{O}(\log_2 N_t)$, where N_t is the number of frames obtained from the simulation over time t. Once the frame at which the contact takes place is identified, we compute the root mean square width of the slab as

$$\delta = \sqrt{\frac{1}{N_\mathrm{s}} \sum_{i}^{N_\mathrm{s}} (z_i - \bar{z})^2}, \tag{5.73}$$

where the sum extends over the N_s surface atoms, z_i is the position along the surface normal of an interfacial atom, and $\bar{z} = \sum z_i / N_s$. Figure 5.12 shows the averages of δ over all trajectories observed for a given linear system size L as $l^*(L)$.

5.5.2. Results

Figure 5.10 shows the data obtained using the (1+1)-dimensional Ising model together with a fit to the predicted scaling (5.58). The data is in excellent agreement with the predicted scaling.

For (2+1)-dimensional interfaces two predictions have been made in Sec. 5.4 that are derived from assuming different dynamics of the maximum relative height of the interface expressed by the rate function $k(\ell)$. In Figs. 5.11 and 5.12 fits to both

[3] Available at `https://github.com/Marcello-Sega/pytim`.

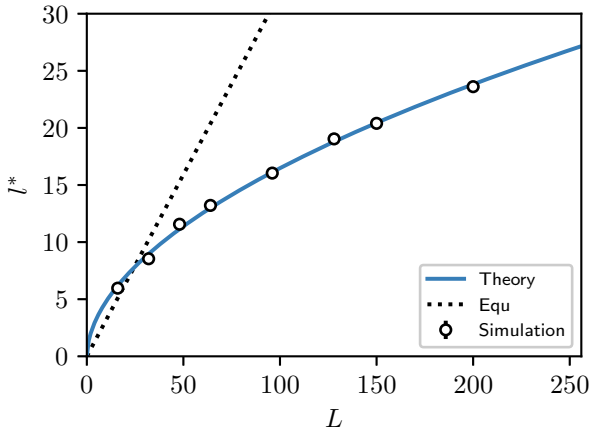

Figure 5.10.: $l^*(L)$ for the (1+1)-dimensional Ising model. The widths ℓ^* are the average of the full-width at half-maximum (FWHM) of the spatial distribution of spins that belong to a cluster that is observed just prior to a hole forming. Error bars indicating an error level of one standard deviation are smaller than the symbol size. The blue line is a fit to $C_1\sqrt{LW(C_2L)}$ in line with Eq. (5.58). The resulting parameters are shown in Tab. 5.1. The dotted black line indicates the slab width below which a disk-shaped cluster becomes the stable configuration in equilibrium.

predicted scalings are shown and the resulting parameters are listen in Tab. 5.1. Note, that the second term in the scaling law for the (2+1)-dimensional case, Eq. (5.70), requires knowledge of the surface tension γ. In case of the (2+1)-dimensional Ising model we use a value of $\gamma = 1.15095$ as obtained in Ref. 204. We use the surface tension extrapolated to $L = \infty$ here, since finite size effects are already included in the EW model. In the case of the LJ liquid-vapor interface we use a value of $\gamma = 1.97$, which is obtained from a linear extrapolation of the data provided in Ref. 205 to the temperature used in the simulations presented here.

For the (2+1)-dimensional Ising model the best fit is obtained by assuming a Gaussian form for $k(\ell)$, while the prediction for exponential $k(\ell)$ shows systematic deviations. The agreement between data and the prediction for a Gaussian rate function is excellent, indicating that the fluctuations of the interfaces in the system are, indeed, well described by Gaussian rate functions.

In the (2+1)-dimensional LJ system such a clear distinction can not be made. Both

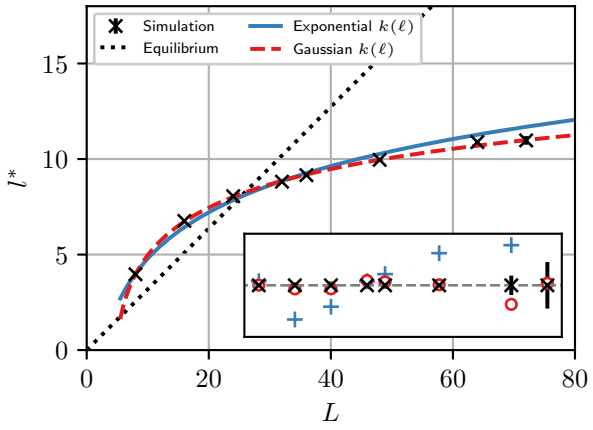

Figure 5.11.: $l^*(L)$ for the (2+1)-dimensional Ising model obtained by calculating the full-width at half-maximum (FWHM) of the spatial distribution of spins that belong to a cluster that is observed just prior to a hole forming. Error bars indicate an error level of one standard deviation. The lines are fits to $\alpha_1 \log(\alpha_2 L)$ and $\beta_1\sqrt{\log(\beta_2 L)} + S(L) + \tilde{\zeta}_0$, corresponding to choosing $k(\ell)$ as an exponential function and a Gaussian, respectively (see Eqs. (5.66) and (5.70)). The resulting parameters are shown in Tab. 5.1. The dotted black line indicates the slab width below which a cylindrical cluster becomes the stable configuration in equilibrium. The inset shows the deviations of the fitted functions from the observed data for exponential $k(\ell)$ (blue crosses) and Gaussian $k(\ell)$ (red circles).

Table 5.1.: Parameters obtained by the fits shown in Figs. 5.10 through 5.12. All parameters are given in reduced units.

Ising (1+1)-dim.	Ising (2+1)-dim.	LJ (2+1)-dim.
$C_1 = 0.43$	$\alpha_1 = 3.5$	$\alpha_1 = 0.84$
$C_2 = 2.6 \times 10^5$	$\alpha_2 = 0.39$	$\alpha_2 = 2.6$
	$\beta_1 = 6.1$	$\beta_1 = 1.6$
	$\beta_2 = 0.21$	$\beta_2 = 7.4$
		$\beta_3 = 0.49$

assumptions for $k(\ell)$ yield fits of similar quality. Note, that since the value of Δx is unknown in the case of the LJ model, we have used its value as an additional fit parameter. Nevertheless, the slow growth of the contact distance is confirmed.

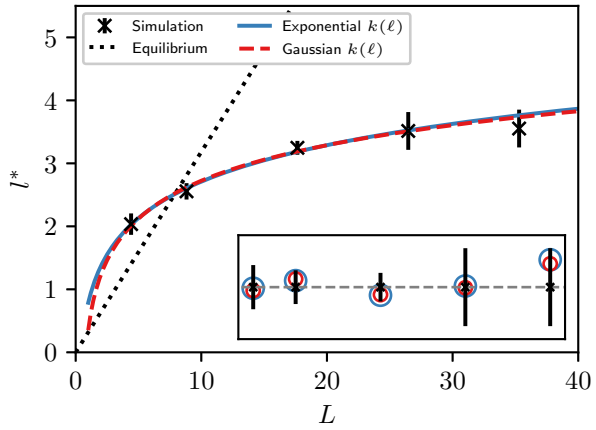

Figure 5.12.: $l^*(L)$ for the (2+1)-dimensional Lennard-Jones system where a slab of liquid coexists with a slab of gas. The widths are determined by averaging the values δ in Eq. (5.73) over all observed trajectories. The error bars indicate an error level of one standard deviation. The lines are fits to $\alpha_1 \log(\alpha_2 L)$ and $\beta_1 \sqrt{\log(\beta_2 L)} + S(\beta_3 L)$, corresponding to choosing $k(\ell)$ as an exponential function and a Gaussian, respectively (see Eqs. (5.66) and (5.70)). The resulting parameters are shown in Tab. 5.1. The dashed black line indicates the slab width below which a cylindrical hole becomes the stable configuration in equilibrium. The inset shows the deviations of the fitted functions from the observed data for exponential $k(\ell)$ (large blue circles) and for Gaussian $k(\ell)$ (small red circles).

Figures 5.10 through 5.12 also show equilibrium expectations for the stability of slabs. For values of the distance between the two interfaces ℓ below the dashed black lines, slabs are thermodynamically unstable with respect to other geometries. From both theory and simulations we find that slabs persist to much smaller interface separations. For large enough system sizes, the transition from slab to the other geometries is suppressed in all cases by the slow dynamics of extreme interfacial fluctuations. Also, the discrepancy with equilibrium expectations grows with increasing system size. Conversely, for small system sizes, we see that slabs are unstable even though they are predicted to be stable based on their volume alone, which is consistent with our fits and follows from the modulation of the surfaces by capillary waves. Also this regime is well described by the theory developed in this paper.

5.6. Summary and Conclusions

We have presented a general approach to calculate the distribution of contact distances between two surfaces that are modulated by fluctuations and at the same time diffuse freely relative to each other. The corresponding stochastic PDE (Eq. (5.6)), which can be understood as a generalized reaction-diffusion equation, is solved approximately for different rate functions $k(\ell)$ using a path-integral method. This calculation yields the distribution of contact distances as well as a condition for the most likely contact distance, ℓ^* (Eq. (5.39)).

The rate function $k(\ell)$, which represents the rate of forming a closing fluctuation between two interfaces that are on average ℓ apart, is in principle system specific. We have presented simulations using a basic interface model—the Edward-Wilkinson [89] (EW) model in both (1+1)- and (2+1) dimensions—where we calculated the rate functions $k(\ell)$ numerically. Our results on the (1+1)-dimensional interface confirmed previous results [100] that the rate function $k(\ell)$ is a Gaussian function of ℓ. In the (2+1)-dimensional system a more complex behavior was observed where $k(\ell)$ for small system sizes is a Gaussian, whose mean and variance are consistent with expectations from the known free energy landscape. For larger system sizes, $k(\ell)$ instead decays exponentially.

Based on these functional forms of $k(\ell)$, we calculated expressions for the distribution of contact distances, $u(\ell)$, and the most likely contact distance ℓ^*. A comparison to the results of numerical calculations of $u(\ell)$ shows excellent agreement with our theory in the limit of slow diffusion of the interface, i.e. for small but finite D. Furthermore, a scaling analysis based on the results achieved using the EW model, yielded a scaling law for ℓ^* that shows remarkably slow growth of the most likely contact distance with system size. In particular, in the (1+1)-dimensional case the growth is given by $\ell^* \sim \sqrt{L \log(cL)}$ and in the (2+1)-dimensional case ℓ^* grows like $\ell^* \sim \log(cL)$ if $k(\ell)$ is exponential and like $\ell^* \sim \sqrt{\log(cL)} + \sqrt{2/(\pi\beta\gamma)} \log(L/\Delta x) + \tilde{\zeta}_0$ for Gaussian $k(\ell)$. Here, $\beta\gamma$ is the reduced interface tension, Δx is the chosen discretization length, and $\tilde{\zeta}_0$ is a constant. In either case the growth of ℓ^* is slow in the sense that the L-dependence enters into the fastest growing terms through $\log L$ only.

As an application of these results, we investigated the stability of slabs of particles in molecular simulations, in particular, the widths ℓ at which they are found to collapse into more compact cluster shapes. The expectation from equilibrium considerations

alone, is that $\ell^* \sim L$ in all cases. However, in order for this collapse to occur, the two interfaces of a given slab have to come into contact with each other first. Assuming that the dynamics of the interfaces formed in these simulations are similar to the ones exhibited by the EW model, it follows that the scaling laws derived above also apply to the most likely collapse distance; a result that is in stark contrast to equilibrium expectations. Indeed, our simulations of the (1+1)-dimensional Ising model show that ℓ^* scales proportional to $\sqrt{L \log(cL)}$, as stated above. The results obtained with the (2+1)-dimensional Ising model are best fit by a model that assumes $k(\ell)$ to be Gaussian in shape and also here the fit is excellent. Another set of simulations was performed using a slab of a Lennard-Jones liquid that forms two liquid-gas interfaces. In this case, based on our results we can not distinguish, whether a better fit can be achieved using a $k(\ell)$ that is exponential or one that is Gaussian. However, both theories fit well to the data obtained, once again confirming the extremely slow growth of contact distance with system size. These results imply that, even in the macroscopic limit, the most likely contact distance ℓ^* is microscopic, an observation that has been made in experiments using colloidal dispersions [165], where colloidal droplets coalesce under the influence of gravity when there is a gap on the order of 1 µm between them.

An interesting consequence of our results is the dependence of ℓ^* on $\log\left(\sigma^2/(D\tau_0)\right)$, where σ is a length scale related to the roughness of the interface[4], τ_0 is a dynamical factor related to the timescales of fluctuations of the interface, and D is the diffusion coefficient that governs the evolution of the center-of-mass distance of the two interfaces. A decrease of D (while keeping all other coefficients constant) implies an increase of ℓ^*, highlighting the importance of dynamical fluctuations in scenarios of interfacial contact. The diffusivity of two interfaces can thus be viewed as a control parameter for tuning the distance at which they come into contact.

The results presented in this work have been achieved by using results about the maximum relative height (MRH) observed in the Edward-Wilkinson model and extending them to other systems. This yielded an excellent match between simulation results and theory for the systems that were investigated. These results should be transferable to other interfacial systems provided that the dynamics of the MRH are qualitatively similar to the EW model. An extension to other situations can be made using the remarkably simple condition (5.39) that allows a prediction of the likely

[4]The length scale σ is subtly different in the (1+1)- as opposed to (2+1) dimensional system. See Secs. 5.4.3 and 5.4.4 for details.

contact distance under some general assumptions, should interfaces exhibit different dynamics.

5.7. Acknowledgments

C.M. has been supported by an uni:docs fellowship of the University of Vienna and acknowledges support from the Austrian Science Fund (FWF) Project No. P27738-N28. C.M., M.I., and C.D. acknowledge support from FWF Project No. I3163-N36. P.G. acknowledges the generous support of the Erwin Schrödinger Institute for Mathematics and Physics (ESI). The computational results presented have been achieved in part using the Vienna Scientific Cluster (VSC).

6. The microscopic mechanism of bulk melting of ice

The contents of this chapter have previously been published in *The Journal of Chemical Physics*. Reproduced from

> Moritz, C., Geissler, P. L., Dellago, C. *The microscopic mechanism of bulk melting of ice.* J. Chem. Phys. **155**, 124501 (2021),

with the permission of AIP Publishing.

Abstract

We study the initial stages of homogeneous melting of a hexagonal ice crystal at coexistence and at moderate superheating. Our trajectory-based computer simulation approach provides a comprehensive picture of the events that lead to melting; from the initial accumulation of 5+7 defects, via the formation of L-D and interstitial-vacancy pairs, to the formation of a liquid nucleus. Of the different types of defects that we observe to be involved in melting, a particular kind of 5+7 type defect (type 5) plays a prominent role as it often forms prior to the formation of the initial liquid nucleus and close to the site where the nucleus forms. Hence, like other solids, ice homogeneously melts via the prior accumulation of defects.

6.1. Introduction

In this paper we present a computer simulation study of the initial stages of melting of hexagonal water ice (Ice Ih) at ambient pressure and superheating up to 11% above the melting point in a regime where the formation of a liquid nucleus of sufficient size is the rate limiting step. Our analysis of ensembles of trajectories yields a detailed,

time-resolved picture of the different dynamical pathways that lead to the formation of such a liquid nucleus and the role that different types of defects play. We find that prior to melting a number of so-called 5+7 defects and larger defect structures in the hydrogen-bond network accumulate in the volume that later becomes the liquid nucleus and that the size and number of these defects becomes larger as the degree of superheating is reduced.

The microscopic mechanisms that lead to melting of crystalline solids are a long-standing subject of solid state theory. In most situations melting originates at the surfaces of a crystal [206], however, under particular circumstances a solid may melt from within the bulk of a crystal as opposed to its surfaces [207] (so called homogeneous melting). For example, micrometer sized single crystal spheres made of silver melt homogeneously if their surfaces are covered by layers of gold atoms. This shell of atoms suppresses surface melting [208] by having a higher melting point while forming a lattice that is compatible with the silver lattice. Using this method, substantial superheating of the Ag lattice can be achieved that is preempted by surface melting in a conventional setting.

A multitude of theories exist that put increasingly stringent limits on the amount of superheating a crystal can be subjected to before it becomes mechanically unstable [209–215]. However, in equilibrium all of these instabilities are preempted by thermal melting of the crystal via a nucleation and growth mechanism [216]. In many recent studies preexisting defects have been found to play a major role [105, 106, 216–223] in melting mechanisms and to significantly influence the stability limits of crystals.

Melting of ice Ih—the ordinary form of ice that can be seen around the liquid nucleus in Fig. 6.1—is a particularly interesting example of a melting crystal, as its open structure is held together by a network of hydrogen bonds. At temperatures around the ambient pressure melting point, these bonds can rupture and form with relative ease compared to, e.g., covalent bonds, and, hence, a multitude of hydrogen bonding defects occurs in ice under these conditions. While ice usually melts heterogeneously, homogeneous nucleation has been induced by internal heating. This is achieved by exciting the OH stretching mode of water with IR laser light [224–228]. Such experiments strongly suggest that defects play a key role in determining the stability of ice crystals [226].

Previous computer simulation studies of ice melting support the finding that defects

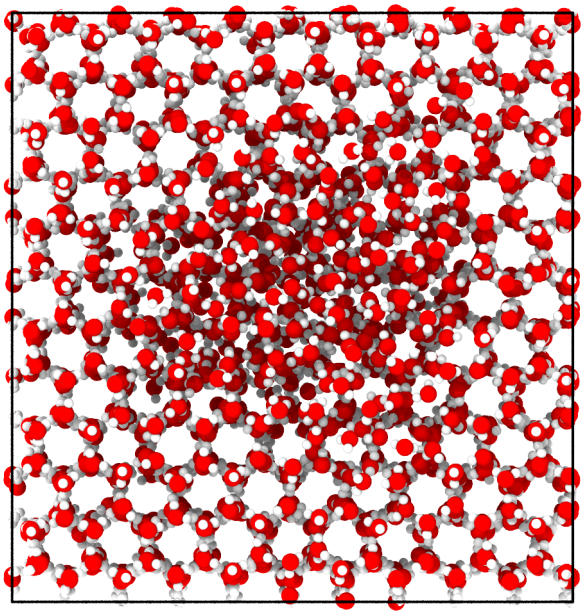

Figure 6.1.: Example configuration containing a spherical liquid cluster. For clarity, the potential energy of the configuration has been locally minimized. The configuration has been prepared by selecting the molecules in a sphere of radius 1.5 nm and melting them by heating. Afterwards the configuration is briefly equilibrated at a temperature of 303 K.

play an important role. Donadio *et al.* [105] investigated the free energy landscape of melting at the melting point, finding that so-called 5+7 defects form a minimum in the free energy landscape (see Sec. 6.2 for a description of the various defect types found in ice). Furthermore, they observed the formation of large defect structures in the hydrogen bond network that involve on the order of 50 molecules. Mochizuki *et al.* [106] studied spontaneous melting under higher superheating (around 19% above melting temperature) where melting events occur spontaneously in simulations within a timeframe of a few nanoseconds. They identified the formation of separated defect pairs (either interstitial-vacancy or L-D pairs) as the controlling step in the melting process at these conditions and also observed 5+7 defects as part of the melting mechanism.

In this paper we follow a similar approach to the one presented in Ref. 106 where an

ensemble of trajectories is generated and the effect of defects is investigated. However, due to the lower degree of superheating the critical step in the nucleation process is the formation of a liquid nucleus of sufficient size. At the temperatures we consider, the rate of formation of such critical nuclei is much lower than the rate of melting observed in Ref. 106. As a result, the required number of melting trajectories cannot be feasibly obtained from MD simulations simply by waiting for spontaneous melting events to occur. In this paper we generate unbiased melting trajectories based on the expectation of a nucleation-growth mechanism near phase coexistence, yielding hundreds of statistically independent samples. With the help of these trajectories we then assemble a detailed, time-resolved picture of the dynamic pathways that lead from a frozen crystal to a liquid nucleus at different degrees of superheating. This analysis yields a comprehensive picture of the roles different defects play in the mechanism of homogeneous melting as a function of temperature.

The remainder of the paper is organized as follows: in Sec. 6.2 we introduce the types of defects that we refer to throughout the paper. In Sec. 6.3 we lay out our simulation methodology and in Sec. 6.4 we present the results of our simulations. Section 6.5 summarizes and discusses our findings.

6.2. Ice defects

As part of our analysis we classify different point defect types that can occur in ice. Here we briefly introduce the types of defects we consider and summarize previous results on the role they play in melting. Higher dimensional defects such as dislocations and disclinations do not form spontaneously in the simulations presented in this paper and, hence, we limit this discussion to point defects only.

In order to discuss defects within the ice Ih structure it is instructive to first reiterate some of the properties of hexagonal ice [229]: (1) the water molecules (H_2O) are laid out in a wurtzite structure [102, 230]; (2a) each molecule takes part in four hydrogen bonds to its nearest neighbors; (2b) two of the hydrogen bonds are donated to other molecules. Observations (2a) and (2b) together are known as the Bernal-Fowler ice rules[230, 231]. (3) The hydrogen bond network of a defect-free Ice Ih crystal can be decomposed into an array of 6-membered rings. However, the direction of hydrogen bonds in the bond network is not uniquely determined and, consequently, there is no long range proton order in Ice Ih [102, 230].

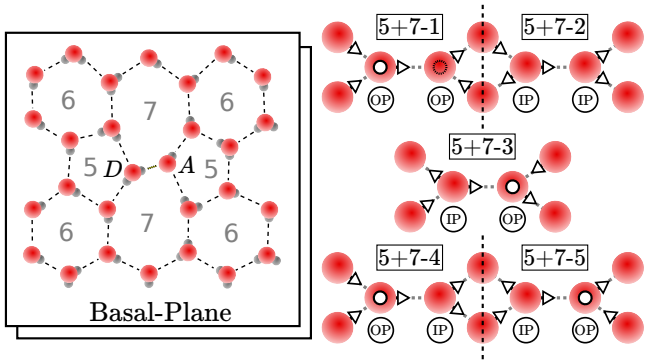

Figure 6.2.: Sketches of 5+7 defects. Red circles indicate oxygen atoms. Left: 5+7 defect in the basal plane of a hexagonal ice crystal. *D* and *A* mark the central molecules of the 5+7 defect that form a hydrogen bond that is part of two 7-rings. Numbers indicate how many molecules comprise the rings that enclose them. Right: Classification of different 5+7 defect types according to the local arrangement of hydrogen bonds as defined in Ref. 104 and used in this paper. White arrows point from donor to acceptor oxygen in hydrogen bonds. The circles on oxygens indicate hydrogen bonds that are formed along an orthogonal plane. IP and OP stands for in-plane and out-of-plane molecules, respectively, and indicates whether the plane that is spanned by the H-O-H triangle is parallel to the basal plane or orthogonal to it.

Breaking rule (1), i.e. displacing a molecule far from its location in the perfect lattice, leads to an interstitial-vacancy (I-V) pair. It has been shown that translational diffusion within ice occurs by the movement of whole molecules [102, 232] and that the concentration of ionic defects is low compared to molecular defects [229, 233]. Hence, we expect that whole molecules also form the majority of I-V defects in the lattice (and not ionic defects). In our simulations we only consider I-V defects where whole molecules are moved out of their lattice position. No ionic defects can occur in our simulations.

Breaking condition (2) while keeping condition (1) intact leads to so-called Bjerrum-or L-D pairs [101]. L and D defects are, respectively, characterized by a missing or an excess proton within a small region of space so that the ice rules are not satisfied and can not be satisfied until a matching defect of the other type is encountered. Nevertheless, L-D pairs are often found bound to each other forming an L+D complex

that exhibits a lower potential energy than a separated L-D pair [104]. In this work, we do not distinguish between separated L-D pairs and L+D complexes and call all structures where the ice rules are broken L-D defects.

I-V and L-D defects will be referred to as *mobile defects* throughout this work because, once a pair of these defects is formed and separated from each other, their movement through the system is relatively facile [234]. Ref. 106 discusses the critical role of mobile defect pairs in melting under high superheating conditions, where the separation of a mobile defect pair is found to drastically lower the free energy barrier that needs to be overcome in order for melting to occur.

Finally, breaking of rule (3) while keeping rule (2) intact constitutes another class of defects, which (in line with Ref. 105) we will call *topological defects*. These are defects where the 6-ring structure of the perfect lattice is broken and instead there are other ring combinations present. Note that the ice rules are still fulfilled in these defects and that the molecules that take part are only shifted by small distances from their positions in the perfect lattice. The most prominent of these defects is the so-called 5+7 defect, first found in simulations by Tanaka & Mohanty [235] and described in detail by Grishina & Buch [104]. In 5+7 defects two 5- and two 7-membered rings are found neighboring each other. These defects can then be further classified into different types according to the placement of protons around the central bond of the 5+7 defect (see Fig. 6.2) and according to the crystal plane they are formed in. 5+7 defects are readily observed in equilibrium simulations that use the TIP4P family of water models [235, 236].

Other combinations of ring sizes are also possible: for example we encounter 455778 defects that center around a 4-ring while still satisfying the ice rules (see Fig. 6.3). Larger defect structures (such as the ones observed in Ref. 105) are frequently observed in melting trajectories and we will subsume all of these structures under the name *extended topological defect* or E defect. All topological defects have in common that there is no efficient mechanism for these defects to move which is why we will refer to them as *immobile defects* in the following.

In the next section we present the simulation methodology used to generate trajectories that are then analyzed in terms of the defects that occur at various stages of melting.

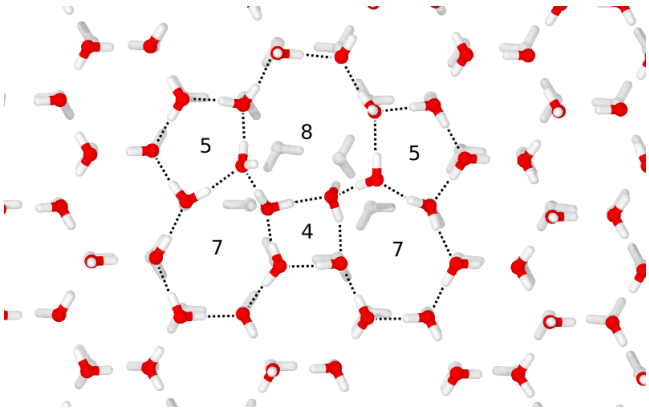

Figure 6.3.: Snapshot of a 455778 defect that is embedded into the basal plane of an Ice Ih crystal. The numbers mark the 4-, 5-, 7- and 8-membered rings in the H-bond network that make up the defect. The white molecules are located in an adjacent, defect free plane.

6.3. Methods

6.3.1. Generating parts of reactive trajectories

Our aim is to investigate the melting transition starting from configurations that contain an Ice Ih crystal with possibly a few 5+7 defects (state $\mathcal{A}$ in Fig. 6.4) and ending in the liquid state (state $\mathcal{B}$). In particular, we are interested in the initial stages of these trajectories up to a state where a liquid nucleus has formed (state $\mathcal{S}$ in Fig. 6.4). Note that we include configurations that contain 5+7 defects into the definition of state $\mathcal{A}$. Such defect states occur readily in equilibrium trajectories under the conditions considered in this paper where the Ice Ih crystal is metastable with respect to the liquid state.

Under these conditions the two states $\mathcal{A}$ and $\mathcal{B}$ are separated by a free energy barrier so that the melting transition is a rare event. This means that the average waiting time $\tau_{\mathcal{AB}}$ between preparing a system in an equilibrium frozen state in $\mathcal{A}$ and a melting event that leads the system from state $\mathcal{A}$ to the liquid state $\mathcal{B}$ exceeds the timescale of relaxation in state $\mathcal{A}$, $\tau_{\mathcal{A}}$, by orders of magnitude:

$$\tau_{\mathcal{A}} \ll \tau_{\mathcal{AB}} \tag{6.1}$$

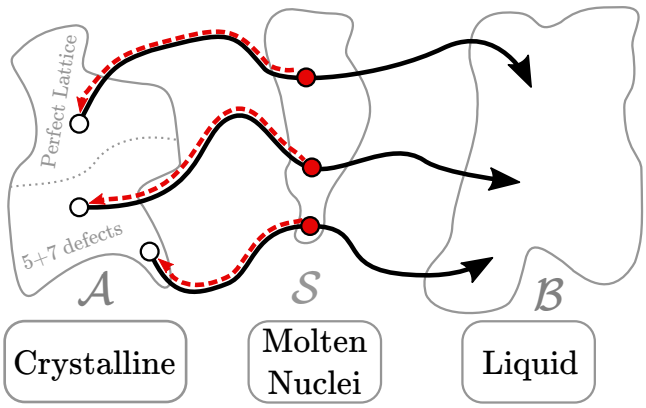

Figure 6.4.: Schematic representation of the method used to generate trajectories. Region $\mathcal{A}$ contains configurations that are completely solid with possibly a few 5+7 defects remaining. Region $\mathcal{B}$ contains configurations that are liquid and region $\mathcal{S}$ contains molten nuclei prepared by the procedure laid out in Sec. 6.3.1. Our aim is to generate a sample of the early stages of melting trajectories (black curves with arrows). To do so, we integrate trajectories starting from configurations in $\mathcal{S}$ until they reach $\mathcal{A}$ (red, dashed arrows) and subsequently invert the direction of time. Trajectories that reach $\mathcal{B}$ before $\mathcal{A}$ are discarded.

This so-called *separation of timescales* guarantees that the way melting events occur does not depend on the details of how frozen configurations are prepared and that, instead, we can think of the two states as being connected by an ensemble of melting trajectories that leave $\mathcal{A}$ and end in $\mathcal{B}$ without visiting $\mathcal{A}$ in the meantime. This ensemble of trajectories is called the *transition path ensemble* [58, 237] (indicated by black arrows in Fig. 6.4).

To generate the initial parts of melting trajectories we take the following approach:

1. Pick a sample of configurations from equilibrium simulations of ice Ih performed at the chosen temperature and pressure.

2. Construct a liquid domain inside this configuration and locally equilibrate the resulting configuration. The resulting ensemble is denoted with $\mathcal{S}$.

3. Run molecular dynamics simulations using a time-reversible integration scheme

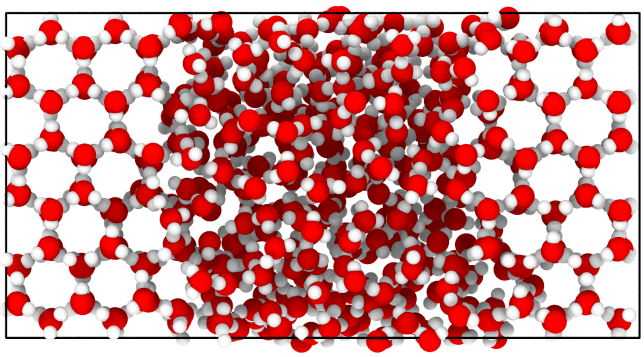

Figure 6.5.: Example of a configuration that contains a slab of liquid that consists of half the molecules in a 720-molecule water system. For clarity the potential energy of the configuration has been locally minimized.

starting from $\mathcal{S}$ until state $\mathcal{A}$ or $\mathcal{B}$ is reached. The resulting trajectories are referred to as *backwards trajectories*.

4. Invert the time direction of the backwards trajectories that end in $\mathcal{A}$ to get a sample of trajectories that lead from $\mathcal{A}$ to $\mathcal{S}$.

The use of a time-reversible integration scheme guarantees that the trajectories obtained by integrating backwards in time and subsequently inverting the momenta are valid solutions of the forward integrator that lead from $\mathcal{A}$ to $\mathcal{S}$ [145].

Similar to the so-called seeding method [30, 107–109] we choose the liquid clusters to be spherical in shape. In reality, the shape of the liquid nuclei that form during homogeneous melting is likely not perfectly spherical due to slight differences in the interface tension associated with different crystal planes [30, 238–240] as well as due to the different dynamics of crystal growth along the plane normals [31, 241–243]. To assess the effect different cluster shapes have on the early stages of melting trajectories, we perform additional simulations at the ice-liquid coexistence temperature that start from configurations with a slab shaped liquid domain such as the one shown in Fig. 6.5.

We refer to trajectories that are constructed from spherically shaped liquid domains as *spherical-geometry* trajectories and to the ones constructed from slab shaped liquid domains as *slab-geometry* trajectories.

6.3.2. Simulation details

The simulations presented in this paper are obtained using the TIP4P/Ice water model [244] with a time-reversible rigid body integration scheme [245, 246] as implemented in the LAMMPS simulation package [247][1]. Thermo- and barostats are implemented using Nosé-Hoover chains [199, 248, 249] where the x, y and z directions are independently barostatted to a pressure of 1 bar. Long-range interactions are treated using a particle-mesh Ewald method (PPPM [250, 251]) with an accuracy of 10^{-4} and the timestep is set to 1 fs. Snapshots are saved for analysis every 10 ps.

Spherical-geometry trajectories

MD simulations used to generate spherical geometry trajectories are carried out with 2880 molecules in an almost cubic simulation box (see Fig. 6.1). The initial dimensions of the boxes are $44.9 \times 46.7 \times 44.0\,\text{Å}^3$ in the directions orthogonal to the secondary-prism plane, the prism plane and the basal plane, respectively. To generate initial configurations for the backward trajectories we follow the following procedure:

1. Construct a proton ordered Ice XI lattice and randomly reorder the hydrogen bonds using a Monte Carlo procedure [252] in order to obtain ice Ih. Here we require that the total dipole moment of the configuration is zero at the end of the procedure.

2. Equilibrate these configurations in a 30 ns parallel tempering [253–256] trajectory using replicas starting from a temperature of 258 K up to and including 328 K spaced 5 K apart.

3. Pick a sample of configurations from the parallel tempering simulation at the desired temperature.

4. Pick a random center for the liquid nucleus in each of the configurations and find the molecules within a radius of 15 Å.

5. Heat the selected molecules using a thermostat while keeping the molecules outside the sphere fixed until the crystal structure in the selected region breaks down.

[1] LAMMPS version (Aug 22 2018) has been used to generate trajectories.

6. Equilibrate at the target temperature by first keeping the molten fraction fixed and propagating the molecules in the crystalline phase (for 20 ps) and then keeping the crystalline molecules fixed and propagating the molten molecules (for 25 ps). This procedure hinders the molecules from recrystallizing because the molecules inside and outside of the selected volume can not collectively reorder into a frozen configuration.

It should be noted that given the initial volume of the liquid domain the spherical shape is not the lowest free energy geometry. Instead, arranging the liquid domain in the shape of a cylinder that wraps around the periodic boundary conditions of the simulation box would lead to a lower overall surface area and, hence, a lower free energy [80, 83]. These competing cluster shapes—which are an artifact of the periodic boundary conditions—are separated from each other by significant free energy barriers [80, 81, 171]. We see only small changes in the asphericity of the liquid domains in the generated trajectories and no transitions to the cylinder geometry and therefore assume that the existence of the competing cylindrical phase has no effect on the generated trajectories.

Slab-geometry trajectories

Slab-geometry trajectories are generated using 720 molecules in an elongated box with initial dimensions $44.9 \times 23.3 \times 22.0\,\text{Å}^3$ (see Fig. 6.5 for an example configuration). The volume that contains the liquid is chosen so that the solid-liquid interfaces are parallel to the secondary prism face of the Ice Ih crystal. This is the geometry that has been found to preferentially form in Ref. 257. No initial equilibration is performed because the system has sufficient time to equilibrate before the slab collapses into one of the two competing phases.

The resulting trajectories are quite different from the spherical-geometry trajectories at the same temperature of 268 K. The spherical liquid domains shrink rapidly and predictably due to surface tension. For the slab geometry, periodic boundary conditions eliminate contributions from the surfaces where the liquid domain wraps around the simulation box [80, 83]. Surface tension therefore does not drive the growth of the slab-shaped liquid domains because a change in the volume of the liquid domain has no effect on the overall liquid-solid surface area.

The temperature of $T = 268\,\text{K}$ was chosen so that roughly half of the trajectories

started with a slab-shaped domain melt and the others freeze, further reducing the thermodynamic force that drives the growth and shrinkage of the liquid domain. This temperature is slightly below the melting temperature at 1 bar of 272.2 K reported by Abascal *et al.* [244]; a discrepancy that is likely due to the non-negligible influence of the solid-liquid interfaces in the comparatively small simulation box with 720 molecules. The result are trajectories where the two solid-liquid interfaces that delimit the liquid domain diffuse in the direction of their surface normal until they are close enough that a fluctuation in the shape of the interfaces brings them into contact. The distance between the interfaces at which this contact occurs is small, roughly one layer of 6-rings or 7 Å.

A larger simulation cell would yield a larger, and more realistic, contact distance. Increasing this distance considerably, however, comes at great computational cost, for two reasons: first, the contact distance scales logarithmically with the size of the simulation box [258]. Secondly, increasing the size of the simulation box slows down the diffusion of the two interfaces which in turn sharply increases the length of the required trajectories. The system size with interface areas of $23.3 \times 22.0\,\text{Å}^2$ was chosen as a compromise between maximizing the contact distance between the two interfaces and minimizing the simulation time required to obtain trajectories.

Gathered data

In total, three sets of trajectories leading from the prepared configurations $\mathcal{S}$ to the frozen state $\mathcal{A}$ were generated: 108 slab-geometry trajectories at a temperature of $T = 268\,\text{K}$, 504 spherical-geometry trajectories at $T = 268\,\text{K}$, and 448 spherical-geometry trajectories at $T = 303\,\text{K}$.

The temperature of 303 K is 11% superheated relative to the melting point [244] and has been chosen so that the spherical nuclei with a radius of 15 Å are slightly subcritical. Out of the 504 trajectories that were run we observed 56 trajectories that melted before they could reach the frozen state $\mathcal{A}$. On average $\mathcal{A}$ is reached in 13.6 ns (slab, 268 K), 5.1 ns (spherical, 268 K), and 2.3 ns (spherical, 303 K).

Data on equilibrium properties presented in this paper were obtained from the parallel tempering simulations that were also used to generate initial configuration for the backward simulation runs. The data from different replicas is combined using the weighted histogram analysis method (WHAM [86, 87]) as implemented in the

PyEMMA package [259].

We now invert the direction of time in these generated trajectories, which become examples of the early stages of melting. We also set $t = 0$ at the crystalline endpoint of each trajectory, so that the system adopts a frozen configuration at time zero and melting commences as time increases. These time conventions will be used throughout the remainder of the paper.

6.3.3. Defect detection

To detect defects in the hexagonal ice structure we adapt an array of different techniques previously used to investigate the properties of water and ice. These include, after locally minimizing the potential energy of a configuration, an analysis of the hydrogen bond network [106, 260], in particular the ring structures found therein [105], as well as the analysis of configurations relative to a reference configuration to facilitate the detection of molecular interstitials and vacancies [106]. See App. D.1 for a detailed description of the algorithms used.

These techniques yield an analysis like the one shown in Figs. 6.6 and 6.7. It includes counts of the number of 4- and 5- membered rings ($n_4(t)$ and $n_5(t)$, respectively) that are roughly proportional to the size of the liquid domain. It also indicates whether certain defects have been detected in the configuration. The defect types distinguished are I-V pairs, L-D pairs, and topological defects in the H-bond network: 5+7 defects, 455778 defects, and extended topological defect structures where the ice rules are fulfilled (E defects). The 5+7 defects are further split into the five horizontal types [104] (5+7-1 through 5+7-5) that are formed within the basal plane of the lattice and the vertical type (5+7-V) where the 5+7 defect is formed in a plane orthogonal to the basal plane.

Note that the algorithm used to detect defects of type I-V, L-D, and E does so in an exclusive fashion: if an I-V pair is present, L-D and E defects can not be detected and if an L-D pair is present, E defects can not be detected (see App. D.1, Fig. D.1).

As part of the analysis we determine three times along each melting trajectory: $t_{\mathcal{A}}$, t_{E}, and t_{m}:

- $t_{\mathcal{A}}$ is the time when the system leaves state $\mathcal{A}$ for the last time, i.e. it is the last time where there are only 5+7 or 455778 defects present in the system.

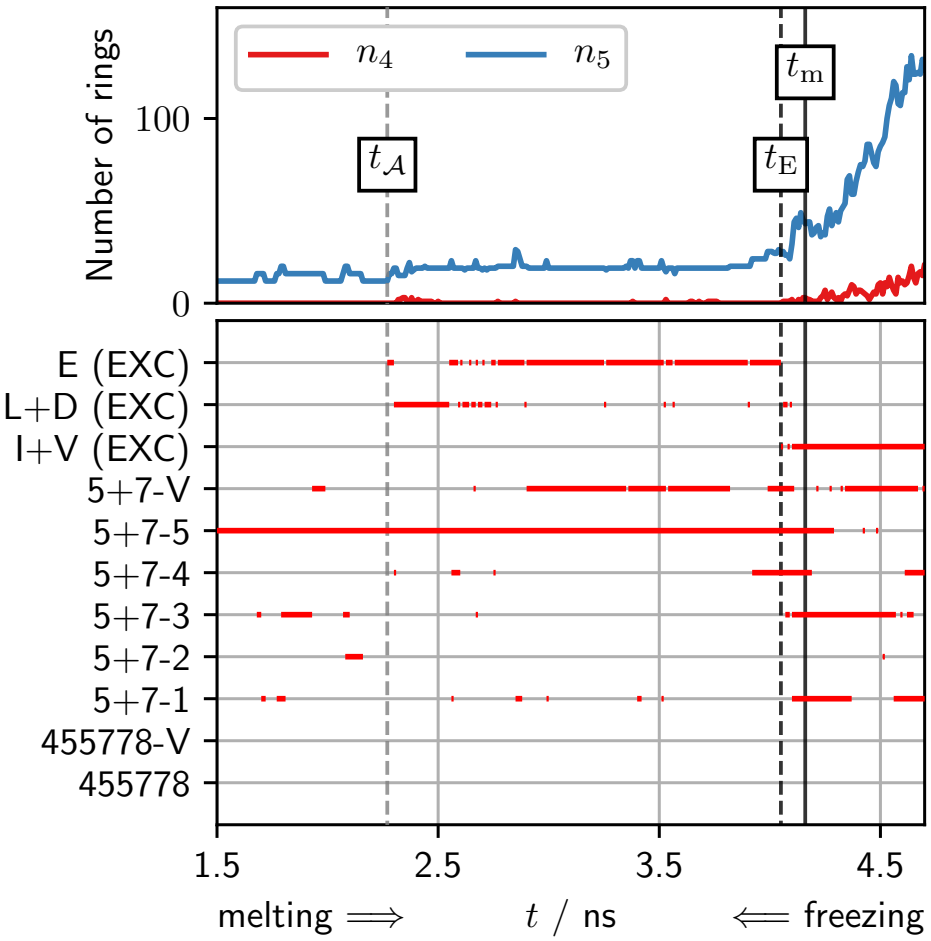

Figure 6.6.: Analysis of an example melting trajectory. At the beginning of the chosen timeframe a number of 5+7-5 defects are present in an otherwise frozen configuration. The vertical lines indicate the times used to split the trajectory into the three stages decribed in Sec. 6.4. Red markings in the lower half of the plot indicate the presence of at least one defect of the given type in the system. Due to the algorithm used only one of the defect types marked with (EXC) can be detected at a time (see App. D.1). The corresponding analysis for the other trajectories can be found in the data supplement.

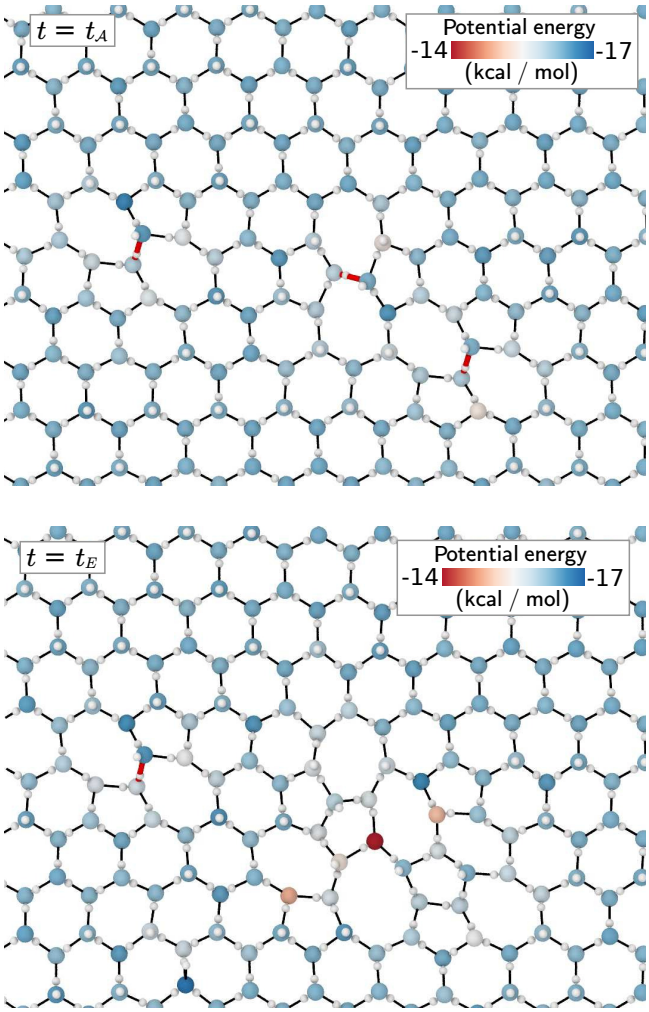

Figure 6.7.: Snapshots of the trajectory analyzed in Fig. 6.6 at time $t_{\mathcal{A}}$ (top) and at time t_{E} (bottom). Shown is a single basal plane that contains the 5+7 defects present at time $t_{\mathcal{A}}$ (red, thick bonds). The colors of molecules indicate their contribution to the total potential energy. The black lines indicate hydrogen bonds between molecules.

Table 6.1.: Thresholds in the growth of the number of 5-rings over a 200 ps period, Δn_5, used to detect time t_m.

Geometry	Temperature (T)	Δn_5
Slab	268 K	8
Sphere	268 K	8
Sphere	303 K	15

- t_E is the last time when no mobile defects are present in the system. In the time between $t_\mathcal{A}$ and t_E, E defects are present in the system; L-D and I-V pairs may also form during this interval, but by definition they must recombine before time t_E. If no E defect occurs along a trajectory, then $t_\mathcal{A}$ equals t_E.

- t_m is the time when the extended liquid domain forms. This event is associated with an increase in the rate at which 5-membered rings appear, i.e., the slope of $n_5(t)$. Because this increase occurs on top of significant background fluctuations in $n_5(t)$, we look for an increase of $n_5(t)$ over a timespan of 200 ps that is larger than a given threshold Δn_5 (see Tab. 6.1).

In the supplement we include the defect analysis for each trajectory that is used in this study, including the times $t_\mathcal{A}$, t_E, and t_m.

6.4. The three stages of melting

Based on the times defined in the previous section we now define three stages of the melting mechanism (cf. Fig. 6.8): stage I ($0 \leq t < t_\mathrm{E}$) where only immobile defects are present in the system, stage II ($t_\mathrm{E} \leq t < t_\mathrm{m}$) where one or more mobile defects have formed and stage III ($t \geq t_\mathrm{m}$) where an extended liquid nucleus has formed. In the following sections we first discuss the spherical-geometry trajectories. Section 6.4.3 then discusses the differences found in slab-geometry trajectories.

6.4.1. Stage I: topological defects ($t \leq t_\mathrm{E}$)

In equilibrium as well as in stage I of melting trajectories, the bulk of defects that are present are of type 5+7. A prominent role in melting is played by 5+7-5 defects as can be seen in Fig. 6.9 where we report the average numbers of defects found at time

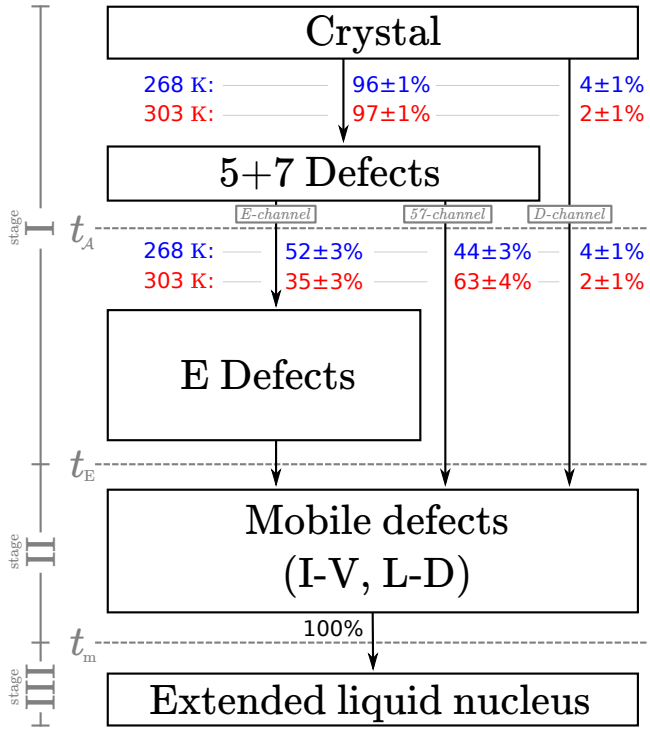

Figure 6.8.: Diagram of the stages observed during the melting of hexagonal ice crystals and the pathways that are taken by trajectories in which a spherical liquid nucleus forms. The percentages represent the fractions of trajectories that proceed along the indicated pathway relative to the total number of melting trajectories.

$t_{\mathcal{A}}$ compared to the average numbers found in equilibrium. The difference in defect numbers between these two scenarios is listed in Tab. 6.2.

At both temperatures the overall excess of defects found at time $t_{\mathcal{A}}$ is mostly accounted for by the excess of 5+7-5 defects. At $T = 268\,\mathrm{K}$ the number of 5+7-V defects is also significantly enhanced while the number of 5+7-3 and 5+7-4 defects is slightly reduced. At $T = 303\,\mathrm{K}$ the average number of defects of type 5+7-V and types 5+7-1 through 5+7-4 are roughly equal to the numbers observed in equilibrium.

At time $t_{\mathcal{A}}$ one of two things happens: either an E defect forms (*E-channel*) or a mobile defect forms directly (*57-channel*). Figure 6.8 shows the fractions of trajectories that pass through each of these channels. As the temperature decreases from 303 K to

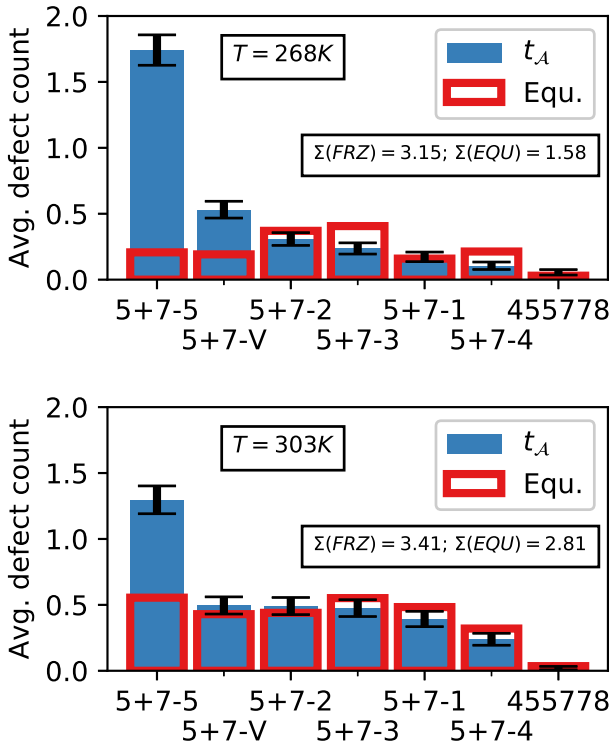

Figure 6.9.: Average number of 5+7 defects found in a cubic simulation box with 2880 molecules in equilibrium, alongside the probability of finding them in melting trajectories at time $t_{\mathcal{A}}$. Results are shown in the top panel for $T = 268\,\mathrm{K}$ and in the bottom panel for $T = 268\,\mathrm{K}$. The black error bars indicate a confidence level of 95%. Σ(FRZ) and Σ(EQU) indicate the average overall defect counts at time $t_{\mathcal{A}}$ and in equilibrium, respectively.

Table 6.2.: Average numbers of defects $\langle n \rangle$ at time $t_{\mathcal{A}}$ and in equilibrium, as well as the difference Δ between the two numbers, for different defect types and at different temperatures T. Reported errors are 95% confidence intervals calculated assuming that the numbers of defects are Poisson distributed. This assumption is supported by an analysis of the defect statistics presented in App. D.3, Fig. D.8.

T = 268 K	$\langle n \rangle\,(t = t_{\mathcal{A}})$	$\langle n \rangle$ (Equ.)	Δ
5+7-5	1.74 ± 0.12	0.21	1.53
5+7-V	0.53 ± 0.06	0.19	0.34
5+7-2	0.31 ± 0.05	0.37	−0.06
5+7-3	0.24 ± 0.04	0.41	−0.17
5+7-1	0.17 ± 0.04	0.16	0.01
5+7-4	0.11 ± 0.03	0.21	−0.11
455778	0.06 ± 0.02	0.03	0.03
SUM	3.15 ± 0.16	1.58	1.57
T = 303 K	$\langle n \rangle\,(t = t_{\mathcal{A}})$	$\langle n \rangle$ (Equ.)	Δ
5+7-5	1.30 ± 0.11	0.55	0.74
5+7-V	0.50 ± 0.07	0.43	0.07
5+7-2	0.49 ± 0.06	0.44	0.05
5+7-3	0.48 ± 0.06	0.55	−0.08
5+7-1	0.39 ± 0.06	0.48	−0.09
5+7-4	0.24 ± 0.05	0.32	−0.08
455778	0.02 ± 0.01	0.04	−0.02
SUM	3.41 ± 0.17	2.81	0.60

268 K the number of trajectories that involve an E defect increases from 35% to 52%.

In order to assess the role of 5+7 defects in the melting mechanism, we analyze the locations of defects relative to the center of the volume where the liquid nucleus eventually forms (the *nucleus volume*), as well as relative to the sites where mobile defects form at time t_{E}. To do so, we define the pair-correlation function between defects of reference type S and defects of target type T,

$$g_{ST}(r) = \frac{1}{c_S} \frac{H_{ST}(r, \Delta r)}{\rho_T \, V(r, \Delta r)}, \tag{6.2}$$

where $H_{ST}(r, \Delta r)$ is a histogram of all pairwise distances between defects of type S and type T observed in a set of configurations, ρ_T is the equilibrium number density of defects of type T, and c_S is the total number of defects of type S observed. $V(r, \Delta r)$ is

the volume of a spherical shell with inner radius $r - \Delta r/2$ and outer radius $r + \Delta r/2$, where Δr is the bin width of the histogram. Note, that $g_{ST}(r)$ is not symmetric in S and T because $c_S \neq \rho_S$. Nevertheless, we expect $\lim_{r\to\infty} g_{ST}(r) = 1$.

We also define $n_{ST}(r)$ as the average number of defects T within a sphere of radius r centered on a defect of type S, i.e.

$$n_{ST}(r) = \rho_T \sum_{r_i<r} V(r_i, \Delta r)\, g_{ST}(r_i). \tag{6.3}$$

$g_T(r)$ and $n_T(r)$ are the analogous quantities where the reference points are the center of the spherical nucleus volume.

Figure 6.10 shows $g_T(r)$ and $n_T(r)$ obtained from configurations observed at time t_E (including trajectories that proceed through both the 57- and E-channels). At $T = 268\,\mathrm{K}$ there is up to a 50-fold excess over equilibrium in the density of 5+7 defects inside the radius of the liquid bubble that forms later on. The most abundant defect type inside this volume is the 5+7-5 defect with an average of 1.2 defects found within the radius of 15 Å while the average total number of 5+7 defects within this volume is 2.2. The next most common defect within the nucleus volume are 5+7-V defects.

Under superheating conditions at $T = 303\,\mathrm{K}$ the excess is slightly less pronounced. Nevertheless, on average we find 1.5 5+7 defects within 15 Å of the center of the forming bubble (5+7-5 defects: 0.7).

At $T = 268\,\mathrm{K}$ we observe a suppression of defects outside the nucleus volume relative to equilibrium. This suppression develops despite the fact that we used equilibrium configurations to seed the simulations, a procedure that enforces that the environment around the liquid domain is initially in equilibrium. The suppression of defect densities around the liquid nucleus indicates that the presence of the nucleus facilitates annealing of existing defects in the ice structure. We expect this effect to subside with increasing distance from the nucleus, however, the simulation box used in our simulations is not large enough to observe this return to average densities.

It is important to note here that precisely at coexistence the radius of the critical nucleus is macroscopically large, and that the nucleus radius of 15 Å used to seed our simulations was chosen for comparison with simulations performed under superheating. At the physically more realistic temperature of 303 K the nucleus size used to seed simulations is chosen close to the critical nucleus size at this temperature. This allows

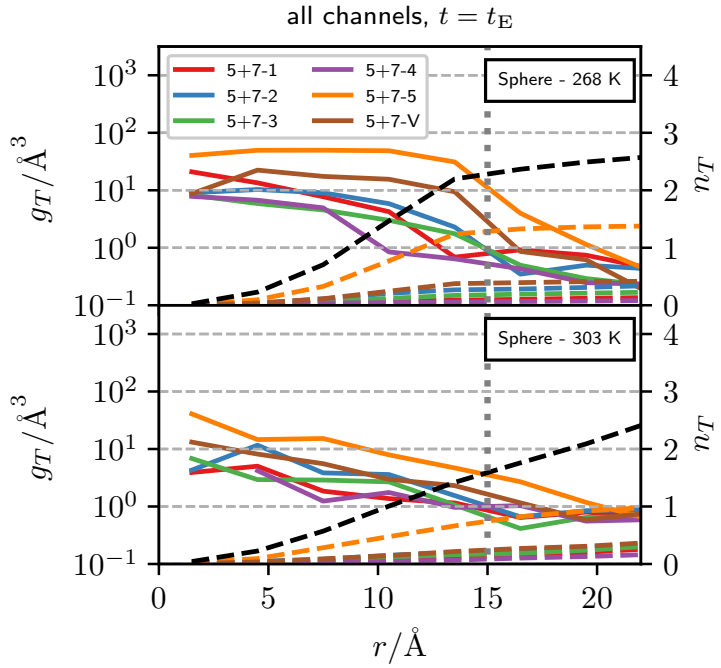

Figure 6.10.: Abundance of 5+7 type defects as a function of distance r from the center of the liquid nuclei that were used to seed the simulations. The gray vertical dashed line indicates the 15 Å radius of the liquid nucleus. Shown are the normalized defect densities $g_T(r)$ (solid) and the number $n_T(r)$ of defects within a spherical volume of radius r around the center of the nascent liquid nucleus (dashed). The dashed black line indicates the sum of n_T over all defect types, T.

us to extrapolate these simulation results to larger system sizes. Notably, under these conditions there is no significant suppression of defect densities outside the nucleus volume.

6.4.2. Stage II: mobile defects ($t_E < t \leq t_m$)

In this next stage, a mobile defect, i.e., either an L-D or an I-V pair has formed. Which defect type has formed as a function of time relative to t_E is shown in Fig. 6.11 for different temperatures and cluster geometries. Just over half of the configurations (56%) observed at temperature $T = 303\,\text{K}$ contain an L-D pair, while the other ones

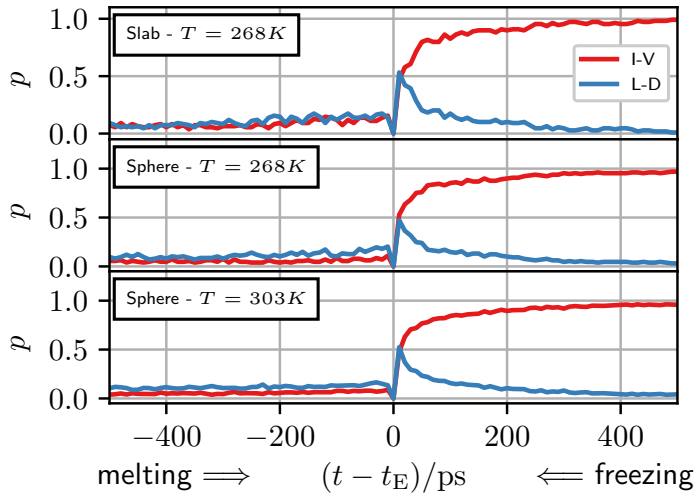

Figure 6.11.: Probabilities of finding the system with defects of type I-V or L-D, as functions of time. To calculate the time-dependent averages, trajectories have been aligned on time t_E. The states shown are detected in a mutually exclusive fashion, i.e. if there exists at least one I+V defect in the system, it is considered to be in the I+V state regardless of the number of L+D defects in the system. Notice the similarity between the data obtained with the slab and the spherical geometry; the probabilites are largely independent of the shape of cluster that is formed as well as of temperature. The probabilities of finding the system in state I+V and L+D by definition vanish at t_E and sum to one for $t > t_E$.

contain an I-V pair. The fraction of configurations where an I-V pair is present then rapidly increases, reaching 98% 0.5 ns later. Similar behavior can be observed at $T = 268$ K regardless of the geometry of the liquid nucleus, giving us confidence that the observed timescale of roughly 0.5 ns for the time between forming an L-D pair and forming an I-V pair is largely independent of the geometry of the nucleus that forms and of temperature.

We have already shown in the previous section that 5+7 defects tend to form within the eventual volume of the liquid nucleus. Figure 6.12 assesses the analogous behavior for mobile defects. While at $T = 268$ K the first mobile defect that leads to melting forms inside the volume of the future liquid bubble 80% percent of the

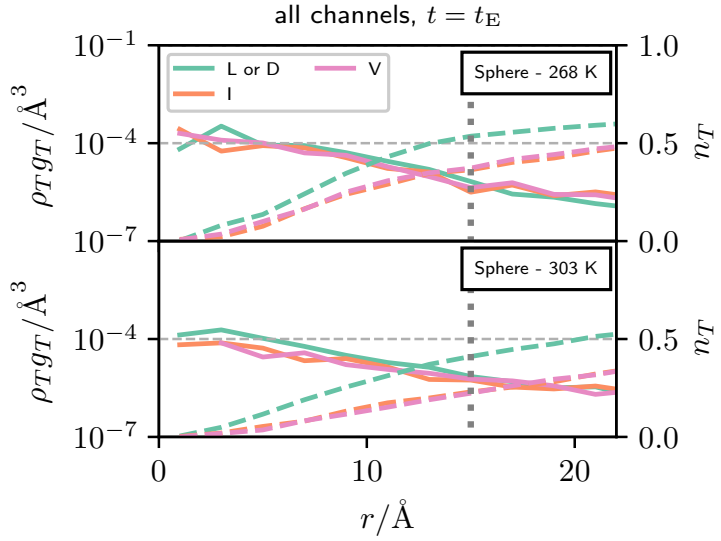

Figure 6.12.: Analysis of locations where L-D pairs, and I and V defects form at time t_E relative to the center of the future liquid nucleus. Shown are the densities $\rho_T g_T(r)$ (solid) and the number of defects within a spherical volume of radius r around the center, $n_T(r)$ (dashed). The gray dotted line indicates the 15 Å radius of the nucleus volume.

time, at $T = 303\,\mathrm{K}$ this share has declined to 64%. In both cases, the formation site is correlated with the center of the liquid nucleus (i.e. $g(r)$ is not flat), however, the mobile defects are formed outside the nucleus volume in a significant number of trajectories.

To investigate the role of 5+7 defects in the creation of mobile defects, Fig. 6.13 shows an analysis of the defect densities around the site where a mobile defect forms. Only trajectories that proceed via the 57-channel are included in this analysis. Note, that due to the sampling frequency of $(10\,\mathrm{ps})^{-1}$ 5+7 defects with a life time smaller than 10 ps may not be detected in this analysis.

At both temperatures we find that the density of 5+7 defects is enhanced close to the site where a mobile defect forms and we find the closest 5+7 defect within 6 Å in 71% of trajectories at 268 K (303 K: 57%). The average number of defects within 6 Å is 0.87 (303 K: 0.70). While at $T = 303\,\mathrm{K}$ all 5+7 defect types roughly contribute equally to the nearby defect population, at $T = 268\,\mathrm{K}$ there is a preference for 5+7-5

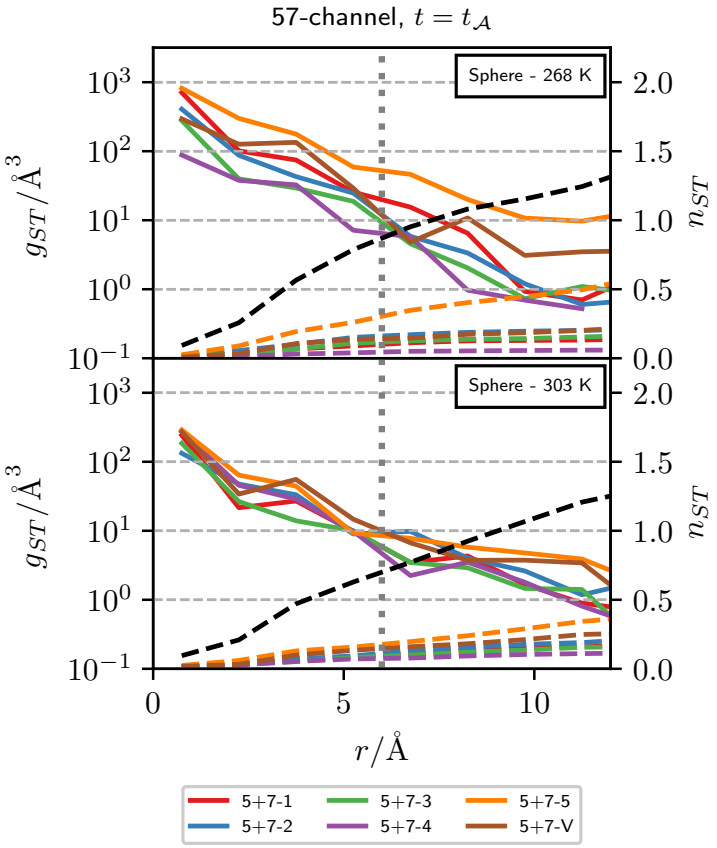

Figure 6.13.: Analysis of the positions of immobile defects around the site where a mobile defect pair of type I-V or L-D forms at time $t_{\mathcal{A}}$. Shown are the pair-correlation functions g_{ST} (solid) and the average numbers of defects within a sphere of radius r, n_{ST} (dashed). Here, the reference defect type S are the defect types L, D, I, and V combined. Black lines are the sum over all defect types T. For clarity the densities are shown on a semi-logarithmic scale while n_{ST} is shown on a linear scale. Included in the analysis are configurations observed at time $t_{\mathcal{A}}$ in trajectories that proceed through the 57-channel. The corresponding analysis for trajectories that pass through the E-channel can be found in App. D.3 (Fig. D.9).

defects.

In trajectories that pass through the E-channel, mobile defects can also form close to the E defect. Hence, due to volume exclusion, the density of 5+7 defects around the site where a mobile defect forms is suppressed relative to the densities found in trajecotories that pass through the 57-channel (see App. D.3, Fig. D.9).

After an I-V defect pair has formed we can track the motion of the two defects through the system. In Fig. 6.14 we show the average distances between the I and the V defects as a function of the elapsed time since the I-V pair has formed. The average is calculated over all configurations where a single I-V pair is present and each trajectory is included until time t_m. Within roughly 0.5 ns the average distance between I and V defects approaches the value expected if one were to randomly place two particles in the simulation box (dotted lines in Fig. 6.14). In Fig. 6.15 we show the mean-square-displacements, $\langle \mathbf{r}^2(t) \rangle$, of I and V defects during the same timespan. After a subdiffusive regime that lasts roughly 100 ps, $\langle \mathbf{r}^2(t) \rangle$ is close to linear indicating that the defects freely diffuse through the system. At 268 K the ratio of the self-diffusion constants of intersitials and vacancies, D_I/D_V, equals approximately 2 (303 K: 1.75).

Together these two datasets suggest that in the timespan between t_E and t_m both defect types independently diffuse through the simulation box. Indeed we find that the non-equilibrium pair correlation function between interstitials and vacancies obtained from configurations observed in this timespan is flat for distances larger than 10 Å (see App. D.3, Fig. D.10).

To further investigate the role of I and V defects in the formation of a liquid nucleus, Fig. 6.16 shows the position of the I-V defect pair that is closest to the center of the nucleus volume at time t_m. We find that at 268 K in 98% of trajectories there is at least a single I or V defect present inside the volume that later becomes the liquid nucleus. In 82% of trajectories both the closest I and V defect are found in this volume. No significant imbalance between the two types of defects can be detected.

Note that Fig. 6.16 shows the probabilities of finding the I and V defect closest to the center of the liquid nucleus. Even for an ideal gas, the analogous distribution of the closest gas atom to a given location is not flat but has a maximum at a distance that is determined by the density of the gas. In App. D.2 we calculate the expected shape of this distribution and compare it to the data shown in Fig. 6.16. We find that there is a strong excess of I and V defects that are close to the liquid nucleus' center at

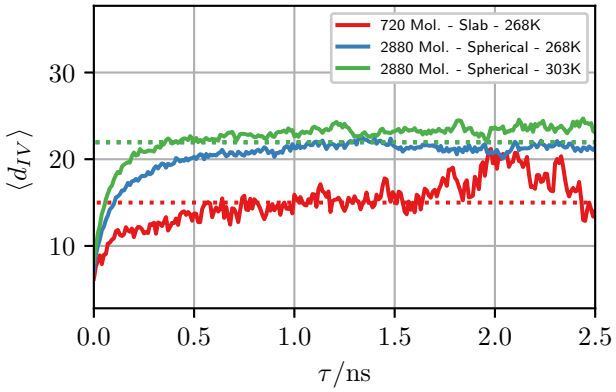

Figure 6.14.: Average distance between interstitial and vacancy as a function of time after their first creation in melting trajectories. Shown are different simulation box- and cluster geometries and temperatures. The data shown has been calculated considering configurations with a single I-V pair because the assignment of defects into pairs is unambiguous in this case. The dashed horizontal lines indicate the average distance between two randomly chosen points in the simulation box of the respective geometry.

time t_m relative to the expected distances based on uncorrelated density fluctuations.

At 303 K the distribution of defect positions at time t_m is broader. Here we find that in 90% of trajectories at least one I or V defect is close to the center of the liquid nucleus at time t_m. V defects are found outside of the nucleus volume slightly more often than I defects. Note, that the change in slope of $n_5(t)$ at time t_m is less pronounced at $T = 303\,\mathrm{K}$ than at 268 K, making the determination of t_m less precise. The broader distribution of defect positions is at least in part a consequence of this reduced precision. Nevertheless, also here we find a strong excess of I and V defects close to the center of the nucleus volume compared to a uniform distribution of defect positions.

6.4.3. Analysis of trajectories with slab shaped clusters

The results obtained for slab-geometry trajectories at $T = 268\,\mathrm{K}$ are largely similar to the ones obtained for spherical clusters at the same temperature. The transition

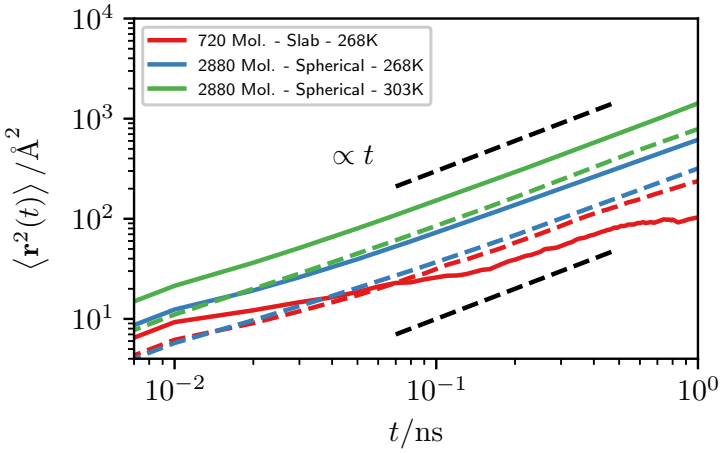

Figure 6.15.: Mean squared displacement of interstitial (solid lines) and vacancy defects (dashed lines) as observed in between the time of their first formation in melting trajectories up to the time where an extended liquid cluster forms, t_m. Different colors represent different system sizes and temperatures, and the dashed black lines are a guide to the eye indicating linear behavior. Refer to Fig. D.11 in the appendix for a breakdown of $\langle \mathbf{r}^2(t) \rangle$ into different directional components $\langle r_i^2(t) \rangle$.

proceeds via the E-channel in $57 \pm 7\%$ of trajectories, via the 57-channel in $42 \pm 6\%$ and via the D-channel in $1 \pm 1\%$ of trajectories. This is in good agreement with the data obtained using spherical nuclei. Furthermore, also in this case we find that mobile defects are preferentially formed around 5+7 defects and in particular around 5+7-5 defects, as can be seen in Fig. 6.17. Figure 6.11 demonstrates that the dynamics of forming I-V pairs after t_E are essentially identical to the ones observed with spherical cluster geometries.

A notable difference can be observed in the mobility of interstitial defects (Fig. 6.15): while all I and V defects exhibit some subdiffusivity at timescales below 100 ps regardless of cluster geometry and temperature, this effect is strongly enhanced in interstitials that form when the liquid slab decays. The same is not true for the corresponding vacancies. An analysis that separates the contributions to the MSD in different lattice directions (see App. D.3, Fig. D.11) also suggests that the movement of interstitials is hindered in both the direction orthogonal to the secondary prism

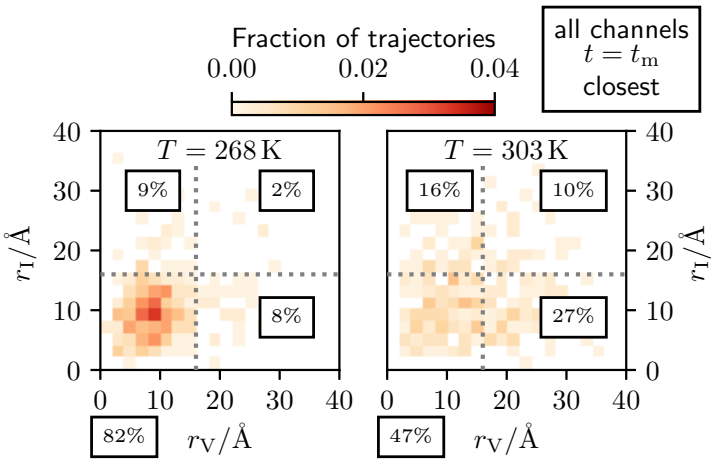

Figure 6.16.: Analysis of the locations of I-V defects at the time of formation of a liquid nucleus, t_m, using the center of the nucleus volume as reference. Shown are the fractions of trajectories in which the closest vacancy and the closest interstitial are found at distances r_V and r_I,respectively. The gray dotted lines indicate distances of 16 Å, just larger than the radius of the liquid nucleus volume of 15 Å. The percentages indicate the fraction of trajectories where the distances fall within the areas outlined by gray dotted lines. The percentage of trajectories where both defects are within 16 Å of the center of the bubble is given in the lower left corner.

plane and the direction orthogonal to the basal plane. An analysis of the positions of interstitial defects in these trajectories shows that they are confined to the volume that later becomes the slab shaped liquid domain. This suggests that interstitials are more likely to not leave the volume of the liquid domain between the time they are formed and t_m if the cluster is slab shaped.

We also analyzed the distribution of waiting times between t_E and t_m (Fig. 6.18). Here we find a strong dependence of the waiting time on the simulation geometry where (at the same temperature of 268 K) the decay time τ decreases from 4.1 ns in the sphere-geometry simulations to 0.7 ns in the slab-geometry. This reduction in waiting time may in part be a consequence of the pinning of interstitials in the slab volume. However, based on calculations by Le Vot *et al.* [261] for one-dimensional systems, we would expect a significant dependence of waiting times on system size even in the case of equal diffusivities.

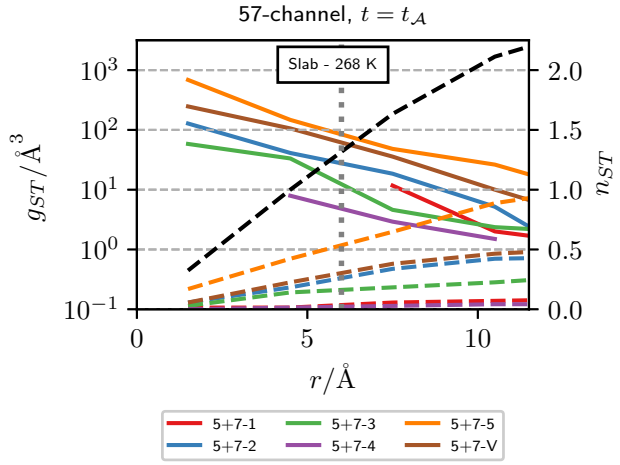

Figure 6.17.: Same analysis as shown in Fig. 6.13 for trajectories that end in a slab-shaped cluster in a 720 molecule system.

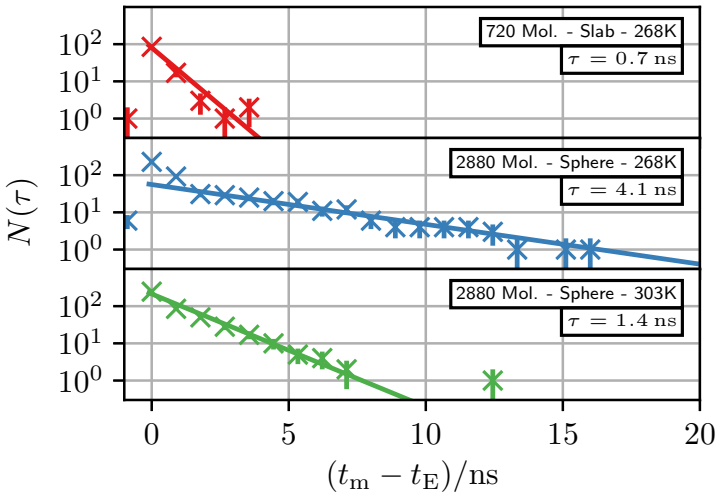

Figure 6.18.: Distributions of waiting time $t_\text{m} - t_\text{E}$ between the last time melting trajectories contain only defects of type 5+7, 455778, or extended defects of type E and the formation of an extended liquid cluster. Shown are fits of the normalized exponential distribution $\tau^{-1}e^{-t/\tau}$ to all data points with $t_\text{m} - t_\text{E} > 0$ except for the simulations with a spherical cluster at $T = 268\,\text{K}$ where only the data points with $t_\text{m} - t_\text{E} > 1.5\,\text{ns}$ are used.

6.5. Discussion and outlook

We analyzed melting trajectories that were obtained using molecular dynamics simulations at coexistence and at 11% superheating. At superheating conditions we observed the following sequence of events: (i) on average 1.5 5+7 defects form within the volume that later becomes the liquid nucleus; 0.7 of these defects are 5+7-5 defects; (ii) in roughly 1/3 of trajectories a larger topological defect structure that fulfills the ice rules (an E defect) forms; (iii) a mobile defect (an L-D or an I-V pair) forms close to either an E if one exists or close to a 5+7 defect; (iv) if an L-D pair has formed, an I-V pair forms within a timescale of 0.5 ns; (v) the I-V defects freely diffuse through the system; (vi) a liquid nucleus forms as a result of the interaction of the mobile defects with the 5+7 defects that are already present in the volume that is later occupied by the critical liquid nucleus.

Previous studies [105, 106] have pointed out the role of 5+7 defects and larger defect structures in the melting mechanism of ice (modelled by the TIP4P water model). Our results show that the role of 5+7 defects is two-fold: 5+7 defects are often found close to the site where the first mobile defect is formed and, secondly, 5+7 and E defects create a defective region that is succeptible to the formation of a liquid nucleus when a mobile interacts with it.

As the temperature is reduced this defective region tends to become larger as demonstrated by the increase of melting trajectories that pass through the E-channel (52% at 268 K compared to 35% at 303 K) and the increase in the average number of 5+7 defects found close to the site where the liquid nucleus forms (2.2 compared to 1.5). This finding is consistent with the results of of Mochizuki *et al.* [106] who reported that at 19% superheating 5+7 defects play a role in the formation of mobile defects but no accumulation of these defects occurs prior to melting.

In Ref. 106 it was also shown that the formation of a separated interstitial-vacancy pair is the rate limiting step in the limit of high superheating. Under the conditions investigated in this paper, the rate limiting step is the formation of a liquid nucleus of critical size, however, also in this case interstitials and vacancies play a crucial role in that they cooperate with 5+7 defects to form the initial liquid nucleus.

Prior to the formation of the liquid nucleus the interstitials and vacancies diffuse freely through the simulation box. This has interesting implications when one wants to extrapolate simulations results to the thermodynamic limit. Since interstitials and

vacancies are only weakly bound to each other they are also not limited to form close to the accumulation of immobile defects they later interact with to form a liquid nucleus. This is underscored by the finding that even in the strongly confined environment of our simulation boxes we find that a considerable number (36% at 303 K) of mobile defects forms outside of the eventual volume of the liquid nucleus. This suggests that mobile defects may diffuse for considerable distances before they encounter an accumulation of other defects and form a liquid nucleus.

In summary, the results of our simulations further support the observation that interstitials and vacancies play an integral role in the microscopic mechanism of ice melting and establish that, as the degree of superheating becomes smaller, increasingly large immobile defect structures are present within the volume where the initial liquid nucleus forms prior to its formation. Interstitial and vacancy defects then interact with these immobile defects to form an initial liquid nucleus that later grows and melts the ice crystal. This adds ice to the list of solids with a melting mechanism that involves the prior accumulation of defects.

6.6. Acknowledgments

C.M. has been supported by an uni:docs fellowship of the University of Vienna. C.M. and C.D. acknowledge support from the Austrian Science Fund (FWF) Project No. I3163-N36. P.G. acknowledges the generous support (2/17 to 5/17) of the Erwin Schrödinger Institute for Mathematics and Physics (ESI). P.G. was supported (6/17 to 5/21) by the U.S. Department of Energy, Office of Basic Energy Sciences, through the Chemical Sciences Division (CSD) of Lawrence Berkeley National Laboratory (LBNL), under Contract DE-AC02-05CH11231. The computational results presented have been achieved in part using the Vienna Scientific Cluster (VSC).

Data Availability

The data that support the findings of this study are available from the corresponding author upon reasonable request.

Part III.

Concluding Remarks

Understanding rare event mechanisms

In the three papers contained in this thesis I, together with my collaborators, explored different rare events in order to understand their mechanism by connecting them to the underlying free energy landscapes and the systems dynamics.

In Sec. 2.3 of the introduction I discussed two key quantities used in the analysis of rare event mechanisms: the committor $p_{\mathcal{B}}(\mathbf{x})$ and the transition path density $\rho(\mathbf{x}|\mathrm{TP})$[2]. These two quantities represent two of the major questions we can ask ourselves about a system and its rare events. The first is, "what are the likely pathways a system takes during a rare event?" represented by $\rho(\mathbf{x}|\mathrm{TP})$ and the second is "given my system is in a particular state, what is (likely) going to happen next?" which is answered by the committor. A reaction coordinate that can be used to predict where a system goes next for all the relevant pathways is also a good reaction coordinate for a rate calculation and, hence, answering these questions helps us to construct better reaction coordinates and improves our estimates of a rare events rate in addition to adding to our understanding of rare event mechanisms in general.

In our investigation of the disk-to-slab transition at constant magnetization we found a committor that seemed to be at odds with the underlying free energy landscape. Our first attempts to reconcile this discrepancy were to look for another configurational collective variable that improved our prediction. However, this effort turned out to be fruitless. With hindsight we can now say: it had to be! This is because the ultimate reason for the shape of the committor in this system lies in the dynamics of the system in connection with the free energy landscape. No configurational collective variable could have provided the information necessary to complete the picture.

The importance of dynamics for undestanding a barrier crossing can also be seen in the second paper, where we investigated how close the centers-of-mass of two fluctuating interfaces approach each other before they come into contact for the first time. The contact distance turns out to be determined by a competition of two timescales: how fast do the interfaces diffuse relative to each other vs. the dynamics of the fluctuations of the interface shapes. As we increase the former, the interfaces are likely come closer to each other before a gap-closing fluctuation occurs while the contact distance is likely to increase if fluctuations of the interfaces occur more rapidly and thus a gap-forming fluctuation is likely to occur sooner, when the interfaces are

[2] $p_{\mathcal{B}}(\mathbf{x})$ and $\rho(\mathbf{x}|\mathrm{TP})$ are actually closely related quantities as shown in e.g. E & Vanden-Eijnden [55].

still further apart. In other words, the likely path that is taken by a system that contains two interfaces to a state where these interfaces are in contact with each other—i.e. the "tubes" of large $\rho(\mathbf{x}|\mathrm{TP})$ [55]—depends on the dynamics along two coordinates: the distance between the centers-of-mass of the two interfaces and the amplitude of the interface fluctuations.

In the third and final paper we investigated the early stages of the melting mechanism of ice. In this case the existence of many different defect types in the ice Ih structure prohibits us from mapping out a low-dimensional free energy landscape that covers all the possible different defect states the system can find itself in. Instead we generated a large number of dynamic trajectories and analyzed them in order to identify the important states that lie between the perfect crystal and a molten nucleus.

Doing so we found that there is quite a bit of variation between pathways as they differ in the types of defects that are involved, in whether an extended topological defect forms along the trajectory, and in where the mobile defect pair that ultimately leads to the formation of a liquid nucleus forms. Nevertheless, our analysis of a large number of trajectories allowed us to identify some common trends between them: the prominent role of 5+7 defects in the melting mechanism, and the tendency towards larger topological defects being a part of the melting trajectories as the degree of undercooling is reduced, are two examples.

One result of our analysis of defects in the melting process is that the abundance of a given defect type in equilibrium (i.e. a defects free energy) is only a weak indication of their role in the melting mechanism. For example, the 5+7-5 and the 5+7-V defect are less likely to be found in equilibrium than the 5+7-2 and 5+7-3 defects. Nevertheless, they are found considerably more often than these defects in melting trajectories at 268 K just before a mobile defect pair or an extended topological defect forms, indicating that they offer a favourable starting point for generating both of these defect types as compared to the other types of 5+7 defects. Once again, this is an effect that stems from the dynamics of the system.

These observations made in many-particle systems confirm the assertion made in the introduction that in order to gain a detailed understanding of rare event's mechanism, we have to understand the dynamics of the important degrees-of-freedom in the system as well as the population of important states in the system. The works presented in this thesis use a number of different approaches to gain such an understanding and, in

turn, provide detailed descriptions of the rare events they investigate.

They thus deepen our appreciation of the specific processes themselves, of rare events and their mechanisms in general, and of the simulation methods we use to investigate them.

Part IV.

Appendices

A. A 1-dimensional double-well system

In Sec. 1.2 I demonstrated the basic properties of rare events using a simple, 1-dimensional model system. The trajectory shown there is an approximate solution of the following system of Langevin equations:

$$\begin{aligned} \mathrm{d}x &= v(t)\,\mathrm{d}t \\ \mathrm{d}v &= \left[\frac{F(x(t))}{m} - \gamma v(t)\right]\mathrm{d}t + \sqrt{\frac{2\gamma}{\beta m}}\,\mathrm{d}W(t) \end{aligned} \tag{A.1}$$

Here, x and $v = \dot{x}$ are the position and the velocity of a particle, respectively, m is the particles mass, $F(x)$ is the force acting upon the partice at position x, γ is a friction coefficient, t is time and $\beta = (k_\mathrm{B}T)^{-1}$, where k_B is Boltzmann's constant and T is temperature. $W(t)$ is a Wiener process with variance $\mathrm{Var}\left[W(t)\right] = t$. Additionally, we choose

$$F(x) = -\frac{\partial V(x)}{\partial x}, \tag{A.2}$$

where $V(x)$ is the potential energy.

The trajectory shown in Fig. 1.3 was obtained by numerically integrating the Langevin equations using the OVRVO integrator described in Ref. 262. The double well potential $V(x)$ used to generate this trajectory is given by

$$V(x) = \frac{A}{4}\left(x^2 - d^2\right)^2, \tag{A.3}$$

where A and d are parameters. The parameters used to generate the trajectory are shown in Tab. A.1.

Table A.1.: Parameters used to obtain the trajectory shown in Fig. 1.3.

m	$=$	$1\ [m]$	d	$=$	$0.5\ [l]$	γ	$=$	$0.5\ [t]^{-1}$
$k_\mathrm{B}T/(m\gamma^2 d^2)$	$=$	1.42	$Ad^2/(m\gamma^2)$	$=$	43.2			

B. Interplay of fast and slow dynamics in rare transition pathways: The disk-to-slab transition in the 2d Ising model

Mean first passage time in a linear potential

The estimate of the drift time in Equ. (4.14) is given by the mean first passage time (MFPT) in a potential with constant slope, i.e.

$$\tilde{F}(s) = \left(\frac{\partial F(\tilde{s})}{\partial \tilde{s}}\right)_{\tilde{s}=s_0} (s - s_0)\,, \tag{B.1}$$

where in the following we assume $\partial F(s)/\partial s > 0$.

Given the one-dimensional Fokker-Planck equation

$$\frac{\partial \rho(s,t)}{\partial t} = -\frac{\partial}{\partial s}\left[A(s)\rho(s,t)\right] + \frac{1}{2}\frac{\partial^2}{\partial s^2}\left[B(s)\rho(s,t)\right], \tag{B.2}$$

the MFPT $T(a; s_0)$ at an absorbing barrier a with a reflective barrier b located at $b > a$ and given that trajectories are started at s_0 is given by [54]

$$T(a; s_0) = 2\int_a^{s_0} \mathrm{d}s' \left[\frac{1}{\psi(s')}\int_{s'}^{b} \mathrm{d}s'' \frac{\psi(s'')}{B(s'')}\right], \tag{B.3}$$

with

$$\psi(s) = \exp\left[\int_a^s \mathrm{d}s' \frac{2A(s')}{B(s')}\right]. \tag{B.4}$$

Substituting $A(s) = -\beta D_s\,(\partial F/\partial s)$ and $B(s) = 2D_s$ with constant diffusion coefficient

D_s and carrying out the integration yields

$$T(a; s_0) = \frac{e^{\beta g(a-b)} - e^{\beta g(s_0-b)} + \beta g(s_0 - a)}{D_s \beta^2 g^2}, \tag{B.5}$$

where $g = (\partial F(s)/\partial s)_{s=s_0}$. By setting $a = s_0 - \Delta s$ and carrying out the limit $b \to \infty$ we arrive at the expression

$$T(s_0 - \Delta s; s_0) = \tau_{\text{drift}}(s_0) = \frac{\Delta s}{D_s \beta \left(\frac{\partial F(s)}{\partial s}\right)_{s=s_0}}. \tag{B.6}$$

C. Weak scaling of the contact distance between two fluctuating interfaces with system size

C.1. Generalization to arbitrary dimension

We discretize the Hamiltonian Eq. (5.44) on a d-dimensional grid with grid spacing $(\Delta x)_i$ in direction i. We arrive at

$$\mathcal{H} = \frac{\gamma}{2}\left[\prod_{k=1}^{d-1}(\Delta x)_k\right]\sum_{j_1}^{n_1-1}\cdots\sum_{j_{d-1}}^{n_{d-1}-1}\left\{ \sum_{i=1}^{d-1}\frac{\left(h_{j_1,\ldots,j_i+1,\ldots,j_{d-1}} - h_{j_1,\ldots,j_i,\ldots,j_{d-1}}\right)^2}{(\Delta x)_i^2}\right\}, \tag{C.1}$$

where $h_{j_1,\ldots,j_{d-1}} = h_{\{j\}} = h(j_1(\Delta x)_1, \ldots, j_{d-1}(\Delta x)_{d-1})$ and n_i and $(\Delta x)_i$ are the number of nodes and the discretization step size in dimension i, respectively. Calculating the derivative with respect to $h_{\{j\}}$ yields the force

$$F_{\{j\}} = \gamma\left[\prod_{k=1}^{d-1}(\Delta x)_k\right] \times \sum_{i=1}^{d-1}\frac{h_{\ldots,j_i+1,\ldots} - 2h_{\ldots,j_i,\ldots} + h_{\ldots,j_i-1,\ldots}}{(\Delta x)_i^2}. \tag{C.2}$$

and the equation of motion

$$\dot{h}_{\{j\}} = \beta\gamma\Pi D_0\sum_{i=1}^{d-1}\delta_i^2 h_{\{j\}} + \sqrt{2D_0}\eta_{\{j\}}. \tag{C.3}$$

Here we have introduced the abbreviations

$$\Pi = \left[\prod_{k=1}^{d-1} (\Delta x)_k\right] \tag{C.4}$$

and

$$\delta_i^2 h_{\{j\}} = \frac{h_{\ldots,j_i+1,\ldots} - 2h_{\ldots,j_i,\ldots} + h_{\ldots,j_i-1,\ldots}}{(\Delta x)_i^2}. \tag{C.5}$$

C.2. Contact distance density distributions

In Sec. 5.3.2 we have derived an approximate solution for the distribution of contact distances between two interfaces, $u(l)$, given a rate function $k(\ell)$:

$$u(\ell) \approx \frac{k(\ell)^{3/4} e^{-\tilde{S}_0(\ell)}}{2{D_{\text{int}}}^{1/2} k(\ell_0)^{1/4} Z}. \tag{C.6}$$

In this section we explicitly calculate $u(\ell)$ for exponential and Gaussian rate functions and test our results by comparing $u(l)$ to distributions obtained from a simple Gaussian random walk model. Random walkers are started at ℓ_0 and their positions are updated according to

$$\ell_{i+1} = \ell_i + \sqrt{2D\Delta t}\xi \tag{C.7}$$

where ξ is a random number chosen from a Gaussian distribution with zero mean and unit variance. Each timestep the walker reacts with probability

$$P_{\text{r}} = 1 - e^{-k(\ell_i)\Delta t}. \tag{C.8}$$

If a reaction occurs the position is saved and added to a histogram. The results of these simulations are shown in Figs. C.1 and C.2.

C.2.1. Exponential rate functions

We first calculate $u(l)$ for the exponential rate function

$$k(\ell) = \nu e^{-\ell/\Lambda}, \tag{C.9}$$

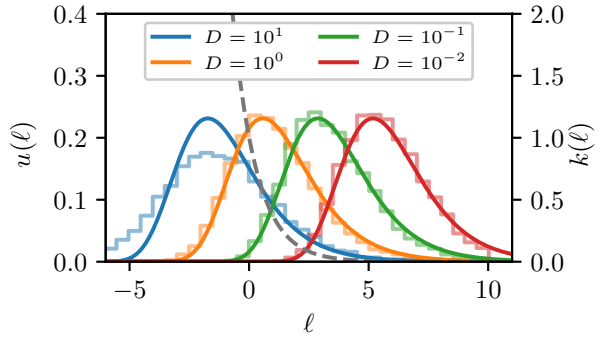

Figure C.1.: Comparison of Eq. (C.11) (lines) to results obtained from random walk simulations (histograms) for an exponential rate function $k(\ell)$ (dashed line) and different values of the diffusion coefficient D_{int}. The other parameters are: $\nu = 1$, $\Lambda = 1$, $\ell_0 = 10$ and $\Delta t = 0.1$. The dashed gray curve indicates the values of the rate function $k(\ell)$. D decreases from left to right.

where $\ell_0 > \ell$. Substituting the "action" $\tilde{S}_0$, given by

$$\begin{aligned}\tilde{S}_0(\ell) &= \sqrt{\frac{\nu}{D}} \int_{\ell_0}^{\ell} \mathrm{d}\ell' \; e^{-\ell'/(2\Lambda)} \\ &= \sqrt{\frac{4\Lambda^2\nu}{D}} \left[e^{-\ell/(2\Lambda)} - e^{-\ell_0/(2\Lambda)} \right],\end{aligned} \tag{C.10}$$

into Eq. (C.6) yields the distribution

$$u(\ell) = \frac{1}{Z} k(\ell)^{3/4} \exp\left[-\sqrt{\frac{4\Lambda^2\nu}{D}} e^{-\ell/(2\Lambda)} \right]. \tag{C.11}$$

This result becomes exact in the limit $D \to 0$ and, indeed, it is in excellent agreement with the data obtained from random walk simulations as D becomes small. The results are shown in Fig. C.1. Note that the constants Z have been obtained by numerically normalizing the distribution $u(\ell)$.

We can also predict the most likely contact distance ℓ^* by setting the derivative of

$\log u(\ell)$ to zero and solving the resulting equation, which yields

$$\ell^* = \Lambda \log \left[\frac{16}{9} \frac{\Lambda^2 \nu}{D} \right]. \tag{C.12}$$

C.2.2. Gaussian rate functions

The rate function $k(\ell)$ is now given by a Gaussian,

$$k(\ell) = \nu \exp \left[-\frac{\ell^2}{2w^2} \right], \tag{C.13}$$

where we assume that $\ell_0 \gg w > 0$, ν is a positive prefactor, and $\ell < \ell_0$. Substituting this rate function into Eq. (5.35) yields

$$\tilde{S}_0 = \sqrt{\frac{\nu}{D_{\text{int}}}} \int_{\ell_0}^{\ell} \mathrm{d}\ell' \ \exp \left[-\frac{\ell^2}{4w^2} \right], \tag{C.14}$$

which can be expressed in terms of an error function:

$$\tilde{S}_0 = \sqrt{\frac{\nu \pi w^2}{D_{\text{int}}}} \left[\operatorname{erf} \left(\frac{\ell_0}{2w} \right) - \operatorname{erf} \left(\frac{\ell}{2w} \right) \right] \tag{C.15}$$

Substituting into Eq. (C.6) we arrive at

$$u(\ell) = \frac{1}{Z} k(\ell)^{3/4} \exp \left[\sqrt{\frac{\nu \pi w^2}{D_{\text{int}}}} \operatorname{erf} \left(\frac{\ell}{2w} \right) \right]. \tag{C.16}$$

The maximum of this $u(\ell)$ can again be calculated, yielding

$$(\ell^*)^2 = 2w^2 W \left(\frac{8}{9} \frac{w^2 \nu}{D} \right), \tag{C.17}$$

where W is the Lambert-W function. In the limit of large L we can approximate $W(x) \sim \log(x)$, yielding

$$\ell^* = w \sqrt{2 \log \left(\frac{8}{9} \frac{w^2 \nu}{D} \right)}. \tag{C.18}$$

Figure C.2 shows a comparison of this solution to the simulation results where the

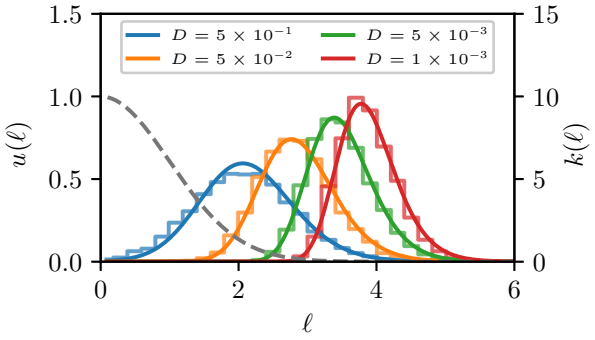

Figure C.2.: Comparison of Eq. (C.16) (lines) to results obtained from random walk simulations (histograms) for different values of the diffusion coefficient D_{int}. The other parameters are: $\nu = 10$, $w = 1$, $\ell_0 = 10$, and $\Delta t = 0.1$. The dashed gray curve indicates the values of the rate function $k(\ell)$. D decreases from left to right.

distribution $u(\ell)$ has been normalized numerically. Also here the agreement between the two is excellent in the limit $D_{\text{int}} \to 0$.

C.3. Mean first passage time calculation

In Sec. 5.4.2 we have outlined two different methods of calculating the mean first-passage times (MFPTs): the *direct* method and what we termed the *Poisson* method. In this appendix we provide the parameters used to carry out these calculations as well as the algorithmic details of the direct method.

Both methods require a choice of the equilibrium region $\mathcal{E}$ which are gathered in Tabs. C.1 and C.2. These regions were chosen based on a previous calculation of the free energy $\beta F(\zeta) = -\log P(\zeta)$, where $P(\zeta)$ is the equilibrium probability density as a function of the maximum relative height, ζ. The results of this calculation are shown in Fig. C.3 together with the chosen regions that are centered around the minimum of the respective free energy.

In the direct method we average the waiting times between configurations in $\mathcal{E}$ and the system reaching a checkpoint ζ_i the next time (see Fig. 5.5). Here, we write $T_j^{(i)}$ for the times a crossing of checkpoint ζ_i occurs and $t_{jk}^{(i)}$ for the times when the system

Table C.1.: Simulation parameters used to calculate MFPT data for the (1+1)-dimensional EW interface. Shown are the length of individual simulations $\mathcal{T}$, the extent of the equilibrium region $\mathcal{E}$, and the number trajectories used, n_R, as a function of linear system size L. For ζ_low and ζ_high the corresponding value of $\tilde{\zeta}$ is given in brackets.

L	$\mathcal{T}$	$\mathcal{E}$		n_R
		ζ_low	ζ_high	
10	1.5×10^7	1.298 (0.410)	1.614 (0.510)	16
20	1.5×10^7	2.000 (0.447)	2.447 (0.547)	16
50	1.5×10^7	3.423 (0.484)	4.130 (0.584)	12
100	1.5×10^7	5.209 (0.521)	6.209 (0.621)	12
150	1.5×10^7	6.380 (0.521)	7.605 (0.621)	12
200	1.5×10^7	7.367 (0.521)	8.781 (0.621)	12
400	1.5×10^7	11.155 (0.558)	13.160 (0.658)	10
500	1.5×10^7	12.477 (0.558)	14.713 (0.658)	10
1000	1.5×10^7	17.646 (0.558)	20.808 (0.658)	8
2500	1.5×10^7	27.900 (0.558)	32.900 (0.658)	10
5000	1.5×10^7	39.457 (0.558)	46.528 (0.658)	9

Table C.2.: Simulation parameters used to calculate MFPT data for the (2+1)-dimensional EW interface. Shown are the length of individual simulations $\mathcal{T}$, the number of trajectories used, n_R, and the extent of the equilibrium region $\mathcal{E}$ as a function of linear system size L. For ζ_low and ζ_high the corresponding value of $\tilde{\zeta}$ is given in brackets.

L	$\mathcal{T}$	$\mathcal{E}$		n_R
		ζ_low	ζ_high	
10	3×10^7	1.287 (-0.55)	2.388 (0.55)	11
20	3×10^7	1.840 (-0.55)	2.941 (0.55)	11
40	3×10^7	2.393 (-0.55)	3.494 (0.55)	11
80	3×10^7	2.946 (-0.55)	4.047 (0.55)	10
120	3×10^7	3.269 (-0.55)	4.371 (0.55)	9
200	2.14×10^7	3.677 (-0.55)	4.778 (0.55)	6
400	2.63×10^7	4.230 (-0.55)	5.331 (0.55)	7
800	1.22×10^7	4.783 (-0.55)	5.884 (0.55)	4

is found in region $\mathcal{E}$ in between the hits at time $T_{j-1}^{(i)}$ and $T_j^{(i)}$, i.e. all the times where the next crossing occurs at $T_j^{(i)}$. $N_j^{(i)}$ is the number of times $t_{jk}^{(i)}$ observed. The MFPT

for checkpoint ζ_i is then given by

$$\tau(\zeta_i) = \frac{1}{\sum_j N_j^{(i)}} \sum_j \sum_{k=1}^{N_j^{(i)}} \left(T_j^{(i)} - t_{jk}^{(i)} \right), \tag{C.19}$$

where the $\sum_j$ runs over all checkpoint crossings j. This can be rewritten in the computationally more convenient form of

$$\tau(\zeta_i) = \frac{1}{\sum_j N_j^{(i)}} \sum_j \left(N_j^{(i)} T_j^{(i)} - \sum_{k=1}^{N_j^{(i)}} t_{jk}^{(i)} \right). \tag{C.20}$$

Hence, to calculate the MFPTs directly, two sums have to be kept and updated each time the interface ζ_i is crossed: $\sum_j N_j^{(i)}$, $\sum_j (N_j^{(i)} T_j^{(i)} - \sum_{k=1}^{N_j^{(i)}} t_{jk}^{(i)})$.

C.4. Direct- vs. Poisson method in the (1+1)-dimensional EW model

In Sec. 5.4.2 we present mean first-passage times (MFPTs) calculated using two different methods: (i) a direct average of waiting times between visiting the $\mathcal{E}$ region (see App. C.3) and crossing a given checkpoint ζ_i, and (ii) an evaluation that assumes that the statistics of these crossing are Poissonian statistics. In this appendix we present an analysis of the differences between the results obtained using these two methods and their dependence on system size L.

Figures C.4 and C.5 show the ratios of the MFPTs calculated using the direct- and the Poisson method, $q(\zeta) = \tau_{\text{direct}}/\tau_{\text{Poisson}}$, for the (1+1)- and the (2+1)-dimensional EW interface, respectively.

As was noted in the main text, the direct method is limited by the length of trajectories used because the a priori probability of observing a given waiting time is not the same for all waiting times t_{w}. We assume the distribution of waiting times, $\rho_{\text{w}}(t_{\text{w}})$, to be time-independent and that subsequent checkpoint crossings are independent of each other. Consider a set of simulation runs of length $\mathcal{T}$ over which we calculate the average waiting time of such events.

We first calculate the waiting time for a single fixed starting time of the waiting

period, $0 \leq t < \mathcal{T}$. The expected observed average waiting time starting from t, $\langle t_\mathrm{w} \rangle_t$, is given by

$$\begin{aligned} \langle t_\mathrm{w} \rangle_t &= \frac{1}{Z(t)} \int_t^{\mathcal{T}} \mathrm{d}t'' \left(t'' - t\right) \rho_\mathrm{w}(t'' - t) \\ &= \frac{1}{Z(t)} \int_0^{\mathcal{T}-t} \mathrm{d}t' t' \rho_\mathrm{w}(t'), \end{aligned} \tag{C.21}$$

where in the second line we have substituted $t' = (t'' - t)$ and $Z(t) = \int_0^{\mathcal{T}-t} \mathrm{d}t' \rho_\mathrm{w}(t')$ normalizes the distribution of events observed in the limited time $\mathcal{T} - t$. Now we can average over the starting points t to arrive at the overall expectation value for the observed waiting times:

$$\langle t_\mathrm{w} \rangle = \frac{1}{\mathcal{T}} \int_0^{\mathcal{T}} \mathrm{d}t \frac{1}{Z(t)} \int_0^{\mathcal{T}-t} \mathrm{d}t' t' \rho_\mathrm{w}(t') \tag{C.22}$$

As an illustrative example, consider waiting times that are distributed according to a Poisson distribution: $\rho_\mathrm{w}(t_\mathrm{w}) = \tau^{-1} e^{-t_\mathrm{w}/\tau}$. A calculation of $\langle t_\mathrm{w} \rangle_t$ yields

$$\langle t_\mathrm{w} \rangle_t = \tau + \frac{\mathcal{T} - t}{1 - e^{(\mathcal{T}-t)/\tau}}. \tag{C.23}$$

As expected, the second term vanishes in the limit $\mathcal{T} \to \infty$ to recover the well-known result for Poisson distributions.

The result of the second integration in Eq. (C.22) can not be expressed in terms of basic functions, however, in order to assess the effect of limited simulation time we now consider the regime where $\mathcal{T} - t \ll \tau$. Expanding $\langle t_\mathrm{w} \rangle_t$ to first order in $(\mathcal{T} - t)/\tau$ yields

$$\langle t_\mathrm{w} \rangle_t \approx \frac{1}{2} \left(\mathcal{T} - t\right). \tag{C.24}$$

With this approximation carrying out the second integral in Eq. (C.22) then gives

$$\langle t_\mathrm{w} \rangle \approx \frac{\mathcal{T}}{4}, \tag{C.25}$$

which is solely determined by the length of the trajectories. The same result can be achieved by simply assuming that $\rho_\mathrm{w}(t_\mathrm{w})$ is a constant over the range $[0, \mathcal{T}]$. This result is represented by dashed lines in Figs. C.4 and C.5 and is in excellent agreement with the observed decline of $q(\zeta)$ at large ζ.

For both dimensionalities we observe an exponential decay of $q(\tilde{\zeta})$ with $\tilde{\zeta}$ before the deviations due to finite $\mathcal{T}$ drop q to zero. The indicated fits of $q(\tilde{\zeta}) = 1 + A\exp[-(\tilde{\zeta} - \tilde{\zeta}_0)/\kappa(L)]$ to the data reveal a qualitative difference between the (1+1)- and the (2+1)-dimensional system: while the parameter $\kappa(L)$ approaches a constant value as L increases for (1+1)-dimensional interfaces, in the (2+1) dimensional case $\kappa(L)$ grows with system size.

C.5. Scaling of MFPTs with system size

In Figs. 5.6 and 5.8 in the main part, we have shown examples of the scaling behavior of $\tau(L)$ at fixed values of $\tilde{\zeta}$. Figures C.6 and C.7 show the functional form of $\tau(L)$ for a broader range of $\tilde{\zeta}$ values.

C.6. Detection of cluster geometry in the Ising model

We present an algorithm, that detects the geometry of a given cluster in simulations of the 2- and 3-dimensional Ising model with periodic boundary conditions. This includes the detection of holes in slabs. As a first step, we identify the largest cluster of neighboring spins that point in a particular direction within the system, the so called geometric cluster [142, 143]. The neighbors of a given spin are all spins that can be reached by making a step of ± 1 in each direction separately. Diagonally displaced spins are not considered neighbors.

The number of distinct geometries that are thermodynamically stable states if one fixes the magnetization of the system, depends on the number of dimensions. Consider clusters in two dimensions that consist of spins that point up. There are three stable geometries in order of increasing magnetization [80]: a disk of spins pointing up, a slab that points up next to a slab that points down, and a disk that points down (see Fig. C.8). In the following we will refer to these states as disk, slab, and opp-disk, using the *opp-* prefix to identify configurations in which the largest cluster of spins that point in the opposite direction has the given geometry.

To distinguish between these geometries, we introduce an algorithm that counts the directions in which a cluster is connected to itself. Figure C.8 shows a sketch of the principle used to identify these geometries. We pick a random spin σ from our cluster and ask the question: how many periodic copies of σ, that are found in adjacent copies

of the simulation box, are connected to σ via a path that does not leave the cluster? Additionally, we require that these copies are distinct, in the sense that they are not related to each other by an inversion around σ.

Table C.3.: Table of possible geometries in two dimensions, the number of closest periodic images of a spin that can be reached without leaving the cluster, n_c, and the value for the largest cluster in the opposite direction $\bar{n}_c$.

n_c	$\bar{n}_c$	Geometry	
0	2	Disk	non-spanning
0	1	Disk[1]	non-spanning
0	0	Disk[1]	non-spanning
1	1	Slab	spanning
1	0	Opp-Disk[1]	spanning
2	0	Opp-Disk	spanning

Table C.4.: Table of possible geometries in three dimensions, the number of closest periodic images of a spin that can be reached without leaving the cluster, n_c, and the value for the largest cluster in the opposite direction $\bar{n}_c$.

n_c	$\bar{n}_c$	Geometry	
0	3	Sphere	non-spanning
1	3	Cylinder	spanning
2	2	Slab	spanning
2	3	Hole	spanning
3	3	Hole-Opp-Hole	spanning
3	2	Opp-Hole	spanning
3	1	Opp-Cylinder	spanning
3	0	Opp-Sphere	spanning

In the case of a disk, the answer is 0; there is no path to any periodic copy of a given spin. If the cluster is a slab the answer is 1 since we can find a path along the y-direction to a spin offset one box-length up and another one, one box-length down. However, these two spins are related to each other by an inversion around σ, and, hence, we discard one of them. The last example is the opp-disk; here we can reach copies in y-direction and copies in x-direction so the answer is 2.

In order to also handle unusual cluster geometries like slabs that are aligned along the diagonals of the simulation box or clusters that span multiple periodic boxes before

they are connected to themselves, we can generalize this concept by looking for the "closest" copies of our spin in terms of a *box-distance*, Δ. To define Δ we first note that the offset of each periodic copy of σ, can be written as

$$\Delta\mathbf{r} = \sum_i b_i \mathbf{s}_i, \tag{C.26}$$

where the b_i are integer coefficients and the vectors $\mathbf{s}_i$ $(i = x, y, \ldots)$ span the simulation box. The box-distance Δ is then given by

$$\Delta = \sqrt{\sum_i b_i^2}. \tag{C.27}$$

By looking for the copies with smallest Δ, we make sure that we start searching for copies in the neighboring boxes first.

The algorithm that distinguishes between different geometries then proceeds as follows:

1. Pick a random spin σ from the largest cluster in the system that points in the direction of interest.

2. For d dimensions, up to $2d$ of the periodic images of σ that can be reached via a path that does not leave the cluster, will have the minimum value of Δ, $\Delta_{\min}$. Find all periodic images with $\Delta_{\min}$.

3. Pairs of these images will be related by an inversion around σ. Keep only one copy of each of these pairs.

4. Count the number of these periodic images found, n_c.

5. Repeat steps 1 to 4 for the largest cluster pointing in the opposite direction. The resulting count is called $\bar{n}_c$.

6. To determine the geometry refer to tables C.3 and C.4 that summarize the possible geometries in two and three dimensions and the associated values of n_c and $\bar{n}_c$,.

The additional geometries encountered in 3 dimensions shown in Tab. C.4, are cylinders, slabs with a hole (i.e. slabs where there is a connected path through the

slab that consists of spins that point in the opposite direction), and the corresponding opp-geometries. Also, in small systems configurations that contain an up-slab and a down-slab, both with holes, can be found[1] (Hole-Opp-Hole).

C.7. MC simulations

In the case of a (1+1)-dimensional interface the equations of motion (5.43) are derived from the Hamiltonian

$$\mathcal{H} = \frac{\gamma}{2} \sum_{i=0}^{N-1} \Delta x \left(\frac{x_{i+1} - x_i}{\Delta x} \right)^2 . \tag{C.28}$$

The generalization to higher dimensions is straightforward and given in App. C.1.

Free energy landscapes as a function of ζ, $F(\zeta)$, are obtained using Metropolis Monte Carlo [263] umbrella sampling [264] simulations. Configurations are biased using a set of harmonic spring potentials and the resulting histograms are subsequently joined using the Weighted-Histogram-Analysis-Method [86–88] (WHAM)[2].

C.8. Calculation of cluster size from the magnetization

If a configuration from an Ising model simulation consists of a single large cluster, the size of the cluster can be estimated from the total magnetization. This estimate will be accurate, if the average magnetizations inside and outside of the cluster are close to the bulk values $m_\mathrm{u} = -m_\mathrm{d} = \langle m \rangle$. This is expected to be true in the bulk of the cluster, if the cluster is a large enough slab, so that the width of the interfaces is small relative to the width of the cluster. Due to the symmetry of the Ising model with respect to a flip of all the spins, effects that stem from the surfaces of the cluster average out. Hence, we can write

$$Nm \approx n \langle m \rangle - (N - n) \langle m \rangle , \tag{C.29}$$

where m is the magnetization of configuration, N is the total number of spins and n is the number of spins in the cluster of interest. The cluster size can then be estimated

[1] Think of two slabs next to each other. A hole is formed in one of them by flipping a path of spins that connect the opposite cluster to itself. Afterwards the same can be done for the opposite cluster as well, since those two paths do not necessarily cross

[2] Code available at `http://membrane.urmc.rochester.edu/`, Version 2.0.9.

by simply rearranging to

$$n \approx \frac{N}{2}\left(\frac{m}{\langle m \rangle} + 1\right). \tag{C.30}$$

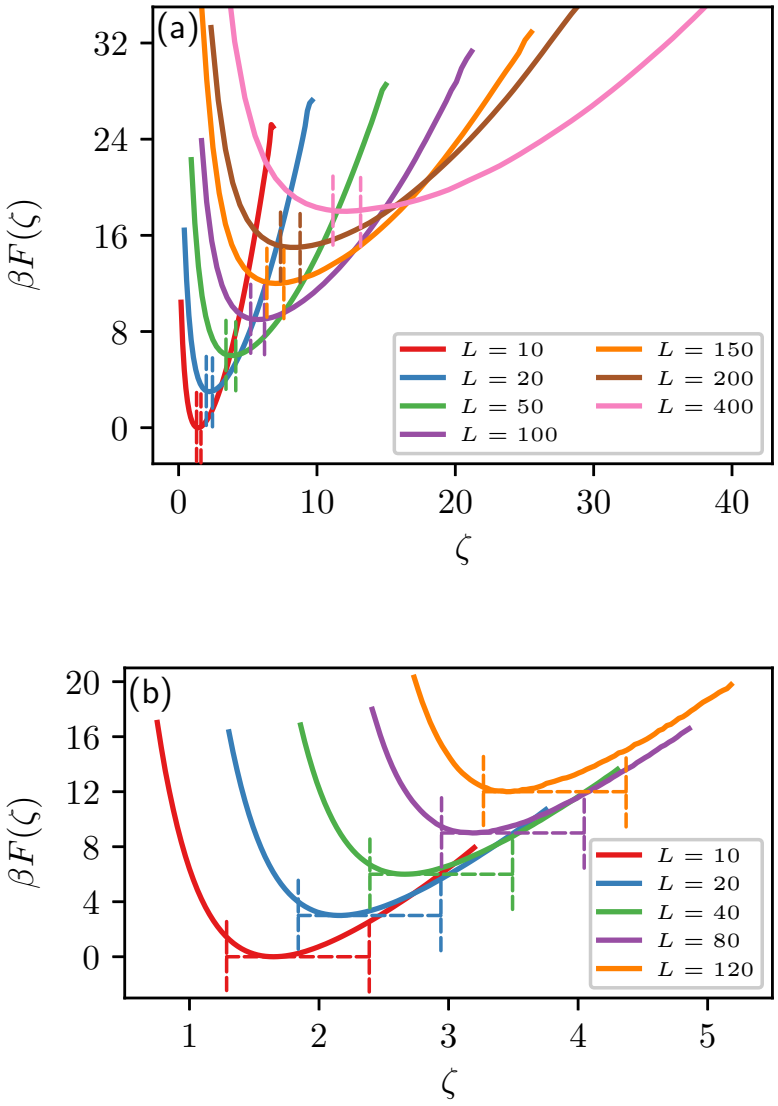

Figure C.3.: Free energies $\beta F(\zeta) = -\log P(\zeta)$ as a function of the maximum relative height, ζ, for the (1+1)- (subplot (a)) and (2+1)-dimensional (subplot (b)) Edward Wilkinson interface. For clarity, the curves have been shifted for different system sizes so that L increases from the bottom line to the top. The dashed vertical lines indicate the equilibrium regions $\mathcal{E}$ that were used in the MFPT calculations. These results have been obtained using umbrella sampling simulations with harmonic biases that were subsequently matched using the WHAM method [86–88]. For details on these simulations see App. C.7.

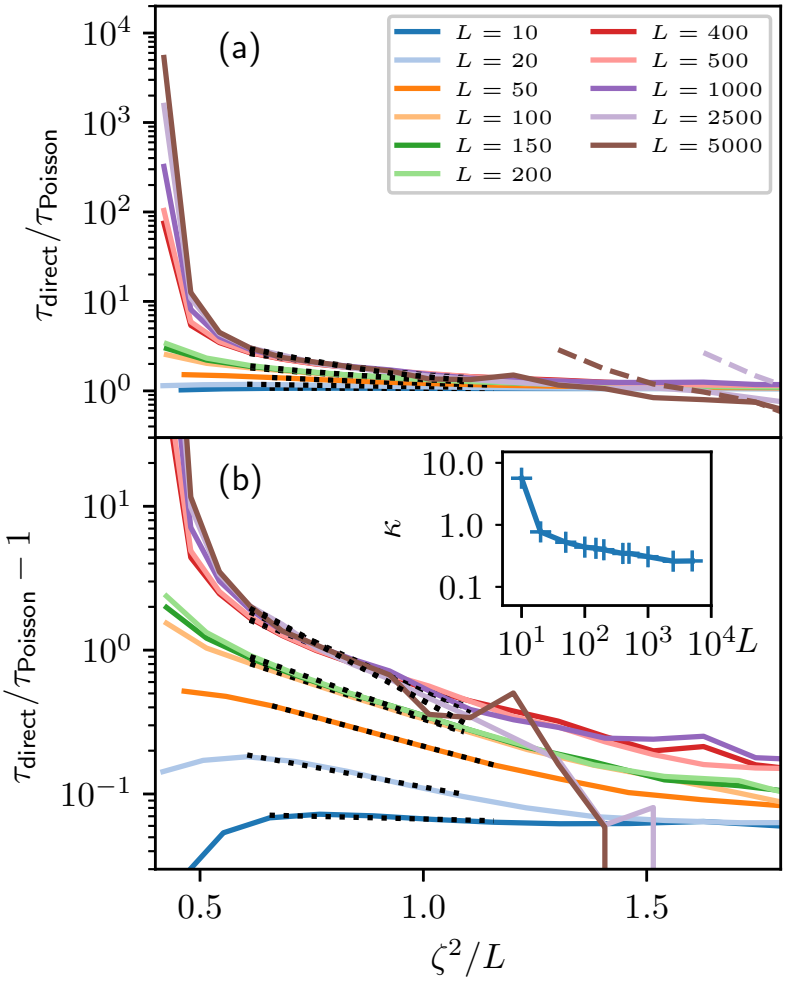

Figure C.4.: (a) Ratios of mean first-passage times for (1+1)-dimensional EW interfaces calculated using the direct method to the ones obtained using the Poisson method, $q = \tau_{\text{direct}}/\tau_{\text{Poisson}}$. The dashed lines represent the expected values for large $\zeta - S(l)$, $(\mathcal{T}/4)/\tau_{\text{Poisson}}$, that come about due to the finite length of the trajectories used to calculate τ_{direct}. The dotted black lines are fits to the function $q = 1 + A\exp(-\tilde{\zeta}/\kappa)$. (b) $q - 1$ plotted on a logarithmic scale. Inset: fitted parameters κ as a function of inverse system size $1/L$.The data suggests that $\lim_{L\to\infty}\kappa(L) = const.$ In both plots system size increases from the bottom line to the top line.

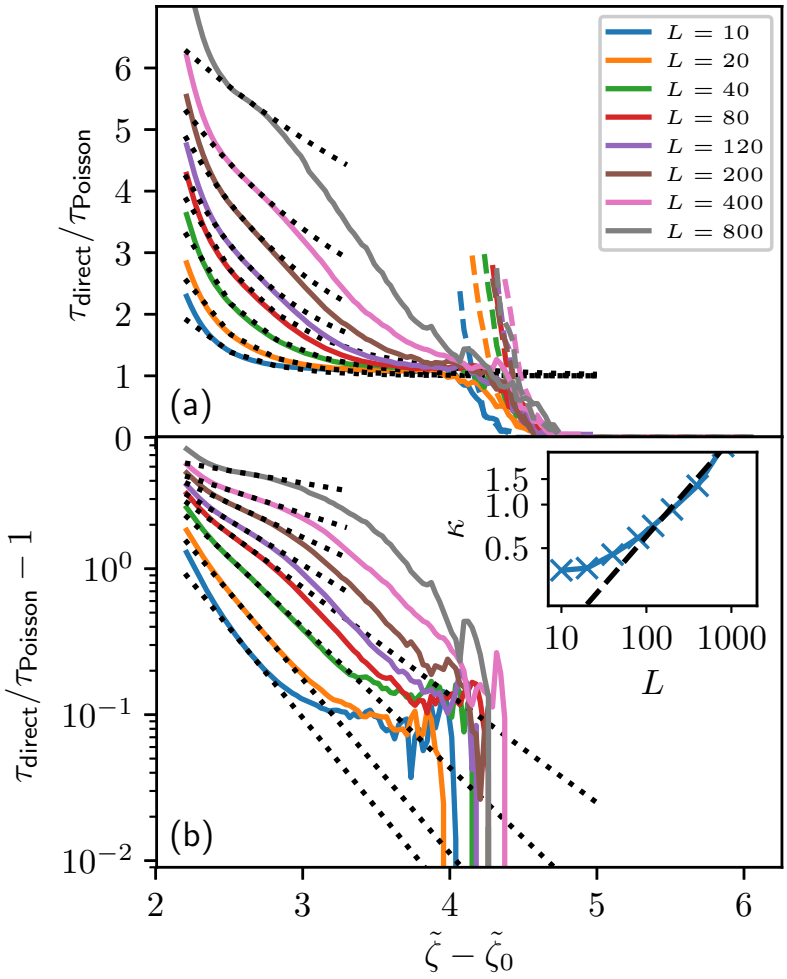

Figure C.5.: Same analysis as in Fig. C.4 for the (2+1)-dimensional interface. Inset: κ as a function of L. The dashed line indicates a fit of $\kappa(L) = AL^B$, where $A \approx 0.03$ and $B \approx 0.67$. In contrast to the (1+1)-dimensional system, κ grows with system size. System size increases from the bottom to the top line.

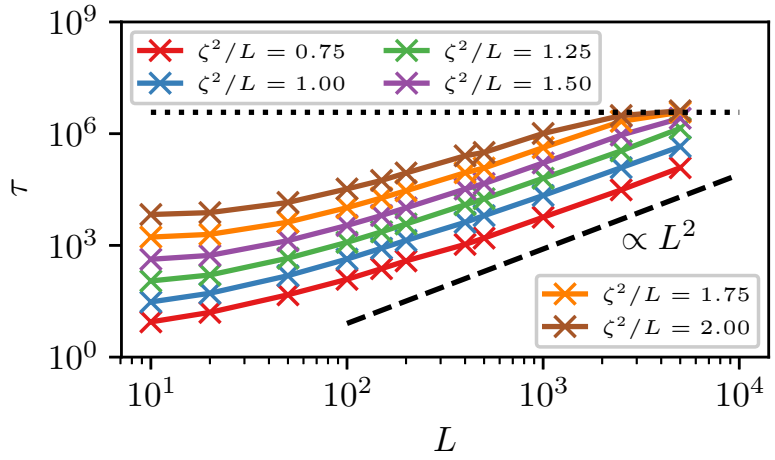

Figure C.6.: Mean first passage times τ as a function of linear system size L at fixed values of $\tilde{\zeta} = \zeta/L^2$ for (1+1) dimensional EW interfaces. The dotted line indicates a value of $\tau = \mathcal{T}/4$, where $\mathcal{T}$ is the length of the simulations used to calculate the MFPTs. ζ^2/L increases from the bottom to the top line.

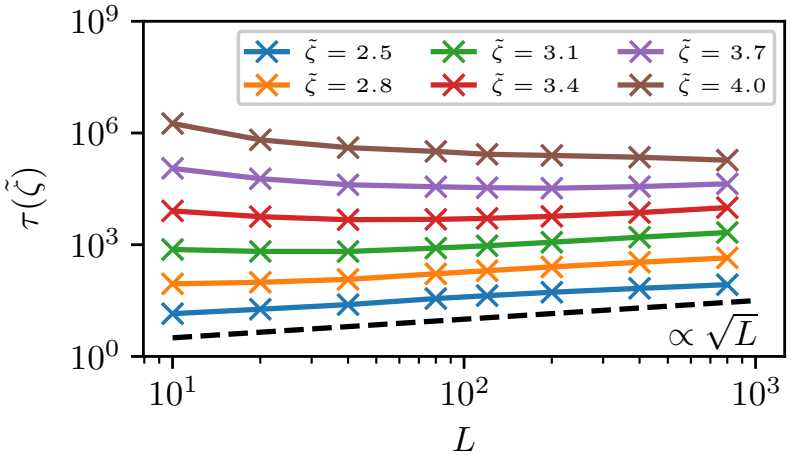

Figure C.7.: Mean first passage times τ as a function of linear system size L at fixed values of $\tilde{\zeta} = \zeta - S(L)$ for (2+1) dimensional EW interfaces. $\bar{\zeta}$ increases from the bottom to the top line.

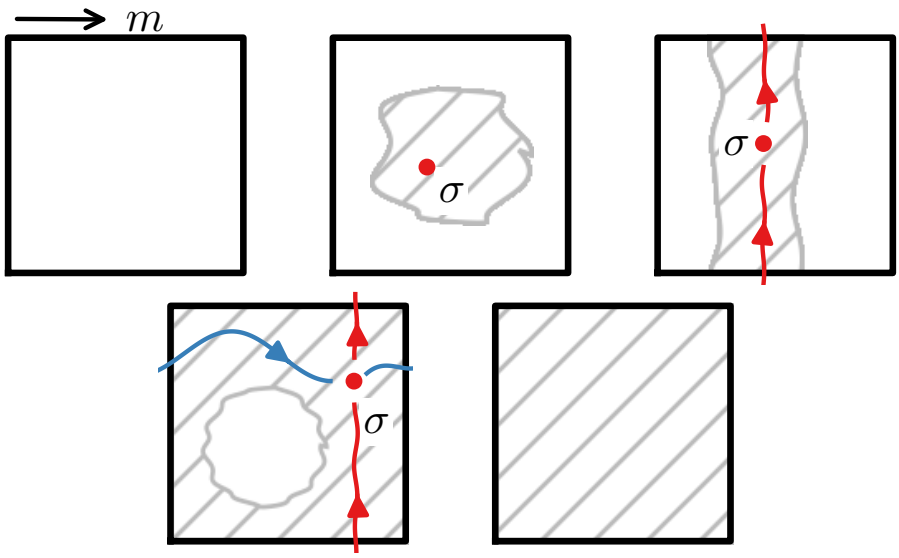

Figure C.8.: Sketch of 5 different states that are observed as a function of increasing magnetization in the 2d Ising model. In order from top left to bottom right they are referred to as: homogeneous-down, disk-up, slab, disk-down, and homogeneous-up. The red dots are randomly chosen spins and the lines indicate paths that connect those spins to one of their periodic images without leaving the cluster. In the disk-down configuration two paths are found. One leading to a copy of the spin that is offset by the $\mathbf{s}_y$ box vector (red) and one that leads to a spin that is offset by the $\mathbf{s}_x$ vector (blue).

D. The microscopic mechanism of bulk melting of ice

D.1. The defect detection scheme

Figure D.1 presents the scheme used to detect defects in configurations throughout the paper. We start by minimizing the potential energy of a given configuration by setting the momenta of atoms to zero and annealing the system to a temperature of 1 K using a Langevin thermostat. The cooled configurations are then analyzed using a number of algorithms the details of which can be found below.

In the course of this analysis deviations from a perfect hexagonal ice lattice are detected and, if possible, attributed to known defect structures. The attribution of anomalies in the H-bond network to a defect may reveal other known defect structures and, hence, the analysis is run iteratively until no new defects are found.

The last part of the detection scheme assigns each configuration to a global state based on the criteria shown in Fig. D.1.

D.1.1. Detection of the hydrogen bond network and of L-D defects

Hydrogen bonds are detected in annealed configurations using the HB2 criterion proposed in Ref. 260 using a custom implementation for the LAMMPS simulation package. This criterion considers a set of two oxygen atoms and one hydrogen atom to form a hydrogen bond if the O-O distance is smaller than 3.5 Å and the O-H-O angle is larger than 140°. This analysis yields a network of HBs from which an undirected graph is constructed using the *networkx* python package [265]. This package provides a large number of graph analysis functions we use to carry out parts of the following analysis.

The simplest task is the count of the number of HBs each molecule donates (n_d) and accepts (n_a). In the perfect lattice one expects $n_\mathrm{d} = n_\mathrm{a} = 2$ for all molecules. If

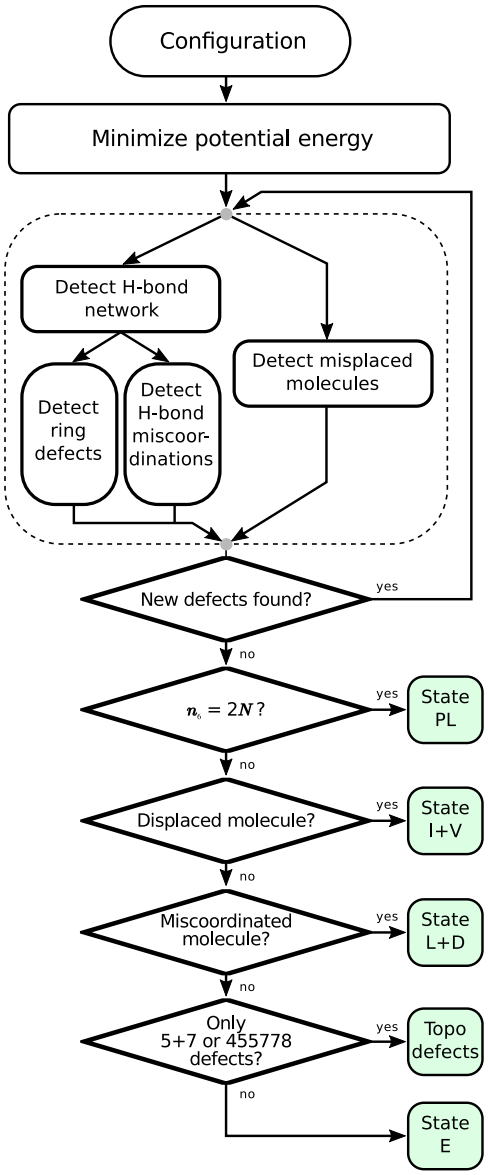

Figure D.1.: Sketch of the algorithm used to detect defects in the ice Ih structure throughout this paper. It consists of two stages: in the first stage the configuration is analyzed and deviations from the pristine Ice Ih structure are marked using different approaches (see the descriptions in this appendix). In the second stage a state is assigned based on the deviations found. n_6 and N are the number of 6-rings detected and the number of molecules in the system, respectively.

either of these two criteria is not fulfilled for a given molecule it is considered to be *miscoordinated*. This can be the result of both, an interstitial-vacancy and an L-D pair. If no I-V pair is found, an L-D pair is considered to be present. Note, that L-D pairs where L and D stay bound to each other form frequently in hexagonal ice and that their separation is associated with an additional free energy barrier [104]. Here we do not distinguish between bound and unbound L-D pairs.

D.1.2. Detection of topological defects in the hydrogen bond network

Defects in the ice Ih structure such as the 5+7 defect can present very similar molecular environments to what can be seen in the perfect lattice. The hydrogen bonds in the region of 5+7 defects fulfill the ice rules and the changes in the bond angles are comparatively small. This makes it hard to detect defects based on the positions of molecules around a given molecule alone. In order to detect such defects, algorithms that are based on detecting the topology of the hydrogen-bond network have been proposed [105, 106]. Here we use a similar scheme that analyzes the rings that can be found in the network formed by H-bonds in a hexagonal Ice crystal.

We define a ring in the H-bond network as a path that leads from a molecule to itself, where we move from one molecule to the next following H-bonds. We do not allow the path to cross itself, i.e. each intermediate molecule may only be visited once. In principle, with the use of periodic boundary conditions, a given molecule may be part of an infinite number of rings of arbitrary size. To make our ring definition unique we restrict ourselves to a smaller set of rings: the set of shortest rings around each molecule that contain the molecule and two of its neighbors.

Consider a molecule O that is H-bonded to n_{hb} other molecules as depicted in Fig. D.2. In order to construct the shortest rings we iterate through all $n_{\mathrm{hb}}(n_{\mathrm{hb}}-1)/2$ pairs of neighbor molecules A and B. For each of these pairs we look for the shortest path between A and B that do not pass through the molecule O. These paths are constructed using Dijsktra's algorithm[266] as implemented in networkx. There may be more than one path of the same length and—in order to make the result reproducible—we include all rings in the following analysis. Repeating this procedure for all molecules in the crystal yields a set of rings and a list of rings that pass through a given molecule which we use to identify defect types.

5+7 defects [104, 234] can be formed both in the c-plane ("horizontally") or parallel

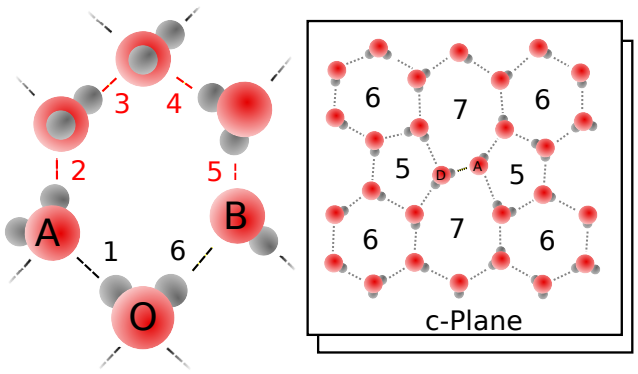

Figure D.2.: Illustration of the ring-detection scheme used to detect topological defects in Ice Ih crystal lattice. Left: rings are detected by selecting a molecule O and all pairs of molecules it is conencted to via hydrogen-bonds, A and B. Rings are then found by finding all shortest paths from A to B that do not pass through edges $O-A$ and $O-B$ (H-bonds 1 and 6 respectively). Subsequently the ring is closed by adding molecule O to the ring. Right: Illustration of a 5+7 Type 3 defect [104, 234] as seen projected onto the c-plane of the crystal structure. The numbers within the rings count the number of molecules that are within the respective ring. D and A mark what we call the donor- and the acceptor molecule of the 5+7 defect.

to the prism-, or the secondary-prism plane. The basic ideas for detecting these defects is demonstrated in the right part of Fig. D.2: the donor and the acceptor molecule of the 5+7 defect must be part of at least two 7-rings and one 5-ring in the c-plane alone. If we also consider the rings that pass through molecules in the adjacent plane, donor and acceptor molecules of a horizontal 5+7 defect are part of 8 7-rings, 4 6-rings and 2 5-rings. This ring fingerprint is used to pick out 5+7 defects from a given configuration.

In order to further distinguish the different types of 5+7 defects described in Ref. 104 we also take into account where the other H-bonds of donor and acceptor are pointing (cf. Tab. D.1). The HBs of each molecule can either both point towards a molecule in the same layer (in-plane, IP) or one of the HBs points towards a molecule in the same plane and the other one to a molecule in an adjacent plane (out-of-plane, OP). Hence, to detect these different types one needs to associate each molecule with a layer of the configuration. Type 3 and Type 5 defects are additionally distinguished by the

Table D.1.: Table of horizontal 5+7 defect types. The 5+7 defects can be distinguished by the orientation of the donor and acceptor molecule. They can either be in-plane (IP, both outgoing hydrogen bonds are formed with molecules in the same *c*-plane) or out-of-plane (OP, one H-bond to a molecule in the same *c*-plane, one with a molecule in an adjacent plane)[104]. To distinguish Type 3 from Type 5 defects the orientation of the in-plane $O-H$ vector of both molecules has to be taken into account.

Type	Donor	Acceptor	in-plane $O-H$ vectors
1	OP	OP	-
2	IP	IP	-
3	IP	OP	antiparallel
4	OP	IP	-
5	IP	OP	orthogonal

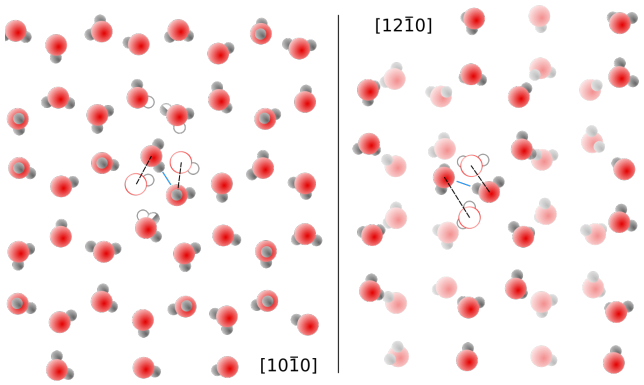

Figure D.3.: Sketches of vertical 5+7 defects seen projected onto the prism- ([12$\bar{1}$0]) and the secondary prism plane. The molecules that are only outlined indicate the position of the respective molecule in the perfect lattice. The shaded molecules on the right are roughly 2 Å closer to the reader than the unshaded molecules.

direction the in-plane H-bonds of donor and acceptor are pointing to.

In addition to horizontal 5+7 defects with donor-acceptor pairs that are in the same *c*-plane, also vertical 5+7 defects can be observed. Figure D.3 shows two examples of such defects where the donor-acceptor pair lies in the prism- ([10$\bar{1}$0]) and the secondary prism-plane ([12$\bar{1}$0]). Together these defects are referred to as 5+7-V defects.

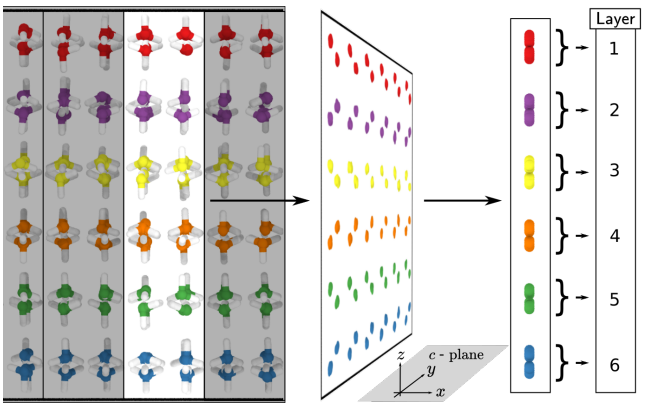

Figure D.4.: Schematic representation of the algorithm used to assign molecules to layers. The white area on the left indicates a single slice used for the analysis, which is carried out on each slice separately. The resulting layers are then matched across neighboring slices in order to arrive at a consistent numbering of layers throughout the system.

The algorithm that assigns each molecule to a layer is sketched in Fig. D.4. First, the configuration is sliced along the x-axis into slices that contain two layers of molecules. Next, the configuration is squashed leaving only the z-coordinates of the oxygen atom of each molecule. These z-positions are clustered using the *AgglomerativeClustering* hierarchical clustering algorithm implemented in the scikit-learn python package [267][1]. As metric we use the distances between the molecules taking periodic boundary conditions into account. *Average* linkage is used and we set the number of clusters to be found to the number of c-planes expected (6 in the example shown). This procedure is applied to each slice along the x-direction separately and afterwards the resulting layers are matched across the slices using the center-of-mass of the layers found in each slice to identify which neighboring layers belong together. This slicing procedure is used to accommodate capillary waves that modulate the layer positions as one moves along the x-direction. The result of this procedure is that each molecule is now associated with a number that identifies the layer the molecule is in.

The detection of defect structures is complicated if multiple defects are close to each other. In this case, the ring counts of different defects can influence each other. To be able to detect 5+7 defects that are close to each other, we compiled a list of different

[1] scikit-learn version 0.18.2 is used.

ring fingerprints by inspecting a large number of configurations with unknown defect structures.

D.1.3. Detection of interstiatial-vacancy defects

In order to identify interstitials and vacancies in configurations we compare the minimized configuration with a template configuration that contains a perfect ice Ih crystal of the same size. This procedure is a simplified version of the method previously employed by Mochizuki *et al.* [106] where we skip the calculation of the edit distance.

To do so, we first align the configuration that is analyzed (denoted by $\mathcal{C}$) with the template configuration ($\mathcal{T}$) using the following procedure:

1. Identify the set of molecules in the system, $\mathcal{I}$, whose contribution to the potential energy in the system is lower than $-16\,\mathrm{kcal/mol}$. These molecules are in ice-like configurations.

2. Align these molecules with their counterparts in the template configuration. To do so, use a global shift of the configuration, $\mathbf{s}$, to minimize the summed mean square displacement

$$F(\mathbf{s};\mathcal{C},\mathcal{T}) = \sum_{i\in\mathcal{I}} \left|\mathbf{x}_i^{\mathcal{C}} - \mathbf{X}(\mathbf{x}_i^{\mathcal{C}};\mathcal{T}+\mathbf{s})\right|^2, \tag{D.1}$$

   wherein $\mathbf{X}(\mathbf{x}_i^{\mathcal{C}};\mathcal{T}+\mathbf{s})$ is the position of the closest neighbor of molecule i in $\mathcal{C}$ that can be found in $\mathcal{T}$ that has been shifted by $\mathbf{s}$. As the position of a molecule we use the position of the oxygen. This yields an optimized vector $\mathbf{s}^{(1)}$ and a value of the MSD function $F_{\mathrm{min}}^{(1)}$.

3. If $F_{\mathrm{min}}^{(1)}/N_{\mathrm{mol}}$ is larger than a threshold value $f_{\mathrm{max}} = 0.03\,\mathrm{\AA}^2$, shift the vector $\mathbf{s}^{(1)}$ by one layer distance in the z-direction and redo the optimization using this shifted vector as initial condition.

4. If $F_{\mathrm{min}}^{(2)}/N_{\mathrm{mol}}$ is still larger than f_{max}, again, shift the output vector of the previous configuration and redo the optimization. If this optimization does not succeed, the procedure fails.

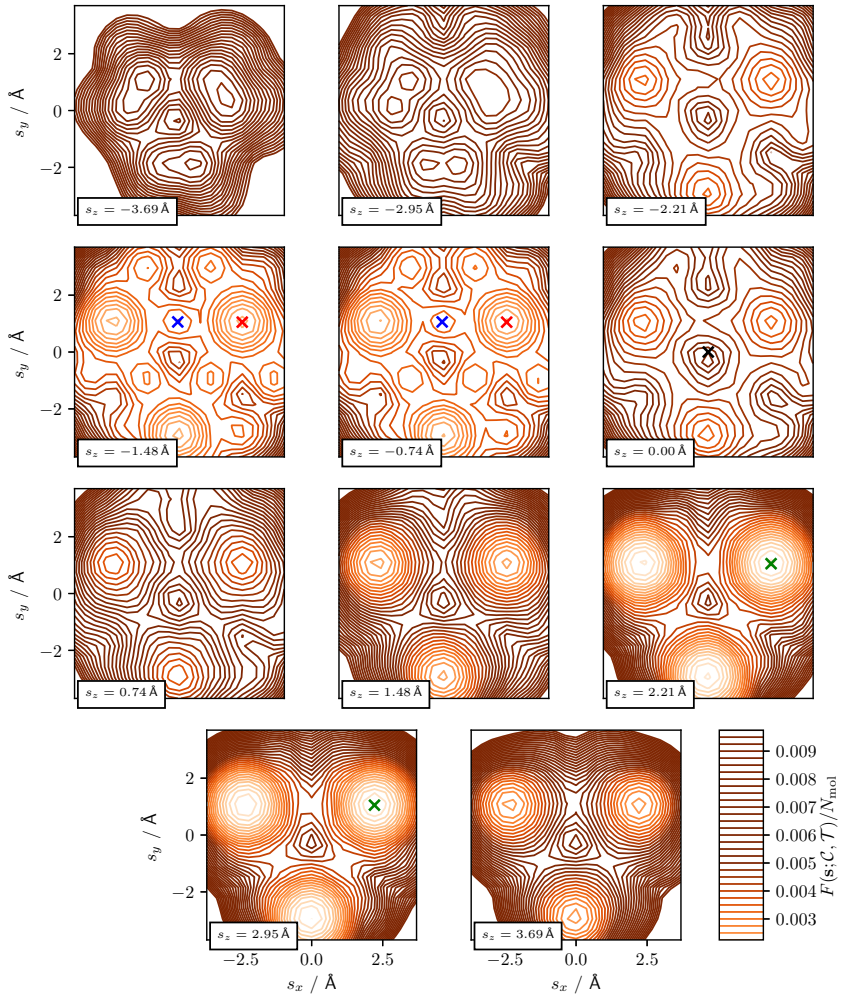

Figure D.5.: Example contour plot of summed mean-square deviation $F(\mathbf{s};\mathcal{C},\mathcal{T})$ as a function of the shift vector $\mathbf{s}$. The example shows the landscape used to align a configuration that containes 720 molecules that are arranged in a mostly pristine lattice except for a small number of defects. The black cross indicates the vector $\mathbf{s}$ at which the first optimization is started. The blue cross indicates the value of $\mathbf{s}$ after the first optimization ($s_z^{(1)} = -1.14$, in between the two levels shown), which corresponds to a shift of the template configuration relative to the optimal alignment along both the prism- and the c-axis. The red cross indicates another local minimum, which corresponds to an alignment where the crystal is shifted by exactly one layer in the z-direction (i.e. layers of type A are on top of type B layers). The green cross marks the value of $\mathbf{s}$ after the second optimization which finds the best alignment of the two configurations ($s_z^{(2)} = 2.56$).

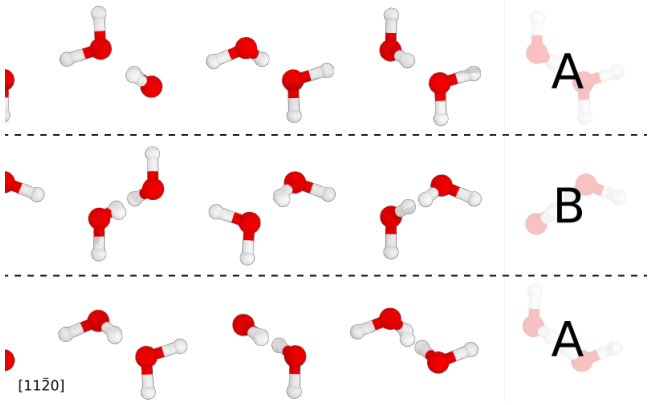

Figure D.6.: Ice Ih structure as seen facing the prism face. The structure is comprised of alternating layers A and B with respect to the position of the oxygen atoms. Protons are arranged in a random pattern that fulfills the ice rules.

The reason for this multi-step procedure becomes clear when we examine the landscape $F(\mathbf{s};\mathcal{C},\mathcal{T})$ shown in Fig. D.5 that consists of multiple local and global minima. Figure D.6 shows the alternating layers that an hexagonal ice crystal is comprised of. Depending on the initial shift of the template, an optimization of F can lead into the local minimums marked by green and red dots in Fig. D.5. These minima correspond to shifts where the template configuration is offset by exactly one layer width along the z-direction, i.e., such that the B-layers of the template is found on top of the A-layers of the configuration.

Fortunately, at the densities observed in the simulations presented here, there are no local minima if $\mathbf{s}$ is chosen such that the layers match. Hence, by performing multiple optimizations where $\mathbf{s}$ is shifted by one layer in the z-direction after the first optimisation, we find the correct alignment of the two configurations. Only in some cases the third optimization is required because the initial $\mathbf{s}$ of the first optimization finds a small local minimum. The optimizations are performed using the BFGS algorithm as implemented in the scipy python package[152].

Given the optimal alignment of $\mathcal{T}$ to $\mathcal{C}$ we can now assign each molecule in $\mathcal{C}$ to the site in $\mathcal{T}$ that is its nearest neighbor and count the number of times that each site in $\mathcal{T}$ is found as a nearest site. In a defect free crystal this count, $n_i^{\mathcal{T}}$, is equal to one for

each site. However, if there are interstitial-vacancy pairs in the system, some of the $n_i^{\mathcal{T}}$s are different from one. These sites are marked as template mismatches (TMM).

To avoid false positives that come about due to molecules translating only locally (e.g. to form a 5+7 defect), an additional step is performed where, if a site with an excess molecule and a site with a missing molecule are neighbors of each other (in the sense that they are H-bonded to each other in the template configuration), this pair of template mismatches is ignored.

The TMM that remain are marked as interstitials if $n_i^{\mathcal{T}} > 1$ and as vacancies if $n_i^{\mathcal{T}} < 1$.

D.2. Ideal gas closest distance distribution

In Fig. 6.16 (Sec. 6.4) we presented the histograms of the distances of the closest interstitial and the closest vacancy to the center of the liquid domain. It is important to note that even for a homogeneous distribution of defects (i.e. an ideal gas), the distribution of the closest defect is not uniform but instead has a maximum that is determined by the density of the gas and the volume of the simulation box [268].

Consider the probability of finding the atom closest to a given location at a distance that falls into the interval $[r, r + \mathrm{d}r]$ for an ideal gas. Because the atom positions are not correlated with each other in the ideal gas, this probability can be decomposed into three factors: the probability that a specific atom is found at a distance inside $[r, r + \mathrm{d}r]$ times the probability that none of the $N - 1$ other atoms are closer than $r + \mathrm{d}r$, times the number of particles that can be picked. With the total system volume V and the sphere volume $v(r) = 4\pi r^3/3$ the probability density p_{id} can be written as

$$\begin{aligned} p_{\mathrm{id}}(r)\,\mathrm{d}r &= \left(\frac{V - v(r)}{V}\right)^{N-1} \frac{4\pi r^2}{V} N\,\mathrm{d}r \\ &= 4\pi\rho r^2 \exp\left[(N-1)\log\left(1 - v(r)/V\right)\right]\mathrm{d}r. \end{aligned} \tag{D.2}$$

In the thermodynamic limit ($N \to \infty$, $V \to \infty$ such that $N/V = \rho = \text{const.}$) this can be approximated by

$$p_{\mathrm{id}}(r)\,\mathrm{d}r \approx 4\pi\rho r^2 \exp\left[-4\pi\rho r^3/3\right]. \tag{D.3}$$

To calculate the joint probability that the closest ideal gas-like interstitial is found at a distance in the interval $[r_{\mathrm{I}}, r_{\mathrm{I}} + \mathrm{d}r_{\mathrm{I}}]$ and the closest ideal-gas vacancy in the

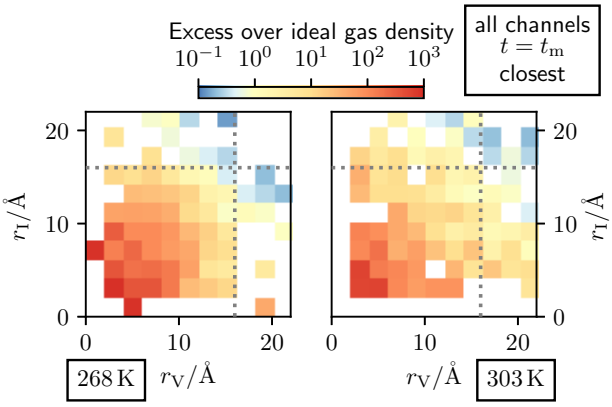

Figure D.7.: Analysis of the locations of I-V defects at the time of formation of a liquid nucleus, t_m, using the center of the nucleus volume as reference. Shown are the ratios between the observed joint probability of the closest vacancy and the closest interstitial, $P(r_V, r_I)$, to the expected density assuming the defects follow ideal gas statistics $P_{id}(r_V, r_I)$. $P(r_V, r_I)$ is shown in Fig. 6.16 in the main part.

interval $[r_V, r_V + dr_V]$ we multiply the two probabilities:

$$p_{id}(r_V, r_I)\, dr_V\, dr_I = p_V(r_V) p_I(r_I)\, dr_V\, dr_I \tag{D.4}$$

Integration over the size of a histogram bin, Δr, yields the probabilities

$$P(r_V, r_I) = \int_{r_V}^{r_V+\Delta r} \int_{r_I}^{r_I+\Delta r} dr_V\, dr_I\, p_V(r_V) p_I(r_I) \tag{D.5}$$

To compare this expected distribution to the ones obtained from melting trajectories we need to determine the average densities ρ_I and ρ_V at time t_m. To do so we count the total number of defects of type i observed in configurations at time t_m, n_i, and divide by the number number of trajectories n and the average volume of the simulation box V.

Figure D.7 shows the ratio between the observed probabilities, $P(r_V, r_I)$, and the ideal gas probabilities $P_{id}(r_V, r_I)$. There is a strong excess of configurations where interstitials and vacancies are close to the center of the liquid nucleus compared to what is expected in an ideal gas.

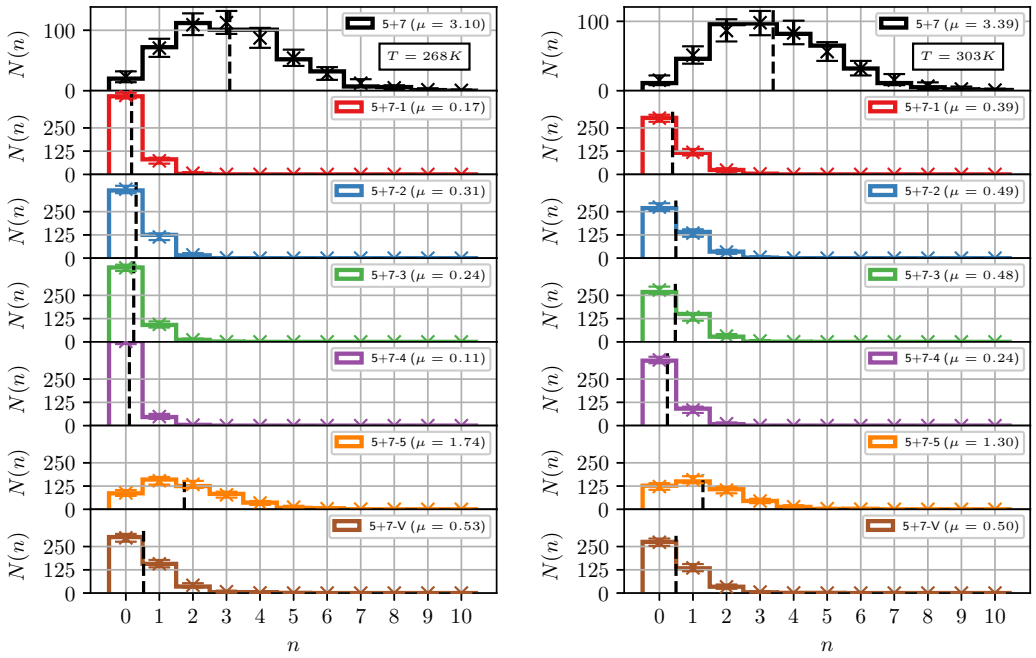

Figure D.8.: Statistics of the number of immobile defects of given types found at time $t_{\mathcal{A}}$ in freezing/melting trajectories that end in a spherical nucleuls at temperature $T = 268\,\mathrm{K}$ (left) and $T = 303\,\mathrm{K}$ (right). The histograms indicate the counts observed in trajectories and the vertical dashed line indicates the average defect count, μ. The crosses represent the expected counts based on a Poisson distribution with average count μ and the errorbars indicate the interval into which 95% of counts would fall based on this distribution.

D.3. Data supplement

Here we present a number of additional graphs that were not included in the main part for clarity.

- Figure D.8 shows the immobile defect counts found at time $t_{\mathcal{A}}$ in spherical-geometry trajectories obtained at 268 K and 303 K.
- Figure D.9 shows the defect densities of 5+7 defects around the site where a mobile defect forms for trajectories that pass through the E-channel. See Figs.

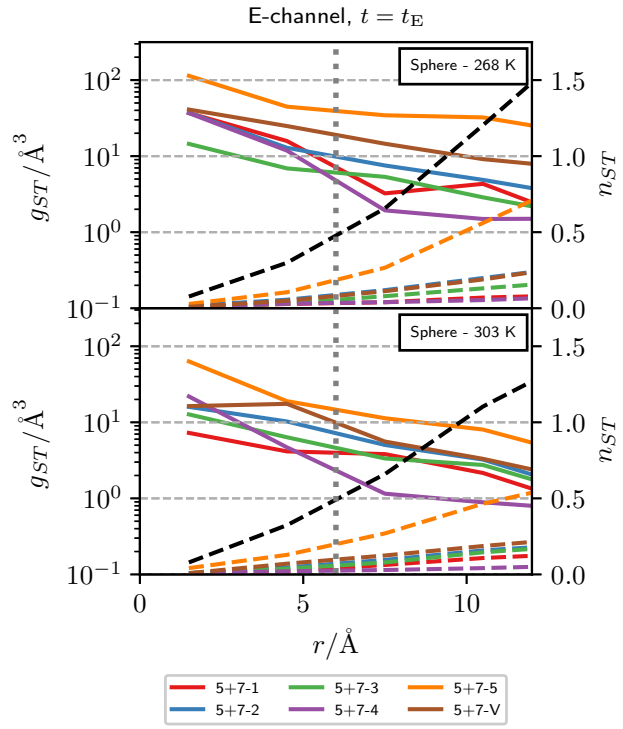

Figure D.9.: Analysis of the positions of the closest defect to the site where L-D or I-V defects form at time t_E in trajectories that pass through the E-channel. Shown are the pair-correlation functions g_{ST} (solid) and the average numbers of defects within a sphere of radius r, n_{ST} (dashed). Black lines are the sum over all defect types T. For clarity the densities are shown on a semi-logarithmic scale while n_{ST} is shown on a linear scale.

6.13 and 6.17 for the corresponding plots that include all trajectories.

- Figure D.10 shows the non-equlibrium pair correlation functions for I and V defects obtained in the timespan between t_E and t_m.
- Figure D.11 shows the one-dimensional contributions to the mean square displacements of I and V defects in the same time period but only when there is a single I-V pair present.

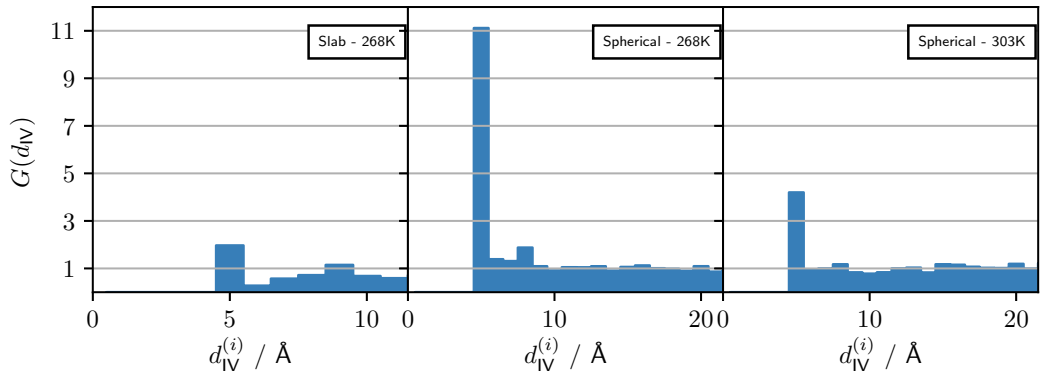

Figure D.10.: Pair correlation functions G between interstitial and vacancy defects found in melting trajectories between time t_E and t_m. Note that only configurations where a single defect pair is present are included in the analysis and that the trajectories in the underlying ensemble start at the creation of a defect pair. As a consequence, G is not an equilibrium property since finding defect pairs a short distance apart is guaranteed. The distribution has been normalized with the density $\rho = V^{-1}$, where V is the box volume resulting in an assumed number density of the defects of V^{-1}.

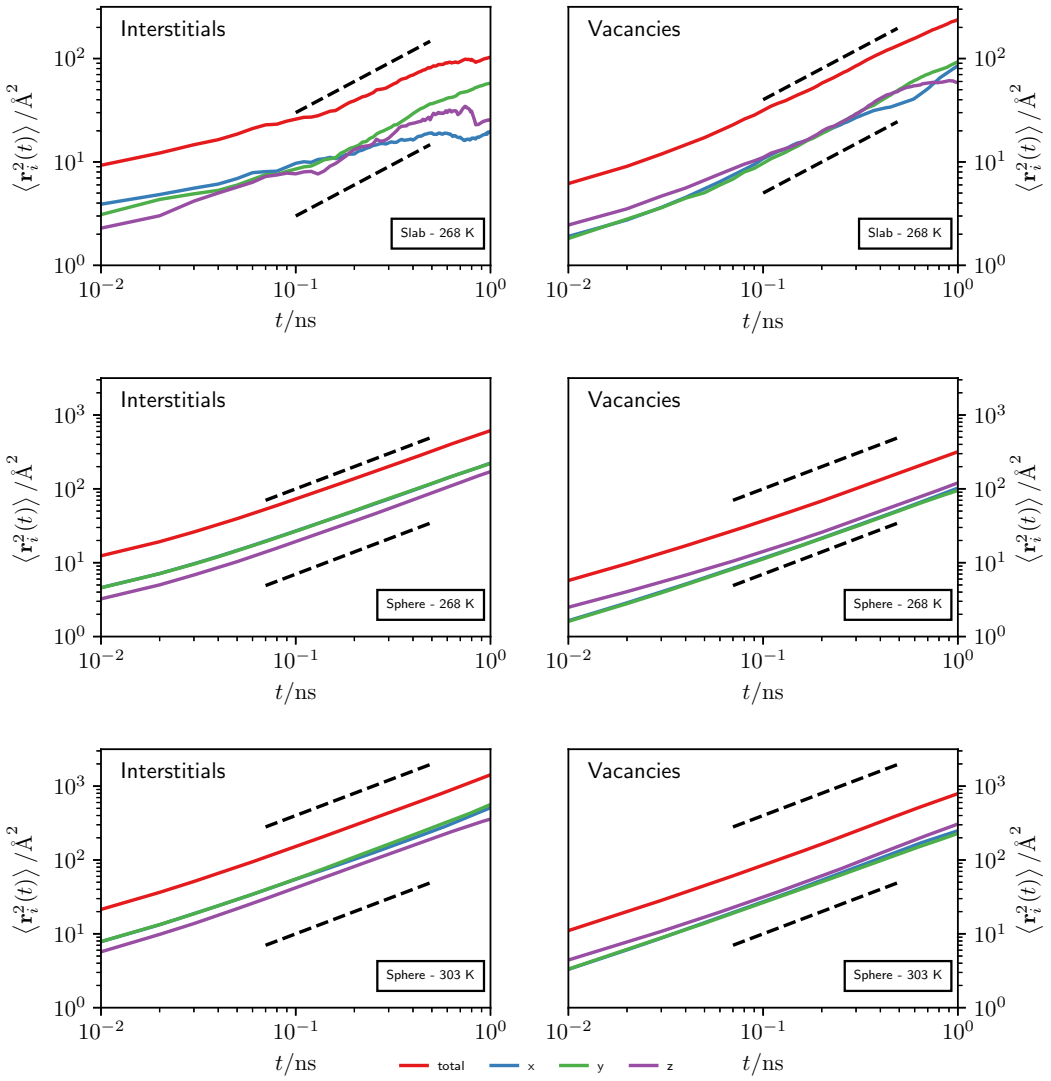

Figure D.11.: Mean square displacements calculated for interstitials and vacancies at different temperatures and for different cluster geometries. The x, y, and z component are shown separately. The dashed lines indicate diffusive behavior where $r^2(t) \sim t$.

E. Zusammenfassung

In dieser Dissertation untersuche ich die Mechanismen von Rare Events mit der Hilfe von Computersimulationen in verschiedenen physikalischen Systemen; von einfachen Modell-Systemen bis hin zu einer Untersuchung des Schmelzvorgangs von Eis auf der molekularen Ebene. Immer wieder begegnet uns bei diesen Untersuchungen eine ähnliche Feststellung: um den Mechanismus eines Rare Events vollständig zu verstehen, ist eine detaillierte Betrachtung der Dynamik des Systems unumgänglich.

Im ersten von drei Papern, die Teil dieser Arbeit sind, untersuchen wir den Disk-Slab Übergang im 2-dimensionalen Ising Modell. Beim Vergleich der freien Energielandschaft, die den Übergang beschreibt, mit den ebenfalls berechneten Committor Wahrscheinlichkeiten zeigt sich eine scheinbare Diskrepanz dieser beiden Größen. Im Zuge dieser Arbeit zeigen wir, dass dieser scheinbare Gegensatz aufgelöst werden kann, wenn wir den großen Unterschied in den Relaxationszeiten entlang der beiden kollektiven Variablen berücksichtigen, mit denen dieser Übergang beschrieben wird. Das Resultat ist ein diffusives Modell, das, basierend auf der freien Energielandschaft und gemessenen Diffusionskoeffizienten, die Committor Wahrscheinlichkeiten reproduzieren kann.

Im zweiten Paper befassen wir uns mit dieser Frage: wenn wir zwei parallele Oberflächen, deren Form fluktuieren darf, frei diffundieren lassen, wie nahe kommen sich dann die Schwerpunkte der Oberflächen, bevor sie sich das erste Mal berühren? Auch hier zeigt sich, dass dieser Kontaktabstand durch das Zusammenspiel von zwei Zeitskalen bestimmt wird: wie schnell diffundieren auf der einen Seite die Schwerpunkte der Oberflächen und wie schnell gehen Fluktuationen in der Form der Oberflächen vonstatten. Wir vereinfachen dieses Problem auf eine Differenzialgleichung, ähnlich einer Reaktions-Diffusionsgleichung, die es uns erlaubt, Verteilungen der Kontaktabstände zu berechnen. Anschließend wenden wir diese Theorie auf den Zerfall von plattenförmigen Clustern in molekularen Simulationen an.

Im dritten und letzten Paper dieser Dissertation untersuchen wir den molekularen Mechanismus des Schmelzens von Eis. Der Schmelzvorgang zeichnet sich durch eine

deutlich kompliziertere Landschaft an möglichen Zuständen aus, die am Schmelzvorgang beteiligt sein könnten, da zu jedem Zeitpunkt eine Vielzahl von unterschiedlichen Defekttypen existieren kann. Um die frühen Stadien von Schmelztrajektorien zu untersuchen, erzeugen wir mithilfe von Molekulardynamik Trajektorien, deren Endpunkte eine Blase mit flüssigem Wasser enthalten. Die Analyse dieser Trajektorien zeigt nicht nur die Zustände, die für den Schmelzvorgang wichtig sind, sondern auch die Reaktionspfade, die zum Schmelzen eines Eiskristalls führen können. Diese Arbeit zeichnet ein detailliertes Bild der unterschiedlichen, präkritischen Stadien des Schmelzvorganges, sowie der Defekttypen, die in ihnen eine wichtige Rolle spielen.

F. Abstract

In this dissertation, I study the mechanisms of rare events with the help of computer simulations for a number of different systems; from simple model systems to an investigation of the melting mechanism of ice on the molecular level. During these investigations, we find time and time again, that, in order to fully understand the mechanism of a rare event, a detailed investigation of the dynamics of a system is indispensable.

In the first of three papers that are part of this thesis, we study the disk-to-slab transition in the 2d-Ising model and find a free energy landscape that is seemingly at odds with committor probabilities that were also calculated. However, in this work, we show that the two quantities can be reconciled by taking into account the large difference in the relaxation timescales along two different order parameters that were used to describe the system. The result is a simplified diffusive model that, based on the free energy landscape and measured diffusion coefficients, is able to reproduce the committor probability.

In the second paper, we start out with the following question: if left to diffuse freely, how close will the centers of mass of two parallel, fluctuating interfaces approach each other before they come into contact due to the random fluctuations of their shape? Just like in the disk-to-slab transition, this contact distance depends on a balance of the timescales of two processes: how fast the interfaces are diffusing relative to each other vs. the time it takes the interfaces to change their shape. In this case, we capture this balance by analyzing a differential equation similar to a reaction-diffusion equation that allows us to calculate theoretical expressions for the contact-distance distribution. We then apply our findings to the decay of slabs in molecular simulations.

In the third and final paper, we investigate the microscopic mechanism of the melting of ice. Melting presents us with a considerably more complex landscape of possible states that could play a role in the melting mechanism due to the large number of different defect types that could be present in our system at any point in

time. In order to study the early stages of melting trajectories, we generate molecular-dynamics trajectories that end in a spherical liquid nucleus. A detailed analysis of these trajectories not only shows the states that are important for melting, but also the pathways that lead through these states toward the melting of an ice crystal. This work provides a detailed account of the different pre-critical stages of melting and the important defect types that play a role in each stage.

Bibliography

1. Fahrenheit, D. G. *Experimenta & Observationes de Congelatione Aquæ in Vacuo Factæ*. Philos. Trans. R. Soc. Lond. **33,** 78–84 (1724).
2. Fahrenheit, D. G., de Réaumur, R.-A. F. & Celsius, A. *Abhandlungen Über Thermometrie, von Fahrenheit, Réaumur, Celsius, (1724, 1730-1733, 1742)* (ed v. Oettingen, A.) (Wilhelm Engelmann / archive.org, Leipzig, 1894).
3. Kelton, K. & Greer, A. L. *Nucleation in condensed matter: applications in materials and biology* (Elsevier, Amsterdam, 2010).
4. Jungblut, S. & Dellago, C. *Pathways to self-organization: Crystallization via nucleation and growth*. Eur. Phys. J. E **39,** 77 (2016).
5. Butenko, Y. V., Kuznetsov, V. L., Chuvilin, A. L., Kolomiichuk, V. N., Stankus, S. V., Khairulin, R. A. & Segall, B. *Kinetics of the Graphitization of Dispersed Diamonds at "Low" Temperatures*. J. Appl. Phys. **88,** 4380–4388 (2000).
6. Marcus, R. A. *On the Theory of Oxidation-Reduction Reactions Involving Electron Transfer. I*. J. Chem. Phys. **24,** 966–978 (1956).
7. Dill, K. A. & MacCallum, J. L. *The Protein-Folding Problem, 50 Years On*. Science **338,** 1042–1046 (2012).
8. Thirumalai, D., O'Brien, E. P., Morrison, G. & Hyeon, C. *Theoretical Perspectives on Protein Folding*. Annu. Rev. Biophys. **39,** 159–183 (2010).
9. Kerner, B. S. & Konhäuser, P. *Structure and Parameters of Clusters in Traffic Flow*. Phys. Rev. E **50,** 54–83 (1994).
10. Helbing, D. *Traffic and Related Self-Driven Many-Particle Systems*. Rev. Mod. Phys. **73,** 1067–1141 (2001).
11. Gamow, G. *Zur Quantentheorie des Atomkernes*. Z. Für Phys. **51,** 204–212 (1928).

12. Gurney, R. W. & Condon, E. U. *Wave Mechanics and Radioactive Disintegration*. Nature **122,** 439–439 (1928).

13. Volmer, M. & Weber, A. *Keimbildung in übersättigten Gebilden*. Zeitschrift für Phys. Chemie **119U,** 277–301 (1926).

14. Becker, R. & Döring, W. *Kinetische Behandlung der Keimbildung in übersättigten Dämpfen*. Ann. Phys. **416,** 719–752 (1935).

15. Turnbull, D. & Fisher, J. C. *Rate of Nucleation in Condensed Systems*. J. Chem. Phys. **17,** 71–73 (1949).

16. Peters, B. *Reaction Rate Theory and Rare Events* (Elsevier, 2017).

17. Bustamante, C., Bustamante, C., Alexander, L., MacIuba, K. & Kaiser, C. M. *Single-Molecule Studies of Protein Folding with Optical Tweezers*. Annu. Rev. Biochem. **89,** 443–470 (2020).

18. Neupane, K., Foster, D. A. N., Dee, D. R., Yu, H., Wang, F. & Woodside, M. T. *Direct Observation of Transition Paths during the Folding of Proteins and Nucleic Acids*. Science **352,** 239–242 (2016).

19. Woodside, M. T. & Block, S. M. *Reconstructing Folding Energy Landscapes by Single-Molecule Force Spectroscopy*. Annu. Rev. Biophys. **43,** 19–39 (2014).

20. Woodside, M. T., Anthony, P. C., Behnke-parks, W. M., Larizadeh, K., Herschlag, D. & Block, S. M. *Landscape of a Nucleic Acid*. Science, 1001–1005 (2006).

21. Greenleaf, W. J., Woodside, M. T., Abbondanzieri, E. A. & Block, S. M. *Passive All-Optical Force Clamp for High-Resolution Laser Trapping*. Phys. Rev. Lett. **95,** 1–4 (2005).

22. Svoboda, K., Schmidt, C. F., Schnapp, B. J. & Block, S. M. *Direct Observation of Kinesin Stepping by Optical Trapping Interferometry*. Nature **365,** 721–727 (1993).

23. Chung, H. S. & Gopich, I. V. *Fast Single-Molecule FRET Spectroscopy: Theory and Experiment*. Phys. Chem. Chem. Phys. **16,** 18644–18657 (2014).

24. Chung, H. S. & Eaton, W. A. *Protein Folding Transition Path Times from Single Molecule FRET*. Current Opinion in Structural Biology **48,** 30–39 (2018).

25. Yau, S.-T. & Vekilov, P. G. *Direct Observation of Nucleus Structure and Nucleation Pathways in Apoferritin Crystallization*. J. Am. Chem. Soc. **123,** 1080–1089 (2001).

26. Schubert, R., Meyer, A., Baitan, D., Dierks, K., Perbandt, M. & Betzel, C. *Real-Time Observation of Protein Dense Liquid Cluster Evolution during Nucleation in Protein Crystallization*. Crystal Growth & Design **17,** 954–958 (2017).

27. Schreiber, R. E., Houben, L., Wolf, S. G., Leitus, G., Lang, Z.-L., Carbó, J. J., Poblet, J. M. & Neumann, R. *Real-Time Molecular Scale Observation of Crystal Formation*. Nature Chem **9,** 369–373 (2017).

28. Cao, K. *et al. Atomic Mechanism of Metal Crystal Nucleus Formation in a Single-Walled Carbon Nanotube*. Nat. Chem. **12,** 921–928 (2020).

29. Li, Y., Bunes, B. R., Zang, L., Zhao, J., Li, Y., Zhu, Y. & Wang, C. *Atomic Scale Imaging of Nucleation and Growth Trajectories of an Interfacial Bismuth Nanodroplet*. ACS Nano **10,** 2386–2391 (2016).

30. Espinosa, J. R., Sanz, E., Valeriani, C. & Vega, C. *Homogeneous ice nucleation evaluated for several water models*. J. Chem. Phys. **141,** 18C529 (2014).

31. Espinosa, J. R., Navarro, C., Sanz, E., Valeriani, C. & Vega, C. *On the time required to freeze water*. J. Chem. Phys. **145,** 211922 (2016).

32. Chandler, D. *Introduction to modern statistical mechanics* (Oxford Univ. Press., 1987).

33. Peters, B. *Common features of extraordinary rate theories*. J. Phys. Chem. B **119,** 6349–6356 (2015).

34. Kramers, H. *Brownian motion in a field of force and the diffusion model of chemical reactions*. Physica **7,** 284–304 (1940).

35. Grote, R. F. & Hynes, J. T. *Energy Diffusion-Controlled Reactions in Solution*. J. Chem. Phys. **77,** 3736–3743 (1982).

36. Berne, B. J. & Borkovec, M. *Classical Theories of Reaction Dynamics: Transition State Theory, Spatial Diffusion Controlled Reactions, and the Energy Diffusion Limit*. Faraday Trans. **94,** 2717–2723 (1998).

37. Laio, A. & Gervasio, F. L. *Metadynamics: A Method to Simulate Rare Events and Reconstruct the Free Energy in Biophysics, Chemistry and Material Science*. Rep. Prog. Phys. **71,** 126601 (2008).

38. Shaw, D. E. *et al. Anton 3: Twenty Microseconds of Molecular Dynamics Simulation before Lunch*. Int. Conf. High Perform. Comput. Netw. Storage Anal. SC (2021).

39. Hänggi, P., Talkner, P. & Borkovec, M. *Reaction-rate theory: fifty years after Kramers*. Rev. Mod. Phys. **62,** 251–341 (1990).

40. Eastman, P. *et al. OpenMM 7: Rapid Development of High Performance Algorithms for Molecular Dynamics*. PLOS Comput. Biol. **13** (ed Gentleman, R.) e1005659 (2017).

41. Eastman, P. *et al. OpenMM 4: A Reusable, Extensible, Hardware Independent Library for High Performance Molecular Simulation*. J. Chem. Theory Comput. **9,** 461–469 (2013).

42. Friedrichs, M. S., Eastman, P., Vaidyanathan, V., Houston, M., Legrand, S., Beberg, A. L., Ensign, D. L., Bruns, C. M. & Pande, V. S. *Accelerating Molecular Dynamic Simulation on Graphics Processing Units*. J. Comput. Chem. **30,** 864–872 (2009).

43. Eastman, P. & Pande, V. S. *Efficient Nonbonded Interactions for Molecular Dynamics on a Graphics Processing Unit*. J. Comput. Chem. **32,** NA–NA (2009).

44. Eastman, P. & Pande, V. S. *Constant Constraint Matrix Approximation: A Robust, Parallelizable Constraint Method for Molecular Simulations*. J. Chem. Theory Comput. **6,** 434–437 (2010).

45. Eastman, P. & Pande, V. *OpenMM: A Hardware-Independent Framework for Molecular Simulations*. Comput. Sci. Eng. **12,** 34–39 (2010).

46. Dodda, L. S., Vilseck, J. Z., Tirado-Rives, J. & Jorgensen, W. L. *1.14$_*$CM1A-LBCC: Localized Bond-Charge Corrected CM1A Charges for Condensed-Phase Simulations*. J. Phys. Chem. B **121,** 3864–3870 (2017).

47. Dodda, L. S., De Vaca, I. C., Tirado-Rives, J. & Jorgensen, W. L. *LigParGen Web Server: An Automatic OPLS-AA Parameter Generator for Organic Ligands*. Nucleic Acids Res. **45,** W331–W336 (2017).

48. Jorgensen, W. L. & Tirado-Rives, J. *Potential Energy Functions for Atomic-Level Simulations of Water and Organic and Biomolecular Systems*. Proc. Natl. Acad. Sci. U. S. A. **102,** 6665–6670 (2005).

49. Peters, B. *Reaction Coordinates and Mechanistic Hypothesis Tests*. Annu. Rev. Phys. Chem. **67,** annurev–physchem–040215–112215 (2016).

50. Frenkel, D. & Smit, B. *Understanding molecular simulation: from algorithms to applications* (Elsevier, Singapore, 2009).

51. Maragliano, L., Fischer, A., Vanden-Eijnden, E. & Ciccotti, G. *String method in collective variables: minimum free energy paths and isocommittor surfaces.* J. Chem. Phys. **125,** 24106 (2006).

52. Frenkel, D. *Simulations: The dark side*. Eur. Phys. J. Plus **128,** 10 (2013).

53. Metzner, P., Schütte, C. & Vanden-Eijnden, E. *Illustration of transition path theory on a collection of simple examples.* J. Chem. Phys. **125,** 084110 (2006).

54. Gardiner, C. W. *et al. Handbook of stochastic methods* (Springer Berlin, 1985).

55. E, W. & Vanden-Eijnden, E. *Transition-path theory and path-finding algorithms for the study of rare events.* Annu. Rev. Phys. Chem. **61,** 391–420 (2010).

56. Dellago, C., Bolhuis, P. G. & Chandler, D. *On the calculation of reaction rate constants in the transition path ensemble*. J. Chem. Phys. **110,** 6617 (1999).

57. Dellago, C., Bolhuis, P. G. & Chandler, D. *Efficient transition path sampling: Application to Lennard-Jones cluster rearrangements*. J. Chem. Phys. **108,** 9236 (1998).

58. Dellago, C., Bolhuis, P. G., Csajka, F. S. & Chandler, D. *Transition path sampling and the calculation of rate constants*. J. Chem. Phys. **108,** 1964 (1998).

59. Mullen, R. G., Shea, J.-E. & Peters, B. *Easy Transition Path Sampling Methods: Flexible-Length Aimless Shooting and Permutation Shooting*. J. Chem. Theory Comput. **11,** 2421–2428 (2015).

60. Swenson, D. W. H., Prinz, J.-H., Noe, F., Chodera, J. D. & Bolhuis, P. G. *OpenPathSampling: A Python Framework for Path Sampling Simulations. 1. Basics*. J. Chem. Theory Comput. **15,** 813–836 (2019).

61. Swenson, D. W. H., Prinz, J.-H., Noe, F., Chodera, J. D. & Bolhuis, P. G. *OpenPathSampling: A Python Framework for Path Sampling Simulations. 2. Building and Customizing Path Ensembles and Sample Schemes*. J. Chem. Theory Comput. **15,** 837–856 (2019).

62. Hummer, G. *From transition paths to transition states and rate coefficients.* J. Chem. Phys. **120,** 516–23 (2004).

63. Peters, B. & Trout, B. L. *Obtaining reaction coordinates by likelihood maximization.* J. Chem. Phys. **125,** 054108 (2006).

64. Bolhuis, P. G. *Transition Path Sampling on Diffusive Barriers*. J. Phys. Condens. Matter **15** (2003).

65. Klosek, M. M., Matkowsky, B. J. & Schuss, Z. *The Kramers Problem in the Turnover Regime: The Role of the Stochastic Separatrix*. Berichte Bunsenges. Für Phys. Chem. **95,** 331–337 (1991).

66. Du, R., Pande, V. S., Grosberg, A. Y., Tanaka, T. & Shakhnovich, E. S. *On the Transition Coordinate for Protein Folding*. J. Chem. Phys. **108,** 334–350 (1998).

67. Geissler, P. L., Dellago, C. & Chandler, D. *Kinetic Pathways of Ion Pair Dissociation in Water*. J. Phys. Chem. B **103,** 3706–3710 (1999).

68. Bolhuis, P. G., Dellago, C. & Chandler, D. *Reaction Coordinates of Biomolecular Isomerization*. Proc. Natl. Acad. Sci. U. S. A. **97,** 5877–5882 (2000).

69. Ma, A. & Dinner, A. R. *Automatic method for identifying reaction coordinates in complex systems.* J. Phys. Chem. B **109,** 6769–79 (2005).

70. Berezhkovskii, A. M. & Szabo, A. *One-dimensional reaction coordinates for diffusive activated rate processes in many dimensions.* J. Chem. Phys. **122,** 14503 (2005).

71. Peters, B. *Reaction Coordinates and Mechanistic Hypothesis Tests*. Annu. Rev. Phys. Chem. **67,** 669–690 (2016).

72. Peters, B. *Using the histogram test to quantify reaction coordinate error.* J. Chem. Phys. **125,** 241101 (2006).

73. Wigner, E. *The transition state method.* Trans. Faraday Soc. **34,** 29–41 (1938).

74. Stukowski, A. *Visualization and Analysis of Atomistic Simulation Data with OVITO–the Open Visualization Tool*. Modelling Simul. Mater. Sci. Eng. **18,** 015012 (2009).

75. Allen, M. P. & Tildesley, D. J. *Computer Simulation of Liquids* (Oxford university press, 1991).

76. Ewald, P. P. *Die Berechnung optischer und elektrostatischer Gitterpotentiale*. Ann. Phys. **369,** 253–287 (1921).

77. Tröster, A., Schmitz, F., Virnau, P. & Binder, K. *Equilibrium between a Droplet and Surrounding Vapor: A Discussion of Finite Size Effects*. J. Phys. Chem. B **122,** 3407–3417 (2018).

78. Vögele, M. & Hummer, G. *Divergent Diffusion Coefficients in Simulations of Fluids and Lipid Membranes*. J. Phys. Chem. B **120,** 8722–8732 (2016).

79. Binder, K. *Theory of first-order phase transitions*. Reports Prog. Phys. **50,** 783–859 (1987).

80. Leung, K. & Zia, R. K. P. *Geometrically induced transitions between equilibrium crystal shapes*. J. Phys. A. Math. Gen. **23,** 4593–4602 (1990).

81. Neuhaus, T. & Hager, J. S. *Exponential Slowing Down in Simulations of First-Order Phase Transitions*. J. Stat. Phys. **113,** 47–83 (2003).

82. Debenedetti, P. G. *Metastable liquids: concepts and principles* (Princeton University Press, Princeton, New Jersey, 1996).

83. Tröster, A., Dellago, C. & Schranz, W. *Free energies of the phi4 model from Wang-Landau simulations*. Phys. Rev. B **72,** 094103 (2005).

84. Binder, K., Block, B. J., Virnau, P. & Tröster, A. *Beyond the Van Der Waals loop: What can be learned from simulating Lennard-Jones fluids inside the region of phase coexistence*. Am. J. Phys. **80,** 1099–1109 (2012).

85. Venturoli, M., Vanden-Eijnden, E. & Ciccotti, G. *Kinetics of phase transitions in two dimensional Ising models studied with the string method*. J. Math. Chem. **45,** 188–222 (2009).

86. Ferrenberg, A. & Swendsen, R. *Optimized Monte Carlo data analysis*. Phys. Rev. Lett. **63,** 1195–1198 (1989).

87. Kumar, S., Rosenberg, J. M., Bouzida, D., Swendsen, R. H. & Kollman, P. A. *The weighted histogram analysis method for free-energy calculations on biomolecules. I. The method*. J. Comput. Chem. **13,** 1011–1021 (1992).

88. Grossfield, A. *WHAM: the weighted histogram analysis method* 2013.

89. Edwards, S. F. & Wilkinson, D. R. *The Surface Statistics of a Granular Aggregate*. Proc. R. Soc. A Math. Phys. Eng. Sci. **381,** 17–31 (1982).

90. Rácz, Z. & Plischke, M. *Width distribution for (2+1)-dimensional growth and deposition processes*. Phys. Rev. E **50,** 3530–3537 (1994).

91. Barabási, A.-L. & Stanley, H. E. *Fractal concepts in surface growth* (Cambridge university press, 1995).

92. Antal, T. & Rácz, Z. *Dynamic scaling of the width distribution in Edwards-Wilkinson type models of interface dynamics*. Phys. Rev. E - Stat. Physics, Plasmas, Fluids, Relat. Interdiscip. Top. **54,** 2256–2260 (1996).

93. Pal, S. & Landau, D. *The Edwards–Wilkinson model revisited: large-scale simulations of dynamic scaling in 2+1 dimensions*. Phys. A Stat. Mech. its Appl. **267,** 406–413 (1999).

94. Györgyi, G., Holdsworth, P. C. W., Portelli, B. & Rácz, Z. *Statistics of extremal intensities for Gaussian interfaces*. Phys. Rev. E **68,** 056116 (2003).

95. Majumdar, S. N. & Comtet, A. *Airy Distribution Function: From the Area Under a Brownian Excursion to the Maximal Height of Fluctuating Interfaces*. J. Stat. Phys. **119,** 777–826 (2005).

96. Lee, D.-S. *Distribution of Extremes in the Fluctuations of Two-Dimensional Equilibrium Interfaces*. Phys. Rev. Lett. **95,** 150601 (2005).

97. Oliveira, T. J. & Aarão Reis, F. D. A. *Maximal- and minimal-height distributions of fluctuating interfaces*. Phys. Rev. E **77,** 041605 (2008).

98. Carrasco, I. S. & Oliveira, T. J. *Width and extremal height distributions of fluctuating interfaces with window boundary conditions*. Phys. Rev. E **93,** 1–10 (2016).

99. Gross, M. *First-passage dynamics of linear stochastic interface models: weak-noise theory and influence of boundary conditions*. J. Stat. Mech. Theory Exp. **2018,** 033213 (2018).

100. Gross, M. *First-passage dynamics of linear stochastic interface models: numerical simulations and entropic repulsion effect*. J. Stat. Mech. Theory Exp. **2018,** 033212 (2018).

101. Bjerrum, N. *Structure and Properties of Ice*. Science (80-.). **115,** 385–390 (1952).

102. Petrenko, V. F. & Whitworth, R. W. *Physics of ice* (OUP Oxford, New York, 1999).

103. Tanaka, H. & Mohanty, U. *On the Debye-Waller factor of hexagonal ice: A computer simulation study*. J. Am. Chem. Soc. **124,** 8085–8089 (2002).

104. Grishina, N. & Buch, V. *Structure and dynamics of orientational defects in ice I*. J. Chem. Phys. **120,** 5217–5225 (2004).

105. Donadio, D., Raiteri, P. & Parrinello, M. *Topological Defects and Bulk Melting of Hexagonal Ice*. J. Phys. Chem. B **109** (ed Intergovernmental Panel on Climate Change) 5421–5424 (2005).

106. Mochizuki, K., Matsumoto, M. & Ohmine, I. *Defect pair separation as the controlling step in homogeneous ice melting.* Nature **498,** 350–354 (2013).

107. Bai, X. M. & Li, M. *Test of classical nucleation theory via molecular-dynamics simulation*. J. Chem. Phys. **122,** 1–4 (2005).

108. Bai, X.-M. & Li, M. *Calculation of solid-liquid interfacial free energy: A classical nucleation theory based approach*. J. Chem. Phys. **124,** 124707 (2006).

109. Espinosa, J. R., Vega, C., Valeriani, C. & Sanz, E. *Seeding approach to crystal nucleation*. J. Chem. Phys. **144,** 034501 (2016).

110. Chahine, J., Oliveira, R. J., Leite, V. B. P. & Wang, J. *Configuration-dependent diffusion can shift the kinetic transition state and barrier height of protein folding*. Proc. Natl. Acad. Sci. **104,** 14646–14651 (2007).

111. Krivov, S. V. & Karplus, M. *Diffusive reaction dynamics on invariant free energy profiles.* Proc. Natl. Acad. Sci. U. S. A. **105,** 13841–6 (2008).

112. Hinczewski, M., von Hansen, Y., Dzubiella, J. & Netz, R. R. *How the diffusivity profile reduces the arbitrariness of protein folding free energies*. J. Chem. Phys. **132,** 245103 (2010).

113. Best, R. B. & Hummer, G. *Coordinate-dependent diffusion in protein folding.* Proc. Natl. Acad. Sci. U. S. A. **107,** 1088–93 (2010).

114. Best, R. B. & Hummer, G. *Diffusion models of protein folding*. Phys. Chem. Chem. Phys. **13,** 16902–16911 (2011).

115. Trinkaus, H. *Theory of the nucleation of multicomponent precipitates*. Phys. Rev. B **27,** 7372–7378 (1983).

116. Peters, B. *Competing nucleation pathways in a mixture of oppositely charged colloids: out-of-equilibrium nucleation revisited.* J. Chem. Phys. **131,** 244103 (2009).

117. Northrup, S. H. & McCammon, J. A. *Saddle-point avoidance in diffusional reactions*. J. Chem. Phys. **78,** 987–989 (1983).

118. Moro, G. J. & Cardin, F. *Saddle point avoidance due to inhomogeneous friction*. Chem. Phys. **235,** 189–200 (1998).

119. Yang, S., Onuchic, J. N., García, A. E. & Levine, H. *Folding Time Predictions from All-atom Replica Exchange Simulations*. J. Mol. Biol. **372,** 756–763 (2007).

120. Weinan, E. & Vanden-Eijnden, E. *Towards a Theory of Transition Paths*. J. Stat. Phys. **123,** 503–523 (2006).

121. E, W., Ren, W. & Vanden-Eijnden, E. *Transition pathways in complex systems: Reaction coordinates, isocommittor surfaces, and transition tubes*. Chem. Phys. Lett. **413,** 242–247 (2005).

122. Singh, C., Jackson, A. M., Stellacci, F. & Glotzer, S. C. *Exploiting substrate stress to modify nanoscale SAM patterns*. J. Am. Chem. Soc. **131,** 16377–16379 (2009).

123. Singh, C., Hu, Y., Khanal, B. P., Zubarev, E. R., Stellacci, F. & Glotzer, S. C. *Striped nanowires and nanorods from mixed SAMS*. Nanoscale **3,** 3244–3250 (2011).

124. Santos, A., Singh, C. & Glotzer, S. C. *Coarse-grained models of tethers for fast self-assembly simulations*. Phys. Rev. E **81,** 011113 (2010).

125. Kumar, V., Sridhar, S. & Errington, J. R. *Monte Carlo simulation strategies for computing the wetting properties of fluids at geometrically rough surfaces*. J. Chem. Phys. **135,** 184702 (2011).

126. Prestipino, S., Caccamo, C., Costa, D., Malescio, G. & Munaò, G. *Shapes of a liquid droplet in a periodic box*. Phys. Rev. E **92,** 022141 (2015).

127. Lum, K. & Chandler, D. *Phase diagram and free energies of vapor films and tubes for a confined fluid.* Int. J. Thermophys. **19,** 845–855 (1998).

128. Nicolaides, D. & Evans, R. *Monte Carlo study of phase transitions in a confined lattice gas*. Phys. Rev. B **39,** 9336–9342 (1989).

129. Evans, R. *Fluids adsorbed in narrow pores: Phase equilibria and structure*. J. Phys. Condens. Matter **2,** 8989–9007 (1999).

130. Bolhuis, P. G. & Chandler, D. *Transition path sampling of cavitation between molecular scale solvophobic surfaces*. J. Chem. Phys. **113,** 8154–8160 (2000).

131. Leung, K. & Luzar, A. *Dynamics of capillary evaporation. II. Free energy barriers*. J. Chem. Phys. **113,** 5845 (2000).

132. Luzar, A. & Leung, K. *Dynamics of capillary evaporation. I. Effect of morphology of hydrophobic surfaces*. J. Chem. Phys. **113,** 5836–5844 (2000).

133. Vishnyakov, A. & Neimark, A. V. *Nucleation of liquid bridges and bubbles in nanoscale capillaries*. J. Chem. Phys. **119,** 9755–9764 (2003).

134. Remsing, R. C., Xi, E., Vembanur, S., Sharma, S., Debenedetti, P. G., Garde, S. & Patel, A. J. *Pathways to dewetting in hydrophobic confinement.* Proc. Natl. Acad. Sci. U. S. A. **112,** 8181–8186 (2015).

135. Plateau, J. *Statique des liquides soumis aux seuls forces moléculaires (tome second)* (Gauthiers-Villars, Paris, 1873).

136. Rayleigh, L. *On The Instability Of Jets*. Proc. London Math. Soc. **s1-10,** 4–13 (1878).

137. Safran, S. A. *Statistical thermodynamics of surfaces, interfaces, and membranes* (Westview Press, 2003).

138. Tröster, A. & Binder, K. *Positive Tolman Length in a Lattice Gas with Three-Body Interactions*. Phys. Rev. Lett. **107,** 265701 (2011).

139. Tröster, A., Oettel, M., Block, B., Virnau, P. & Binder, K. *Numerical approaches to determine the interface tension of curved interfaces from free energy calculations.* en. J. Chem. Phys. **136,** 064709 (2012).

140. Trebst, S., Huse, D. A. & Troyer, M. *Optimizing the ensemble for equilibration in broad-histogram Monte Carlo simulations*. Phys. Rev. E **70,** 046701 (2004).

141. Kawasaki, K. *Diffusion Constants near the Critical Point for Time-Dependent Ising Models. I*. Phys. Rev. **145,** 224–230 (1966).

142. Schmitz, F., Virnau, P. & Binder, K. *Monte Carlo tests of nucleation concepts in the lattice gas model*. Phys. Rev. E **87,** 053302 (2013).

143. Binder, K. & Virnau, P. *Overview: Understanding nucleation phenomena from simulations of lattice gas models*. J. Chem. Phys. **145,** 211701 (2016).

144. Geissler, P. L., Dellago, C. & Chandler, D. *Chemical dynamics of the protonated water trimer analyzed by transition path sampling*. Phys. Chem. Chem. Phys. **1,** 1317–1322 (1999).

145. Dellago, C., Bolhuis, P. G. & Geissler, P. L. in *Adv. Chem. Phys.* 1–78 (John Wiley & Sons, Inc., Hoboken, NJ, USA, 2002).

146. Risken, H. *The Fokker-Planck Equation: Methods of Solution and Applications* (Springer, Berlin, Heidelberg, 1984).

147. Im, W. & Roux, B. *Ions and counterions in a biological channel: a molecular dynamics simulation of OmpF porin from Escherichia coli in an explicit membrane with 1 M KCl aqueous salt solution.* J. Mol. Biol. **319,** 1177–97 (2002).

148. Pan, A. C., Sezer, D. & Roux, B. *Finding transition pathways using the string method with swarms of trajectories.* J. Phys. Chem. B **112,** 3432–40 (2008).

149. Hummer, G. *Position-dependent diffusion coefficients and free energies from Bayesian analysis of equilibrium and replica molecular dynamics simulations*. New J. Phys. **7,** 34–34 (2005).

150. Bicout, D. J. & Szabo, A. *Electron transfer reaction dynamics in non-Debye solvents*. J. Chem. Phys. **109,** 2325–2338 (1998).

151. Al-Mohy, A. H. & Higham, N. J. *A New Scaling and Squaring Algorithm for the Matrix Exponential*. SIAM J. Matrix Anal. Appl. **31,** 970–989 (2010).

152. Jones, E., Oliphant, T., Peterson, P., *et al. SciPy: Open source scientific tools for Python*

153. Schulten, K., Schulten, Z. & Szabo, A. *Dynamics of reactions involving diffusive barrier crossing*. J. Chem. Phys. **74,** 4426–4432 (1981).

154. Tupper, P. F. & Yang, X. *A paradox of state-dependent diffusion and how to resolve it*. Proc. R. Soc. A Math. Phys. Eng. Sci. **468,** 3864–3881 (2012).

155. Craster, R. V. & Matar, O. K. *Dynamics and stability of thin liquid films*. Rev. Mod. Phys. **81,** 1131–1198 (2009).

156. Vrij, A. & Overbeek, J. T. *Rupture of thin liquid films due to spontaneous fluctuations in thickness*. J. Am. Chem. Soc. **90,** 3074–3078 (1968).

157. Vrij, A. *Free Liquid Films*. Discuss. Faraday Soc. **42,** 23–33 (1966).

158. Eggers, J. & Villermaux, E. *Physics of liquid jets*. Reports Prog. Phys. **71,** 036601 (2008).

159. Hennequin, Y., Aarts, D. G. A. L., van der Wiel, J. H., Wegdam, G., Eggers, J., Lekkerkerker, H. N. W. & Bonn, D. *Drop Formation by Thermal Fluctuations at an Ultralow Surface Tension*. Phys. Rev. Lett. **97,** 244502 (2006).

160. Eggers, J. *Dynamics of Liquid Nanojets*. Phys. Rev. Lett. **89,** 084502 (2002).

161. Moseler, M. & Landman, U. *Formation, Stability, and Breakup of Nanojets*. Science (80-.). **289,** 1165–1169 (2000).

162. Shi, X. D., Brenner, M. P. & Nagel, S. R. *A Cascade of Structure in a Drop Falling from a Faucet*. Science (80-.). **265,** 219–222 (1994).

163. Perumanath, S., Borg, M. K., Chubynsky, M. V., Sprittles, J. E. & Reese, J. M. *Droplet Coalescence is Initiated by Thermal Motion*. Phys. Rev. Lett. **122,** 104501 (2019).

164. Aarts, D. G. A. L., Lekkerkerker, H. N. W., Guo, H., Wegdam, G. H. & Bonn, D. *Hydrodynamics of Droplet Coalescence*. Phys. Rev. Lett. **95,** 164503 (2005).

165. Aarts, D. G. A. L., Schmidt, M. & Lekkerkerker, H. N. W. *Direct Visual Observation of Thermal Capillary Waves*. Science (80-.). **304,** 847–850 (2004).

166. Eggers, J., Lister, J. R. & Stone, H. A. *Coalescence of liquid drops*. J. Fluid Mech. **401,** 293–310 (1999).

167. Bradley, S. G. & Stow, C. D. *Collisions between Liquid Drops*. Philos. Trans. R. Soc. A Math. Phys. Eng. Sci. **287,** 635–675 (1978).

168. Stone, J. *An Efficient Library for Parallel Ray Tracing and Animation*. MA thesis (Computer Science Department, University of Missouri-Rolla, 1998).

169. Humphrey, W., Dalke, A. & Schulten, K. *VMD – Visual Molecular Dynamics*. J. Mol. Graph. **14,** 33–38 (1996).

170. Ponthus, N., Scheibert, J., Thøgersen, K., Malthe-Sørenssen, A. & Perret-Liaudet, J. *Statistics of the separation between sliding rigid rough surfaces: Simulations and extreme value theory approach*. Phys. Rev. E **99,** 023004 (2019).

171. Moritz, C., Tröster, A. & Dellago, C. *Interplay of fast and slow dynamics in rare transition pathways: The disk-to-slab transition in the 2d Ising model*. J. Chem. Phys. **147,** 152714 (2017).

172. Dietrich, S., Nightingale, M. P. & Schick, M. *Applicability of mean-field theory to wetting in binary-liquid mixtures*. Phys. Rev. B **32,** 3182–3185 (1985).

173. Hunter, J. D. *Matplotlib: A 2D graphics environment*. Comput. Sci. Eng. **9,** 90–95 (2007).

174. *Solids far from equilibrium* (ed Godrèche, C.) (Cambridge Univ. Press, Cambridge, 1991).

175. Wilemski, G. & Fixman, M. *General theory of diffusion-controlled reactions*. J. Chem. Phys. **58,** 4009–4019 (1973).

176. Mattis, D. C. & Glasser, M. L. *The uses of quantum field theory in diffusion-limited reactions*. Rev. Mod. Phys. **70,** 979–1001 (1998).

177. Prüstel, T. & Meier-Schellersheim, M. *Unified path integral approach to theories of diffusion-influenced reactions*. Phys. Rev. E **96,** 022151 (2017).

178. Wiegel, F. W. *Introduction to Path-integral Methods in Physics and Polymer Science* (World Scientific, 1986).

179. Parisi, G. *Statistical field theory* (ed Pines, D.) (Addison-Wesley, 1988).

180. Kleinert, H. *Path integrals in quantum mechanics, statistics, polymer physics, and financial markets* 4th ed. (World scientific, New Jersey, 2006).

181. Kac, M. *On distributions of certain Wiener functionals*. Trans. Am. Math. Soc. **65,** 1–1 (1949).

182. Bastianelli, F., Corradini, O. & Pisani, P. A. *Worldline approach to quantum field theories on flat manifolds with boundaries*. J. High Energy Phys. **2007** (2007).

183. Chaichian, M. & Demichev, A. *Path integrals in physics: Volume I stochastic processes and quantum mechanics* (IOP Publishing, 2001).

184. Mathews, J. *Mathematical methods of physics* 2. ed.. (Benjamin, New York, NY, 1970).

185. Kampen, N. V. *A soluble model for diffusion in a bistable potential.* J. Stat. Phys. **17,** 71–88 (1977).

186. Caroli, B., Caroli, C. & Roulet, B. *Diffusion in a bistable potential: The functional integral approach*. J. Stat. Phys. **26,** 83–111 (1981).

187. Autieri, E., Faccioli, P., Sega, M., Pederiva, F. & Orland, H. *Dominant reaction pathways in high-dimensional systems*. J. Chem. Phys. **130,** 064106 (2009).

188. Kardar, M., Parisi, G. & Zhang, Y.-C. *Dynamic Scaling of Growing Interfaces*. Phys. Rev. Lett. **56,** 889–892 (1986).

189. Majumdar, S. N. & Comtet, A. *Exact Maximal Height Distribution of Fluctuating Interfaces*. Phys. Rev. Lett. **92,** 225501 (2004).

190. Majumdar, S. N., Pal, A. & Schehr, G. *Extreme value statistics of correlated random variables: A pedagogical review*. Phys. Rep. **840,** 1–32 (2020).

191. Reimann, P., Schmid, G. J. & Hänggi, P. *Universal equivalence of mean first-passage time and Kramers rate*. Phys. Rev. E **60,** R1–R4 (1999).

192. Kolmogorov, A. N. *The Wiener spiral and some other interesting curves in Hilbert space.* in *Dokl. Akad. Nauk SSSR* **26** (1940), 115–118.

193. Mandelbrot, B. B. & Van Ness, J. W. *Fractional Brownian Motions, Fractional Noises and Applications*. SIAM Rev. **10,** 422–437 (1968).

194. Krug, J., Kallabis, H., Majumdar, S. N., Cornell, S. J., Bray, A. J. & Sire, C. *Persistence exponents for fluctuating interfaces*. Phys. Rev. E - Stat. Physics, Plasmas, Fluids, Relat. Interdiscip. Top. **56,** 2702–2712 (1997).

195. Hassani, M. *Approximation Of The Lambert W Function And Hyperpower Function* tech. rep. 4 (School of Communications, Informatics, Faculty of Engineering, and Science, Victoria University of Technology, 2005), 5.

196. Preumont, A. *Vibrations des structures, interactions avec les fluides, sources d'excitations aleatoires*. J. Sound Vib. **133,** 527–528 (1989).

197. Abraham, M. J., Murtola, T., Schulz, R., Páll, S., Smith, J. C., Hess, B. & Lindahl, E. *GROMACS: High performance molecular simulations through multi-level parallelism from laptops to supercomputers*. SoftwareX **1,** 19–25 (2015).

198. Nosé, S. *A molecular dynamics method for simulations in the canonical ensemble.* Mol. Phys. **52,** 255–268 (1984).

199. Hoover, W. G. *Canonical dynamics: Equilibrium phase-space distributions*. Phys. Rev. A **31,** 1695–1697 (1985).

200. Parrinello, M. & Rahman, A. *Polymorphic transitions in single crystals: A new molecular dynamics method*. J. Appl. Phys. **52,** 7182–7190 (1981).

201. Pártay, L. B., Hantal, G., Jedlovszky, P., Vincze, Á. & Horvai, G. *A new method for determining the interfacial molecules and characterizing the surface roughness in computer simulations. Application to the liquid–vapor interface of water*. J. Comput. Chem. **29,** 945–956 (2008).

202. Sega, M., Hantal, G., Fábián, B. & Jedlovszky, P. *Pytim: A python package for the interfacial analysis of molecular simulations*. J. Comput. Chem. **39,** 2118–2125 (2018).

203. Sega, M. *The role of a small-scale cutoff in determining molecular layers at fluid interfaces*. Phys. Chem. Chem. Phys. **18,** 23354–23357 (2016).

204. Bittner, E., Nußbaumer, A. & Janke, W. *Anisotropy of the interface tension of the three-dimensional Ising model*. Nucl. Phys. B **820,** 694–706 (2009).

205. Neyt, J.-C., Wender, A., Lachet, V. & Malfreyt, P. *Prediction of the Temperature Dependence of the Surface Tension Of SO ₂ , N ₂ , O ₂ , and Ar by Monte Carlo Molecular Simulations*. J. Phys. Chem. B **115,** 9421–9430 (2011).

206. Cahn, R. W. *Materials science: Melting and the surface*. Nature **323,** 668–669 (1986).

207. Mei, Q. & Lu, K. *Melting and superheating of crystalline solids: From bulk to nanocrystals*. Prog. Mater. Sci. **52,** 1175–1262 (2007).

208. Daeges, J., Gleiter, H. & Perepezko, J. *Superheating of metal crystals*. Phys. Lett. A **119,** 79–82 (1986).

209. Lindemann, F. A. *Über die Berechnung molekularer Eigenfrequenzen*. Phys. Zeitschrift **11,** 1–4 (1910).

210. Born, M. *Thermodynamics of crystals and melting*. J. Chem. Phys. **7,** 591–603 (1939).

211. Mori, H., Okamoto, H. & Isa, S. *Theory of melting*. Physica **73,** 237–248 (1974).

212. Fecht, H. J. & Johnson, W. L. *Entropy and enthalpy catastrophe as a stability limit for crystalline material*. Nature **334,** 50–51 (1988).

213. Tallon, J. L. *A hierarchy of catastrophes as a succession of stability limits for the crystalline state*. Nature **342,** 658–660 (1989).

214. Jin, J. H., Gumbsch, P., Lu, K. & Ma, E. *Melting mechanisms at the limit of superheating*. Phys. Rev. Lett. **87,** 55703–1–55703–4 (2001).

215. Belonoshko, A. B., Skorodumova, N. V., Rosengren, A. & Johansson, B. *Melting and critical superheating*. Phys. Rev. B - Condens. Matter Mater. Phys. **73,** 1–3 (2006).

216. Lu, K. & Li, Y. *Homogeneous Nucleation Catastrophe as a Kinetic Stability Limit for Superheated Crystal*. Phys. Rev. Lett. **80,** 4474–4477 (1998).

217. Fecht, H. J. *Defect-induced melting and solid-state amorphization*. Nature **356,** 133–135 (1992).

218. Forsblom, M. & Grimvall, G. *How superheated crystals melt.* Nat. Mater. **4,** 388 (2005).

219. Luo, S.-N., Zheng, L., Strachan, A. & Swift, D. C. *Melting dynamics of superheated argon: Nucleation and growth*. J. Chem. Phys. **126,** 034505 (2007).

220. Bai, X.-M. & Li, M. *Ring-diffusion mediated homogeneous melting in the superheating regime*. Phys. Rev. B **77,** 134109 (2008).

221. Wang, Z., Wang, F., Peng, Y., Zheng, Z. & Han, Y. *Imaging the Homogeneous Nucleation During the Melting of Superheated Colloidal Crystals*. Science (80-.). **338,** 87–90 (2012).

222. Samanta, A., Tuckerman, M. E., Yu, T.-Q. & E, W. *Microscopic mechanisms of equilibrium melting of a solid.* Science **346,** 729–32 (2014).

223. Liang, S., Yi, L. & Liang, D. *Molecular insights into the homogeneous melting of methane hydrates*. J. Phys. Chem. C **118,** 28542–28547 (2014).

224. Iglev, H., Schmeisser, M., Simeonidis, K., Thaller, A. & Laubereau, A. *Ultrafast superheating and melting of bulk ice*. Nature **439,** 183–186 (2006).

225. Schmeisser, M., Thaller, A., Iglev, H. & Laubereau, A. *Picosecond temperature and pressure jumps in ice*. New J. Phys. **8,** 104–104 (2006).

226. Schmeisser, M., Iglev, H. & Laubereau, A. *Maximum superheating of bulk ice*. Chem. Phys. Lett. **442,** 171–175 (2007).

227. Schmeisser, M., Iglev, H. & Laubereau, A. *Bulk Melting of Ice at the Limit of Superheating*. J. Phys. Chem. B **111,** 11271–11275 (2007).

228. Fanetti, S., Falsini, N., Bartolini, P., Citroni, M., Lapini, A., Taschin, A. & Bini, R. *Superheating and Homogeneous Melting Dynamics of Bulk Ice*. J. Phys. Chem. Lett. **10,** 4517–4522 (2019).

229. De Koning, M. & Antonelli, A. *Modeling equilibrium concentrations of Bjerrum and molecular point defects and their complexes in ice Ih*. J. Chem. Phys. **128,** 164502 (2008).

230. Pauling, L. *The Structure and Entropy of Ice and of Other Crystals with Some Randomness of atomic arrangement*. J. Am. Chem. Soc. **57,** 2680–2684 (1935).

231. Bernal, J. D. & Fowler, R. H. *A Theory of Water and Ionic Solution, with Particular Reference to Hydrogen and Hydroxyl Ions*. J. Chem. Phys. **1,** 515–548 (1933).

232. Geil, B., Kirschgen, T. M. & Fujara, F. *Mechanism of proton transport in hexagonal ice*. Phys. Rev. B **72,** 014304 (2005).

233. Eigen, M. & De Maeyer, L. *Self-dissociation and protonic charge transport in water and*. Proc. R. Soc. London. Ser. A. Math. Phys. Sci. **247,** 505–533 (1958).

234. Podeszwa, R. & Buch, V. *Structure and Dynamics of Orientational Defects in Ice*. Phys. Rev. Lett. **83,** 4570–4573 (1999).

235. Tanaka, H. & Mohanty, U. *On the Debye-Waller Factor of Hexagonal Ice: A Computer Simulation Study*. J. Am. Chem. Soc. **124,** 8085–8089 (2002).

236. Kolafa, J. & Ončák, M. *Hydrogen-bond defect in the structure of ice Ih*. J. Phys. Chem. C **114,** 20518–20522 (2010).

237. Bolhuis, P. G., Dellago, C. & Chandler, D. *Sampling ensembles of deterministic transition pathways*. Faraday Discuss. **110,** 421–436 (1998).

238. Handel, R., Davidchack, R. L., Anwar, J. & Brukhno, A. *Direct calculation of solid-liquid interfacial free energy for molecular systems: TIP4P ice-water interface*. Phys. Rev. Lett. **100,** 1–4 (2008).

239. Davidchack, R. L., Handel, R., Anwar, J. & Brukhno, A. V. *Ice Ih-water interfacial free energy of simple water models with full electrostatic interactions*. J. Chem. Theory Comput. **8,** 2383–2390 (2012).

240. Espinosa, J. R., Vega, C. & Sanz, E. *Ice–Water Interfacial Free Energy for the TIP4P, TIP4P/2005, TIP4P/Ice, and mW Models As Obtained from the Mold Integration Technique*. J. Phys. Chem. C **120,** 8068–8075 (2016).

241. Nada, H. & Furukawa, Y. *Anisotropy in molecular-scaled growth kinetics at ice-water interfaces*. J. Phys. Chem. B **101,** 6163–6166 (1997).

242. Nada, H. & Furukawa, Y. *Anisotropy in growth kinetics at interfaces between proton-disordered hexagonal ice and water: A molecular dynamics study using the six-site model of H2O*. J. Cryst. Growth **283,** 242–256 (2005).

243. Rozmanov, D. & Kusalik, P. G. *Anisotropy in the crystal growth of hexagonal ice, I h*. J. Chem. Phys. **137,** 094702 (2012).

244. Abascal, J. L. F., Sanz, E., García Fernández, R. & Vega, C. *A potential model for the study of ices and amorphous water: TIP4P/Ice.* J. Chem. Phys. **122,** 234511 (2005).

245. Miller, T. F., Eleftheriou, M., Pattnaik, P., Ndirango, A., Newns, D. & Martyna, G. J. *Symplectic quaternion scheme for biophysical molecular dynamics*. J. Chem. Phys. **116,** 8649–8659 (2002).

246. Kamberaj, H., Low, R. J. & Neal, M. P. *Time reversible and symplectic integrators for molecular dynamics simulations of rigid molecules*. J. Chem. Phys. **122,** 224114 (2005).

247. Plimpton, S. *Fast Parallel Algorithms for Short-Range Molecular Dynamics*. J. Comput. Phys. **117,** 1–19 (1995).

248. Martyna, G. J., Tuckerman, M. E., Tobias, D. J. & Klein, M. L. *Explicit reversible integration algorithms for extended systems.* Mol. Phys **87,** 1117–1157 (1996).

249. Martyna, G. J., Klein, M. L. & Tuckerman, M. E. *Nosé-Hoover chains: The canonical ensemble via continuous dynamics*. J. Chem. Phys. **97,** 2635–2643 (1992).

250. Hockney, R. W. & Eastwood, J. W. *Computer simulation using particles* (crc Press, 1988).

251. Darden, T., York, D. & Pedersen, L. *Particle mesh Ewald: An N·log(N) method for Ewald sums in large systems*. J. Chem. Phys. **98,** 10089–10092 (1993).

252. Ayala, R. B. & Tchijov, V. *A molecular dynamics study of ices III and V using TIP4P and TIP5P water models*. Can. J. Phys. **81,** 11–16 (2003).

253. Lyubartsev, A. P., Martsinovski, A. A., Shevkunov, S. V. & Vorontsov-Velyaminov, P. N. *New approach to Monte Carlo calculation of the free energy: Method of expanded ensembles*. J. Chem. Phys. **96,** 1776–1783 (1992).

254. Marinari, E. & Parisi, G. *Simulated Tempering: A New Monte Carlo Scheme*. Europhys. Lett. **19,** 451–458 (1992).

255. Okabe, T., Kawata, M., Okamoto, Y. & Mikami, M. *Replica-exchange Monte Carlo method for the isobaric–isothermal ensemble*. Chem. Phys. Lett. **335,** 435–439 (2001).

256. Mori, Y. & Okamoto, Y. *Generalized-Ensemble Algorithms for the Isobaric–Isothermal Ensemble*. J. Phys. Soc. Japan **79,** 074003 (2010).

257. Małolepsza, E. & Keyes, T. *Water Freezing and Ice Melting*. J. Chem. Theory Comput. **11,** 5613–5623 (2015).

258. Moritz, C., Sega, M., Innerbichler, M., Geissler, P. L. & Dellago, C. *Weak scaling of the contact distance between two fluctuating interfaces with system size*. Phys. Rev. E **102,** 062801 (2020).

259. Scherer, M. K., Trendelkamp-Schroer, B., Paul, F., Pérez-Hernández, G., Hoffmann, M., Plattner, N., Wehmeyer, C., Prinz, J. H. & Noé, F. *PyEMMA 2: A Software Package for Estimation, Validation, and Analysis of Markov Models*. J. Chem. Theory Comput. **11,** 5525–5542 (2015).

260. Vila Verde, A., Bolhuis, P. G. & Campen, R. K. *Statics and dynamics of free and hydrogen-bonded OH groups at the air/water interface.* J. Phys. Chem. B **116,** 9467–81 (2012).

261. Le Vot, F., Yuste, S. B., Abad, E. & Grebenkov, D. S. *First-encounter time of two diffusing particles in confinement*. Phys. Rev. E **102,** 32118 (2020).

262. Sivak, D. A., Chodera, J. D. & Crooks, G. E. *Time Step Rescaling Recovers Continuous-Time Dynamical Properties for Discrete-Time Langevin Integration of Nonequilibrium Systems*. J. Phys. Chem. B **118,** 6466–6474 (2014).

263. Metropolis, N., Rosenbluth, A. W., Rosenbluth, M. N., Teller, A. H. & Teller, E. *Equation of State Calculations by Fast Computing Machines*. J. Chem. Phys. **21,** 1087 (1953).

264. Torrie, G. & Valleau, J. *Nonphysical sampling distributions in Monte Carlo free-energy estimation: Umbrella sampling*. J. Comput. Phys. **23,** 187–199 (1977).

265. Aric, H. A., Schult, D. A. & Pieter, S. J. *Exploring Network Structure, Dynamics, and Function using NetworkX*. in *Proc. 7th Python Sci. Conf. (SciPy 2008)* (eds Varoquaux, G., Vaught, T. & Jarrod Millman) (2008), 11–15.

266. Dijkstra, E. W. *A note on two problems in connexion with graphs*. Numer. Math. **1,** 269–271 (1959).

267. Pedregosa, F. *et al. Scikit-learn: Machine Learning in {P}ython*. J. Mach. Learn. Res. **12,** 2825–2830 (2011).

268. Hertz, P. *Über den gegenseitigen durchschnittlichen Abstand von Punkten, die mit bekannter mittlerer Dichte im Raume angeordnet sind*. Math. Ann. **67,** 387–398 (1909).